UAB
Universitat Autònoma de Barcelona

Ph.D. Thesis

Piezoelectric Micromachined Ultrasonic Transducers (PMUTs) integrated on CMOS

A dissertation submitted in fulfillment of the requirements for the degree of

Doctor in Electronic and Telecommunication Engineering

in the

Department of Electronic Engineering

Universitat Autònoma de Barcelona

Author:
Eyglis Ledesma Valdés

Supervisor:
Núria Barniol Beumala

July, 2022

La Dra. Núria Barniol Beumala, Catedràtica d'Electrònica del Departament d'Enginyeria Electrònica de la Universitat Autònoma de Barcelona,

CERTIFICA:

que la memòria: "Piezoelectric Micromachined Ultrasonic Transducers (PMUTs) integrated on CMOS" que presenta Eyglis Ledesma Valdés per optar al grau de Doctor en Enginyeria Electrònica, ha estat realizada sota la seva direcció.

Bellaterra, Junio del 2022

To my beloved family...

ACKNOWLEDGMENTS

ABSTRACT

The need for new minute and compact ultrasound systems for non-invasive applications in limited area (such as wearables or intravascular ultrasound systems) has recently inspired the scientific community to develop novel ultrasound devices based on thin-film piezoelectrical materials following a MEMS technology process. Robustness of the MEMS technology along with low power needs for transduction on the piezoelectrical material (in comparison with capacitive ultrasound transducers), provides high yield fabrication towards a large number of equal devices in an arrayed form. Additionally, the possibility of the integration with CMOS will further allow edge processing directly at the chip level, providing smartness in a very compact system. In this context, the research presented in this dissertation focuses on improving the performance of piezoelectric micromachined ultrasonic transducers (PMUTs) ensuring the capability to be integrated monolithically on CMOS substrates. The goal is to provide a compact device with improved performance and reliability as an ultrasound system compared to the state-of-the-art. The technology provided by Silterra ensures the possibility of integrating with the CMOS circuitry with minimal parasitic capacities and a high fill factor in array systems.

In particular, this research deals, firstly, with the optimization of single PMUTs devices towards the improvement of their acoustic performance following three main approaches: (1) innovative modifications of the design structure, (2) variations in the piezoelectric materials, and (3) layers thicknesses scaling. Several designs of PMUTs (single and in array configurations), AlN, and AlScN as piezoelectric materials, and thicknesses ranging from 1 μm to 1.5 μm for the passive layer and from 0.6 μm to 1.3 μm for the active layer are analyzed, modeled, and characterized throughout this thesis. Finally, the application of these PMUT-on-CMOS devices in imaging systems and as a fluid sensor to extract the hydrodynamic properties of liquids, demonstrate the versatility achieved by the developed systems.

RESUMEN

La necesidad de nuevos sistemas de ultrasonido compactos y de tamaño reducido para aplicaciones no invasivas de área limitada (como dispositivos portátiles o sistemas de ultrasonido intravascular) ha inspirado recientemente a la comunidad científica a desarrollar nuevos dispositivos de ultrasonido basados en materiales piezoeléctricos de película delgada siguiendo un proceso basado en tecnología MEMS. La robustez de la tecnología MEMS junto con las necesidades de baja potencia para la transducción en el material piezoeléctrico (en comparación con los transductores de ultrasonido capacitivos), proporciona una fabricación de alto rendimiento para una gran cantidad de dispositivos iguales en forma de matrices. Además, la posibilidad de integración con CMOS permitirá aún más el procesamiento directamente a nivel de chip, proporcionando inteligencia en un sistema muy compacto. En este contexto, la investigación presentada en esta tesis se centra en mejorar el rendimiento de los transductores ultrasónicos micromecanizados piezoeléctricos (PMUT), asegurando la capacidad de integrarse monolíticamente en sustratos CMOS. El objetivo es proporcionar un dispositivo compacto con un rendimiento y una fiabilidad mejorados como sistema de ultrasonido en comparación con el estado del arte. La tecnología proporcionada por Silterra asegura la posibilidad de integración con el circuito CMOS con mínimas capacidades parásitas y con un alto factor de relleno en sistemas de matriz.

En particular, esta investigación trata, en primer lugar, de la optimización de dispositivos PMUT individuales para mejorar su rendimiento acústico siguiendo tres enfoques principales: (1) modificaciones innovadoras de la estructura de diseño, (2) variaciones en los materiales piezoeléctricos y (3) variaciones de los espesores de las capas. Varios diseños de PMUT (configuraciones simples y en matrices), AlN y AlScN como materiales piezoeléctricos, y espesores que van desde 1 μm hasta 1,5 μm para la capa pasiva y desde 0,6 μm hasta 1.3 μm para la capa activa se analizan, modelan y caracterizan a lo largo de esta tesis.

Finalmente, la aplicación de estos dispositivos PMUT-on-CMOS en sistemas de imagen y como sensor de fluidos para extraer las propiedades hidrodinámicas de los líquidos, demuestran la versatilidad lograda por los sistemas desarrollados.

CONTENTS

LIST OF FIGURES

LIST OF TABLES

PREFACE

Miniaturization, low power consumption, and low manufacturing cost are becoming progressively imperative requirements in an increasing number of fields in the sensor market, including ultrasound as a characterization technique. In this sense, ultrasound MEMS/NEMS technologies show fast growth in huge companies such as Samsung, Philips, or TDK InvenSense to implement devices that include sensors for positioning, gesture recognition, imaging, health care, biometrics, etc. In recent years, Piezoelectric Micromachined Ultrasonic Transducers (PMUTs) are becoming a powerful, straightforward, and economical alternative in these sectors, since a small device, at the same time, can achieve high sensitivities as a transmitter and receiver with low power consumption and, also, is capable of integration on CMOS circuitry. For this, many efforts have been carried out by the scientific community to optimize their layouts, materials, and layers in order to achieve PMUT-CMOS-based systems with improved capabilities, and under our knowledge, only heterogeneous solutions have been demonstrated. In this context, this thesis focuses on developing ultrasound systems with high performance based on PMUT on CMOS. To accomplish this, two main tasks were developed at each stage.

- **Design and Model:** In this step, a deep analysis of the PMUT's theory was carried out. Dimensions, thickness, and piezoelectric materials were studied to obtain and optimize different shapes and configurations of PMUTs devices compatibles with the CMOS process.

- **Characterize and Validate:** This task consists of the electrical and acoustic characterization of the fabricated PMUTs-on-CMOS and subsequent validation as ultrasound systems for several applications.

The achievements reached during these years were presented in recognized journals and conferences in the field.

Compendium of Publications (contribution as the first author) included in this thesis.

- **Jour4**: **E. Ledesma**, I.Zamora, J.Yáñez, A.Uranga, N.Barniol, "Single-Cell system using monolithic PMUTs-on-CMOS to monitor fluid hydrodynamic properties". Microsystems & Nanoengineering, DOI : 10.1038/s41378-022-00413-y (in process of publication, accepted in June 2022).

- **Jour3**: **Ledesma, E.**; Zamora, I.; Uranga, A.; Torres, F.; Barniol, N. Enhancing AlN PMUTs' Acoustic Responsivity within a MEMS-on-CMOS Process. Sensors 2021, 21, 8447. https://doi.org/10.3390/s21248447

- **Jour2**: **Ledesma, E.**; Zamora, I.; Uranga, A.; Barniol, N. Multielement Ring Array Based on Minute Size PMUTs for High Acoustic Pressure and Tunable Focus Depth. Sensors 2021, 21, 4786. https://doi.org/10.3390/s21144786

- **Jour1**: **E. Ledesma**, I. Zamora, A. Uranga and N. Barniol, "Tent-Plate AlN PMUT With a Piston-Like Shape Under Liquid Operation," in IEEE Sensors Journal, vol. 20, no. 19, pp. 11128-11137, 1 Oct.1, 2020, doi: 10.1109/JSEN.2020.2995643

Complementary contributions (sharing the first authorship with I.Zamora).

- I. Zamora, **E. Ledesma**, A. Uranga and N. Barniol, "Phased Array Based on AlScN Piezoelectric Micromachined Ultrasound Transducers Monolithically Integrated on CMOS," in IEEE Electron Device Letters, vol. 43, no. 7, pp. 1113-1116, July 2022, doi: 10.1109/LED.2022.3175323.

- I. Zamora, **E. Ledesma**, A. Uranga and N. Barniol, "Monolithic Single PMUT-on-CMOS Ultrasound System With +17 dB SNR for Imaging Applications," in IEEE Access, vol. 8, pp. 142785-142794, 2020, doi: 10.1109/ACCESS.2020.3013763.

Other contributions of the author in international journals as second author.

- Zamora, I.; **Ledesma, E.**; Uranga, A.; Barniol, N. High Accuracy Ultrasound Micro-Distance Measurements with PMUTs under Liquid Operation. Sensors 2021, 21, 4524. https://doi.org/10.3390/s21134524

- Zamora, I.;**Ledesma, E.**; Uranga, A.; Barniol, N. Miniaturized 0.13-μm

CMOS Front-End Analog for AlN PMUT Arrays. Sensors 2020, 20, 1205. https://doi.org/10.3390/s20041205

Contribution to scientific conferences.

- **E. Ledesma**; I. Zamora; A. Uranga; N. Barniol, "A 0.5 mm^2 pitch-matched AlN PMUT-on-CMOS ultrasound imaging system," accepted for lecture presentation in IEEE IUS 2022 (October 10-13, 2022. Venice, Italy).

- J.Yanez, **E. Ledesma**, A. Uranga and N. Barniol, "AlN-based HBAR ultrasonic sensor for fluid detection in microchannels with multi-frequency operation capability over the GHz range," 2021 IEEE International Ultrasonics Symposium (IUS), 2021, pp. 1-4, doi: https://doi.org/10.1109/IUS52206.2021.9593369

- **E. Ledesma**, I. Zamora, A. Uranga and N. Barniol, "Monolithic PMUT-on-CMOS Ultrasound System for Single Pixel Acoustic Imaging," 2021 IEEE 34th International Conference on Micro Electro Mechanical Systems (MEMS), 2021, pp. 394-397, doi: 10.1109/MEMS51782.2021.9375231

- **E. Ledesma**, I. Zamora, A. Uranga and N. Barniol, "9.5 % Scandium Doped ALN PMUT Compatible with Pre-Processed CMOS Substrates," 2021 IEEE 34th International Conference on Micro Electro Mechanical Systems (MEMS), 2021, pp. 887-890, doi: 10.1109/MEMS51782.2021.9375359

- J. Yanez, **E. Ledesma**, A. Uranga and N. Barniol, "Improved Electromechanical Transduction for PiezoMUMPS HBAR Impedance Sensors," 2020 Joint Conference of the IEEE International Frequency Control Symposium and International Symposium on Applications of Ferroelectrics (IFCS-ISAF), 2020, pp. 1-5, doi: 10.1109/IFCS-ISAF41089.2020.9234913.

- **E. Ledesma**; I. Zamora; V. Tzanov; F. Torres; A. Uranga; N. Barniol; E. Marigó; Mohan Soundara-Pandian, "Liquid operable AlN PMUT with high output pressure capabilities," 2019 IEEE International Ultrasonics Symposium (IUS), 2019, pp. 251-254, doi: 10.1109/ULTSYM.2019.8926234

- **E. Ledesma**; I. Zamora; F. Torres; A. Uranga; V. Tzanov; N. Barniol; E. Marigó; Mohan Soundara-Pandian, "AlN Piezoelectric Micromachined Ultrasonic Transducer Array Monolithically Fabricated on Top of Pre-Processed CMOS Substrates," 2019 20th International Conference on Solid-State Sensors, Actuators and Microsystems & Eurosensors XXXIII (TRANSDUCERS & EUROSENSORS XXXIII), 2019, pp. 655-658, doi: 10.1109/TRANSDUC-

ERS.2019.8808706

- **E. Ledesma**; V. Tzanov; I. Zamora; F. Torres; A. Uranga; N. Barniol; E. Marigó; Mohan Soundara-Pandian, "ALN Pmut with Crossed-Cavity for Better Acoustic Pressure Outputs in Liquid at High Frequency," 2019 20th International Conference on Solid-State Sensors, Actuators and Microsystems & Eurosensors XXXIII (TRANSDUCERS & EUROSENSORS XXXIII), 2019, pp. 825-828, doi: 10.1109/TRANSDUCERS.2019.8808260

- Tzanov, Vassil, **Eyglis Ledesma**, Francesc Torres and Núria Barniol. "Ultrasound Pressure Field Of A Resonating Piezoelectric Membrane With Three Excitation Electrodes," COMSOL 2018.

- I. Zamora, **E. Ledesma**, A. Uranga and N. Barniol, "DESIGN OF A FULLY INTEGRATED CMOS-PMUT SYSTEM," 2018 Conference on Design of Circuits and Integrated Systems (DCIS), 2018, pp. 1-5, doi: 10.1109/DCIS.2018.8681498

- I. Zamora, **E. Ledesma**, A. Uranga and N. Barniol, "Fully Integrated CMOS-PMUT Transceiver," 2018 25th IEEE International Conference on Electronics, Circuits and Systems (ICECS), 2018, pp. 149-152, doi: 10.1109/ICECS.2018.8618044

- **Ledesma, E.**; Zamora, I.; Torres, F.; Uranga, A.; Tzanov, V.; Barniol, N.; Marigó, E.; Soundara-Pandian, M. Squared PMUT with Enhanced Pressure Sensitivities. Proceedings 2018, 2, 925, doi: 10.3390/proceedings2130925

These contributions are organized in the thesis as follows:

Chapter 1 consists of the introductory chapter which provides a general overview of ultrasound devices and their market evolution, focusing the attention on Micromachined Ultrasonic Transducers (MUTs). In addition, topics regarding the integration approaches with the CMOS circuitry have been dissected in order to understand the benefits of monolithic integration. Following the same idea, **Chapter 2** covers the working principle of the PMUTs devices in the air and immersed in a fluid (resonance frequencies, displacement, transmitted and sensed pressure, etc.). In addition, it includes an overview of the properties of the piezoelectricity and thin-film piezoelectric materials. **Chapter 3**, in contrast, shows a general description of the simulation tools, PMUT fabrication process based on MEMS-on-CMOS Silterra technology, as well as the experimental tools and procedures with emphasis on their limitations, used during

this PhD Thesis. **Chapter 4** and **Chapter 5** provide main results achieved and which are published in the journals. Chapter 4 deals with the individual PMUT optimization while Chapter 5 deals with the arrayed configuration.

Geometric optimization in the layouts of single PMUT devices is the first aspect discussed in **Chapter 4**. In this context, a tent-plate PMUT is modeled, simulated, and characterized to demonstrate the benefits of modifying the clamping boundaries of a square PMUT to achieve a softer flexural resonator in its first mode and consequently produce higher output acoustic pressure as an acoustic source and higher electrical signal as sensor. The analysis, the simulations and the experimental characterization is fully explained in **Jour1**, while in Chapter 4 some complementary information is given. The second undertaken approach to achieve improved PMUTs was the analysis and proposal of the optimum layer thicknesses, i.e. piezoelectric layer and passive layer. In this case, after analysis through FEM simulations, several proposals to Silterra foundry were made, and finally, some of them were successfully fabricated and conveniently characterized. Again the analysis and main experimental characterization can be found in the paper **Jour3**, and some additional aspects are included in the chapter. The third but not least improvement is related to the piezoelectric material, where AlN with a 9.5 % Scandium concentration ensures better results as an ultrasound transceiver. Once the best single PMUT is determined, we apply the PMUT-on-CMOS system for developing a single-cell fluid monitoring capable to determine the density, viscosity, compressibility, and sound velocity of the fluid media. This study is explained in the paper **Jour4**. In this Chapter 4 a final comparison of the different implemented PMUTs and its comparison with other approaches from the literature is also provided. It is important to highlight that in this Chapter, is reported, under our knowledge, for the first time a PMUT integrated monolithically on CMOS substrate.

On the other hand, **Chapter 5** deals with PMUT arrays where the aims of this chapter will be to demonstrate their potential of them as suitable ultrasound systems with imaging capabilities as can be focus depth tuning for 3D imaging. First, a PMUT-on-CMOS linear array is analyzed, and an ultrasound image is achieved as a final result demonstrating the performance in a pitch-matched pulse-echo system with an area of 0.5 mm^2 (these results will be presented at the IUS 2022 conference). Second, a multi-element ring array is in-deep studied due to their ability for tunable depth focus. The paper **Jour2** contains the analysis, simulations and experimental results for this multi-element ring array with PMUTs without integrated CMOS. In the last

part of Chapter 5, some experiments using a CMOS-integrated multi-element ring array are shown to further validate the liquid sensing capabilities of the system, even when using some sort of container is used over the PMUT surface.

INTRODUCTION

Ultrasound is defined by the American National Standards Institute as "sound at frequencies greater than 20 kHz". From an historic perspective, ultrasound waves is a very old technology. It was back in 1793 when Lazzaro Spallanzani discovered that bats uses ultrasound waves for navigate and hunt, using echolocation [1]. Echolocation occurs when an ultrasound wave is transmitted, and the echo produced when the ultrasound wave is reflected by an object is received back by a receiver situated at the same position or near-by the transmitter. From the time elapsed between transmission and reception (time-of-flight) and knowing the sound velocity in the media, it is possible to establish the distance from the transmitter to the target (object) (see Fig. 1.1). Ultrasound waves can be transmitted in air, in liquid or in solid materials.
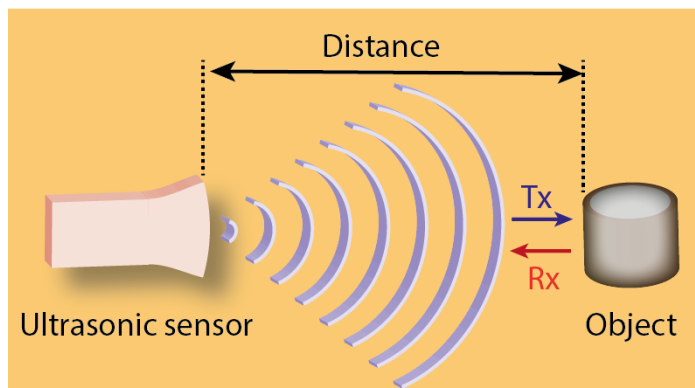
Figure 1.1: Ultrasonic device used in a pulse-echo configuration.

The first technological application of ultrasound was developed by Paul Langevin, for the echolocation of submarines in the sea (known as sonar) in early 1918, using piezoelectrical materials to develop the transducer for generating and detecting the ultrasonic wave in water [2]. In 1947 the first medical imaging system for diagnosis was invented by Karl Theodore Dussik [3], being nowadays one of the most important diagnosis tools not only in the medical field but also for materials characterization due to the non-destructive character [4], [5]. Figure 1.2 from Yole Development group, give an overview of the main applications with details on the used ultrasound frequency [6]. The production and sensing of the ultrasound waves require proper transducers to convert electrical energy into acoustic energy and vice versa, where piezoelectricity is one of the most used transduction techniques. The piezoelectric effect dates back to 1880 when the Curie brothers discovered that crystals of quartz were able to generate an electric charge by applying pressure, and on the contrary, if they applied an electric potential then the quartz vibrated [7].
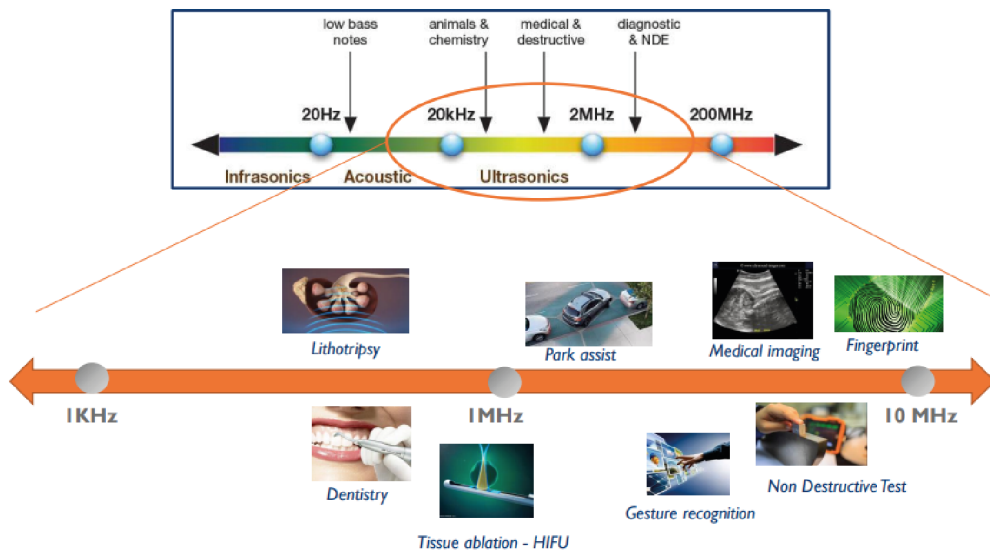
Figure 1.2: Ultrasound Applications by Frequencies [6]

.

Nowadays the big demand on new sensory systems for wearable and hand-held devices, is pushing the development of new compact and versatile ultrasonic transducers which should be reliably manufactured for a wide range of different applications. Yole Développement group has recently published a market forecast that considers several applications, see Figure 1.3, in which a CAGR (Compound Average Growth Rate)

for 2025 of 5.1 % is forecast despite the impact of COVID-19. Based on Fig. 1.3 the most prominent applications are automotive-ADAS (Advanced Driver-Assistance Systems), consumer fingerprint, and industrial automation, however, it has a lot of potential in other scientific branches, but it does not show a rapid increase yet. Specifically, the current state-of-the-art exposes ultrasound as a reliable method for medical applications: intravascular and endoscopy imaging[8]–[10], brain stimulation [5], [11], portable devices [12]–[14], and treatments based on high intensity focused ultrasound (HIFU) [15]. Furthermore, it is used in range-finding applications [16], [17], gesture recognition [18], and consumer devices such as smartphones or laptops with biometric fingerprint sensors [19], [20]. In addition, it is an excellent alternative in biomedical and industrial processes to characterize the mechanical properties of liquids [21]–[23].
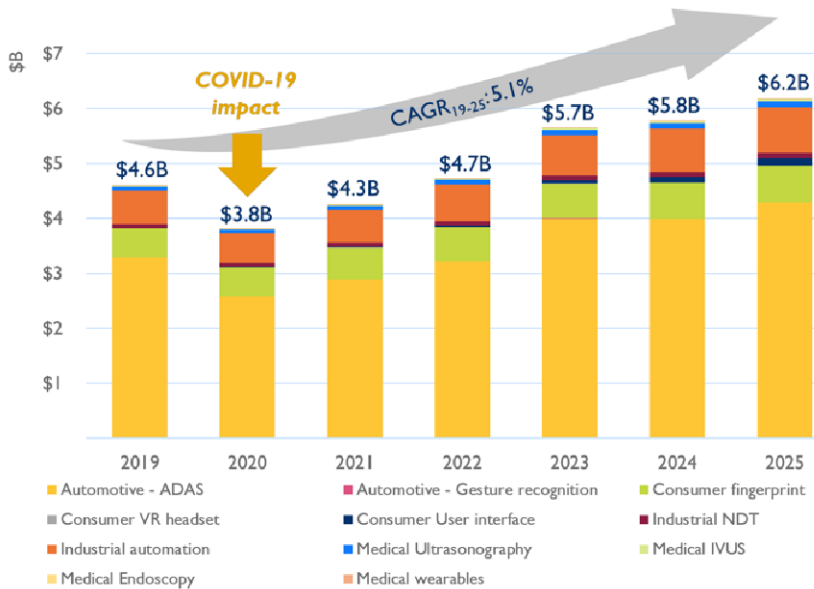
Figure 1.3: Ultrasound sensing modules market forecasts from 2019 to 2025 by applications [24]

Conventional ultrasonic transducers are based on piezoelectric materials operating in their thickness vibration modes, such as bulk piezoelectric or piezocomposite devices. Piezoelectric materials enable electromechanical transduction, which converts mechanical energy to electrical energy or vice versa. In this mode of operation, the longitudinal vibration utilizes the d_{33} coefficient, where an electrical field (E_f) causes a longitudinal displacement, see Fig. 1.4a. Figure 1.4b shows a general configuration

3

of a conventional single-element ultrasonic transducer [25]. Two electrodes placed on each side of the piezoelectric material allow an electrical signal to be applied at a specific frequency, which will result in a flexural motion and thus generate a pressure wave. In contrast, in the sensing mode, an incoming ultrasound wave causes a voltage on the electrodes that will be acquired and processed. Furthermore, two additional materials are used for the matching and backing layers at the front and back of the device. The first one is used to improve the match between the ultrasonic transducer and the medium (i.e., water, tissue), while the backing material avoids the generation of unwanted signals from the backside and allows for a wider bandwidth. However, there are a lot of geometry and frequency limitations when it comes to implementing 2D ultrasonic transducer arrays. The diced process to achieve 2D arrays with high frequencies (around 10 MHz) and the interconnection of every single element increases their complexity, timing, and cost in manufacturing [25], [26].
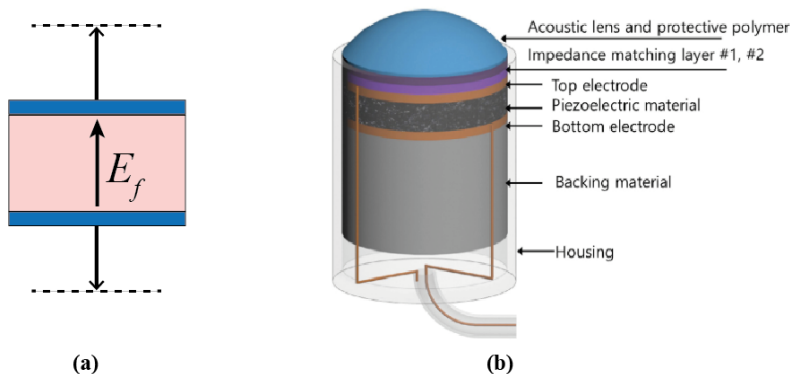
Figure 1.4: Schematic representation of the d_{33} coefficient. Extracted and edited image from [27]. Configuration of packaged single-element ultrasonic transducer [25].

1.1 Micromachined Ultrasonic Transducers (MUTs)

The development of Micro-Electro-Mechanical Systems (MEMS) technology has allowed getting ultrasonic transducers of minute size, lower manufacturing cost, improved bandwidth, and lower power consumption than conventional ultrasonic transducers [28], [29]. In addition MEMS processing provides a very robust technology allowing parallel fabrication of multiple equal ultrasound transducers, as single elements or in an arrayed system, which constitutes a winning advantage compared with other piezomaterials based on crystals or polymers. Furthermore, these new ultrasonic devices can be directly interconnected with the CMOS (complementary metal

oxide semiconductor) circuitry achieving a compact ultrasound system, opening the way towards a real Ultrasound-on-chip system. Micromachined Ultrasonic Transducers (MUTs) as they are known, work in the flexural mode and they can be classified depending on the principle of operation in capacitive (CMUT) and piezoelectric (PMUT), Fig. 1.5a and b, respectively.
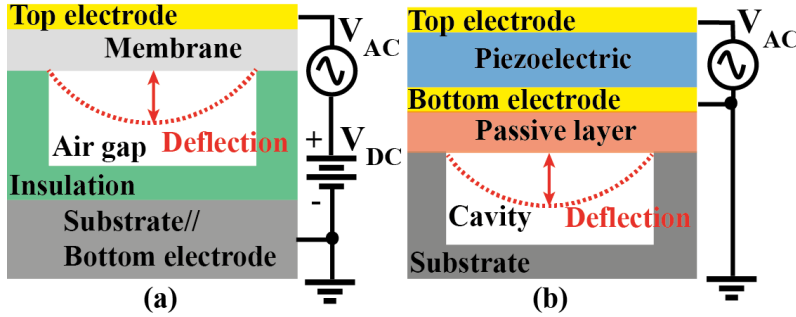
Figure 1.5: Schematic illustrations of a generic (a) Capacitive Micromachined Ultrasonic Transducer (CMUT), and (b) Piezoelectric Micromachined Ultrasonic Transducer PMUT. (Layers not to scale.)Extracted and edited from [26].

1.1.1 Capacitive Micromachined Ultrasonic Transducers (CMUTs)

A Capacitive Micromachined Ultrasonic Transducer (CMUT) is a tiny device fabricated using MEMS technology. A typical CMUT is composed of a thin membrane above a vacuum gap with two electrodes (top and bottom) which are separated by an isolation layer in order to avoid an electrical shortcut between them [10]. As it can be seen in Figure 1.5a, the bottom electrode is commonly made using a conductive silicon wafer while the top electrode could be, for example, aluminum (Al). However, in some designs, conductive silicon material is used in the membrane avoiding to use of a top electrode [30].

The working principle of CMUTs is based on the electrostatic effect and it can be used to generate and receive ultrasound waves. Figure 1.5a shows a schematic representation of a generic CMUT when it works as an actuator. In order to guarantee its proper operation a direct current (V_{DC}) and an alternating current (V_{AC}) voltages are required. The electrostatic force depends quadratically with the applied voltage, and consequently both voltages allows the membrane to vibrate at the same AC driving frequency, achieving its maximum displacement if the AC frequency is the CMUT natural frequency [30]. Likewise, on the sensing mode, a DC voltage is also essential and the incoming ultrasound wave is detected by a capacitive detection. The incident wave causes the vibration of the membrane and therefore, takes place a modulation

5

of the gap height [10]. This fact modifies the overall capacitance of the device and consequently, the generated output current. Finally, this is converted into a voltage that can be detected and processed by read-out circuitry (RX).

In general, CMUTs offer great potential as ultrasonic transducers due to their high electromechanical coupling coefficient, wide bandwidth, and capability of on-chip integration with CMOS circuitry such as amplifiers, and analog-to-digital converters [31]. Meanwhile, well-controlled MEMS technology in each process enables small-volume array implementation [32]. Despite this, the high DC bias voltage (higher than 100V) required for the correct operation increases the power consumption. Also, CMUTs need different air gaps in order to generate a high acoustic pressure (large air gap), and optimize the receive sensitivity (small air gap), which coupled with some technical limitations on the gap height imposed by the foundry manufacturing rules, increase the complexity and cost of fabrication [33], [34].

1.1.2 Piezoelectric Micromachined Ultrasonic Transducers (PMUTs)

A Piezoelectric Micromachined Ultrasonic Transducer (PMUT) is a multilayered minute device with a piezoelectrical layer and, like a CMUT, is capable of transmitting and receiving acoustic pressure waves. Basically, it consists of a membrane over a cavity composed of a thin piezoelectric film sandwiched between two electrodes as well as an elastic layer at the top or bottom of the membrane [26]. A generic schematic of a PMUT is shown in Figure 1.5b.

Unlike conventional ultrasonic devices, PMUTs use the d_{31} coefficient to create a mechanical deformation via bending. This coefficient appears, as shown in Fig. 1.6 when an electric field is applied in the transverse direction creating a displacement perpendicular. Based on this, if an electric field is applied to a PMUT, the effect of the d_{31} coefficient causes a deformation in the adjacent materials generating an acoustic wave [27], see Fig. 1.6. Summarizing, the operation of PMUTs is based
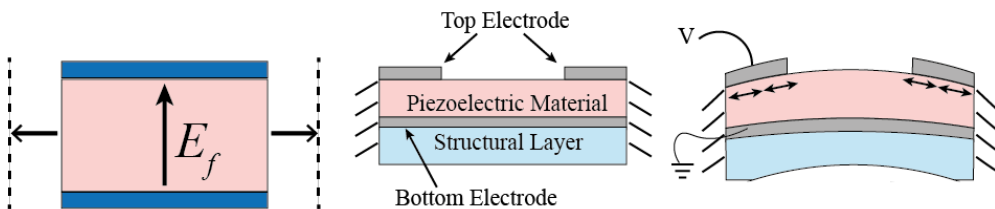
Figure 1.6: (left): Schematic representation of the d_{31} coefficient. (center-right): Cross-section of a PMUT device.Extracted and edited images from [27].

on the inverse and direct piezoelectric effect. As a transmitter (inverse piezoelectric effect) if an AC signal (V_{AC}) is applied to the membrane at the resonance frequency, an ultrasound wave will be generated due to the membrane deflection, see Figure 1.5c. On the sensing mode (direct piezoelectric effect), when an ultrasound wave hits on the PMUT surface it causes a vibration of the membrane which can be detected measuring the electric output between both electrodes and therefore amplified and processed by a read-out circuitry (RX).

PMUTs vs CMUTs

In the new digital era, where low power consumption and small sizes are required, PMUTs are suited for many applications. They are power-efficient devices because they don't require a DC bias voltage, and they aren't limited regarding the cavities height for actuation and sensing, reducing cost and complexity of the fabrication process [26]. Furthermore, PMUTs are less sensitive to parasitic capacitance as a consequence of their low electrical impedance, which also allows a better matching with the electronic circuitry [28], and also, they don't need a matching layer to the acoustic media. However, their main limitation is imposed by the low electromechanical coupling coefficient that ranges between 1 % and 6 % in comparison to an 18 % and 70 % for CMUTs devices [25]. Based on the benefits offered by PMUTs devices, in the last years, they have become an excellent candidate in the ultrasound market devices, showing a high level of integration and miniaturization, see Fig. 1.7.
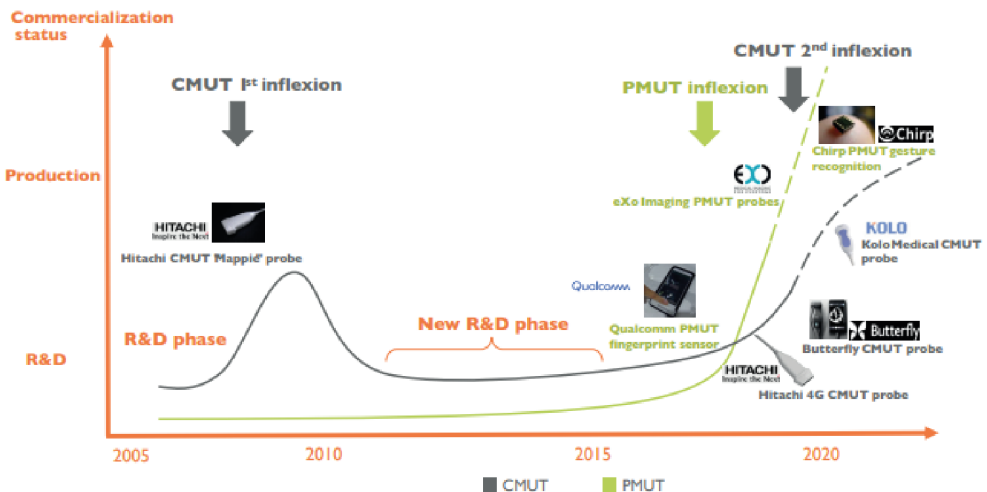
Figure 1.7: Ultrasound sensing: product introduction & technology roadmap [6].

1.2 Integration approaches

CMOS ASICs (Application Specific Integrated Circuits) are used to generate the driving signals, amplify and filter the incoming ultrasound wave, and in the 2D arrays, for example, focus and steer the ultrasound beam. The integration of ultrasound transducers and electronics provides compact systems, offering a single chip that includes the MEMS device and the CMOS circuitry, and therefore reducing the cost of the final commercialized device. Based on this, there are two technologies for integrating MUTs and CMOS-ASICs circuitry: Hybrid multi-chip solution and System-on-Chip (SoC) [35].

1.2.1 Hybrid multi-chip Integration

Hybrid multi-chip integration is a strategy where MEMS devices (MUTs) and CMOS-ASICs circuitry are designed, manufactured, and tested on separate substrates and, eventually, hybridized into a common package. This characteristic gives flexibility to the manufacturing process, allowing to optimize the performance of MUTs and CMOS-ASICs.

Wire bonding side-by-side (or 2D interconnection) is the easiest method to connect multi-chip modules (MUTs and CMOS-ASICs), however, it is quite affected by the wire length, which degrades device performance as a consequence of the large parasitic capacitances. Also, they are limited in applications where the occupancy area needs to be smaller. In order to overcome these issues, System-in-Package, SiP, known as vertical or stacked multi-chip modules, guarantees more compactness, decreases the interconnection length, and achieves a higher integration density. The electric contact between them can be made using different methods such as flip-chip and wire bonding, or even, a combination of the aforementioned, and the interconnection can be made directly or through additional layers [35].

Figure 1.8 shows different ultrasound systems where the interconnection between MUTs devices and CMOS-ASICs circuitry was done through hybrid multi-chip integration. In 2013, the presented ultrasound imaging system in [36] uses two flip-chip approaches to interconnect a 32x32 CMUT array with the CMOS-ASICs circuitry: (a) using an interposer substrate, and (b) using direct flip-chip bonding, see Fig. 1.8a and b respectively. Nowadays, the flip-chip bonding through PCB interposers have continued to be used [37], [38], Fig. 1.8c shows an example using a flex PCB. On the other hand, wire bonding has been widely used in many researches as a first prototype [39], [40]. Figure 1.8d indicates a CMUT array interfaced with a CMOS-ASICs to
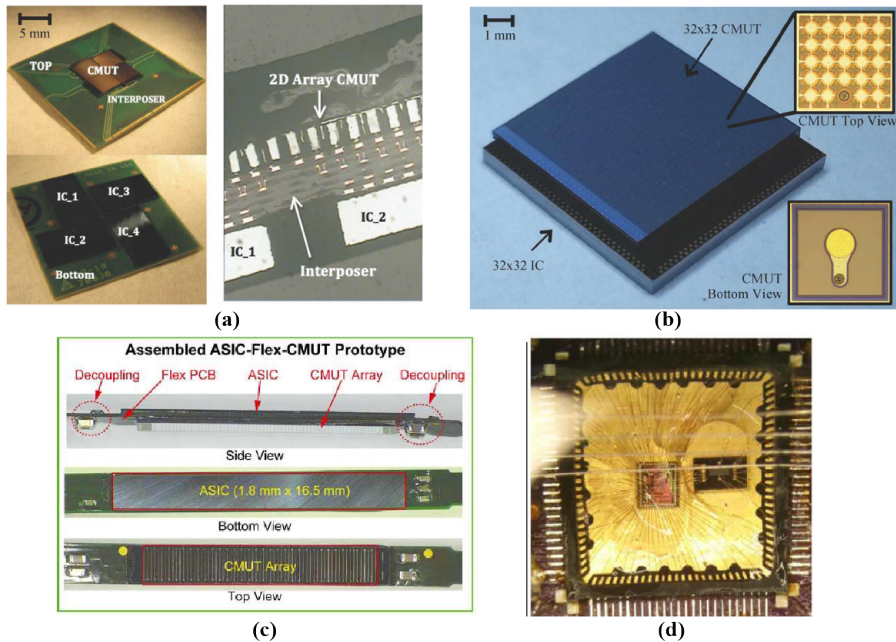
Figure 1.8: Hybrid multi-chip integration using CMUT arrays: (a) Flip-chip interconnection where, Left: Top and bottom view of a integrated CMUT array with the ICs (Integrated circuits) using Interposer substrate, and Right: cross-section view [36], (b) Direct flip-chip bonding [36], (c) Flip-chip interconnection using an interposer flex PCB [38], and (d) Wire bonding interconnection presented in [39].

improve the performance of an Intravascular Ultrasound (IVUS) system [39]. Despite the final goal is implementing a CMUT-on-CMOS system, all tests and the presented packaged device were made using wire bonding.

A hybrid multi-chip integration solution is an approach where flexibility during manufacturing allows for a time-saving and cost-effective process ensuring the best performance of both dies (MUTs and CMOS-ASICs), which could be essential in the high performance of the final ultrasound system. Another advantage of this method is that there are no restrictions on the dimensions of the dies, which do not necessarily have to be the same size [35]. This characteristic isn't applicable when direct flip-chip bonding is used because in this case MUTs and CMOS-ASICs circuitry must have the same pitch to ensure a correct alignment and later flip-chip bonding [36]. Multi-chip integration is a solution limited in small-size applications where high-density integration is needed, and it is quite affected by the large parasitic capacitances as a consequence of the large interconnection path. Further, every die requires a lot of testing packaging steps.

1.2.2 System-on-Chip Integration (SoC)

The main characteristic of the system-on-chip integration is the capability to integrate MEMS (MUTs) devices and CMOS circuitry in the same substrate. This approach can be classified into (a) monolithic, and (b) heterogeneous. In the first one, MUTs devices and CMOS-ASICs circuitry are entirely fabricated on the same substrate, while in the other one, they are separately prefabricated and merged through 3D interconnection techniques. The benefits of this solution lie in the compactness and small size of the chips, also, the cost for packaging and testing (only at the end of the process) is lower than hybrid solutions [35]. In addition, the interconnection length is reduced, decreasing the parasitic capacitances, which improves the performance of the ultrasound system. Unlike hybrid integration, SoC is a complex approach where there is less flexibility during manufacturing, and more time is required for the development of the final device.

Monolithic

In the last decade, monolithic SoC solutions with MUTs devices and CMOS-ASICs circuitry have been carried out with CMUTs based on two approaches. The first one, **CMUTs-in-CMOS**, consists of taking advantage of the manufacturing process of the CMOS circuitry to fabricate CMUTs devices. This integration method does not require any MEMS-related steps in the CMOS process, only sacrificial etching and dielectric deposition are needed as additional post-CMOS actions [41], [42]. The final CMUTs-in-CMOS SoC is a side-by-side (CMUT alongside CMOS-ASICs) system that is not suitable for applications where dense arrays and small size are required. The second approach, **CMUTs-on-CMOS**, is a monolithic solution where CMUTs devices are fabricated on top of the CMOS-ASICs circuitry once the CMOS process has completely finished [43]. This SoC solution allows reducing the parasitic capacitances as a consequence of large interconnection lines in previous integration approaches. Besides, the final device has a small area (CMUT is built on top of the CMOS) which guarantees that it can be used in applications that require a high integration density. Further, unlike CMUT-in-CMOS, the ultrasonic transducer can be optimized (gap height, materials properties, etc.) because is not subject to the CMOS processing steps [44]. However, to ensure the correct CMUT-on-CMOS implementation, a low-temperature fabrication process is also required for the CMUT manufacturing in order to avoid damage to the CMOS-ASICs circuitry [40], [44].

The literature offers several examples regarding the aforementioned monolithic ap-
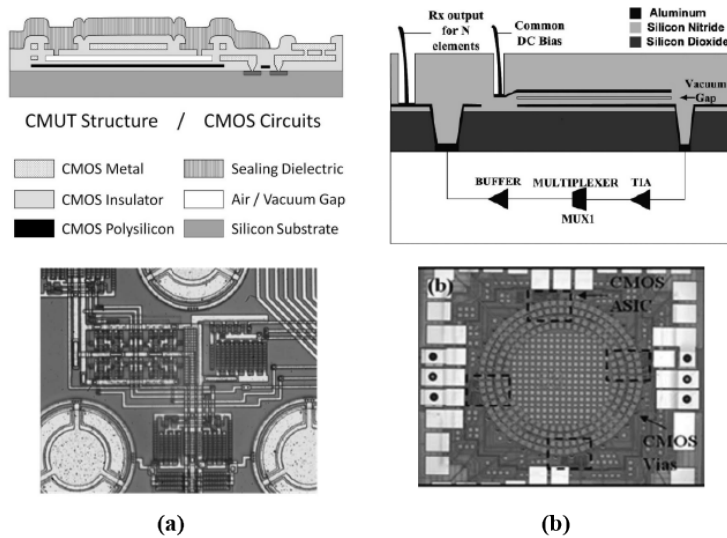
Figure 1.9: Monolithic SoC integration. (a) CMUT-in-CMOS approach reported in [42], and (b) CMUT-on-CMOS approach presented in [44].In both; top: schematic cross-section, and bottom: photograph

proaches [41], [42], [44]–[48]. Figure 1.9a shows a section of a 32x32 CMUTs array interfaced with the CMOS-ASICs circuitry using the CMUT-in-CMOS method [42]. Here, it can seen how the array density is quite affected by the placement of the circuitry. On the other hand, Fig. 1.9b shows the CMUT-on-CMOS system presented in [44] where a dual ring CMUT array is fabricated on top of the CMOS demonstrating the ability to obtain more compact chips.

Heterogeneous

Heterogeneous integration is a technique that leverages the benefits of multi-chip and monolithic approaches. It allows to optimize the performance of the MUTs devices by combining high-performance materials without any compromise with the CMOS manufacturing process (there are no temperature limitations), in addition, this strategy ensures compact devices with high integration densities [49]. The interconnection can be carried out using through wafer vias such as Through Silicon Vias (TSVs) or Through Glass Vias (TGVs), flip-chip bonding with solder bump, eutectic bonding [49], [50], etc.

Ultrasound systems based on CMUTs devices integrated with CMOS-ASICs circuitry through heterogeneous technology have been described in many research [51]–[54]. In 2021, a 32x32 CMUT array used for neurostimulation is interfaced with the CMOS-ASICs through TGVs and flip-chip solder bumps [53], see Fig. 1.10. Despite

achieving compact systems as in the monolithic approach (MUT is on CMOS), it is more complex, time-consuming, and costly, highlighting, for example, the numerous processes involve during vias manufacturing (TSV or TGV) [55], and the need for special equipment for aligning and bonding [56]. Also, there are some limitations regarding the size of the solder ball, which could be a drawback when MUT arrays with a high resolution are needed [19].
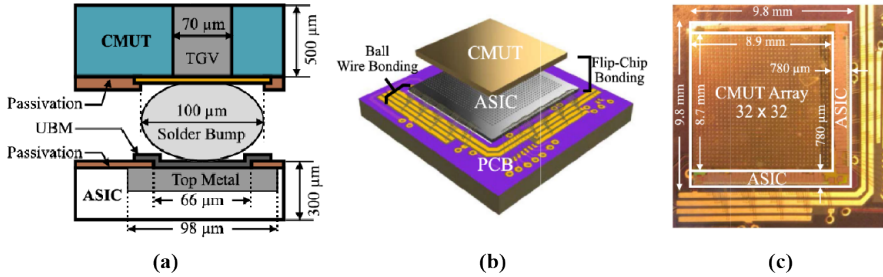
Figure 1.10: Heterogeneous SoC integration using a 32x32 CMUT array [53]. (a) Schematic cross-section after integration, (b) Schematic 3D view of the integration process, and (c) Photograph of the final ultrasound system.

On the other hand, this integration approach is the most used in ultrasound systems based on PMUTs. In 2015, a fabrication platform from InvenSense demonstrated the capability to achieve piezoelectric SoC through eutectic bonding (AlGe) [57]. Systems such as fingerprint sensors [19], [58], [59], microphones [60], and rangefinders [61] are some examples of systems carried out with this technology. Figure 1.11 shows the top-view (a) and cross-section (b-c) of the fingerprint sensor based on 110x56 rectangular PMUT array [19]. PMUTs devices interfaced with CMOS-ASICs
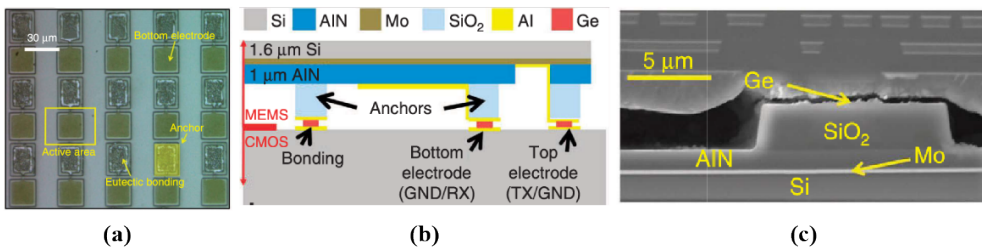
Figure 1.11: Heterogeneous SoC integration using a 110x56 PMUT array [19]. (a) Top view of the rectangular PMUT array, (b) Schematic cross-section of the PMUT interfaced with the CMOS using eutectic bonding process, and (c) Scanning electron microscope (SEM) image of the cross-section of the PMUT.

circuitry using eutectic bonding like any heterogeneous approach has a low fill-factor in the array system (degrading its performance in terms of area and output pressure),

increases the parasitic capacitances, and is a more expensive, and time-consuming process.

Since 2018, SilTerra Malaysia Sdn. Bhd. offers a process platform where the PMUTs are fabricated on the top of the CMOS, achieving a single-chip truly monolithic solution [62], [63]. Currently, as reported by Yole Développement, our research group (ECAS group) is a recognized part of the "R&D" players [24], which in collaboration with Silterra is involved in designing PMUTs systems for the validation of their PMUTs-on-CMOS platform.

ANALYTICAL APPROACH FOR PMUTS DEVICES

Chapter 2 focuses on the analytical approach for PMUTs devices in order to provide the necessary knowledge to design and model them. Beginning with the theory of piezoelectricity, it is intended to give an overview of the principal equations which determine the performance of the PMUTs devices depending on their piezoelectric material. Furthermore, it will present the working principle of the PMUTs devices based on the mathematical analysis, the expressions that describe the frequency, the movement, the transmitted and sensed acoustic pressure, and their behavior when being immersed in a fluid. This chapter will lay the groundwork for understanding analytical models, finite element simulations (FEAs), and experimental results that will be presented later.

2.1 Piezoelectricity

Piezoelectricity is based on materials that lack an inversion center of symmetry and allow internal polarization as a result of an external electric field or mechanical stress [64], [65]. The discovery of piezoelectricity dates back to 1880 when the Curie brothers appreciated this phenomenon in quartz crystals, however, it was not until World War I that this concept found a practical application in an underwater ultrasonic detector. The success of this piezoelectricity-based sonar increased interest in this property and its future applications [66], [67]. There are two mathematical representations to describe it, (a) strain-charge form, and (b) stress-charge form, where either of them

can be converted into the other through a transformation relationship.

In the strain-charge form, an electric field (E [V/m]) and stress (σ [Pa]) can produce a strain (ϵ), and electric polarization (D [C/m^2]), see Eq. 2.1 and 2.2 where S^E [Pa^{-1}] is the compliance matrix coefficient measured at a constant electric field, d [C/N] is the piezoelectric coupling coefficients in the strain-charge form, and ε^σ [F/m] is the relative permittivity with a constant stress [64].

$$\epsilon_I = \sum_J S^E_{IJ}\sigma_J + \sum_j E_j d_{jI} \qquad (2.1)$$

$$D_i = \sum_J d_{iJ}\sigma_J + \sum_j \varepsilon^\sigma_{ij} E_j \qquad (2.2)$$

Considering a small piezoelectric volume with dimensions Δx, Δy, and Δz, see Fig. 2.1, the subscripts i, j take values of 1,2, or 3 and they correspond to the normal vector (x,y, or z) of the surface of interest, while, the uppercase subscripts I, J can take values of 1, 2, 3, 4, 5, or 6 where the last three represent the shear directions (i.e. $xx = 1; yy = 2; zz = 3; yz = 4; xz = 5; xy = 6$).
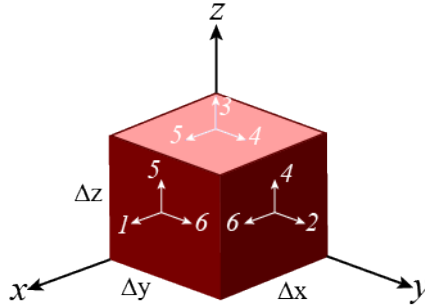
Figure 2.1: Directions on a small differential volume with dimensions Δx, Δy, and Δz.

On the other hand, stress-charge form can be described by Eq. 2.3 and 2.4 being C^E [Pa] the stiffness coefficient matrix with a constant electric field, ε^ϵ [F/m] is the relative permittivity measured at a constant strain, and e [C/m^2] is piezoelectric coupling coefficients in the stress-charge form. The transformation relationship between the piezoelectric coefficients, d, and e, is given by the compliance coefficient matrix ($S = C^{-1}$) measured at a constant electric field through $d = S \cdot e$ [64].

$$\sigma_I = \sum_J C^E_{IJ}\epsilon_J - \sum_j E_j e_{jI} \qquad (2.3)$$

$$D_i = \sum_J e_{iJ}\epsilon_J + \sum_j \varepsilon_{ij}^{\epsilon} E_j \qquad (2.4)$$

2.1.1 Thin-film piezoelectric materials

Requirements related to miniaturization and high integration density have led to advances in thin film technologies and in particular in obtaining high quality piezoelectric materials. Thin-film piezoelectric deposition techniques are based on Micromachined manufacturing technologies, and nowadays their use and interest in the MEMS industry are growing remarkably.

Based on thin-film piezoelectric materials and considering the extreme case of an infinitely rigid substrate on which the piezoelectric capacitor stack is fixed, when a voltage is applied in the z-direction (E_3), the inverse piezoelectric effect, the in-plane piezoelectric strains are zero, thus there are stresses acting in the in-plane directions ($\sigma_1 = \sigma_2$), and out-of-plane motion is possible ($\sigma_3 = 0$). From the piezoelectricity equations (Eq. 2.1 - Eq. 2.4), the effective thin-film piezoelectric coefficients, ($e_{31,f}$ and $d_{33,f}$) can be obtained, giving Eq. 2.5 and Eq. 2.6, respectively [65], [68], [69]. Once these coefficients are determined, in the actuation mode, the out-off plane strain when an electric field is applied can be described as $\epsilon_3 = d_{33,f}E_3$, while the in-plane stresses can be found as $\sigma_{1,2} = -e_{31,f}E_3$.

$$e_{31,f} = \frac{d_{31}}{S_{11}^E + S_{12}^E} \equiv e_{31} - \frac{C_{31}^E}{C_{33}^E}e_{33} \quad |e_{31,f}| > |e_{31}| \qquad (2.5)$$

$$d_{33,f} = \frac{e_{33}}{C_{33}^E} \equiv d_{33} - \frac{2S_{13}^E}{S_{11}^E + S_{12}^E}d_{31} \quad < d_{33} \qquad (2.6)$$

In contrast, with the direct piezoelectric effect, an external force causes deflection of the structure, creating in-plain strains (ϵ_1, ϵ_2) that allow piezoelectric charges to appear on the electrodes. Equation 2.7 describes the displacement field in the z-direction where $\varepsilon_{33,f} = \frac{e_{33}^2}{C_{33}} + \varepsilon_{33}^{\epsilon}$ [29], [68].

$$D_3 = \varepsilon_0\varepsilon_{33,f}E_3 + e_{31,f}(\epsilon_1 + \epsilon_2) + d_{33,f}\sigma_3 \qquad (2.7)$$

In flexural structures based on thin-film piezoelectric materials between two electrodes, it can be defined Figures of Merit (FoM) to characterize the material performance. During the actuation, the FoM is defined by $e_{31,f}$ coefficient due to the membrane vibration depends on the in-plane stresses ($\sigma_{1,2} \propto e_{31,f}$). In the sensing

mode, the measured voltage when the membrane is deflected can be obtained depends on $e_{31,f}/\varepsilon_{33,f}$ [68], [69]. Another parameter to evaluate the efficiency between piezo-electric materials regarding their capability to transform electrical energy in mechanics and vice versa is the piezoelectric coupling factor, K^2. For thin film piezoelectric materials $K^2 = \frac{e_{31,f}^2}{C^E \varepsilon_{33,f}}$ and as it can be seen no losses, shapes or electrode configurations are considered [29], [70].

Table 2.1 shows some published properties of thin AlN, AlScN, and PZT materials [69]. Note how PZT exhibits the best performance as an actuator (highest $e_{31,f}$) achieving about a 14x factor improvement during transmission over AlN (lower $e_{31,f}$). However, in terms of sensing voltage, PZT shows the worst behavior with measured voltage that degrades by about 8x times. Finally, the electromechanical coupling coefficient of PZT only shows a 50 % improvement compared to AlN. In addition, AlScN achieves twice the $e_{31,f}$ coefficient of AlN, the receiving performance is about the same, and the K^2 is 2.5x times higher than AlN, making it a promising piezoelectric material.

Table 2.1: Figure of merit for thin film piezoelectric materials [69]

FoM	AlN	AlScN[1]	PZT[2]
$e_{31,f}(C/m^2)$	1.05	2.25	$15-20$
$e_{31,f}/\varepsilon_{33,f}(GV/m)$	10.8	12.7	$1.4-2.1$
$e_{31,f}^2/\varepsilon_{33,f}(GJ/m^3)$	11.3	28.6	$21-41$

[1] Sc and Al contents around 30% and 70%, respectively.
[2] Zr/Ti compositional ratio is 53/47.

2.2 Mechanics of PMUTs

PMUTs are two-dimensional piezoelectric resonators that can be modeled as multi-layer laminated structures based on thin-film piezoelectric materials [26]. The size of the membrane is defined by the cavity length, and the total thickness depends on the layers involved. Figure 2.2a shows only the membrane corresponding to the schematic four-layers PMUT presented in Fig. 1.5b. The thickness of each layer is given by t_n, where n ranges from 1 to 4 and represents the passive layer, the bottom electrode, the piezoelectric layer, and the top electrode, respectively. Furthermore, the materials in each layer are considered isotropic and they are described through the density, $\rho_n[kg/m^3]$, Young's modulus, $Y_n[Pa]$, and Poisson's ratio, ν_n.

Considering this, the distance from the bottom to the top-plane, h_n, and to the
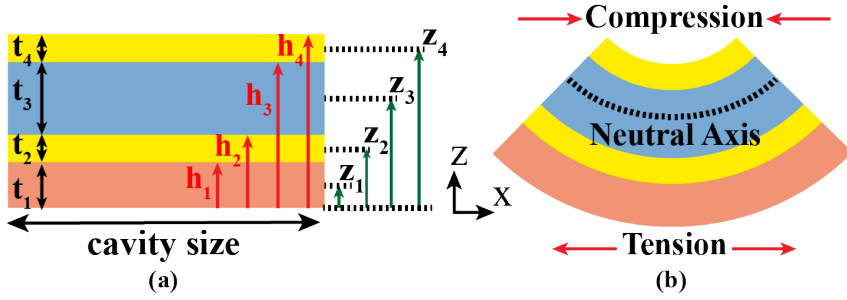
Figure 2.2: (a) Schematic cross-section of a laminate uni-morph PMUT membrane, and (b) Neutral axis of a bent membrane loaded from the topside. Layers and deformation not to scale.

mid-plane, z_n, are obtained using Eq. 2.8.

$$h_n = \sum_{j=1}^{n-1} t_j + t_n \qquad\qquad z_n = \sum_{j=1}^{n-1} t_j + \frac{1}{2}t_n \qquad (2.8)$$

and, the mass per unit area is defined as:

$$\mu = \sum_{n=1}^{N} t_n \rho_n \qquad (2.9)$$

According to Fig. 2.2b, when a force is applied at the top, the membrane bends, causing tensile stress at the bottom while the top side is subjected to compressive stress. However, there is a line, known as neutral axis $Z_{NA}[m]$, defined by Eq. 2.10, where the bending stress is zero.

$$Z_{NA} = \frac{\sum_{n=1}^{N} t_n z_n Y_n'}{\sum_{n=1}^{N} t_n Y_n'} \qquad (2.10)$$

being the coefficient Y_n' the plate modulus which is given by:

$$Y_n' = \frac{Y_n}{1 - \nu_n^2} \qquad (2.11)$$

The resistance to bending is another important parameter in the mechanics of a PMUT structure called flexural rigidity ($D\ [Pa \cdot m^3]$), see Eq. 2.12. It defines the force required to bend the membrane and produce a curvature, which depends on the plate modulus (Y_n'), and the distance between the top-side of each layer and the neutral

19

axis ($\overline{h}_n = h_n - Z_{NA}$, with $\overline{h}_0 = 0$).

$$D = \frac{1}{3} \sum_{n=1}^{N} Y'_n (\overline{h}_n^3 - \overline{h}_{n-1}^3) \tag{2.12}$$

For homogeneous plates this expression can be simplified taking into account the total thickness of the membrane t as $D = \frac{Y' t^3}{12}$

2.2.1 Natural frequency

The natural frequency of an elastic system is that at which it will vibrate once it has been set in motion and the driving force is removed. Depending on the mode shape of the vibration, the value of the natural frequency (f) changes, where the lowest value corresponds to the fundamental resonance frequency. A general expression for a two-dimensional multi-layered structure is defined according to Eq. 2.13 where λ_{ij}^2 is a dimensionless parameter which depends on the vibration mode, the geometry, and the boundary conditions, and a is associated with the membrane size (a is the radius in circular and annular, side in square, etc.) [71].

$$f_{ij} = \frac{\lambda_{ij}^2}{2\pi a^2} \sqrt{\frac{D}{\mu}} \qquad i = 1, 2, 3, ..., j = 1, 2, 3, ..., \tag{2.13}$$

Figure 2.3 shows the simulated mode shapes and λ_{ij}^2 values for a clamped square plate. The coefficient i consists in the number of flexural half-wave along the horizontal direction (x-axis), while j represents the vertical direction (y-axis) [71]
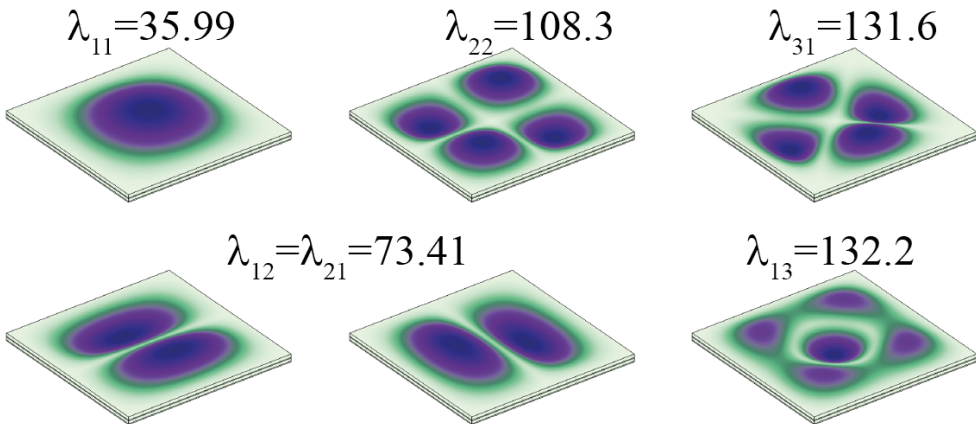
Figure 2.3: Mode shapes for a clamped square plate.
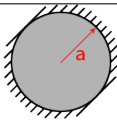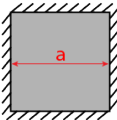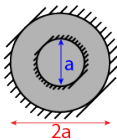
Boundary conditions

The geometric constraints at the edge of each device define its boundary conditions and are not time dependent. Based on this, the principal boundaries definitions can be identified as follows [71]:

- Free: This boundary allows the free vibration of the structure, there are no restrictions on the edges.

- Clamped: Along this boundary, displacements and rotations are not allowed.

- Pinned: Under this condition, the rotation of the structure is allowed, but, is not possible any displacement along this boundary. Following the same idea, in two-dimensional structures this concept is known as simply supported edge.

- Sliding: This boundary condition enables the displacement in a specific direction along the edge, however, a rotation is not possible.

Considering the above mentioned along with the geometry of the structure and the desired mode shape, allows choosing the value of λ_{ij}^2 that has been tabulated [71], [72]. Table 2.2 summarizes the corresponding coefficient associated with circular, square, and annular plates for the first flexural mode when all boundaries are clamped (conventional devices). Note that a clamped multi-layered structure where $\sqrt{\frac{D}{\mu}}$ is constant, square and circular plates with the same dimensions (diameter = side) ensure almost the same frequency ($f_{circular} = 1.14 \cdot f_{square}$) while an annular geometry can achieve an 8.9x frequency larger than circular.

Table 2.2: Coefficient λ_{ij}^2 considering different clamped plates geometries [71].

Geometry	Top View	Values (Modes)		
Circular		10.22 (00)	21.26 (10)	34.38 (20)
Square		35.99 (11)	73.41 (12)	108.3 (22)
Annular		89.2 (00)	90.2 (10)	93.3 (20)

2.3 Quality factor and electromechanical coupling factor

The quality-factor (Q) and the electromechanical coupling factor (k_t^2) are two important parameters that describe the performance of a PMUT device. The first one is represented by the ratio between the stored energy in the vibrating membrane to the total energy lost per cycle regarding different sources. While, the second one, measures the energy conversion efficiency between electrical and mechanical domains [29].

PMUTs devices, as any resonator, can be affected by different dissipation mechanisms which are related to different Q-factors such as: (a) support or anchor loss, which describes the acoustic radiation energy through the PMUT' support ($Q_{anchors}$), (b) piezoelectric loss, which are associated with losses in the piezoelectric materials (Q_{piezo}), (c) bulk losses, which includes, among others, internal friction and thermoelastic dissipation (Q_{bulk}), and (d) medium losses, which consists in the energy loss into a surrounding medium (Q_{medium}) [29], [73]. Equation 2.14 describes the general expression to evaluate the total Q-factor (Q).

$$\frac{1}{Q} = \frac{1}{Q_{medium}} + \frac{1}{Q_{anchors}} + \frac{1}{Q_{piezo}} + \frac{1}{Q_{bulk}} \qquad (2.14)$$

In addition, Q-factor can be written using the frequency response of the PMUT as it's shown in the following equation, where f_0 and BW_{-3dB} are the resonance frequency and the bandwidth at -3 dB respectively. Note that lower energy loss causes higher values of Q and consequently narrow frequency response.

$$Q = \frac{f_0}{BW_{-3dB}} \qquad (2.15)$$

In section 2.1.1, the piezoelectric coupling factor K^2 was defined to describe the transduction efficiency in mutually converting electrical energy to mechanical energy based only on the piezoelectric material's capabilities. In the literature, there is another coefficient regarding this transduction efficiency denoted as k_t^2 (electromechanical coupling factor) which was defined initially for thickness mode resonators and it can be written as is shown in Eq. 2.16 [70], [74].

$$k_t^2 = \frac{\pi^2}{4} \frac{f_s}{f_p} \frac{f_p - f_s}{f_p} \qquad (2.16)$$

However, to evaluate the influence of PMUT as a resonator (flexural membrane considering overall geometry and piezoelectrical losses), it has been introduced the effective coupling factor, k_{eff}^2, see Eq. 2.17a where f_s is the frequency at which the impedance is minimum (series resonance), and f_p is the frequency where the impedance is maximum (parallel resonance) [75]. This coefficient is also related to the piezoelectric coupling factor, K^2, through the expression 2.17b [70], [76].

$$k_{eff}^2 = \frac{f_p^2 - f_s^2}{f_p^2} \tag{2.17a}$$

$$K^2 = \frac{k_{eff}^2}{1 - k_{eff}^2} \tag{2.17b}$$

Based on the equivalent circuit (see next section) the k_{eff}^2 and k_t^2 can be obtained considering the ratio between motional and physical capacitances such as $\frac{C_m}{C_0}$ and $\frac{\pi^2}{8}\frac{C_m}{C_0}$ respectively, as long as $C_m << C_0$.

Finally, for small values of k_{eff}^2, has been defined a figure of merit, M where $M = Qk_{eff}^2$, to evaluate the capability of a resonator in terms of transduction efficiency and energy losses [29], [75].

2.4 Equivalent circuit model

Figure 2.4 shows the equivalent circuit model for a PMUT device that includes electrical (red), mechanical (blue), and acoustical (green) domains[28], [77]. This alternative representation allows a theoretical evaluation of important parameters such as resonance frequency, quality factor (Q-factor), displacement, and output acoustic pressure [17], [78]. The capacitance C_0 represents the PMUT device and it depends on its physical characteristics ($C_0 = \varepsilon_0 \varepsilon_{33} S/d$ where S is the area, d is the piezoelectric thickness, and ε_0, ε_{33} are the vacuum and relative material permittivity respectively). The motional branch conformed by C_m, R_m, and L_m represents the stiffness, damping, and effective mass, respectively and depend on the physical and geometry characteristic of the PMUT devices and they will be defined ahead, while Z_{ac} (MRayl/m^2) is the acoustic impedance.

In the mechanical domain, the force (F_{in}) and membrane velocity (v_m) are related to the voltage (V_{in}) and current (i_m) in the electrical domain through the electromechanical coupling constant (η) giving $F_{in} = \eta V_{in}$ and $v_m = i_m/\eta$. Likewise, in the acoustic domain the volume velocity (V_v), and the output pressure (P_{out}) are associ-
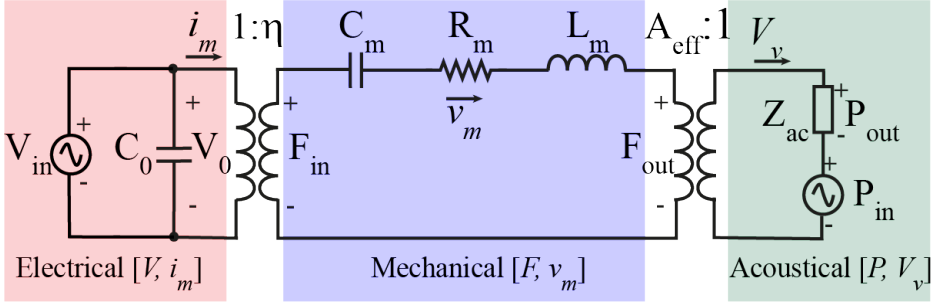
Figure 2.4: General diagram of PMUT equivalent circuit model.

ated with the mechanical domain considering the effective area of the PMUT (A_{eff}) where $V_v = v_m A_{eff}$ and $P_{out} = F_{out}/A_{eff}$. Based on this, when the PMUT is driven with an amplitude V_{in} at its resonance frequency, L_m and C_m are canceled, and the maximum output pressure follows the Eq. 2.18

$$P_{out} = \frac{V_{in}\eta}{A_{eff}} \tag{2.18}$$

In this context, when a pressure P_{in} is the input, the equivalent circuit model can be simplified to an electrical model where all components can be converted into equivalent electric impedances through the electromechanical coupling constant (η) giving $C_M = C_m\eta^2$, $R_M = R_m/\eta^2$, and $L_M = L_m/\eta^2$. At resonance, L_M and C_M are canceled, and the received pressure by the PMUT, P_{in}, is translated to a voltage across C_0. The value of V_0 is obtained by a voltage divider and the maximum value is achieved as long as the impedance of the PMUT ($(2\pi f C_0)^{-1}$) is much larger than the equivalent between the resistivity terms (from mechanical and acoustical domains), giving in this case:

$$V_0 = \frac{P_{in}A_{eff}}{\eta} \tag{2.19}$$

Referring to Fig. 2.2, another important parameter that can be extracted is the static displacement created by the PMUT when a input voltage V_{in} is applied. When a piezoelectric force is the only acting over the PMUT, the work done by the piezoelectric force (W_{piezo}) is equal to the stored strain energy ($E_{elastic}$), see Eq. 2.20 where w_0 is the static displacement, and k_m is the stiffness ($C_m = k_m^{-1}$).

$$W_{piezo} = E_{elastic}$$
$$(V_{in}\eta)w_0 = \frac{1}{2}k_m w_0^2 \tag{2.20}$$

Under these conditions, $U = W_{piezo} - E_{elastic} = 0$ and the static displacement at which this function is minimized can be found as $dU/dw_0 = 0$, see Eq. 2.21. To obtain the maximum displacement at the resonance frequency in a specific acoustic medium, it is only necessary to consider the Q-factor, giving $w_d(f) = Q * w_0$.

$$w_0 = C_m \cdot V_{in} \cdot \eta \tag{2.21}$$

The electromechanical coupling constant, η for two dimensional plates can be defined according to Eq. 2.22 where I_{piezo} (see Eq. 2.28) defines how-well coupled the electrodes design on a specific mode shape and $\overline{z_p}$ is the distance between the mid-plane of the piezoelectric layer and the neutral axis (Z_{NA}).

$$\eta = \frac{1}{2}e_{31,f}\overline{z_p}I_{piezo} \tag{2.22}$$

2.4.1 Lumped parameters estimation for square PMUTs

Moving forward with the evaluation of the motional branch parameters, C_m, L_m, and R_m, the following considerations are taken into account for square PMUTs [79]:

- The boundary conditions for all sides are clamped.

- Every point in x and y coordinates is normalized with the total length a giving $\overline{x} = x/a$ and $\overline{y} = y/a$.

- The vibration mode shape for the first flexural mode is approximated to $\varphi_{1,1}(\overline{x}, \overline{y}) = \varphi_1(\overline{x})\varphi_1(\overline{y}) = (1 - 4\overline{x}^2)^2(1 - 4\overline{y}^2)^2$

These assumptions allow evaluating the stiffness, k_m, as is shown in Eq. 2.23 where D is the flexural rigidity, a is the side, and $I_{elastic}$ describes the effect of the mode shape on the stiffness (see Eq. 2.24), being ν the poisson ratio:

$$k_m = \frac{D}{a^2}I_{elastic} \tag{2.23}$$

$$I_{elastic} = \int_{-1/2}^{1/2}\int_{-1/2}^{1/2}\left[\left(\frac{d^2\varphi(\overline{x}, \overline{y})}{d\overline{x}^2}\right)^2 + \left(\frac{d^2\varphi(\overline{x}, \overline{y})}{d\overline{y}^2}\right)^2 + 2\nu\frac{d^2\varphi(\overline{x}, \overline{y})}{d\overline{x}^2}\frac{d^2\varphi(\overline{x}, \overline{y})}{d\overline{y}^2}\right]d\overline{x}d\overline{y} \tag{2.24}$$

Substituting Eq. 2.24 into Eq. 2.23, the stiffness and consequently the motional capacitance $C_m[m/N] = k_m^{-1}$ can be obtained considering Eq. 2.25

$$k_m = 166.4 + 47.6\nu\frac{D}{a^2} \tag{2.25}$$

Following the same idea, the motional inductance, $L_m[kg]$, is denoted as Eq. 2.26 where the product $a^2\mu$ define the total mass.

$$L_m = a^2\mu \int_{-1/2}^{1/2} \int_{-1/2}^{1/2} \varphi(\overline{x},\overline{y})^2 d\overline{x}d\overline{y}$$
$$= 0.165a^2\mu \tag{2.26}$$

Finally, R_m which models the damping is obtained considering the Q-factor, see Eq. 2.27, and as it can be seen, in PMUTs where the losses are negligible ($Q \rightarrow \infty$), the resistor can be omitted. In addition, the resonance frequency can be obtained taking into account the motional capacitance and inductance from the model as is shown in Eq. 2.27 right.

$$R_m = \frac{\sqrt{L_m/C_m}}{Q} \qquad\qquad f = \frac{1}{2\pi\sqrt{L_mC_m}} \tag{2.27}$$

On the other hand, the piezoelectric coupling integral for square plates is given by the following expression where γ represents the ratio between electrode side and cavity. Figure 2.5 shows how the maximum value of I_{piezo} is reached when the top electrode covers almost 65 % of the cavity. Taking as a threshold of the normalized amplitude a value of 0.9, the top electrode could cover from 53 % to 77 % of the cavity size in order to maximize I_{piezo} and consequently the electromechanical coupling factor (η).

$$I_{piezo} = \int_{-\gamma/2}^{\gamma/2} \int_{-\gamma/2}^{\gamma/2} \left[\frac{d^2\varphi(\overline{x},\overline{y})}{d\overline{x}^2} + \frac{d^2\varphi(\overline{x},\overline{y})}{d\overline{y}^2}\right] d\overline{x}d\overline{y} \tag{2.28}$$
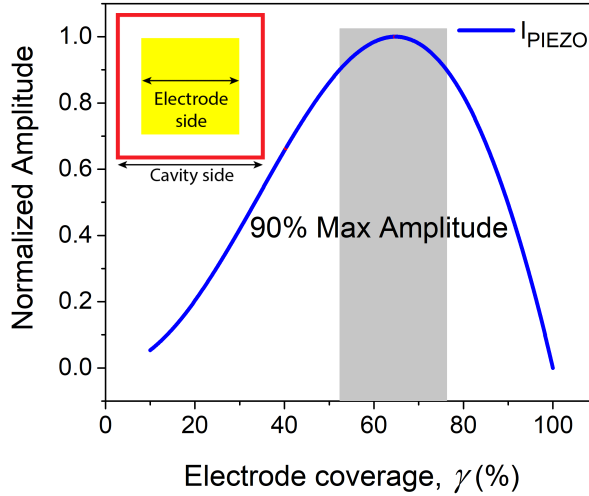
Figure 2.5: Normalized piezoelectric coupling integral as a function of the electrode covering percent (γ), where $I_{piezo} \propto \eta$. In gray is highlighted the region where 0.9 of its maximum is guaranteeing.

2.5 Immersing PMUTs in a fluid

The resonance frequency for a PMUT in the air has been defined by equation 2.13, however, when the PMUT is immersed in a fluid, an extra mass is added causing a drop in frequency, see Eq. 2.29, where β is defined as the added virtual mass [73], [80]. This parameter, described by Eq. 2.30, was introduced for the first time by Lamb where for the same PMUT device only the fluid density (ρ_{liquid}) causes an increase of β and consequently a decrease in the frequency [81]. The coefficient Γ depends on the PMUT geometry and boundary conditions, being, for example, 0.342 for clamped square devices [82].

$$f_{liquid} = \frac{f_{air}}{\sqrt{1 + \beta}} \tag{2.29}$$

$$\beta = \Gamma \frac{\rho_{liquid} \cdot a}{\mu} \tag{2.30}$$

This analysis allows to obtain the resonance frequency for no-viscous liquids, however, the dynamic viscosity (η_d) is an important parameter to take into account when a PMUT is in contact with a fluid where η_d is much greater than 10 cP. Kozlovsky's model is an extension of Lamb's model which redefines the added virtual mass as is shown in Eq. 2.31 based on a dimensionless parameter, ξ, that depends on the kinetic viscosity $\upsilon = \eta_d / \rho_{liquid}$, the angular frequency ω in the liquid environment, and the dimension of the PMUT (a is the side for square devices) [83]. Note that lower

frequencies will be reached if the viscosity in the liquid increases.

$$\beta = \Gamma \frac{\rho_{liquid} \cdot a}{\mu}(1 + 1.057\xi + O(\xi^3)) \qquad where \qquad \xi = \sqrt{\frac{\upsilon}{\omega a^2}} \qquad (2.31)$$

Considering the definition of Q-factor presented in Eq. 2.14 for a PMUT, when the surrounding medium is other than vacuum, the predominant losses are due to the propagation medium and then $Q_{total} \approx Q_{media}$ where Q_{media} can be written as [80]:

$$\frac{1}{Q_{media}} = \frac{1}{Q_{ar}} + \frac{1}{Q_{visc}} \qquad (2.32)$$

Q_{ar} and Q_{visc} consider the effect of the acoustic radiation and viscosity when the device is in contact with a fluid. Equations 2.33 and 2.34 define both parameters where ρ_p is the PMUT mass density, h is the total PMUT thickness, and c_{liquid} is the sound velocity in the liquid [73], [80].

$$Q_{ar} = \frac{\pi f_{liquid}}{\alpha} \qquad where \qquad \alpha = \frac{5\pi^2}{9}\frac{\rho_{liquid}}{\rho_p}\frac{f_{liquid}^2 a^2}{(1+\beta)h \cdot c_{liquid}} \qquad (2.33)$$

$$Q_{visc} = \frac{0.95}{\xi}(\frac{1}{\beta} + 1) \qquad (2.34)$$

2.6 Acoustic Output Pressure

The pressure generated in the far field region at a distance r by the motion of a single PMUT can be described by Eq. 2.35 where P_0 is the surface pressure, R_0 is the Rayleigh distance, $D(\theta)$ is the directivity, ω is the angular frequency and k is the wavenumber ($k = 2\pi/\lambda$; $\lambda = c/f$ is the wavelength) [84].

$$p = \frac{P_0 R_0}{r}D(\theta)e^{j(\omega t - kr)} \qquad (2.35)$$

The directivity function, $D(\theta)$, defines the directional characteristics of a source, see Eq. 2.36, giving an idea of how well it can direct the energy in a particular direction. The index n depends on the boundary conditions of the device being, for example, $n = 1$ for a simply supported. Plotting this function for a clamped device ($n = 2$), see Fig. 2.6, it can be seen that an omnidirectional pattern is achieved if $k \cdot a << 1$ being the dimensions of the device much less than the wavelength. However, if $k \cdot a$ product increases until it is much larger than 1, the beam becomes

directional [84].

$$D(\theta) = \frac{2^{n+1}(n+1)! \, J_{n+1}(kasin(\theta))}{(kasin(\theta))^{n+1}} \tag{2.36}$$
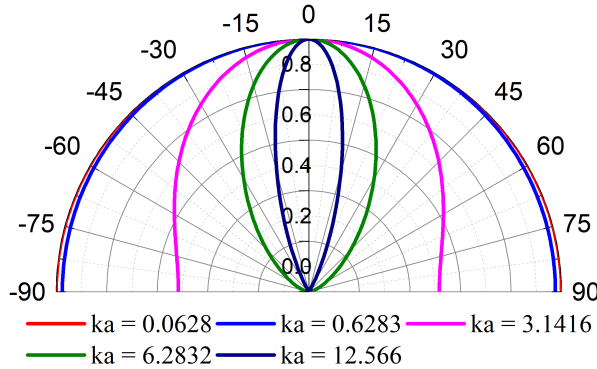
Figure 2.6: Directivity function for a single clamped device considering different $k \cdot a$ values, which can be translated to a/λ is 0.01, 0.1, 0.5, 1, and 2 respectively.

On the other hand, as mentioned above, P_0 represents the surface pressure, but it is important to know that this value is not a real value, it is the pressure that would exist at its face if the dimensions were infinity. P_0 can be computed according to Eq. 2.37 where ρ_0 and c_0 are the density and sound velocity of the propagation medium, and u_0 is the average velocity amplitude, which depends on the dynamic displacement of the membrane ($u_0 = 2\pi f w_d$). The term "average velocity (u_0)" appears because the velocity varies in magnitude over the PMUT surface, i.e., they cannot vibrate uniformly like a piston, being for a clamped PMUT 1/3 of its maximum value [84]. Furthermore, in Eq. 2.37 is shown the Rayleigh distance R_0 where S the area of the source, whatever its shape [85].

$$P_0 = \rho_0 c_0 u_0 \qquad\qquad R_0 = \frac{S}{\lambda} \tag{2.37}$$

The sound field produced by an oscillating membrane as the ones explained previously (PMUTs), follows the fundamental wave equation [84]. The produced sound field can be divided into two regions, see Fig. 2.7. The first is the *near-field*, which represents the zone where there are alternating maximum and minimum and there is no fixed relationship between pressure and distance. The *far-field* is defined as the region where the sound pressure and acoustic particle velocity are in phase, and where the sound pressure level decreases by 6 dB for each doubling of the distance from the

source. In the far field, the source is far enough away to essentially appear as a point in the distance, with no discernable dimension or size. At this distance, the spherical shape of the sound waves has grown to a large enough radius that one can reasonably approximate the wavefront as a plane wave, with no curvature. In this region, the wave will be completely divided in a compression half-wave period and in rarefaction within the other half period. Rayleigh distance is considered as the point where the far-field begins, meanwhile near field, N can be approximated to $R_0/4$ [86].
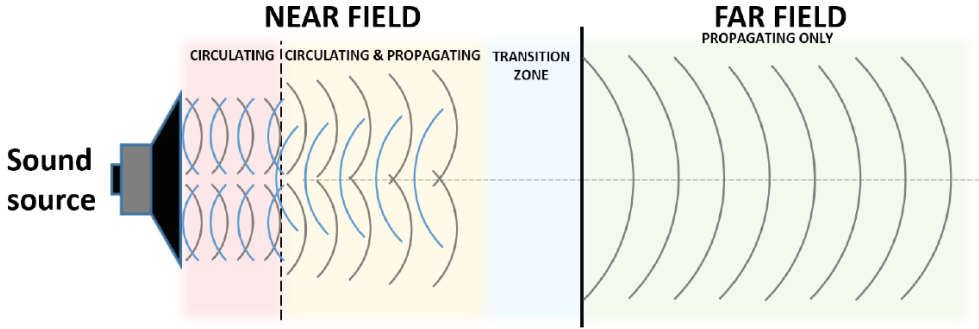
Figure 2.7: Representation of the sound field of an ultrasonic transducer [87].

Based on this, to obtain the pressure on the axis ($D(\theta) = 1$) at a far-field distance z with $z >> R_0$, Eq. 2.35 can be rewritten as:

$$p = \frac{P_0 R_0}{z} \tag{2.38}$$

Up to now, only the separation between the source and the point of interest z has been analyzed as the only influence on the pressure drop. However, in acoustic media where the viscosity is high enough, it is necessary to consider the attenuation of the acoustic pressure traveling in the fluid, represented by an exponential decay due to viscous losses, $e^{-\alpha_{p,visc} \cdot z}$ where the $\alpha_{p,visc}$ represents the damping viscosity coefficient and can be obtained as follows where η_d is the dynamic viscosity.

$$\alpha_{p,visc} \approx \frac{2 \cdot \pi^2 \cdot f_{liquid}^2 \cdot \eta_d}{\rho_{liquid} \cdot c_{liquid}} \tag{2.39}$$

2.7 PMUTs array configuration

High-quality ultrasound imaging systems have become a challenge for the PMUT-based MEMS industry. To achieve a resolution higher than 300 DPI the PMUT size should be less than 85 μm. However, as has been shown in Fig. 2.6, a single small PMUT device has an omnidirectional radiation pattern and, moreover, is expected to generate low acoustic pressure [28], [88]. Array configurations based on small PMUTs allow for an increase in the output pressure with high operation frequencies, and focusing capabilities (generation of a highly directional ultrasound beam). Many researches propose a lot of different array configuration such as linear [89], [90], two dimensional [16], [59], annular [28], hexagonal distribution [91].

The dimensional parameters of an array are shown in Fig. 2.8 considering different array configurations. The pitch and gap indicated as a p, and g_i (where i depends on the direction of the axis, x or y), give the center-to-center distance and the spacing between two adjacent elements, respectively. Considering the element side, a, the total width (W) can be obtained as $W = N \cdot a + (N-1) \cdot g_x$ where N is the number of single elements in x-direction, while the total length (L) uses the same expression but using g_y instead of g_x. On the other side, as can be seen in Fig. 2.8 when PMUTs
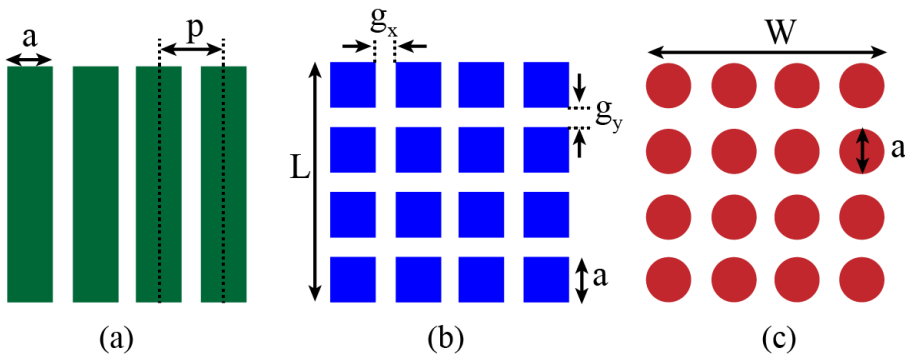
Figure 2.8: Dimensional parameters of different array configurations (a)1-D linear array, (b) 2-D array based on square single PMUTs, and (c)2-D array based on circular single PMUTs.

are configured in an array, there are unused spaces with dimensions g_x and g_y, which decreases the active area capable to generate and sense acoustic pressure. To quantify the effective area of different array designs and compare them, the fill factor (FF) shown in the Eq. 2.40 is defined, where S_A represents the area considering only the active elements and S_T the total area [28]. If the total area is the same, an array made up of circular elements achieves a fill factor $\pi/4$ less than if the elements were square

(see how the empty spaces in Fig. 2.8 c are larger than Fig. 2.8 b).

$$FF(\%) = \frac{S_A}{S_T} * 100 \tag{2.40}$$

The output pressure generated by an array system with NxM elements at a specific point r can be considered as the superposition of the pressure emitted by each element, however, the pressure distribution is affected by the element directivity pattern which includes the individual directivity, $D_{in}(\theta)$ (see Eq.2.36) and the array directivity (D_{arX} and D_{arY}) [2], [84]. This output pressure is given in Eq. 2.41. Note that in this expression is assumed that every element generates the same pressure, which sometimes is far from reality due to variations in the fabrication process.

$$p = \frac{NMP_0R_0}{r}D_{in}(\theta,\phi)D_{arX}(\theta,\phi)D_{arY}(\theta,\phi) \tag{2.41}$$

When the array is symmetric, ($N = M$), it means that D_{arX} and D_{arY} are equal and written as Eq. 2.42, being ϕ the angle to indicate the plane of interest. Taking as an example an 8x8 array of square-clamped PMUTs with a single element of size $a = 0.1\lambda$ and a gap between them of $g_x = 0.1a$, the element directivity ($D_{elem} = D_{in} \cdot D_{arX}$) in the x-z plane ($\phi$=0) is plotted in Fig. 2.9 (dotted black line), which shows the positive influence of array implementation in terms of more directional beams.

$$D_{ar} = \frac{\sin(\frac{1}{2}Nkp\sin(\theta)\cos(\phi))}{N\sin(\frac{1}{2}kp\sin(\theta)\cos(\phi))} \tag{2.42}$$
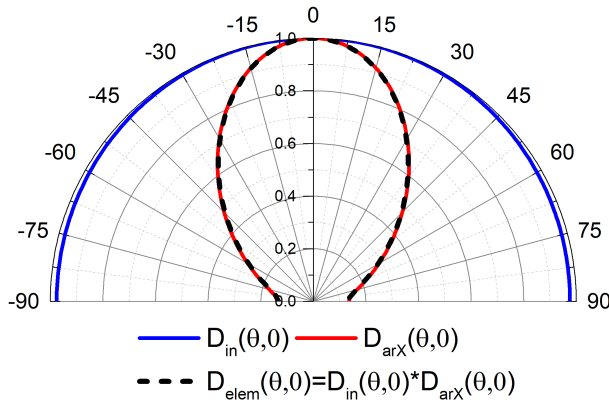
Figure 2.9: Directivity function for an 8x8 array of square-clamped PMUTs with a single element of size $a = 0.1\lambda$ and a gap between them of $g_x = 0.1a$.

In the array context, another important aspect is the spatial resolution which describes the possibility offered by the system to solve two o more objects along the axial and lateral directions, respectively. The first one, known as axial resolution, refers to the minimum separation between two targets distributed along the axial direction which allows the echoes coming from them to be differentiated. This distance, A_z, can be written as Eq. 2.43 where SPL is the "Spatial Pulse Length" [92] (see Fig. 2.10) and considers the number of excitation cycles (n), the wavelength (λ), and the Q-factor (Q). The minimal axial resolution occurs when n is 1 and Q is 0, giving $\lambda/2$.

$$A_z = \frac{SPL}{2} = \frac{\lambda}{2} \cdot \left(n + \frac{Q}{\pi} \right) \tag{2.43}$$

Figure 2.10 shows three objects placed along the axial direction where d_1 and d_2 represent the distance with respect to the first one. If d_1 is less than the A_z, the reflecting echoes are overlapping, and the envelope can not distinguish both targets separately. On the other side, if d_2 is higher than the A_z, the objects can be identified successfully. Since the SPL is proportional to the wavelength, if the frequency increases the wavelength decreases, and therefore, the axial resolution is improved.
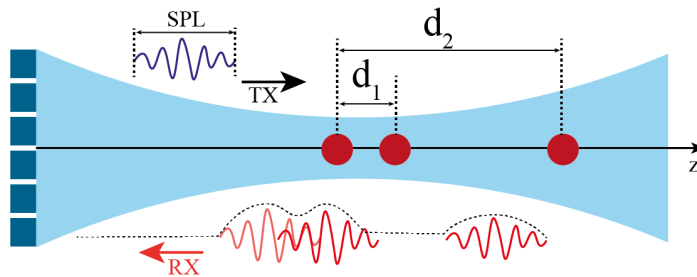
Figure 2.10: Schematic representation of a poor and excellent axial resolution.

The lateral resolution, in contrast, is directly related to the beam width or the beam diameter (BW_{-6dB}) and it defines the ability to detect two objects next to each other at the same axial distance. The lateral resolution is better if the beam is narrower which can be achieved with an array system at high frequencies [92], [93]. Equation 2.44 shows an approximation to estimate this value based on circular apertures, however, it can give an idea of how good a system is given its lateral resolution. The element diameter is D, z is the specific axial position, f is the frequency, and c_0 the sound velocity.

$$BW_{-6dB} \approx 1.02\left(\frac{z \cdot c_0}{f \cdot D}\right) \tag{2.44}$$

Figure 2.11 shows in red two objects which can not be spatially solved because they are closer than the beam width, however, in green, as the targets are further separated than the beam width, the information about both can be obtained.
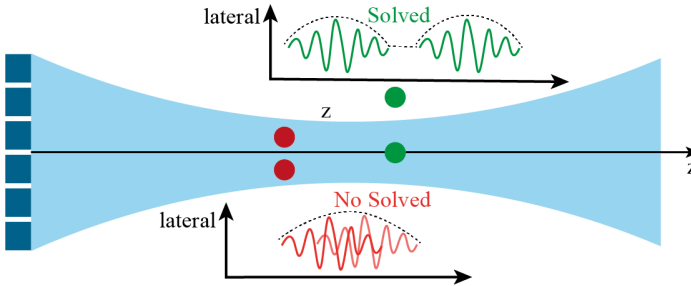
Figure 2.11: Schematic representation of a poor and excellent lateral resolution.

EXPERIMENTAL AND SIMULATION TOOLS

In this chapter the main simulation tool, experimental equipment and techniques used in this thesis will be explained. The main goal here is to structure and show the path followed throughout this period. First, the Finite Element Method (FEM) simulator, COMSOL Multiphysics, used to perform PMUTs modeling, is explained. In addition, Field II as a complementary simulation tool is introduced. Then, a general description about the fabrication process and the studied devices during this thesis are introduced. Finally, the general procedure as well as the required equipment to evaluate the PMUT performance from the electrical measurement to the acoustic characterization after PDMS (Polydimethylsiloxane) deposition is described.

3.1 Simulation Tools

3.1.1 COMSOL Multiphysics

COMSOL Multiphysics is a general-purpose simulation software based on a Finite Element Method (FEM), which allows segmenting a general structure into smaller elements where numerical analysis will be applied [94]. The mesh, as the segmentation process is called, ensures a result closer to the real behavior while the element is finer but more processing time is required. In addition, this software has add-on modules with specialized functionalities that allow the possibility of studying the interaction between multiple physics modules, for instance, structural mechanics, fluid flows, and acoustics. In this sense, to model PMUTs, the modules corresponding to piezoelectric

devices (mechanics and electrostatics) and the acoustic domain were used. Furthermore, regarding the analyzes carried out during this thesis, it can be found mainly:

1. Eigenfrequency Study: allows determining the natural frequencies at which the PMUT can vibrate. This study provides the shape and the frequencies values for different modes.

2. Stationary Study: focuses on the static displacement under a steady-state condition, a constant applied voltage, or constant pressure.

3. Frequency domain Study: gives the behavior of a PMUT when it is immersed in a fluid. The peak frequency, the maximum displacement, and membrane velocity can be obtained, as well as the propagation of a pressure wave for a given frequency.

4. Time domain Study: as the name implies, the time dependence of acoustic wave propagation through a fluid can be modeled.

3.1.2 Field II Simulation Program

Field II was used as a complementary simulation tool, a software that has been released for use on Matlab [95], [96]. This program allows simulating ultrasound transducer fields and ultrasound imaging. It is an excellent choice to obtain the behavior of array systems taking advantage of the fact that the simulation is fast. Furthermore, for array systems, the focusing and steering of the beam can be implemented and the results are easy to obtain.

3.2 MEMS-on-CMOS Silterra Technology

As a result of a collaboration between our research group and the semiconductor foundry Silterra Malaysia Sdn. Bhd, the PMUTs presented in this Ph.D. thesis have been developed with the Silterra MEMS-on-CMOS platform [62]. This process allows piezoelectric devices to grow on the top of the CMOS circuitry (130 nm High Voltage CMOS technology), which has been already used for SAW [97] and circular PMUT [98] devices. During these years different fabrication lots of PMUT devices have been used. Silterra's technology has been improved through changes in the manufacturing process as well as changes in the PMUTs parameters (i.e. piezoelectric material and layer thicknesses). The objective was to obtain better and more competitive devices, which in the future could be implemented in a commercial device. Table 3.1 shows the principal differences between each type of fabricated lots. Note that

Type I and Type II have the same layer thicknesses, however, in the second one the AlN properties were improved, as well as the layouts of the PMUTs.

Table 3.1: Classification of the discussed PMUTs

Layers	Type I	Type II	Type III	Type IV	Type V
Piezoelectric material	AlN[1]	AlN	AlScN	AlN	AlScN
Piezoelectric thick. (μm)	1.3	1.3	1.2	0.6	0.6
Passive thick. (μm)	1.5	1.5	1.5	1/1.25/1.5	1

[1] The AlN properties and layouts are different to type II and type IV.

3.2.1 Fabrication details

Figure 3.1 shows a general schematic cross-section of the PMUT devices that will present throughout this thesis where the piezoelectric and passive layer thicknesses depend on the Type of PMUT (see Table 3.1). As shown, a single PMUT consists of a unimorph structure in which a piezoelectric layer is deposited by Physical Vapor Deposition (PVD) [99] and it is sandwiched between at least two Al electrodes (0.35 μm thickness top electrode and 0.4 μm thickness bottom electrode). The piezoelectric material could be AlN or AlN with a 9.5 % Sc concentration ($Sc_{9.5\%}Al_{90.5\%}N$) where the last one improves the piezoelectric properties of the pure AlN, which causes better transduction efficiency keeping the compatibility with the CMOS process [100]. The cavity size is defined by an etching step which allows to release and define a cavity with a height of 600 nm. Finally, the PMUT device is covered by a Si_3N_4 layer deposited using a low-temperature Plasma Enhanced Chemical Vapor Deposition (PECVD) process. This one acts as an elastic layer and seals the cavity allowing it to work in a liquid environment [98], where any other layer as PDMS deposition like in [101] or additional processes [102] are required. The interconnection between the electrodes with the last metal of the CMOS Back-end-of-line (BEOL) is performed by metal via contacts, avoiding any bonding technique and decreasing the parasitic capacitances [63], [103]. Table 3.2 summarizes all material properties.

3.3 Experimental characterization

Figure 3.2 depicts a general procedure performed in our laboratory in order to obtain a full characterization of the PMUTs. This includes all steps, although the PMUT devices are not always subject to all of them. The electrical characterizations are carried out in two moments: (a) at the beginning using the probe table to choose working devices, and (b) once the PMUT is bonded to a PCB (Printed Circuit Board) to verify
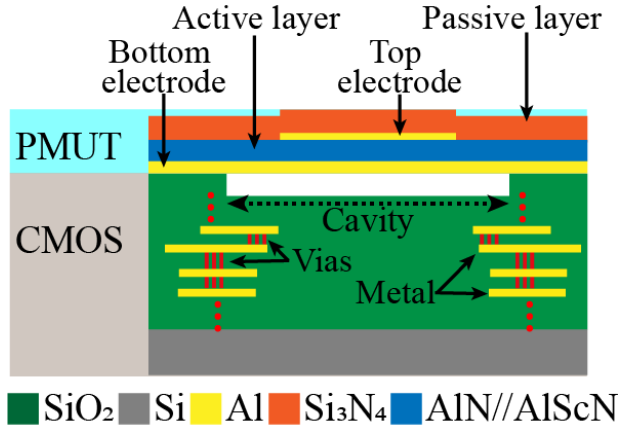
Figure 3.1: Schematic cross-section of a PMUT device using the MEMS-on-CMOS fabrication process from Silterra. (Layers are not to scale)

Table 3.2: Material properties of the PMUT device.

Layer	Material	Young's Modulus (GPa)	Density (kg/m^3)	Poisson's ratio
PMUT Substrate	SiO$_2$	70	2200	0.17
Bottom Electrode	Al	70	2700	0.35
Piezoelectric	AlN[1]	345[2] 279[3]	3330[2] 3230[3]	0.32[2] 0.3[3]
	AlScN[4]	250	3520	0.31
Top electrode	Al	70	2700	0.35
Passive	Si$_3$N$_4$	250	3100	0.23

[1] Piezoelectric coefficient e_{31} = -0.6 C/m^2 and e_{33} = 1.55 C/m^2. Relative permittivity of 9.5.
[2] Extracted from COMSOL and corresponds to PMUTs devices Type I.
[3] Corresponds to PMUTs devices Type II and Type IV.
[4] Piezoelectric coefficient e_{31} = -1.25 C/m^2 and e_{33} = 1.75 C/m^2. Relative permittivity of 10.5.

that the bonding process did not damage the device. Following the same idea, the acoustic measurements are performed twice: (a) without PDMS to obtain the generated and sensed pressure in a liquid environment, and (b) once the PMUT is covered with PDMS to protect the bondings.

Piezoelectric Micromachined Ultrasonic Transducers
↓
Electrical measurement: Probe Table
↓
Bonding Process
↓
Electrical Measurement II
↓
Acoustic Measurement
↓
PDMS deposition Process
↓
Acoustic Measurement II
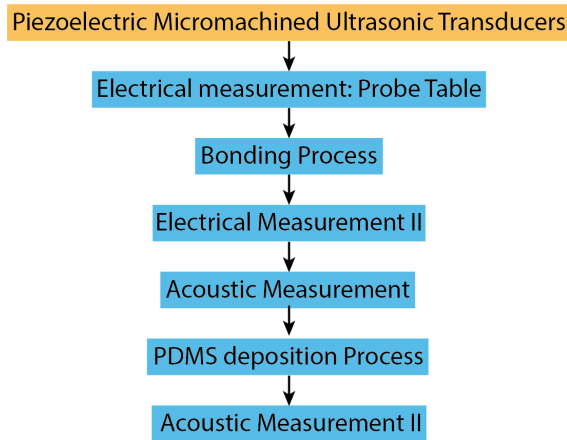
Figure 3.2: General schematic procedure to characterize PMUTs devices

3.3.1 Electrical measurements in the air

Figure 3.3 shows a photo of the complete electrical set-up, whose purpose is to measure the coefficient between the signal coming out of port 2 relative to injected stimulus through port 1, or what is the same, the scattering parameter S_{21}. This simple technique allows obtaining the resonance frequency in the air and then, based on the equivalent circuit model, extracting the motional parameters of the PMUT.

For the first experiment, a direct measurement on chip is carried out using a manual probe station with an optical camera (PM8, SUSS MicroTec, Germany) and GSG (Ground-Signal-Ground) probe tips with a pitch of 100 μm (Z040-K3N-GSG-100, FormFactor, USA) connected to a network analyzer (E5100A or E5071B, Agilent Technologies, USA). The arrangement of the probe tips allows measurements between the top and bottom electrodes only when the PMUT has a single top electrode. Meanwhile, for two-port devices, the bottom electrode is always grounded and the measure is performed using one top electrode as input and the other as output (see top inset). In the second electrical measurement, the PMUT (previously wire bonding to a PCB) is connected to a network analyzer, and here, for two-port PMUTs, the magnitude between the top (inner or outer) and bottom electrodes can be obtained.

3.3.2 Bonding equipment

The wire bonding process was performed with a manual wire bonder machine (4700, Kulicke&Soffa, Singapure) in wedge-wedge mode, see the set-up in Fig. 3.4. The chip was glued to a PCB with silver conductive paint, and the electrical connection between the PMUT pads and the PCB was made using 25 μm Al wire. This pro-
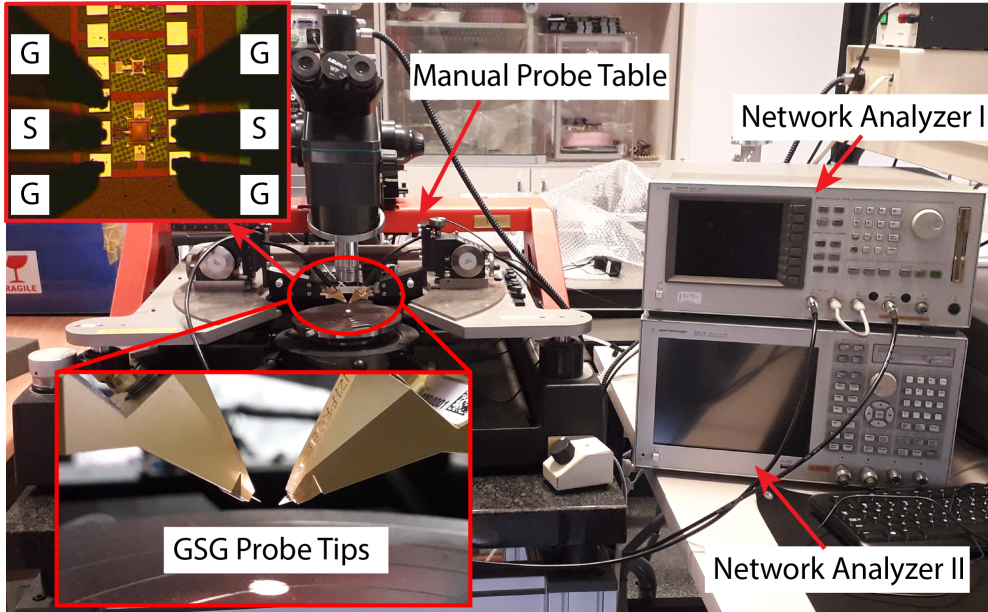
Figure 3.3: Photograph of the electrical measurement set-up in the air. Inset: (Top) optical image of a two-port PMUT with the tips, and (bottom) Zoom of the GSG probe tips.

cess allows each electrode (or CMOS circuitry input/output) to be accessed through an SMA connector, and then be able to characterize the PMUT performance in a surrounding medium different from air.

3.3.3 Acoustic measurements in fluids

The acoustic characterization allows evaluating the ability to use the PMUT devices presented here in an ultrasound system either for medical applications, imaging, etc. or simply to improve the performance of those reported in the state of the art. In this sense, vacuum pump O-ring with 30 mm diameter is used to confine the liquid over PMUT surface, and as a fluid we regularly use Fluorinert (FC70) due to its non-conductive electronic property (c=685 m/s and ρ=1940 kg/m^3) and an acoustic impedance (1.3 MRayl) close to the tissue [58], [104]. A general acoustic set-up is shown in Fig. 3.5, where the performance of the PMUT as an actuator (determining the capacity to generate acoustic pressure, i.e. Pa/V), as a sensor (determining the capacity to transduce the acoustic pressure to a voltage, i.e. V/Pa) and also in a pulse echo system, (using two PMUTs, one PMUT with two electrodes or one PMUT conveniently driven using a time-switched electrode) can be studied. A manual micropositioner system [105] is used to modify the location of the PMUT in space (x-y-z coordinates) with respect to a target (hydrophone, emitting source, or reflecting sur-
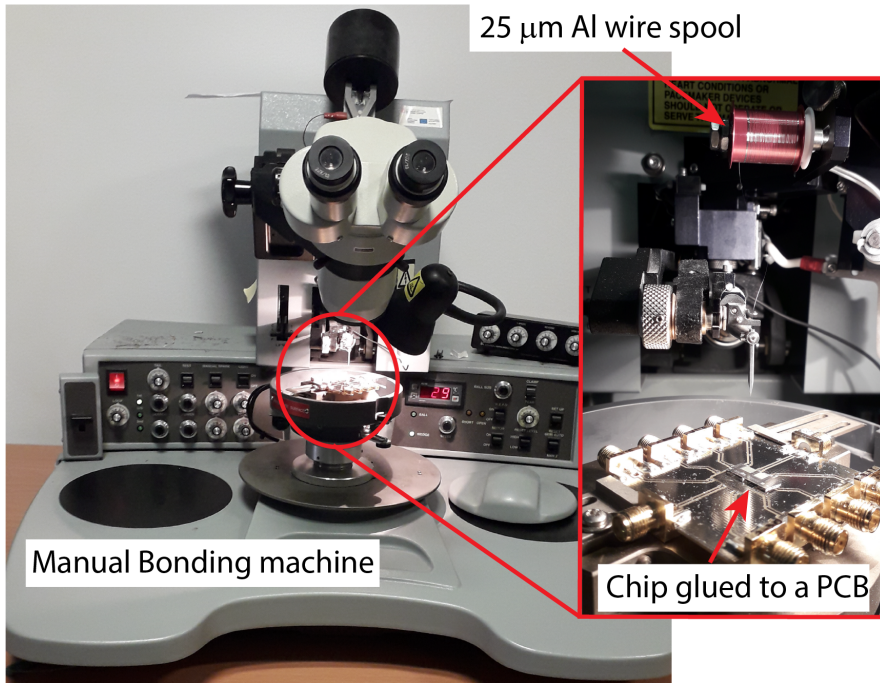
Figure 3.4: Photograph of the wire bonding set-up.

face). The signal generator (81150A, Keysight, USA) is configured to provide the driving signal, and the oscilloscope (DSO-X 3054A, Keysight, USA) allows for the acquisition of the final signal to post-process it. In addition, when the CMOS circuitry (High Voltage (HV) Pulser and Low Noise Amplifier (LNA)) are used, the DC Power Supplies are configured with 32 V, 5 V, and 1.5 V respectively [103], [106]. Acoustic pressure was measured using two commercial hydrophones from ONDA (HNC-0200 and HNC-1500) which, based on their sensitive-frequency dependence (V/Pa), the acoustic pressure generated by the PMUT can be obtained. In contrast, producing an acoustic pressure and validating the sensing capability of the PMUT was carried out by placing over the PMUT a commercial transducer from OPTEL, which was previously calibrated. More details about them will be given below.

Influence of Effective Sensitive Element Size in the acoustic distances

Hydrophones are commonly used to characterize the acoustic pressure emitted by ultrasound transducers converting it to a voltage output and displaying them on an oscilloscope. Hydrophones can distort the incident pressure due to the spatial averaging effect [107]. The maximum effective radius of a hydrophone must be chosen following Eq. 3.1 in order to avoid overestimated beam-widths and underestimated
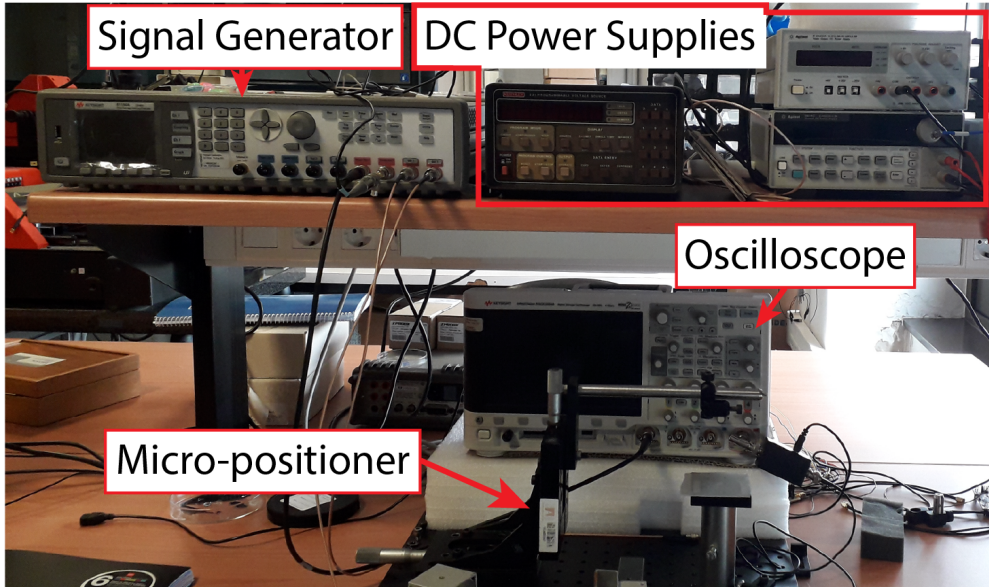
Figure 3.5: Photograph of the acoustic set-up.

spatial peaks [108]:

$$a_h = \frac{\lambda}{8 \cdot a}\left(\sqrt{l^2 + a^2}\right) \tag{3.1}$$

where a_h is the hydrophone effective radius, a is one half of the maximum transducer dimension, l is the distance between the hydrophone and the transducer, and λ is the wavelength. Considering the two commercial hydrophones from ONDA available in our lab, HNC-0200 and HNC-1500 (ONDA, USA) with radii of 100 μm and 750 μm respectively [109], and re-written Eq. 3.1, the normalized distance , $l/2a$, can be found as a function of the wavelength. Taking a value of λ of 100 μm as a reference, the minimum measurable distance when using HNC-1500 hydrophone should be almost 30 times larger than the side of the transducer, which could be a limitation to characterize big arrays transducers in short-range distances. This challenge can be solved using hydrophones with small diameters such as HNC-200 where this ratio decreases until four but, in return, the reception sensitivity is smaller.

Another characteristic that must be taken into account when using a hydrophone is its directivity. As in PMUTs the emitted pressure along the lateral axis is affected by its directivity, in hydrophones the sensed pressure is also affected by its response. This fact causes a convolution between both of them (PMUT+hydrophone), and then, the resulting pattern could be affected if the hydrophone is more directional than the PMUT device. Equation 3.2 describes the directivity function when an incoming wave
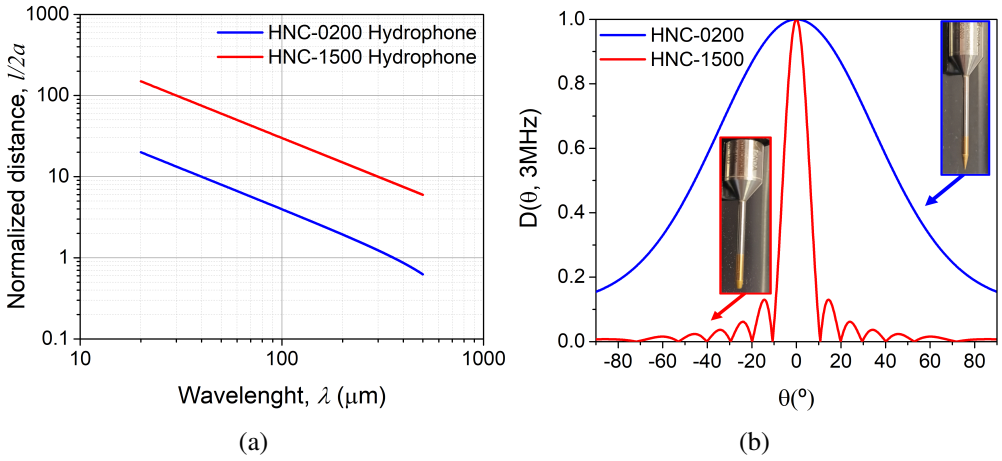
Figure 3.6: (a) Maximum hydrophone size as a function of wavelength (λ), and normalized distance ($l/2a$), and (b) Theoretical directivity response in FC-70 at 3 MHz using HNC-0200 and HNC-1500 Hydrophones from ONDA.

is normal to the hydrophone's tip [110]

$$D(\theta, f) = \left[\frac{1 + \cos(\theta)}{2}\right] \cdot \left[\frac{2J_1(ka_h \sin(\theta))}{(ka_h \sin(\theta))}\right] \tag{3.2}$$

where k is the wave-number ($2\pi/\lambda$), a_h is the radius of the hydrophone, J_1 is the Bessel function of the first kind, and θ is the angle relative to the normal. Substituting the dimensions and considering the same wavelength in Fluorinert ($\lambda = 685/3M = 228\mu m$), the ka_h product is 7x times higher when the hydrophone HNC-1500 is chosen, giving a more directional response, see Fig. 3.6b. The expression proposed in Eq. 3.2 could be used in order to deconvolve the result and obtain the real pattern for the PMUT.

Calibration of an external ultrasound pressure source

The acoustic characterization as a sensor was done using a commercial transducer from OPTEL (Poland) [111]. It consists of a 5 mm diameter element with 10 mm steel housing and a length of 30 mm, see Fig. 3.7a inset. To calibrate the probe in a liquid environment, in our case specifically in Fluorinert. This experiment was performed by modifying the frequency of the excitation signal in a range of 2 MHz to 5.5 MHz and the emitted pressure was obtained by placing the hydrophone (HNC-1500) at 2 mm, 3 mm, and 4 mm respectively. As it is shown in Fig. 3.7a, a linear fit was performed where the slope corresponds to the OPTEL transmitting sensitivity at a specific distance and frequency. Finally, according to the HNC-1500 calibration,

these values were translated into a pressure that gives the experimental transmission sensitivity (kPa/V) shown in Fig. 3.7b, which will allow estimating the incoming pressure wave in the PMUT if the OPTEL is placed at these specific distances.

(a)

(b)
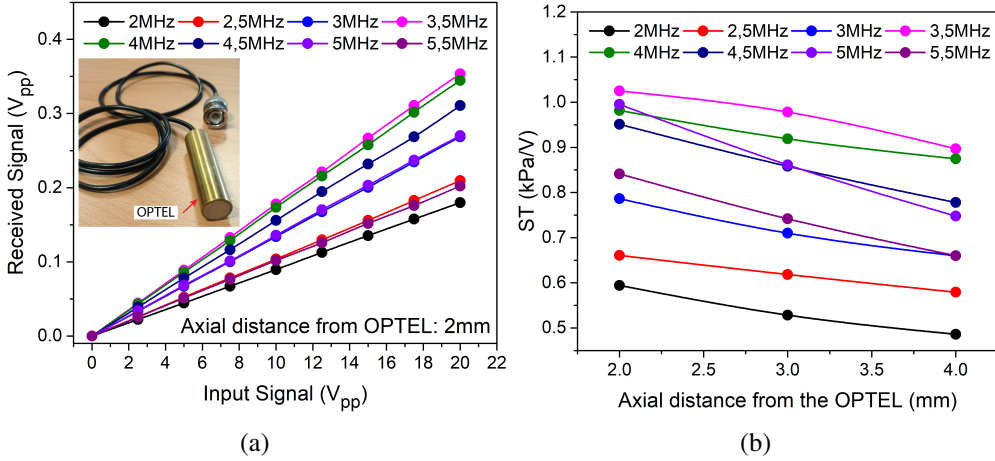
Figure 3.7: (a) Received signal by the HNC-1500 vs OPTEL input voltage at 2 mm. Inset: Photo of the OPTEL, and (b) Measured sensitivity of a commercial transducer from OPTEL at different axial positions in Fluorinert.

3.3.4 PDMS deposition process

Polydimethylsiloxane (PDMS) is a material that offers long durability and whose manufacturing process is simple. Many researchers take advantage of its acoustic impedance (close to 1 MRayl) which makes it suitable for coupling PMUT transducers with the human tissue [34], [112], to model phantoms such as a fingerprint [20] or finger vessel [113], as well as subcutaneous fat and muscle [114]. Furthermore, in applications where the device is immersed in a fluid, it ensures waterproof protection through the total isolation of the wire bonding and an airtight seal of the cavity.

Based on this, some of our PMUT-on-CMOS devices are coated with a layer of PDMS (Sylgard 184, Dow Chemical, Midland, USA) with a thickness around 200 μm. Considering a mix ratio of 10 to 1, a density close to 980 kg/m^3 and a sound velocity of 1000 m/s is achieved, giving an acoustic impedance around 0.98 MRayl. Once the mixture is deposited on the device, a Vacuum plastic desiccator (DE2P-200-001, Labbox, Spain) is used to ensure a layer free of air bubbles. The cured process has been carried out at an ambient temperature, and sometimes is accelerated with an oven at 70°C. Figure 3.8 shows the degassing process and a final system covered with

a PDMS layer.
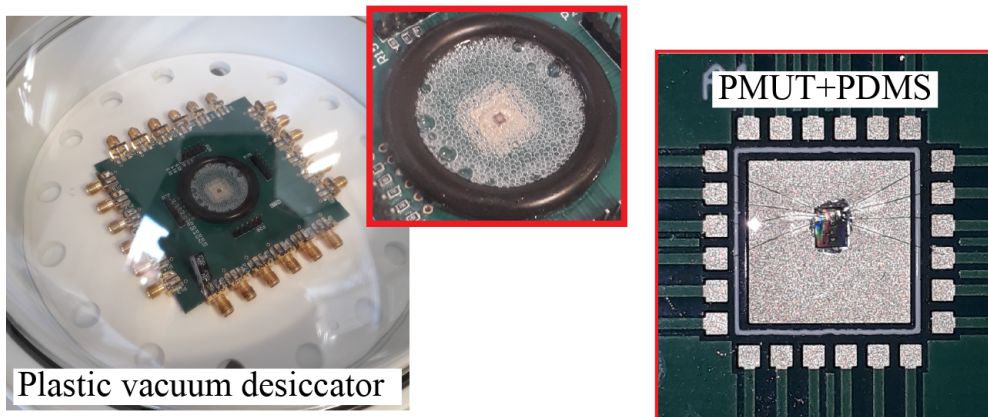
Figure 3.8: PDMS degassing process (left) and a coated device with cured PDMS (right).

FOUR

SINGLE PMUT DEVICES

Nowadays, many efforts have been carried out to improve the performance of PMUTs. Increasing the transmitting and pressure sensitivity, reducing pixel size, increasing operation frequency and bandwidth, and implementing high fill factor arrays are some of the requirements being pursued. This fact causes that various design, thicknesses, and piezoelectric materials will cause interest in many research groups.

The most conventional PMUT architecture studied in the state-of-the-art is the circular clamped device [16], [28], [98], [115], however, these geometry characteristics yield two important aspects, (a) effective area, and (b) fill-factor. Focusing on the first one, (a), the boundaries constraint causes the membrane can not achieve a uniform vibration on the entire surface as a piston. For clamped PMUTs, an effective area of 1/3 of the real area is normally assumed, diminishing by 1/3 the efficiency as an actuator [84], [116]. In this sense, a lot of approaches have been reported in order to increase the effective area capable to generate and sense acoustic pressure, for instance, in 2011, *Guedes et al.* developed a suspended-flexural membrane that achieves an output pressure about twice higher than the clamped device version [117]. *Wang et al.*, in 2015, fabricated etching holes in the membrane to become it more flexible and achieve flatter deflections similar to a piston[118]. More recently, in 2019 and 2020 *Luo et al.* and *Liang et al.* proposed corrugated [116] and pinned [119] piezoelectric micromachined ultrasonic transducers respectively whose main objective was to improve the vibration amplitude. However, these geometric modifications are not the

only solutions when it is desired to increase the output pressure based on unimorph devices. The implementation of dual well-designed top-electrodes improves the PMUT sensitivity and, achieves twice as much of the electromechanical coupling factor (η) when the electrodes are differentially driven [120]–[122]. On the other hand, as was aforementioned, the fill factor is the second aspect to be considered regarding the geometry of the PMUT. In arrayed PMUTs systems, as was explained in section 2.6, the fill factor quantifies their effective area where square PMUTs, for instance, could drive values higher than circular. In the literature, it can be found systems with large fill factors where a single PMUT is a square or a rectangle, for instance, the ultrasound fingerprint sensor presented in [19], where each PMUT is a rectangular device of 30×43 μm^2, achieves a FF of 51.7 %, being three times higher than the previously reported array based on circular PMUTs [58]. In addition, the presented array in [102] achieves a fill factor of 79 % using square PMUTs with 50 μm. Note that these PMUT geometries reach values higher than 50 % of fill-factor.

Ensuring compatibility with CMOS technology and achieving higher piezoelectric coefficients is another challenge during the PMUT designs. Several works propose AlN with Scandium (Sc) concentrations to enhance the piezoelectric coefficients without affecting the compatibility with the manufacturing process used up to now. In 2017, a 15% Sc in a 7x7 PMUT array was reported by *Wang et al.* where, based on the electromechanical coupling coefficient and the transmitting sensitivity, the benefits to use Scandium were demonstrated [123]. Likewise, *Kusano et al.* in 2018 proposed a circular PMUT with Sc concentration of 36%, which achieves (working in air) a 10-fold improvement in transmitted pressure compared to pure AlN [124]. However, in these cases Sc not only increase the e$_{31,f}$ but also the dielectric permittivity (ε_r) is increased too, affecting the performance as a sensor.

In this chapter, we will focus on developing PMUTs devices capable of reaching a high output acoustic pressure level and a high reception sensitivity in a liquid environment compared to the state-of-the-art. Improvements in designs, piezoelectric materials, and thicknesses will be discussed, and the results obtained will be useful to determine the most appropriate PMUT based on the requirements demanded by our application. Two principals dimension has been chosen, 80 μm and 40 μm, as a reference to cover different frequencies range. contributions outputs of this chapter are included in the following papers **Jour1, Jour3** and **Jour4**.

4.1 Piezoelectric Materials

AlN and AlN with a 9.5 % Sc concentration ($Sc_{9.5\%}Al_{90.5\%}N$) will be the piezoelectric materials discussed in this thesis **[Jour1, Jour2]**[100], [125]–[128]. Firstly, only AlN was used as the active material because it can be deposited at low temperatures ensuring the compatibility with the CMOS process [102], [103]. However, the principal drawback of this material is its low thin-film piezoelectric coefficient ($e_{31,f}$) which affects the PMUT's performance as an actuator, and causes low electromechanical coupling factor (k_t^2). Later, AlN with a 9.5 % Sc concentration was introduced to improve the piezoelectric coefficients without affecting the compatibility with the Silterra MEMS-on-CMOS process.

Materials properties, including the thin-film piezoelectric coefficient ($e_{31,f}$) and the relative permittivity (ε_{33}) are listed in Table 4.1 and compared with other reported piezoelectric materials. Both proposed AlN has similar $e_{31,f}$ hence their behavior as actuators should be the same, however, compared with the $Sc_{9.5\%}Al_{90.5\%}N$, is expected around a 39 % degradation in the output pressure. In addition, based on the piezoelectric coupling factor (K^2) introduced in the subsection 2.1.1, the $e_{31,f}^2/\varepsilon_{33}$ ratio is computed, giving an improvement of 1.25x factor when the presented AlN is compared with the AlN in [123]. Likewise, $Sc_{9.5\%}Al_{90.5\%}N$ presents the best value, being a 2.56x factor higher than the AlN (13.48 GPa) and 1.43x factor higher than the reported AlScN PMUT in [123], in which a higher Sc concentration (15 %) was used. These results conclude that AlN with a 9.5 % Sc concentration as piezoelectric material has a great potential as an actuator and sensor.

Table 4.1: Piezoelectric materials properties.

Materials	$e_{31,f}$ (C/m^2)	ε_{33}	Young's Modulus (GPa)	Poisson's ratio	$e_{31,f}^2/\varepsilon_{33}$ (GPa)
AlN[1]	-1.096	10.1	345	0.32	13.43
AlN[2]	-1.065	9.5	279	0.3	13.48
$Sc_{9.5\%}Al_{90.5\%}N$	-1.793	10.5	250	0.31	34.56
AlN[3]	-1.05	10.5	330	-	10.8
$Sc_{15\%}Al_{85\%}N$[3]	-1.6	12	200	0.23	24.1

[1] Corresponds to PMUTs Type I.
[2] Corresponds to PMUTs Type II and Type IV.
[3] Values reported in [123]

4.2 Cavity Size

The Type I and Type II PMUTs were the first modeled and tested devices where only a few changes in the technology were made. Considering the thickness of each layer and ignoring the shape of the electrodes, the total thickness of the membrane is 3.55 μm, and the location of the neutral axis is 1.88 μm, which is outside of the piezoelectric layer, thus allowing the correct behavior of the PMUT [129]. In addition, the mass per unit area, μ, and the laminate's flexural rigidity, D, (see Eq. 2.9 and Eq. 2.12) were computed for both types, giving a μ of 11 g/m^2 and 10.9 g/m^2; and a D of 0.75 $\mu Pa \cdot m^3$ and 0.65 $\mu Pa \cdot m^3$ respectively. Although the values obtained are close, Type II membranes are a little more flexible (lower D), which could translate into a greater displacement, but decrease the resonance frequency by 0.94x factor (ratio between D/μ corresponding to Type I and Type II). Based on this, using Type II, the resonance frequency for the first mode was estimated by Eq. 2.13 for two conventional clamped devices as a function of the cavity size, where a represents the side for the square and the diameter for the circular (Fig. 4.1 Inset). The results (dotted lines) agree very well with the resonant frequencies from a finite element method (FEM) model and as is expected, $f \propto \frac{1}{a^2}$, see Fig. 4.1a. Furthermore, Fig. 4.1b, shows the static displacement at the center of the membrane normalized with respect to the value obtained with the largest used cavity (90 μm). Note that the static displacement scales as a^2, keeping a constant relationship between the size of the top electrode and the cavity.
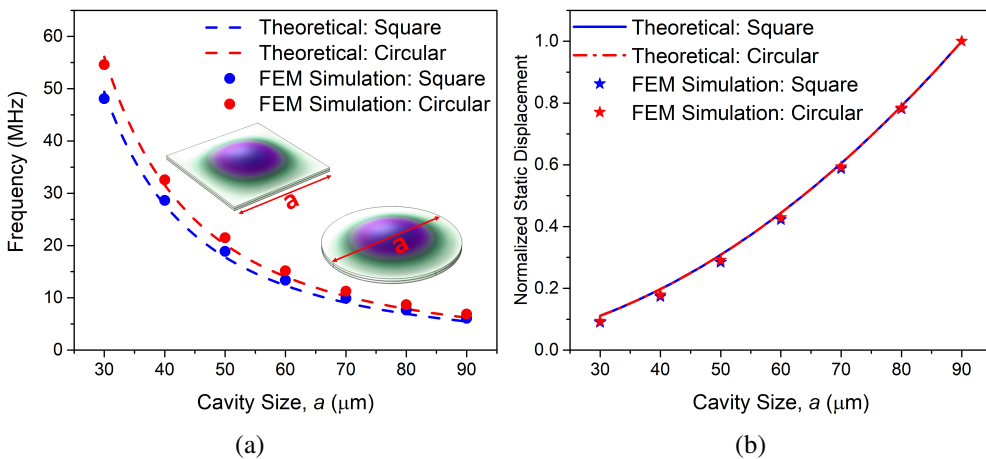
Figure 4.1: (a) Frequency response in air from the simulation and analytical solution. (b) Normalized static displacement of a circular and square membranes obtained via FEM Simulations and theoretical.

In summary, when only the cavity side is modified (keeping the same thickness and materials properties), the frequency and displacement show the aforementioned behavior, i.e., $f \propto \frac{1}{a^2}$ and $w_0 \propto a^2$. Taking into account this and the manufacturing design rules provided by Silterra, the PMUTs devices presented in this thesis use cavity sizes of 80 μm (around 5 MHz in air and high displacement) and 40 μm (around 20 MHz in air but low displacement) as a reference.

4.3 Devices Architecture and Design

The first devices studied will be: (a) a Type I "tent-plate", and (b) a Type I and Type II two-port PMUT. Both designs have the same thicknesses (1.3 μm AlN and 1.5 μm Si$_3$N$_4$), and cavity size (80 μm), which allows them to work in the same frequency range, below 10 MHz in air. In addition, the "tent-plate" PMUT gets its name because it is clamped only at the corners, and the two-port, as its name implies, has two top electrodes and a common bottom electrode. Both designs were intended to enhance the output acoustic pressure. Figure 4.2 shows a conceptual schematic top-view of the proposed PMUTs devices where:

- **a:** Cavity size for both designs.
- **i:** Inner electrode size for both designs.
- **d:** Outer electrode width.
- **g:** Gap between the cavity and the metal layer.
- **e:** Gap between the inner and the outer metal electrodes.
- **O$_i$:** Internal outer electrode side equal to $i + 2e$
- **O$_e$:** External outer electrode side equal to $O_i + 2d$
- **b:** Width of the holes.
- **l:** Large of the holes.

4.3.1 Tent-plate PMUT

The tent-plate PMUT shown in Fig. 4.2a is a square PMUT device with partial free boundaries which pretends to increase the effective area towards a piston-like movement, improve the output pressure and the reception sensitivity in a liquid environment **[Jour1]**. This transducer belongs to Type I where the piezoelectric (AlN) and passive layers are 1.3 μm and 1.5 μm respectively. In the proposed design, the holes go through the piezoelectric layer until the cavity, and they are covered with
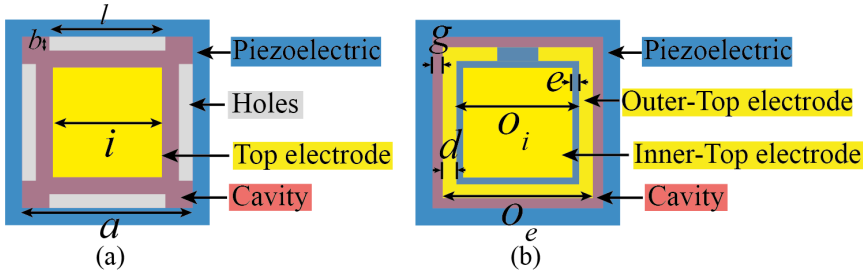
Figure 4.2: Schematic top-view of the PMUTs devices with the piezoelectric in blue, the top electrodes in yellow, and the cavity in red: (a) Tent-plate, the holes go trough the piezoelectric (represent in gray), and (b) Two-port clamped.

an elastic layer (sealed tent-plate). The benefit of the passive layer sealing the holes and allowing liquid operation, comes with a moderate degradation of the maximum achievable displacement of the sealed tent-plate PMUT in comparison with the free tent-plate PMUT (holes in all layers). Despite this, benefits are expected regarding the maximum displacement achieved in comparison with the clamped PMUT.

The dimensions of the holes have been chosen according with the simulation to optimize the membrane displacement (Fig. 4.3a) and the natural frequency (Fig. 4.3b). With these results if the width of the holes, b, increases for the same length, l, the displacement is higher but the resonance frequency decreases. To choose the holes dimensions, it is important to take into account that the passive layer, Si_3N_4, is conformally deposited over all the PMUT (as it is depicted in Fig. 3.1). In this sense, the size of the hole, specifically its width, b, must be chosen small enough to avoid the penetration of the Si_3N_4 layer until the cavity which would convert the tent-plate PMUT to a standard clamped PMUT with smaller size, avoiding a high displacement. Picking 2 μm width as a trade-off to avoid holes filling with Si_3N_4 layer (which allows preserving the modification in the boundary conditions), and considering also that the top electrode needs to be connected to the substrate, the best option for the length of the holes was 54 μm (see Fig. 4 in **[Jour1]**).

Regarding the electrode design, as was shown in section 2.4, there is direct dependence between the η and I_{piezo} (see Eq. 2.22), which makes it a decisive parameter to optimize the electromechanical conversion if the layer stack has been defined. For a clamped square PMUT, the top electrode could cover from 53 % to 77 % of the cavity size to maximize I_{piezo} and consequently the membrane displacement. To translate this into the tent-plate PMUT, a FEM simulation of a homogeneous plate vibrating in a vacuum with four symmetric linear holes with dimensions of 2x54 μm^2 was
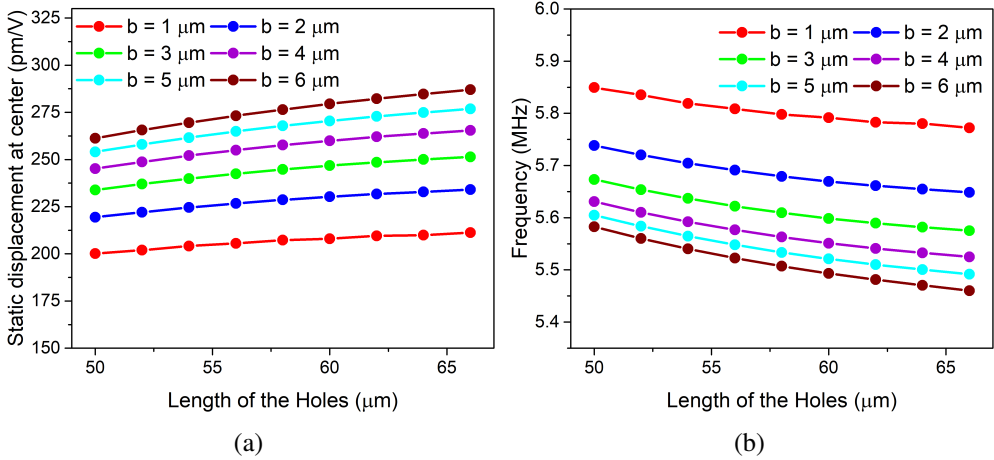
Figure 4.3: FEM simulation of tent-plate PMUT with different dimensions of the holes: (a) Dependence of the static displacement with the dimensions of the holes; (b) Dependence of the resonance frequency with the dimensions of the holes ©2020 IEEE **[Jour1]**.

performed. The resulting stress field, Fig. 4.4a inset, shows only two distinct stress regions, and with this result, a single top electrode configuration will be desirable where it should cover 71% of the cavity size. In order to validate this, the normalized static displacement was obtained changing the top electrode side, Fig. 4.4a. The maximum value is around 224 pm/V and the top side in this case is 56.6 μm, like was expected (0.71 · 80 μm). The final layout is shown in Fig. 4.4b where the holes with a length of 2x54 μm are at the edge of the cavity, and the top electrode side is around 57 μm. Once the final geometry is defined, the resonance frequency for the first flexural mode in air is 5.7 MHz, while when immersed in Fluorinert (FC-70) it drops to 2.175 MHz. Complementary simulations were reported in **[Jour1]** in order to demonstrate the enhancement in the PMUT performance as a consequence of the four linear holes.

4.3.2 Two-port PMUT

The two-port PMUT consists of a square clamped device with two top electrodes which is intended to increase the electromechanical coupling constant, η, and then, the membrane movement. This device has been reproduced in all fabrication lots (Type I-Type IV) but in this sub-section only Type I and Type II will be analyzed to keep the same thicknesses (AlN thickness is 1.3 μm and Si_3N_4 thickness is 1.5 μm).

To begin the physical analysis of a two-port PMUT, the stress field in a homogeneous clamped plate vibrating in vacuum was simulated. The result, shown in Fig.
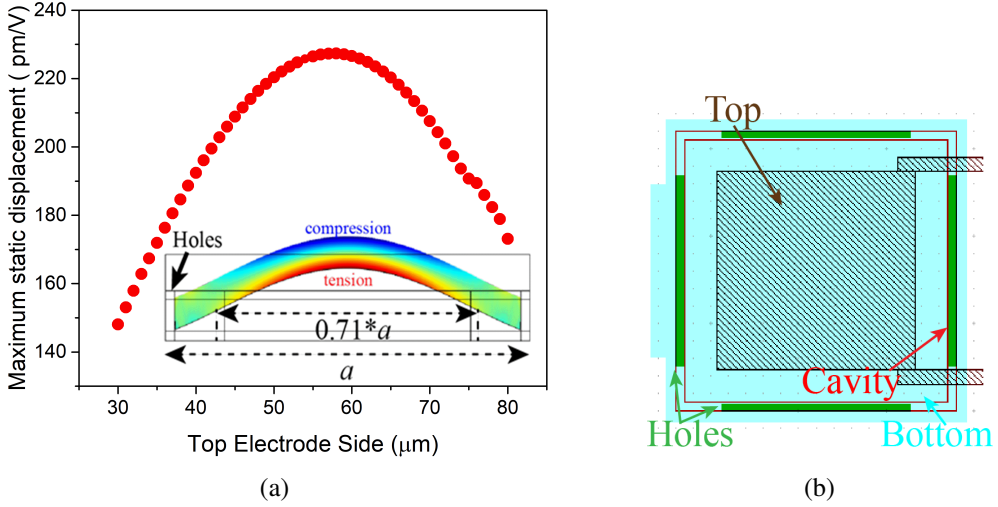
Figure 4.4: FEM simulations where (a) Maximum static displacement changing the side of the top electrode using the holes dimension selected previously and applying 1 V. Inset: Stress field distribution of a homogeneous PMUT with four linear holes (the layers are not to scale) ©2020 IEEE **[Jour1]** (b) Final layout of the tent-plate PMUT with their principal layers.

4.5a, gives six distinct stress regions (tension and compression) alternating around 65 % of the cavity side. As in the previous model, only one central electrode could be designed to cover around a 65 % of the cavity. However, to take advantage of the full stress field and not leave unused regions of materials, an annular electrode (outer) should be added. With this configuration and using Eq. 2.22, two electromechanical coupling constant are defined:

$$\eta_{inner} = 16e_{31,f}\overline{z_p}\Big[\gamma^2(\gamma^2 - 1)(\frac{\gamma^4}{5} - \frac{2\gamma^2}{3} + 1)\Big] \tag{4.1a}$$

$$\eta_{outer} = 16e_{31,f}\overline{z_p}\Big[\gamma_1^2(\gamma_1^2 - 1)(\frac{\gamma_1^4}{5} - \frac{2\gamma_1^2}{3} + 1) - \gamma_2^2(\gamma_2^2 - 1)(\frac{\gamma_2^4}{5} - \frac{2\gamma_2^2}{3} + 1)\Big] \tag{4.1b}$$

where $\gamma = i/a$, $\gamma_1 = o_e/a$, and $\gamma_2 = o_i/a$ (see Fig. 4.2b). When only the inner electrode is used, the maximal transformation energy ($\frac{d\eta_{inner}}{d\gamma} = 0$) takes place at γ=0.65, which is in correspondence with Fig. 4.5a. Likewise, if there is no gap (e=g=0 μm), the electromechanical coupling constant corresponding to outer electrode will have the same magnitude with the opposite sign, ($\eta_{outer} = -\eta_{inner}$). This result ensures a total electromechanical coupling factor that will be doubled when differential excitation is used, and therefore the maximum displacement should also be doubled [121].

Under these conditions (no gaps and V=1), the static displacement as a function of electrode dimensions is described in Fig. 4.5b for Type I and Type II. As expected, the inner and outer electrodes for the same device have the same behavior, reaching the maximum value when the inner electrode side is 52 μm (0.65*80 μm) and the outer width is close to 14 μm. In addition, at this point there is a 27% improvement in the displacement when using Type II, demonstrating the improvement in AlN properties, and the 90% of the maximum value give an inner electrode range from 42 μm to 61 μm. However, according to the technical rules used for PMUT fabrication, the outer electrode width (d) is reduced from the optimal one because it requires a gap between the inner and outer electrodes (Type I: e= 1.5 μm and Type II: e= 2 μm) and between the cavity and metal layer (g=1.5 μm). Figure 4.5c shows the maximum static displacement as a function of the ratio between the dimensions of the electrode (d/i), where it can be seen, that the maximum for the inner is different for the outer. In addition, although the gap between electrodes is greater in Type II, the displacement values are greater, even reaching the outer electrode in Type II to the same value as the inner electrode in Type I. Keep in mind that, when differential excitation is used, the total electromechanical coupling factor is the sum of both, $\eta_t = \eta_{inner} + \eta_{outer}$, giving for instance for a Type II a static displacement of about 232 pm/V, comparable with the tent-plate Type I.

The final layouts for the clamped devices are shown for Type I in Fig. 4.6a, and for Type II in Fig. 4.6b. The electrodes dimensions were chosen to achieve a compromise between both electrodes, being for both types the inner side close to 57 μm while the outer width is 8.4 μm for Type I (d/i=0.15) and 7.9 μm for Type II (d/i=0.14). Furthermore, there are differences in the width of the metal used for the wire connection with the substrate to achieve better symmetry, and in Type II the releasing holes, which are out of the cavity, were optimized, reducing their size.

4.3.3 Tent-plate vs. Clamped Type I-II

Once the final designs were defined, all devices were simulated to obtain a behavior closer to the real one. Table 4.2 summarizes the principal FEA results for each of them. The resonance frequency for the first flexural mode was obtained where the smallest correspond to the tent-plate, being only a 1.2x lower than the clamped Type I (highest value). On the other side, the static simulations demonstrate that tent-plate PMUTs should produce higher output pressure in comparison with the conventional PMUT when it is driven using the inner or outer electrode individuality, 224 pm/V

(a)

(b)

(c)
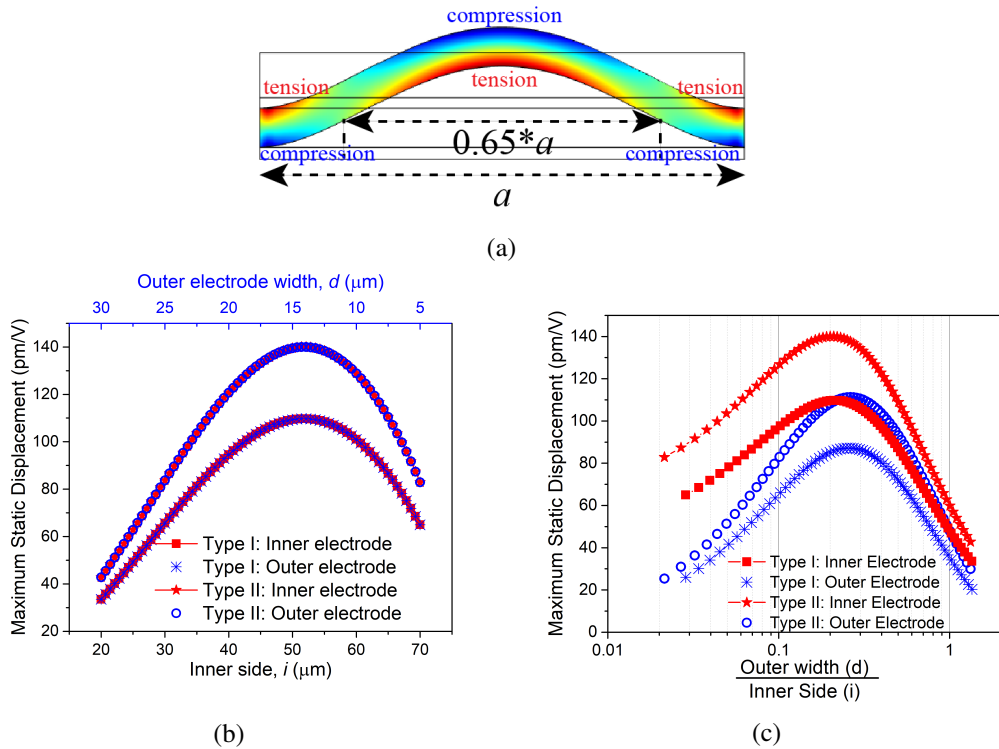
Figure 4.5: (a) Stress field distribution of a homogeneous square clamped PMUT (the layers are not to scale). (b-c) Theoretical maximum static displacement for clamped PMUTs based on Type I and Type II devices when V=1: (b) Ideal case (g=e=0 μm), and (c) Real PMUTs where: in Type I e= 1.5 μm; g=1.5 μm, and in Type II e= 2 μm; g=1.5 μm.

(a)

(b)
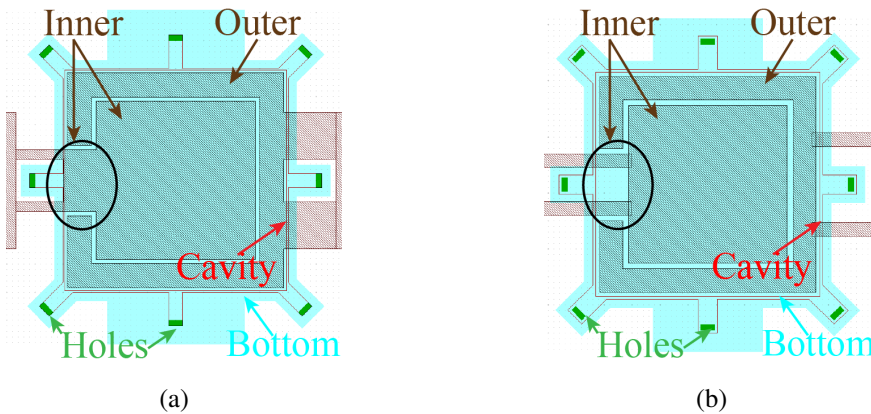
Figure 4.6: Layout of the two PMUT with their principal layers being: (a) Clamped PMUT Type I, (b) Clamped PMUT Type II.

in comparison with 100 pm/V and 150 pm/V when the inner electrode is used. Furthermore, as the output pressure scales with the vibrating area, the mode shape for the tent-plate PMUT is compared with the conventional PMUTs when is only used the inner electrode, see Fig. 4.7, where A_p corresponds to the piston area (the entire area vibrates), and the effective area (A_e) is considers at -6 dB of its maximum. For the tent-plate the movement is closer to a piston, being A_e approximately the half of A_p. However, as it is expected, for the clamped $A_e = 1/3Ap$, and describe a gaussian mode shape. Small asymmetry in the mode shape for the clamped Type I device (blue curve) can be appreciated as a consequence of the single site connection of the top electrode as shown in Fig. 4.6a.
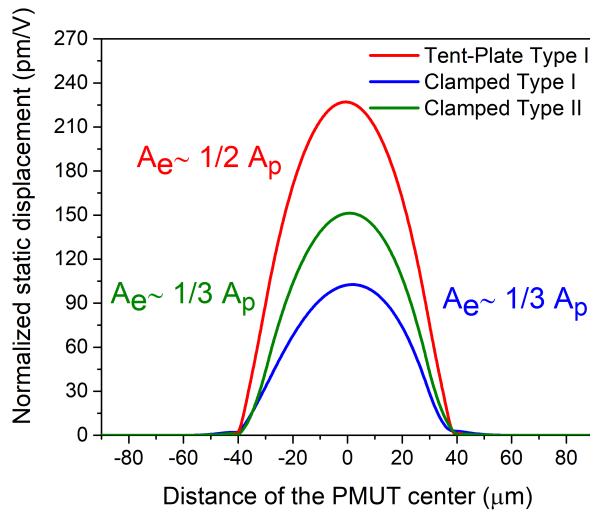
Figure 4.7: Normalized static displacement of the PMUT in x direction: tent-plate (red curve), inner electrode clamped Type I (blue curve) and inner electrode clamped Type II (green curve) ©2020 IEEE **[Jour1]**.

Finally, dynamic simulations were performed in Fluorinert [104], where, as a consequence of the high damping caused by the liquid over the PMUT surface, the resonance frequency decreases. Note there is a clear improvement in the displacement for the tent-plate PMUT in contrast with the clamped PMUT Type I, being 2.9x factor better when the inner electrode is used, and even a 1.4x factor when differential excitation is implemented. In addition, despite being similar clamped structures, Type II produces a maximum dynamic displacement with both electrodes of 805 pm/V, which is 1.6x greater than the 536 pm/V exhibited by Type I, and almost the same when tent-plate is used. On the other hand, the maximum values of velocity (u) are taken at

the center of the membrane, however, due to the devices don't move like a piston, it is necessary to consider the effective area (see Fig. 4.7) to obtain the mean membrane velocity (u_0). Based on this, the final membrane velocity has been re-normalized where the tent-plate will be better than the standard clamped PMUTs. All obtained results with the dynamic FEM simulation are in correspondence with the previous ones, demonstrating the positive influence of the holes to increase the movement of the membrane, as well as, the enhancement in the fabrication process from Type I to Type II.

Table 4.2: FEM Simulation results considering tent-plate (Type I) and clamped Type I and Type II PMUTs.

Parameters	Type I				Type II		
	Tent-plate	Clamped			Clamped		
		Inn	Out	Diff	Inn	Out	Diff
Frequency air [f_{air}] (MHz)	5.7		7.12			6.5	
Max. Static Displ. [w_0] (pm·V^{-1})	224	100	72	195	150	105	272
Frequency FC70 [f_{liquid}] (MHz)	2.175		2.75			2.48	
Max. Dyn. Disp. [w_d] (pm/V)	758	261	193	536	450	305	805
Max. Velocity [u] (mm·s^{-1}·V^{-1})	10.5	4.51	3.4	9.5	7.2	4.8	12.8
Mean Velocity [u_0] (mm·s^{-1}·V^{-1})	5.25	1.5	1.13	3.17	2.4	1.6	4.27

4.4 Experimental results

Figure 4.8 shows the optical images of the analyzed square PMUTs devices. Note the differences regarding the interconnection top-electrodes metals for clamped PMUTs Type I and Type II as well as the four symmetric holes for the tent-plate.

4.4.1 Electrical response in air

In order to characterize the frequency response in the air, PMUTs were initially measured using a manual probe station and a network analyzer as is described in the Chapter 3. Figure 4.9 shows their responses, giving a peak frequency for the first flexural mode of 4.9 MHz, 6 MHz, and 5.8 MHz for the tent-plate, clamped Type I,
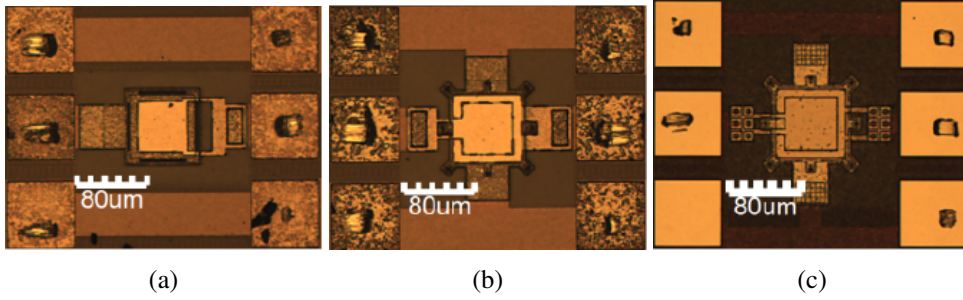
Figure 4.8: Optical images of the proposed devices being: (a) Tent-plate PMUT, (b) Clamped PMUT Type I and (c) Clamped PMUT Type II .

and clamped Type II respectively. The magnitude for clamped PMUTs is lower than the tent-plate because in this case, due to the configuration of the probes (Ground-Signal-Ground), the measurements are made between the inner and outer electrodes which has lower static capacitance, C_0. In addition, as the gap between electrodes is a little higher in Type II, then the capacitance between electrodes increases giving a C_0 a little bit higher. The measured frequencies are lower than the expected ones (see table 4.2), and the reason is due to the simulation doesn't consider any residual stress. The presented PMUT devices, like any multi-layer structure, suffer from residual stress mainly as a consequence of the different coefficients of thermal expansion in each layer [130]. The global residual stress could be tensile (positive value) or compressive (negative value), and if the structure suffers from excessive compressive stress, buckling effects can appear.
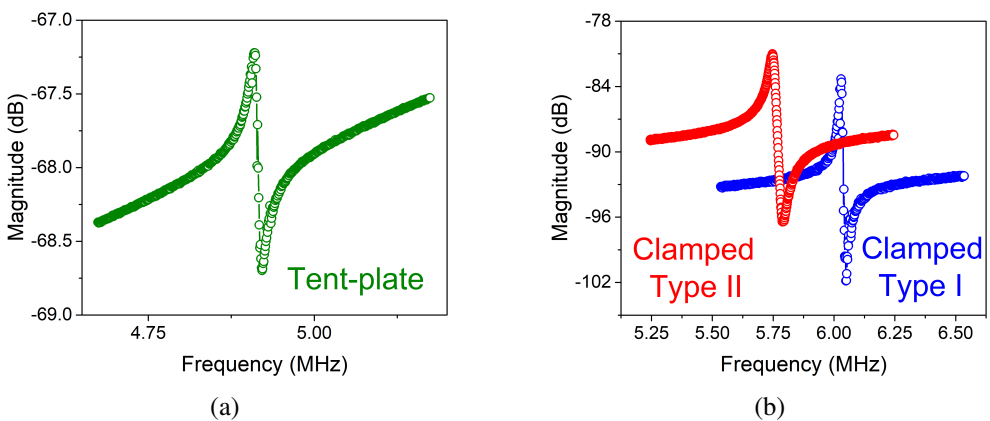
Figure 4.9: Magnitude amplitude of PMUT devices using a probe table: (a) Tent-plate PMUT, (b) Clamped PMUT Type I (blue) and PMUT Type II (red).

Equation 4.2 was used to evaluate the stress in the membrane, where the parameter

T_e represents the pre-tension in the multi-layer plate caused by residual stress (σ) [131]. The pre-tension term is written as $T_e = \sum_i \sigma_i h_i$, and D, μ, a and λ_{ij}^2 have been defined in section 2.2. Computing this equation, clamped devices exhibits T_e values about of -1.44 kPa·m and -1.08 kPa·m for Type I and Type II respectively resulting in a net residual stress of -405 MPa and -304 MPa respectively. For tent-plate is more difficult to obtain it because based in our design the λ_{ij}^2 is not tabulated, however as the fabrication lot (Type I) and the inner electrode side are the same, the global stress should be in the same range.

$$f_{ij} = \frac{1}{2\pi} \sqrt{\frac{\lambda_{ij}^4 D}{\mu a^4} + \frac{\lambda_{ij}^2 T_e}{\mu a^2}} \qquad i = 1,2,3,...,j = 1,2,3,..., \tag{4.2}$$

Furthermore, from the electrical response, the quality factor and the electromechanical coupling coefficient can be extracted, Table 4.3 summarizes all values. From the point of view of the PMUT as a resonator, the Q-factor is related to the energy losses, and in air these losses are mainly due to the anchors, intrinsic piezoelectric properties, etc., being the acoustic resistance negligible in comparison with mechanical damping. Based on this, from Eq. 2.27, if the Q-factor reaches high values in air, the R_m is low, indicating that the PMUT is an efficient resonator. In this sense, the tent plate exhibits the best value with a 2.6x and 1.9x factor improvement compared to Type I and Type II with clamped PMUTs, respectively. On the other hand, going back to section 2.3, the electromechanical coupling factor, k_t^2, is estimated based on the measured resonance and anti-resonance frequencies where clamped PMUTs reach the highest values. This fact is explained considering the alternative form, $\frac{C_m}{C_0}$, to obtain the k_t^2, where the low static capacitance between the two top electrodes ensures a high k_t^2 value.

Table 4.3: Quality-factor (Q-factor) and electromechanical coupling factor (k_t^2) comparison.

PMUT design	Type	Frequency (MHz)	Q-factor	k_t^2 (%)	Reference
Tent-plate	Type I	4.9	392	1	**[Jour1]**
Clamped	Type I	6	153	1.6	[125]
	Type II	5.8	205	1.72	[128]

Finally, the resonance frequency in Fluorinert can be estimated based on Eq. 2.29 where f_{air} is obtained through the electrical measurement (see Table 4.3) and β is the added virtual mass written as Eq. 2.30. Substituting each parameter, the resonance

frequencies predicted by this model are 2 MHz for tent-plate, 2.5 MHz for clamped Type I, and for clamped Type II, 2.4 MHz.

4.4.2 Output Pressure

To evaluate the performance of the discussed PMUTs in a liquid environment, the acoustic output pressure was measured, the used set-up is shown in Fig. 3.5. For this task, since the emitted pressure is acquired by a hydrophone, the minimum distance between this one and the PMUT surface (l) was determined. Taking into account the highest resonant frequency mentioned above (2.5 MHz), which corresponds to the minimum wavelength ($\sim 274 \ \mu$m), the minimum measurable distance was estimated according to Fig. 3.6a. For HNC-0200 the $l/2a$ ratio gives around 1.4 while for HNC-1500 it is 11, resulting in a distance of 112 μm and 880 μm respectively. Based on the previous values, and to avoid underestimating the real acoustic output pressure, HNC-0200 was used to evaluate the performance of the PMUTs devices. However, as a consequence of the high sensitivity (better signal-to-noise ratio) of the bigger hydrophone (HNC-1500), some measures were made using it.

Beginning with PMUTs Type I, the HNC-0200 hydrophone was placed at 1 mm over the PMUT surface by modifying the x and y positions to maximize the amplitude of the hydrophone reading. The driven signal consists of two sine cycles with an amplitude of 22 V_{pp}, and the resonance frequency was optimized giving 2.1 MHz for the tent-plate and 2.4 MHz for the clamped Type I. All experimental results are depicted in Table 4.4. The acquired voltage is converted into pressure through the sensitivity of the hydrophone in FC-70, where the tent-plate achieved, at the same axial distance, an improvement of 43 % compared to the pressure generated by the inner electrode, and even a 13 % when differential excitation is applied. Figure 4.10a shows the temporal response in each case where the start of the echo corresponds to unidirectional Time of Flight of 1.45 μs. In order to determine the transmitting sensitivity of the PMUTs (ST), which is defined as the surface pressure (P_0) per unit input volt, Eq. 2.38 was used. Considering the computed Rayleigh distance (R_0) and the measured pressure, the tent-plate PMUT achieves the best value, being $\sim$ 2x factor better than its counterpart, clamped inner electrode. The experimental results are in concordance with the simulated ones where considering PMUTs Type I, the positive influence of the holes is demonstrated with an improvement of a 1.4x factor is achieved with respect to the differential excitation and a 2x factor when it is only compared with the same dimension of the electrode. The normalized pressure (NP) is introduced in Table

Table 4.4: Output pressure and transmitting sensitivity in FC-70 for PMUTs Type I.

Parameters	Tent-plate	Clamped		
		Inn	Out	Diff
f_{liquid} (MHz)	2.1		2.4	
Pressure (Pa_{pp})	1500	850	564	1300
NP ($Pa \cdot mm \cdot V^{-1}$)	68.2	38.6	25.6	59.1
R_0 (μm)	19.4		22.4	
P_0 (kPa_{pp})	78.3	38.1	25.2	58.1
ST ($kPa \cdot V^{-1}$)	3.6	1.7	1.2	2.6

4.4 for further comparison and it depicts the acoustic output pressure at 1 mm from the PMUT surface when 1 V is applied. An alternative way to also obtain the normalized distance is through the relationship between the emitted pressure and the axial distance. The highest transmitting sensitivities are achieved by tent-plate and clamped PMUT with differential excitation, so the experiment was performed only with them. Figure 4.10b shows the pressure measured when the hydrophone is lifted every 500 μm and the fitted curve is adjusted following Eq. 2.38 giving 1622 Pa·mm and 1274 Pa·mm for tent-plate and clamped PMUTs.
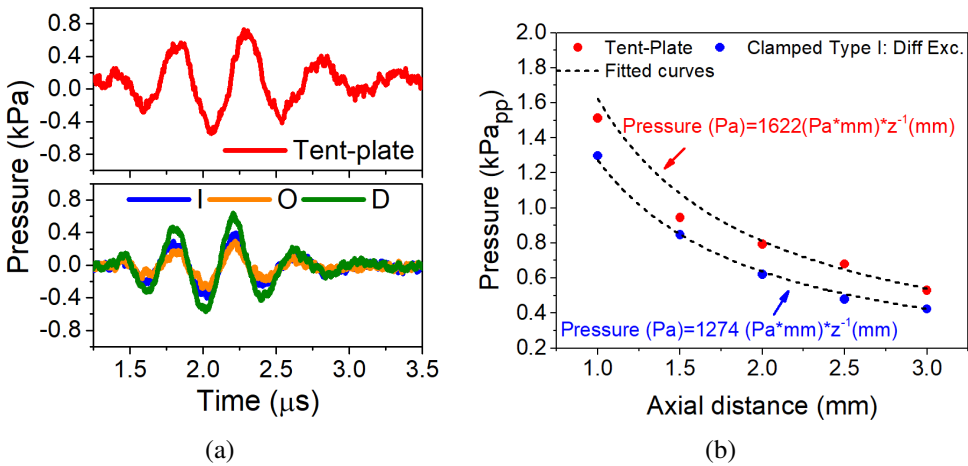
Figure 4.10: (a) Measured acoustic pressure in FC-70 at 1 mm away from the surface of: the tent-plate (Top, red curve) and clamped Type I (bottom, Inner (blue curve), Outer (orange curve) and differential (green curve)), and (b) The measured pressure versus the axial distance and its fitting curve.

Other complementary acoustic measures as actuators in FC-70 were done using the hydrophone HNC-1500, being the first one the frequency dependence response. The normalized time-domain echo at 3 mm when the PMUTs are excited with 4 cycles is

shown in Fig. 4.11a. The ringdown zone corresponds to the vibration of the membrane in absence of any driving signal at its natural frequency and, the duration of this ringdown vibration, τ, is directly related to the Q-factor ($\tau = 2Q/\omega$), which implies that if τ increases, the Q-factor also increases, and therefore the bandwidth decrease ($Q \propto BW^{-1}$, see Eq. 2.15). Observing the time responses, clamped PMUT exhibits a ringdown time larger than the tent-plate, which can be translated into a narrower bandwidth. To validate it, the Fast Fourier Transform (FFT) from the ringdown time domain response was obtained, see Fig. 4.11b. Peak frequencies and Q-factors are summarized in the inset table where as is expected, clamped PMUT achieves the highest values. In addition, the fractional bandwidth at -6 dB has been included, which is defined as the frequency width at half-maximum (BW$_{-6\text{ dB}}$) divided by its center frequency (f_0), i.e. $Fract.B(\%) = \frac{BW_{-6dB}}{f_0} \cdot 100$. Larger fractional bandwidth means that more frequency components are less affected by attenuation. For the proposed tent-plate device the value is 89 %, higher compared with most of the PMUTs reported [19], [101], and only comparable in case of using PDMS as acoustic coupling material with the liquid [101].
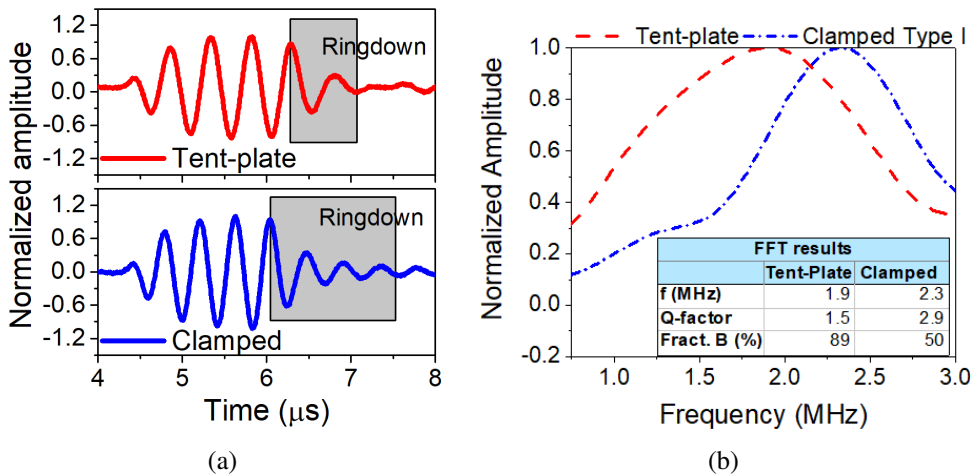
Figure 4.11: (a) Normalized time-domain response measured with the hydrophone situated over the PMUT at 3 mm. The top corresponds to tent-plate PMUT and the bottom to Clamped Type I. (b) Resulting Frequency response from the tent-plate (red) and Clamped (blue). Inset: Table with the principal parameters extracted from the FFT response.

Two-port pulse-echo system Type II

The acoustic characterization of the clamped PMUT Type II was performed using a PMUT-on-CMOS system where the outer electrode is used to transmit and the inner

electrode to receive reported in [103], [128]. Figure 4.12 top shows a general block diagram of the proposed system where a HV Pulser drives the outer electrode applying 32 V monophasic pulses; and the receiver part, directly connected to the inner electrode, consists on a Low-noise Amplifier (LNA) and a source follower buffer circuit for its testing with 50 Ω input load instruments [106]. Furthermore, two low voltage switches were used to avoid the LNA damage, where switch 1, SW1, (between the inner electrode and the LNA input) prevents the gate-to-bulk voltage from exceeding its corresponding breakdown voltage, whereas switch 2, SW2, (between input and output of the LNA) allows the LNA to quickly return to its adequate operation point (Vdd/2) after opening SW1, for the creation of the low impedance path among the LNA input and output [103]. The layout and optical image of the proposed system is shown in Fig. 4.12 highlighting its main blocks.
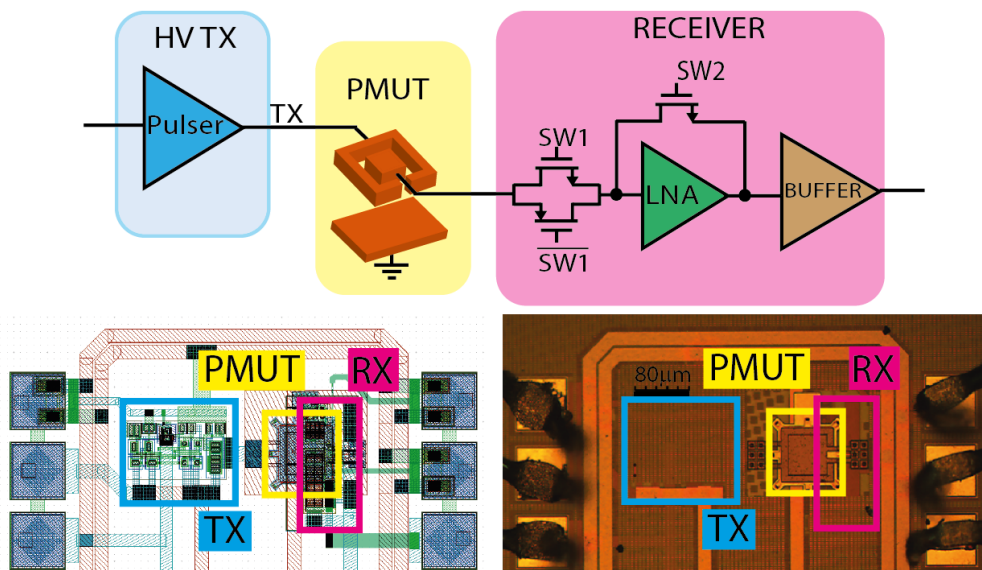
Figure 4.12: Top: Block diagram of the proposed transmission and reception system. Bottom-left: Layout, and Bottom-right: Corresponding optical image of the fabricated PMUT-on-CMOS transceiver. TX: Transmitter CMOS circuit. RX: Receiver CMOS circuit. Modified images extracted from [103], [128].

The driving signal consists in two pulses at 2.4 MHz and hydrophone HNC-0200 was used to acquire the signal. The dependence of the pressure with the axial distance was done lifting each 100 μm from 500 μm until 2 mm giving 2277 Pa·mm, and normalizing with the applied voltage (32 V) is obtaining 71 Pa·mm·V^{-1}. This normalized pressure includes a 1.27x magnification factor as a result of the squared input

signal. Despite this, the obtained value, 56 Pa·mm·V^{-1} (71/1.27), is higher than the clamped inner electrode Type I and comparable with the differential excitation but it is 1.4x factor lower than the tent-plate PMUT. In addition, the transmitting sensitivity was computed using the fitted curve, the Rayleigh distance (22.4 μm) and the input voltage (32V), giving 3.2 kPa·V^{-1}. Finally, considering the FFT response the central frequency, quality factor, and fractional bandwidth give 2.5 MHz, 2.1, and 66% respectively. This measured device corresponds to a different chip hence the dispersion in the results in comparison with [103] (f= 2.4 MHz; Q=2.2; Fract. Bw=63 %). Figure 4.13 shows acoustic pressure measurements at different axial positions and the time domain-response and the FFT from the ringdown.

Summarizing all experimental results as ultrasonic transmitters, tent-plate exhibits the best pressure level, with a transmitting sensitivity of 3.6 kPa·V^{-1}, however, the clamped PMUT Type II demonstrates to be a competitive candidate giving the possibility to use it as a single pulse-echo system with a high sensitivity (3.2 kPa·V^{-1}).
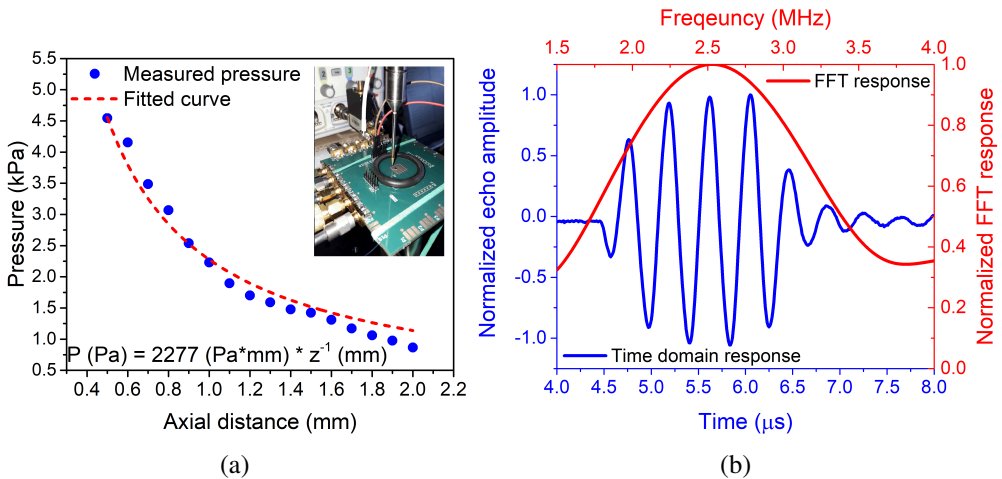
Figure 4.13: (a) The measured echo output pressure versus the axial distance and its fitting [128], and (b) Normalized echo amplitude measured at 3 mm over PMUT surface (blues line corresponding to bottom-left axis). Red line (corresponding with top-right axis) shows the FFT from ring down time-domain response.

4.4.3 Received Signal

The ability of the PMUTs to sense acoustic pressure from an incoming ultrasound wave was performed using a commercial transducer from OPTEL as described in Chapter 3. Its transmitting sensitivity is shown in Fig. 3.7b, giving 11 kPa$_{pp}$@2.1 MHz, and 14 kPa$_{pp}$@2.4 MHz when the OPTEL is placed at 3 mm and the input

voltage is 22V$_{pp}$.

For tent-plate PMUT, the received signal is directly acquired by the oscilloscope using cables of different lengths between them, where for larger cables (higher capacities), the amplitude decreases. Picking a cable length of 5 cm, the peak-to-peak amplitude gives 1.7 mV$_{pp}$ and the receiving sensitivity (SR) is 155 mV·MPa (where SR is computed as the relationship between the measured voltage and the input pressure; Vr/P_{in}). Figure 4.14 shows the dependence of the receiving sensitivity versus total parasitic capacitance (C$_{parasitic}$), which is obtained considering all capacities of the instruments and components that affect the measurement, i.e., the oscilloscope (14 pF), the cables (96 pF/m), and the set-up (3 pF), that includes PCB, connectors, etc. As is expected, the SR decreases if the C$_{parasitic}$ increases, however, each PMUT has an intrinsic sensitivity (SR$_{EOC}$) that should be the same regardless of the parasitic capacitance, see Eq. 4.3 [110]. Based on this, and considering the capacitance associated at the PMUT (C$_{PMUT}$= 255 fF extracted from the electrical measurement for the tent-plate **[Jour1]**), a fitting curve was performed giving a SR$_{EOC}$ of 13.4 V·MPa^{-1} (red curve in Fig. 4.14). This result demonstrates the importance to reduce the parasitic capacities which will be minimized through the monolithic integration on CMOS circuitry allowing much better signal-to-noise ratio. In contrast, the acquired signal when the inner electrode of the two-port PMUT Type I is connected to the oscilloscope through a cable with a length of 5 cm (4.8 pF) is 0.94 mV$_{pp}$, giving a receiving sensitivity around 67 mV·MPa^{-1}. This is 57 % lower than the tent-plate under the same conditions (155 mV·MPa^{-1}), and gives a SR$_{EOC}$ of 7.6 V·MPa^{-1}.

$$SR = SR_{EOC} \cdot \frac{C_{PMUT}}{C_{PMUT} + C_{parasitic}} \qquad (4.3)$$

During the measurements as a sensor, there are different uncertainty sources that mask the real sensitivity. The main error source is associated with the commercial ultrasound transducer from OPTEL calibration because: (a) the generated pressure by the OPTEL was calibrated using HNC-1500 hydrophone without considering the adequate working axial distance, and (b) the diameter of the OPTEL is much larger than the working wavelength. Regarding (a) the used hydrophone is 18.75 times larger than a single PMUT (1500μm/80μm) being very hard to achieve the same position in the x-y plane with respect to the OPTEL, hence is possible that the incoming pressure at the PMUT and hydrophone surfaces will be different. In addition, based on the
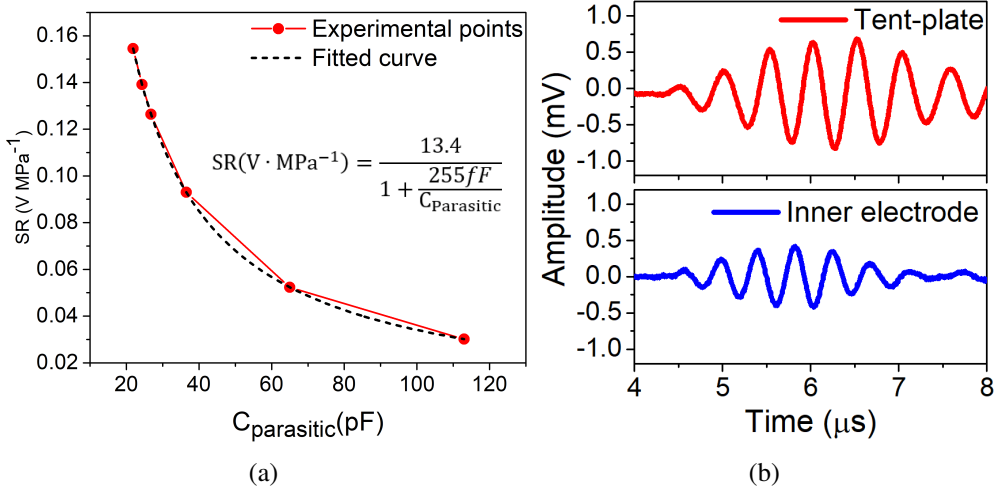
Figure 4.14: (a) Dependence of the reception sensitivity (SR) with the parasitic capacitance, and its fitting curve, and (b) Echo measured when the OPTEL is placed 3 mm over PMUT surface being Top: tent-plate PMUT and Bottom: inner electrode clamped Type I.

minimum measurable distance, is not possible to use our set-up to guarantee that the hydrophone is further away, for instance, if the wavelength is close to 300 μm, the minimum distance, l, is 10 times larger than the transducer dimension which gives 50 mm (see Fig. 3.6a). If we had used the hydrophone HNC-0200, the distance is reduced to 6 mm, but as a consequence of its low sensitivity, will be difficult to measure. Based on (b), the high diameter of the OPTEL ensures to be always in the near-field because we work in a short millimeters distance and the near-field is higher than 10 mm ($N = \frac{R_0}{4} = \frac{S}{4\lambda} = \frac{\pi \cdot (2.5mm)^2}{4 \cdot 300\mu m} = 16mm$). Despite this, OPTEL as an external source allows us to verify the correct operation of our system and the received echo can be distinguished, see Fig. 4.14b.

Finally, to avoid this issues, clamped PMUT Type II was studied as a pulse-echo system where the interface between liquid and air is used as the reflecting surface. Fluorinert thickness was adjusted in order to obtain different acoustic paths (round trip from 3 mm to 7 mm). The results are depicted in Fig. 4.15 and the fitting curve gives a receiving voltage dependence $V_r[mV_{pp}] = 5.6 \cdot z^{-1}[mm]$. In a pulse-echo system, a figure of merit (PE) can be defined according to Eq 4.4 [90] where P_{TX} and P_{RX} are the transmit and incoming pressures, while V_{TX} and V_{RX} are the driving and measured voltages. Assuming that the transmitted pressure an axial distance is the same as the impinging pressure when the acoustic distance traveled is the same, PE is re-written as $PE = \frac{V_{RX}}{V_{TX}}$, giving 175 $\mu V \cdot mm/V$. Furthermore, in terms of pressure,

both fitting curves were divided, giving 2.46 V·MPa^{-1}.

$$PE = \frac{P_{TX}}{V_{TX}} \frac{V_{RX}}{P_{RX}} \tag{4.4}$$
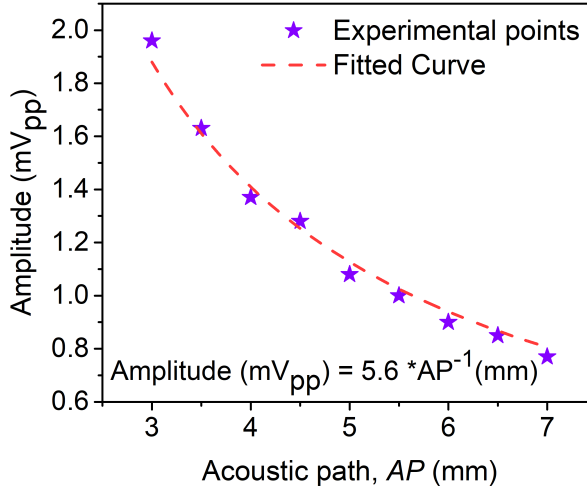
Figure 4.15: The measured output amplitude at different acoustic paths and the fitting curve.

4.5 Enhancing Two-port PMUT acoustic performance

The analysis of the improvement in the acoustic performance via thickness scaling and piezoelectric coefficient will be carried out using a clamped PMUT Type II with only one top electrode, however, the behavior can be extended to all PMUT Types and geometries. The experimental procedure carried out in this section is similar to the aforementioned, so the obtained results will be synthesized. Analysis and results of this thicknesses optimization was reported in paper **Jour3**.

4.5.1 PMUT thickness scaling

Section 2.6 describes the acoustic output pressure generated by a PMUT, which in the far-field region ($z >> R_0$) can be written as Eq. 4.5. Considering an equal-sized PMUT (S), the same acoustic medium (ρ_0), and the same axial position (z), the generated acoustic pressure scales linearly with the displacement of the membrane and quadratically with the resonance frequency, i.e., $p \propto w_d \cdot f_{liquid}^2$. In the previous section, a way of achieving large displacements was described through the tent-plate design. However, keeping the same geometry, boundary conditions, and piezoelectric

material, square AlN-clamped PMUT, the displacement can be increased if the flexural rigidity (D) lessens. In contrast, more flexible membranes cause a decrease in the resonance frequency, so to obtain higher pressure levels it is necessary to find a compromise between both of them. As summary, flexural rigidity (D) depends on the thickness of each layer, see Eq. 2.12, where thin membranes cause lower D, which increases the displacement and decrease the resonance frequency.

$$p = \frac{P_0 R_0}{z} = \frac{\rho_0 c_0 u_0 S}{\lambda z} = \frac{2\pi \rho_{liq} w_d f_{liquid}^2 S}{z} \qquad (4.5)$$

To evaluate the performance of the PMUT with different thicknesses FEM was used. In a first approximation, an axisymmetric model of a circular PMUT was assumed and mechanic–acoustic simulations were done to obtain parameters such as displacement, w_d; frequency, f_0; membrane velocity, u_0, and received output voltage, V_r. Figure 4.16 shows a diagram of the geometry used in FEM. The thickness of the Si_3N_4 passive layer (hP) as well as the AlN piezoelectric layer (hA) was swept from 1 to 2 μm and 0.5 to 1.5 μm, respectively, to obtain an enhanced acoustic performance in an equal-sized PMUT in Fluorinert. The material properties correspond to Type II shown in Table 3.2.
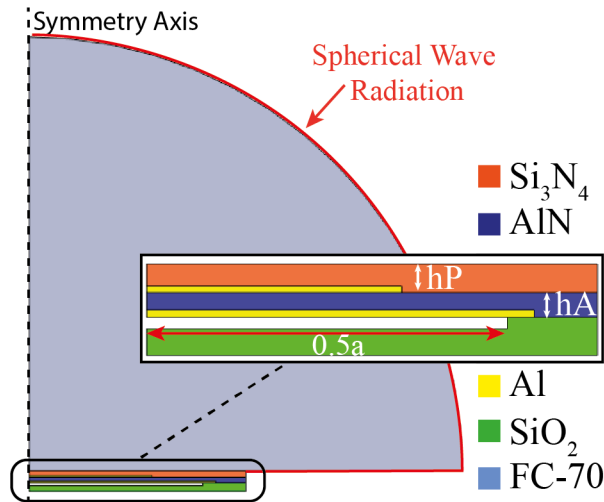
Figure 4.16: Diagram of a 2D geometry used in FEM simulations.

The dependence of resonance frequency and normalized dynamic displacement (in terms of applied voltage) as a function of the AlN and Si_3N_4 layer thicknesses are shown in Fig. 4.17. The results show that the variation in the displacement is greater

than a factor of x77 (from 34 nm·V⁻¹ at minimum thicknesses to 0.44 nm·V⁻¹ at maximum thicknesses) while the variation in frequency does not change by more than a factor of x3.3 (from 3.14 MHz at the maximum thicknesses to 0.95 MHz at the minimum). A figure of merit during the transmission is giving by the product $w_d \cdot f_{liquid}^2$, where it is expected that the output pressure is maximum with the minimum thickness. On the other hand, we are also interested in the PMUT as a receiver, thus we also simulated the normalized output voltage at the central top electrode when an acoustic pressure is applied on the PMUT surface (V·MPa⁻¹), see Fig. 4.18a, giving a maximum terminal voltage when the AlN thickness is close to 0.8 μm. Taking into account the capabilities as an actuator and as a sensor, we define a figure of merit (FoM) that covers both compartments and that allows us to estimate the best combination of thicknesses. Defined as $FoM = w_d \cdot f_{liquid}^2 \cdot V_r$, Fig. 4.18b shows the results where the optimal point appears when the AlN thickness is around of 0.6 μm and the Si_3N_4 thickness is 1 μm.
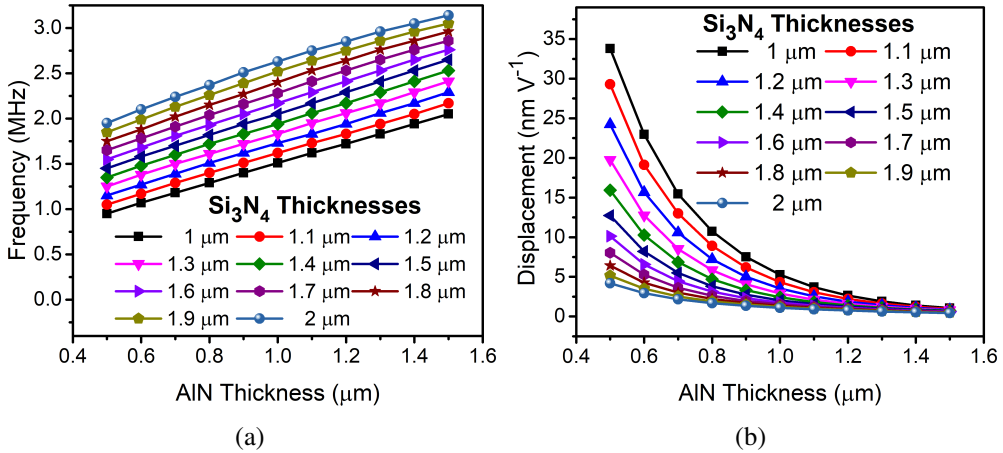
Figure 4.17: (a) Simulated resonance frequency, and (b) normalized dynamic displacement of an equal-sized PMUT sweeping the AlN layer thicknesses and for different Si_3N_4 layer thicknesses as parameters in a liquid environment **[Jour3]**.

Finally, to predict more realistic PMUT behaviors, 3D COMSOL simulations were performed considering all the geometric layout and thicknesses of the PMUTs manufactured. The resonance frequency for the first mode gives 4.19 MHz, 4.67 MHz, and 5.14 MHz considering Si_3N_4 thicknesses of 1 μm, 1.25 μm, and 1.5 μm respectively. Figure 4.19 depicts the computed and simulated static displacement where a good agreement between both of them is achieved: there is no difference when the outer electrodes are used and a small difference with the inner electrodes, which could be
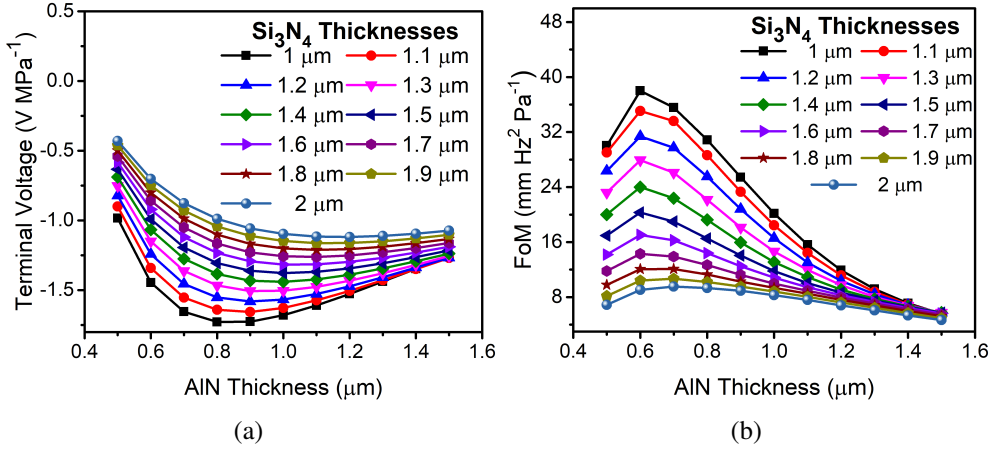
Figure 4.18: (a) Simulated normalized terminal voltage when an acoustic pressure is applied over the surface in a liquid environment. (b) Computed $FoM = w_d \cdot f_{liquid}^2 \cdot V_r$. Equal-sized PMUTs were considered **[Jour3]**.

due to the wire interconnection metals. In addition, it is also clear that bigger displacements are obtained with thin devices, even reaching an improvement of almost 58% for the same thickness of Si_3N_4 (1.5 μm). Dynamic simulations were also performed in FC-70 and the results are shown in Table 4.5.

From the results, thinner passive layers enhance the performance as a sensor but slightly decrease the achievable output pressure ($p \propto u \times f = w_d \times f^2$). Despite this, when the FoM (considering both transmitting and receiving PMUT system) is computed, for thinner PMUTs the value is higher. Comparing the results with clamped PMUTs Type II, where f = 2.48 MHz, w_d = 450 pmV^{-1}, V_r = 1.34 V MPa^{-1} (normalized voltage at inner electrode), is obtained a FoM around 3.71 Hz^2·m·kPa^{-1}, which is a factor of $\times$2.2 lower than that reported in the first column of Table 4.5. In addition, if we compared with the same Si_3N_4 thickness, an improvement of $\times$1.92 is achieved, which clearly highlights the benefits of using thinner piezoelectric layers.

Experimental characterization

As has been discussed so far, three PMUTs Type IV are introduced. To be clear when the results to which they belong are presented and analyzed, they have been classified as:

- **PMUT-1**: 0.6μm AlN and 1 μm Si_3N_4.

- **PMUT-2**: 0.6μm AlN and 1.25 μm Si_3N_4.

- **PMUT-3**: 0.6μm AlN and 1.5 μm Si_3N_4.
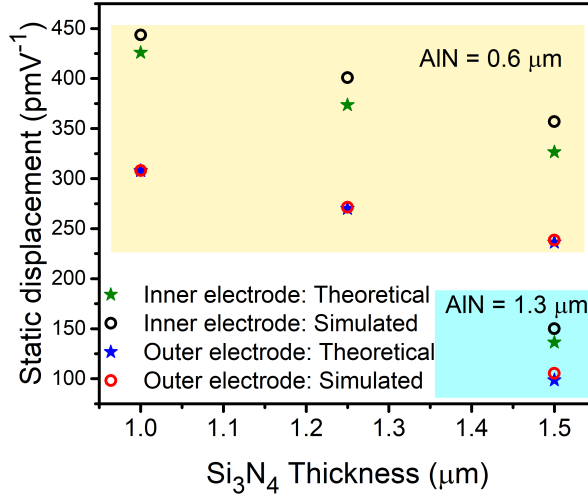
Figure 4.19: Theoretical and simulated static displacement for the proposed devices with different material layer thicknesses **[Jour3]**.

Table 4.5: Simulated performance for different Si_3N_4 layer thicknesses for a PMUT with 0.6 μm AlN piezoelectric layer using the inner or outer electrodes in liquid **[Jour3]**.

Si_3N_4	1 μm		1.25 μm		1.5 μm	
Electrode	Inner	Outer	Inner	Outer	Inner	Outer
Frequency, f (MHz)	1.36		1.58		1.8	
Displacement, w_d(pm·V^{-1})	2309	1539	1809	1175	1431	914
$w_d \times f^2$(m·V^{-1}Hz^2)	4271	2846	4516	2933	4636	2961
Terminal Voltage, V_r[a] (V·MPa^{-1})	1.91	1.78	1.73	1.55	1.54	1.35
FoM (Hz^2·m·kPa^{-1})	8.15	5.06	7.81	4.55	7.14	3.99

[a] Normalized value when 1 Pa is applied over PMUT surface.

The first measurements were done in air to obtain the resonance frequency for the first flexural mode giving 4.47 MHz, 4.87 MHz and 5.21 MHz for PMUT-1, PMUT-2 and PMUT-3 respectively. Computing the pre-tension parameter (T_e) through these values, we obtain 124.3 Pa·m, 93.8 Pa·m, and 6.5 Pa·m, resulting in a global tensile residual stress of 53 MPa, 36 MPa and 2.3 MPa. Note that these results are referred to the net residual stress, so it is not possible to extract level of residual stresses in the layers, specifically the value associated with the piezoelectric layer.

To verify their capabilities in a liquid environment, the acoustic pressure was first acquired with the HNC-1500 hydrophone placed at 3 mm over the PMUT surface.

Figure 4.20 shows the obtained results when each electrode of the PMUT-2 is driven independently with $22V_{pp}$ four cycles at 1.6 MHz. Unexpectedly, driving the inner electrode produces lower amplitude signals than driving the outer electrode. This behavior can be attributed to the additional curvature produced on the PMUT surface by the residual stress from the piezoelectric, passive layer and electrodes during the fabrication. The physical characterization of the surface profiles of the PMUTs using a surface profilometer confirmed that thinner membranes are more prone to bending [132], [133].
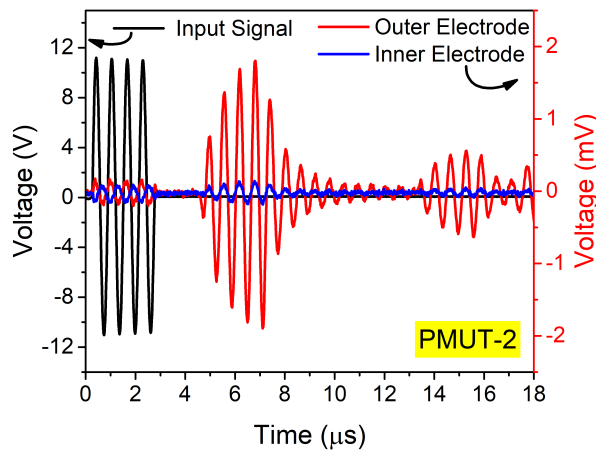
Figure 4.20: Time response of the acoustic signal produced by PMUT-2 when is driving the inner electrode (blue), and the outer electrode (red) (in both cases, the bottom electrode is grounded) **[Jour3]**.

Figure 4.21a shows a maximum central height for the PMUT-2 at around μm. Considering this curvature, several FEM simulations were done with same-sized membranes with two top electrodes in order to see the influence of this buckling. Based on the simulated dynamic displacements, the outer electrode achieves higher movement than the inner electrode response.

The acoustic performance as an actuator and as a sensor using only the outer electrode is summarized in Table 4.6. The generated pressure is measured at 2 mm over the PMUTs by the HNC-0200 hydrophone, while the incoming ultrasound wave is produced by the OPTEL placed at 3 mm. Evaluating each parameter discussed in Table 4.4, and comparing them with PMUT Type II (the pulse-echo system aforementioned), the benefit of thin piezoelectric layers is demonstrated with an improvement of twice as much in the transmitting sensitivity with respect to the PMUT-1 Type IV. Furthermore, there is a weak influence of the Si_3N_4 layer in the behavior of an ac-

<center>(a)   (b)</center>
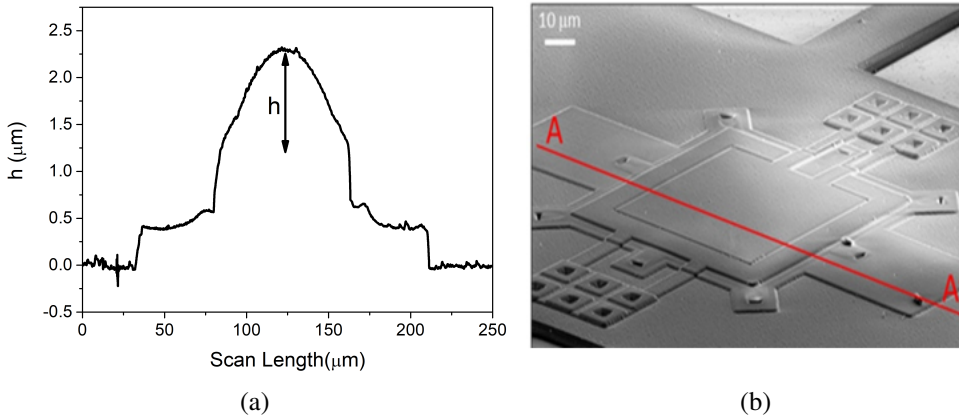
Figure 4.21: (a) Profile for curvature characterization of the PMUT-2 over the red line in the (b) SEM image, showing a h = 1 μm height in the middle of the membrane **[Jour3]**.

Table 4.6: Experimental performance characterization of the PMUT as an ultrasound transmitter and receiver using the outer electrode for electrical actuation/sensing.

Parameters	Type IV			Type II
	PMUT-1	PMUT-2	PMUT-3	
f_{air} (MHz)	4.47	4.87	5.21	5.8
f_{liquid} (MHz)	1.5	1.6	2	2.4
Pressure (Pa$_{pp}$)	743	796	736	1138.5
NP(Pa·mm·V^{-1})	67.6	72.4	66.9	54.7[1]
P_0 (kPa)	107	107	79.2	101.7
ST(kPa·V^{-1})	4.9	4.8	3.6	2.4[1]
V_r (V$_{pp}$)	2.8	2.5	2	-
$ST \times V_r$ (Pa)	13.7	12	7.2	-

[1] PMUT driving voltage in this case was a 32 Vpp squared signal instead of 22 V$_{pp}$ sine signal. To normalize the considering input voltage is 32·1.3.

tuator which could be caused by residual stress (thin membranes are more prone to high curvatures). In the sensing mode, the amplitudes decrease for thicker piezoelectric layers, with a weak dependence in respect to the thickness of the passive layer as was already seen in the simulations. Finally, the best performance as an ultrasound transducer is determined by the $ST \cdot V_r$ product and is achieved with the thinnest membrane (PMUT-1) as was already predicted by the FEM simulations.

Two-port pulse-echo system Type IV

The acoustic characterization as a pulse-echo system was performed using PMUT-1 and PMUT-2, coated with 200 μm of PDMS, where the layouts and optical images are

identical to those depicted in Fig. 4.12. The distance traveled by the ultrasound wave to either the hydrophone needle (a) or to the PMUT surface (b) is estimated through the total time and PDMS thickness. In (a), the unidirectional time of flight (ToF$_{uni}$) can be defined as $ToF_{uni} = \frac{200\mu m}{c_{PDMS}} + \frac{h_{FC70}}{c_{FC70}}$ where c_{PDMS} and c_{FC70} are the sound velocity in PDMS (1000 m/s) and FC70 (685 m/s) respectively, and h_{FC70} is the Fluorinert thickness. Once this is obtained, the axial distance is $z = 200\mu m + h_{FC70}$. In contrast, in (b) is important to take into account that the total time corresponds to the round trip so $ToF = 2(\frac{200\mu m}{c_{PDMS}} + \frac{h_{FC70}}{c_{FC70}})$, and then $AP = 2 \cdot (200\mu m + h_{FC70})$.

Figure 4.22 shows the frequency dependence of PMUT-1 and PMUT-2 considering a ToF of 4.38 μs which corresponds to an acoustic path of around 3 mm. The amplitude at each frequency has been normalized using the maximum peak, reached by PMUT-1 to 2.1 MHz. Regarding PMUT-2, the frequency peak appears at 2.4 MHz and the amplitude decreases a $\times$1.6 factor in comparison with PMUT-1. From these results, note how the PDMS layer causes a higher resonance frequency than FC-70 which can be explained through the effect of the added virtual mass. Computing it using Eq. 2.30 for both materials and considering the measured frequencies in the air, the frequencies in these media were estimated, to be close to the experimental ones. Table 4.7 summarizes the obtained results.
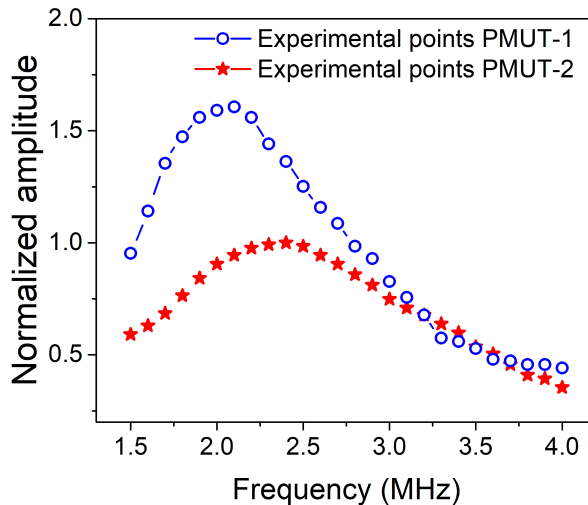
Figure 4.22: Pulse-echo experiment: Frequency dependence considering a ToF of 4.38 μs and PMUT covered by PDMS and immersed in Fluorinert.

Once the frequencies are determined, Fig. 4.23 shows the generated pressure at different axial positions as well as the received signal by the inner electrode adjusting

Table 4.7: Computed added virtual mass (Eq. 2.30) and estimated resonance frequency in FC-70 and PDMS via Eq. 2.29 and using the experimental frequency in the air.

PMUTs	β_{FC70}	β_{PDMS}	f_{air} (MHz)	f_{FC70} (MHz)	f_{PDMS} (MHz)
PMUT-1	7.58	3.84	4.47	1.53	2.03
PMUT-2	6.84	3.46	4.87	1.74	2.31

the FC-70 thickness to modify the acoustic path. From Fig. 4.23a, the normalized pressure can be extracted, giving 103 Pa·mm·V^{-1} and 99 Pa·mm·V^{-1} for PMUT-1 and PMUT-2 respectively. Furthermore, using the Rayleigh distance in both cases (R_0 is 19.6 μm for PMUT-1 and 22.4 μm for PMUT-2)), the transmitting sensitivity is 5.2 kPa·V^{-1} and 4.4 kPa·V^{-1} respectively. To compare with PMUT-1 and PMUT-2 without PDMS, the ×1.27 factor due to the effective amplitude of a square wave is considered, giving a ST of 4 kPa·V^{-1} and 3.5 kPa·V^{-1}. The decreased transmission sensitivity is a reflection of the negative effect of PDMS.

Likewise, Fig. 4.23b depicts the amplitude of the received signal at different acoustic path as well as the adjusted curve. Using the Figure of Merit defined in Eq. 4.4, PMUT-1 achieves a PE= 212 μV·mm/V while for PMUT-2, PE is 117.5 μV·mm/V. Note these values are lower compared with the PMUT Type II, however, here the PDMS layer degrades the signal as a consequence of the mismatch in the PDMS-FC70 interface with a reflection coefficient of 15%. Besides, the inner electrode in these thin devices are quite affected by the residual stress degrading its performance. To obtain the receiving sensitivity, the fitted curves were divided in each case, which leads to 2.05 V·MPa^{-1} for PMUT-1, and 1.2 V·MPa^{-1} for PMUT-2.
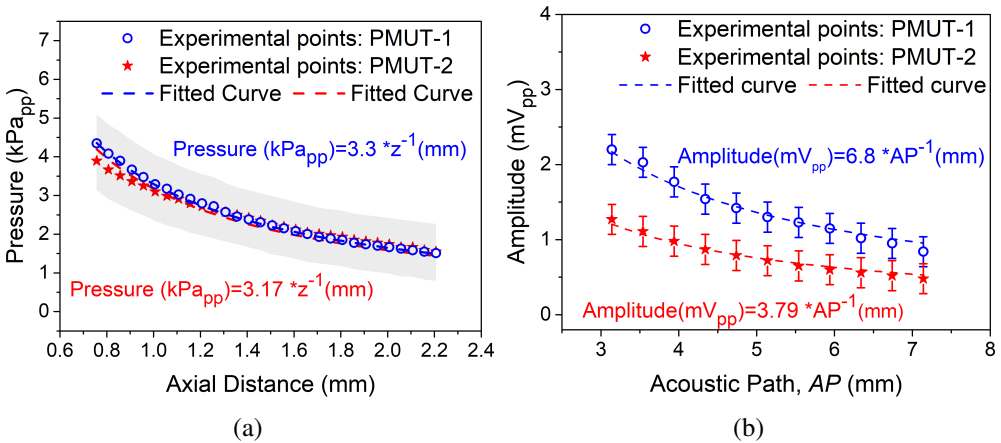
Figure 4.23: (a) The measured pressure versus the axial distance and its fitting curve, and (b) The measured output amplitude at different acoustic paths and the fitting curve.

4.5.2 Thin-film piezoelectric coefficient improvement

AlN with a 9.5 % Sc concentration was discussed in section 4.1 demonstrating a film-thin piezoelectric coefficient enhancement with respect to the AlN pure. Considering this doped piezoelectric material, in this subsection PMUTs Type III and Type V are introduced and their principal results are discussed. A clamped PMUT with two top electrode with an identical layout to the PMUT Type II was used.

The static displacement was computed and simulated considering different piezoelectric thicknesses and keeping the same Al electrodes (0.35 μm top and 0.4 μm bottom) and 1.5 μm Si_3N_4 as a passive layer. Figure 4.24 depicts the results demonstrating a good agreement between them and clearly showing an improvement of around 50 % for the AlScN PMUTs in comparison with the AlN PMUTs with the same piezoelectric thickness. In addition, dynamic simulations in FC-70 were performed and the results are summarized in Table 4.8. As is expected, in thinner devices the resonance frequency decreases and the membrane displacement is higher. Based on the FoM defined during the transmission as $w_d \times f^2$, PMUT Type V achieves an improvement of $\times 1.3$ with respect to Type III and almost an $\times 1.8$ in relation to its counterpart using AlN pure (see Table 4.5 when Si_3N_4 is 1 μm) proving this way the benefits of thin AlN doped with Sc.
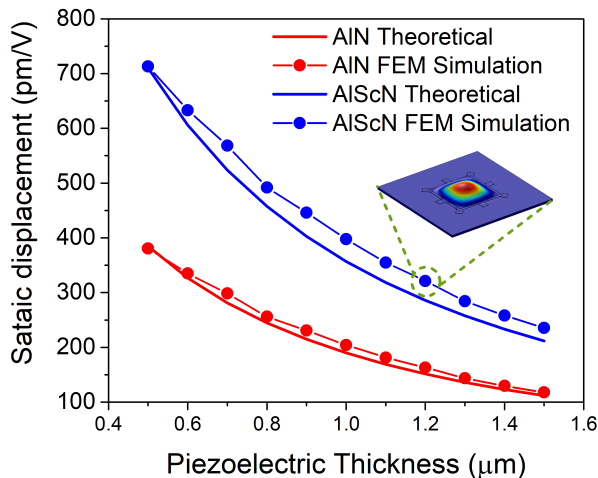
Figure 4.24: Computed and FEM simulated static displacement normalized with the applied voltage as a function of piezoelectric thickness for the AlScN and AlN PMUTs [100].

Table 4.8: FEM Simulation results considering clamped PMUTs Type III and Type V (the piezoelectric layer is AlScN).

Parameters	Type III			Type V		
	Inn	Out	Diff	Inn	Out	Diff
Frequency air $[f_{air}]$ (MHz)		6			4	
Max. Static Displ. $[w_0]$ (pm·V^{-1})	332	231	605	860	580	1495
Frequency FC70 $[f_{liquid}]$ (MHz)		2.3			1.3	
Max. Dyn. Disp. $[w_d]$ (pm/V)	1070	720	1950	4500	3000	8000
Max. Velocity $[u]$ (mm·s^{-1}·V^{-1})	15.5	10.5	28	37	24	65
Mean Velocity $[u_0]$ (mm·s^{-1}·V^{-1})	5.2	3.5	9.3	12.3	8	21.7

Experimental results

The electrical response from the AlScN PMUTs in the air has been done between the two top electrodes, giving a resonance frequency for the first flexural mode of 5.4 MHz and 4.5 MHz. The pre-tension coefficients in these cases give 200 Pa·m and -882 Pa·m, which can be translated into global residual stress of -256 MPa (compressive) for Type III and 93.7 MPa (tensile) for Type V.

Regarding the acoustic performance, several measurements were done in Fluorinert. Figure 4.25 inset shows a PMUT Type III pressure map when the inner electrode is driven with two cycles of 22 V$_{pp}$ at 2.2 MHz. The HNC-0200 hydrophone was lifted each 50 μm achieving axial and lateral displacements of 500 μm and 1 mm respectively. A cut along the z-direction (AA'), see Fig. 4.25a, at the center of the PMUT gives a normalized pressure (NP) of 121 Pa·mm·V^{-1} and a transmitting sensitivity of 5.88 kPa·V^{-1} [100]. In addition, the beam pattern was obtained through a lateral cut at 500 μm (BB') and the result is compared with the computed beam pattern corresponding to the hydrophone and PMUT (curve blue and red respectively). Taking the beam-width at -6 dB is obtained 777 μm instead of 1.14 mm (theoretical value). This difference is caused by the hydrophone directivity, which affects the omnidirectional PMUT response. The center frequency, Q-factor and fractional bandwidth was estimated through the FFT from the ring-down time response giving 2.26 MHz, 2.57, and 64.1% respectively. In terms of the sensed pressure, the OPTEL was

placed at 3 mm over PMUT surface and the amplitude received by the inner electrode is 3.3 mV$_{pp}$.
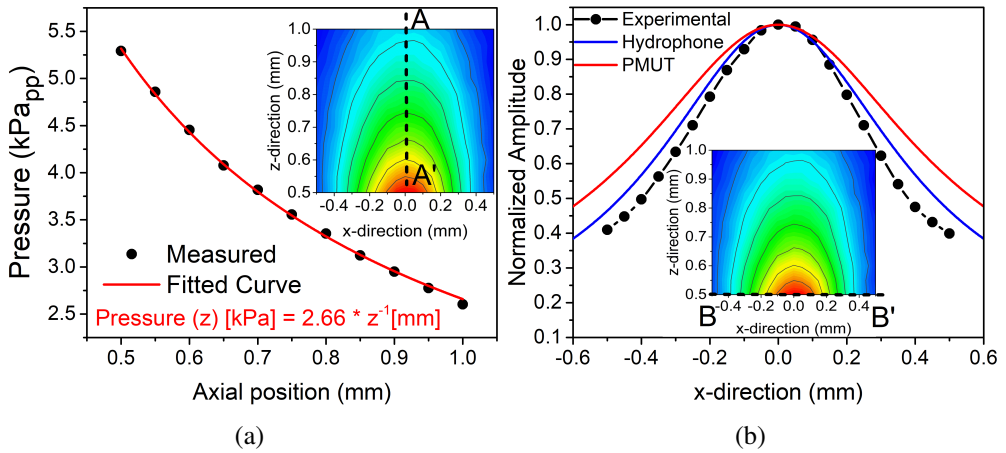
Figure 4.25: AlScN PMUT as actuator in FC-70 (a) Acoustic Pressure distribution along AA' cut (black points) and the fitted curve (red curve) considering 1/z dependence; (b) Normalized pressure at 500 μm over PMUT surface (black points). In blue the calculated hydrophone directivity and in red the calculated clamped PMUT field. Inset: Measured pressure map[100].

On the other hand, PMUT Type V was used in a pulse-echo configuration, where the outer electrode generates the acoustic pressure and the inner electrode is used to sense. As in previous pulse-echo systems, the layout and optical image are identical to those presented in Fig. 4.12. To characterize the generated acoustic pressure, the outer electrode was driving with four cycles at 1.55 MHz, and the pascals measured at 2 mm is about 2760 Pa. The normalized pressure and the transmitting sensitivity under these conditions give 136 Pa·mm·V^{-1} and 9.37 kPa·V^{-1} (considering the applied voltage 32V×1.27).

In addition, a frequency sweep during a pulse-echo experiment was performed to obtain the maximum peak and the Q-factor. Driving the outer electrode with two cycles and considering a ToF of 11 μs, the maximum frequency is reached at 1.49 MHz giving a peak-to-peak of 2.6 mV$_{pp}$, see Fig 4.26. Normalizing the amplitude of the sensed ultrasound wave with the acoustic path ($AP = 676 \cdot 11\mu s \approx 7.4mm$) is around 19 mV$_{pp}$·mm. From this value and applied voltage, the PE Figure of Merit (see Eq. 4.4) gives 594 μV·mm/V, being the highest value achieved with a single PMUT discussed in this thesis until now. Furthermore, taking into account the generated pressure, the receiving sensitivity is 3.6 V/MPa, and if the receiving element area is considered (80×80 μm^2, the receiving sensitivity could be increased

up to 0.45 kV/MPa for a 1 mm^2. Finally, the bandwidth at -3 dB gives 710 kHz and consequently the Q-factor is around 2.1.
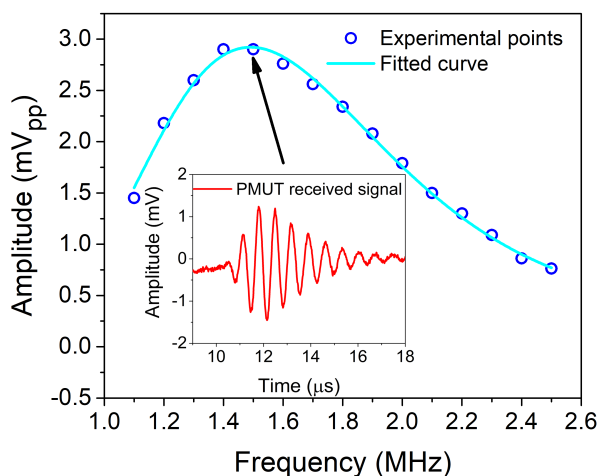
Figure 4.26: Frequency response considering FC-70 and a ToF of 11 μs. Inset: Pulse-echo time domain response at 1.5 MHz.

4.6 PMUTs comparison

This chapter focused into describe the modeling, simulation, design, and testing of several PMUTs in order to determine the most efficient in terms of transmitting and sensing acoustic pressure. In this sense, five types of PMUTs at frequencies in liquid below 3 MHz with different geometric and material properties were discussed. Tables 4.9-4.11 summarizes all simulated and experimental results from which the following conclusions can be extracted:

- The tent-plate design proposes an optimal geometry capable of improving the performance as an acoustic source. However, during the testing procedure in liquid are not always tight, causing the filling of the cavity and consequently being not possible to use in liquid. This fact degrades the yield of the device and becomes it less attractive since many devices need to be tested to ensure the results closest to the simulation. This is the main reason why this design was not replicated into the other Types of PMUTs.

- Clamped PMUTs devices show an improved performance from Type I to Type V where always differential excitation achieves high membrane vibration amplitude but for thin PMUTs inner electrode is not working properly. Using two

top electrodes allows the implementation of pulse-echo systems with a single PMUT.

- The 9.5% Sc concentration with 1.2 μm active layer thickness increases the piezoelectric thin-film coefficient achieving displacements a 50 % larger than the 1.3 μm AlN PMUT.

- A 46% decrease in the piezoelectric layer thickness improves transmission performance by a factor of two (PMUT Type II with respect to PMUT-3 Type IV).

- Type V PMUTs exhibit the highest membrane velocity, demonstrating the benefits to use a thin membrane with AlN with a 9.5% Sc concentration as a piezoelectric material.

The experimental characterization in a liquid environment (Fluorinert) is displayed in two separate tables. The first one, Table 4.10, contains the results regarding single PMUTs without any CMOS circuitry. In contrast, the second one, Table 4.11, summarizes the performance of pulse-echo systems where the outer electrode is connected to an HV transmitter and the inner electrode to an LNA amplifier. Considering the first table, AlN PMUTs with thinner layers guarantee high $ST \times V_\mathrm{r}$ products, which is only improved when 9.5% Sc is used. For the pulse-echo systems, the second table, normalization of pressure with voltage is done with 32V instead of 32×1.27 to demonstrate the benefits of the integrated system. Furthermore, as shown in the simulation, PMUT Type V ensures the most promising device with a transmitting sensitivity of 11.9 kPa·V^{-1} and an SR of 3.6 V·MPa^{-1}.

Table 4.12 summarizes a comparison between the performance of PMUT Type V and other PMUT devices reported in the state of the art that are operated in liquid. It can be stated that the two-port PMUT presented during this thesis achieves high levels of transmitting sensitivity (ST in kPa/V) compared with arrays of PZT PMUTs. In relation to the sensitivity as a sensor, PMUT Type V achieves around 3.6 V·MPa^{-1} being almost the same value reached by a 1-D array of 64 PMUTs. The best performance as an actuator and as a sensor is determined by the $ST \times SR$. Picking the highest value (9.28 [134]) an improvement of 4.6× factor is achieved with an area 36000 lower (230.4mm^2/6.4×10^{-3}mm^2).

Table 4.9: FEM Simulation comparison.

Type	Design	Exc.	f$_{air}$ (MHz)	w$_0$ (pm·V^{-1})	f$_{liquid}$ (MHz)	w$_d$ (pm·V^{-1})	u (mm·s^{-1}·V^{-1})	u$_0$ (mm·s^{-1}·V^{-1})
					Parameters			
I	Tent-plate	Top	5.7	224	2.175	758	10.5	5.25
	Clamped	Inn	7.12	100		261	4.51	1.5
		Out		72	2.75	193	3.4	1.13
		Diff		195		536	9.5	3.17
II	Clamped	Inn	6.5	150		450	7.2	2.4
		Out		105	2.48	305	4.8	1.6
		Diff		272		805	12.8	4.27
III	Clamped	Inn	6	332		1070	15.5	5.2
		Out		231	2.3	720	10.5	3.5
		Diff		605		1950	28	9.3
IV	Clamped	Inn	4.19	443	1.36	2309	19.7	6.6
		Out		308		1539	13.2	4.4
		Inn	4.67	401	1.58	1809	18	6
		Out		271		1175	11.7	3.9
		Inn	5.14	357	1.8	1431	16.2	5.4
		Out		239		914	10.3	3.4
V	Clamped	Inn	4	860		4500	37	12.3
		Out		580	1.3	3000	24	8
		Diff		1495		8000	65	21.7

Table 4.10: Experimental results considering single PMUTs without CMOS circuitry.

Type	Design	Exc.	Parameters					
			f_{air} (MHz)	f_{liquid} (MHz)	NP (Pa·mm·V^{-1})	ST (kPa·V^{-1})	V_r (V)	ST×V_r (Pa)
I	Tent-plate		4.9	2.1	68.2	3.6	1.7	6.12
	Clamped	In	6	2.4	38.6	1.7	0.94	1.6
III	Clamped	In	5.4	2.2	121	5.88	3.3	19.4
IV		Out	4.47	1.5	67.6	4.9	2.8	13.7
	Clamped	Out	4.87	1.6	72.4	4.8	2.5	12
		Out	5.21	2	66.9	3.6	2	7.2

Table 4.11: Experimental results considering single pulse-echo PMUTs-on-CMOS systems.

Type	Parameters					
	f_{air} (MHz)	f_{liquid} (MHz)	NP (Pa·mm·V^{-1})	ST (kPa·V^{-1})	PE (μV·mm·V^{-1})	SR (V·MPa^{-1})
II	5.8	2.4	71	3.6	175	2.46
IV	4.47	2.1	103	5.2	212	2.05
	4.87	2.4	99	4.4	117.5	1.2
V	4.5	1.55	172	11.9	594	3.6

Table 4.12: PMUT Type V comparison with the state-of-the-art.

Parameters	Type V	2017 [19]	2021 [134]	2021 [89]	2022 [90]
Single/Array	Single	Array 1×56	Array 1×64	Array 128×1	Array 1×12
Geometry	Square	Rect.	Circular	Circular	Square
Size	80μm × 80μm	30μm × 43μm	300μm pitch	160μm diameter	85μm × 85μm
Piezoelec. Material	AlScN	AlN	PZT	PZT	PZT
Acoustic media	FC-70	FC-70	Water	Water	Water
Frequency (MHz)	1.55	14	2.5	1.5	5
ST (kPa·V^{-1})	11.9	2.95	2.9	35.9·10^{-3}	9.4
SR (V·MPa^{-1})	3.6	2	3.2	0.19	0.87
ST×SR(×10^{-3})	42.8	5.9	9.28	6.82·10^{-3}	8.2

4.7 Single-cell fluid sensor using two-port Type V

MEMS devices have been widely used as sensors to characterize the hydrodynamic properties of the fluids, taking advantage of their ability to work as a resonator or as an acoustic device. Recently, PMUT-based microfluidic systems have been experimentally validated by exploiting the capabilities of PMUTs as resonators in which only density in low-viscosity liquids is detected. In this context, the best two-port PMUT, which corresponds to Type V, was used as a single cell for monitoring fluids, capable to sense density, acoustic or longitudinal viscosity, speed of sound and compressibility using minute quantities of fluid. Analysis and results of this application was reported in paper [Jour4]. Figure 4.27 shows a schematic representation of the proposed system. Its capability to work as a resonator and as a pulse-echo ultrasound transducer in liquids with a high-density value such as Fluorinert (1940 kg/m^3) and even with high viscosity such as 100 % of Glycerol (648 cP) offers added value compared to the state-of-the-art. As first step, the system is immersed in the fluid under test and working as a resonator, the density is directly obtained from the frequency response shift, achieving a high sensitivity of 482±14 Hz/kg/m^3. Viscosity can be also extracted from the frequency response evaluating its quality factor, but the dependence on the

density is dominant with respect to viscosity, limiting its evaluation.

To overcome this, further information can be extracted from the acoustic wave propagation using the single-cell PMUT in a pulse-echo mode. In this mode, the outer electrode of the PMUT is driven by the CMOS High Voltage integrated transmitter pulser, generating a traveling ultrasound wave in the fluid that is reflected by the interface between fluid and air, and it is received by the inner top electrode of the PMUT. The received ultrasound wave is translated to an electrical signal by the PMUT which is amplified by a CMOS integrated Low Noise Amplifier. In this case, the density can be determined by modifying the frequency of the driving signal and taking the value at which, the amplitude of the received echo is maximum. Additionally, from the temporal response at different axial positions the acoustic attenuation can be computed allowing to extract the viscosity, while the propagation time or time-of-flight allows to obtain the sound velocity in the fluid. Finally, from the density and the sound velocity, the compressibility of the fluid is determined.

The experimental verification shows that this tiny device, manufactured monolithically on a CMOS substrate, is an excellent candidate for a single measurement cell unit for use in microfluidic systems that require the characterization of the properties of small quantities of fluids. Integrated CMOS circuitry with further signal processing can be easily upgraded to provide smart solutions for demanding industrial and biomedical applications, with constraints on area, power consumption and cost.
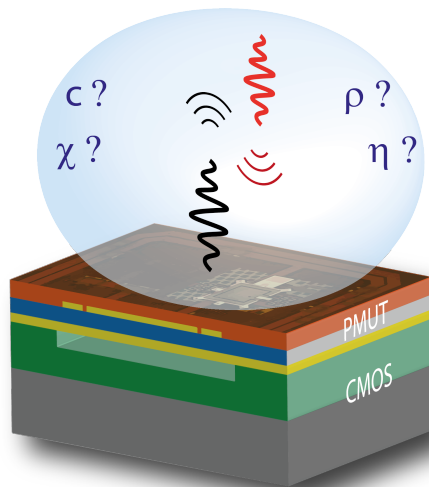
Figure 4.27: Graphical image of the two-port PMUT-on-CMOS Type V for monitoring fluids.

4.8 PMUTs with a pixel size below 50 μm

This last section is dedicated for different PMUTs devices whose dimensions are decreased to obtain higher frequencies keeping their capabilities to achieve higher pressure levels. As was explained in chapter 2, higher frequencies improve the axial resolution and increase the membrane velocity and consequently higher output pressure. To this end, different geometries were modeled, simulated and characterized. Figure 4.28 shows the first natural frequency for four small PMUTs Type I. Clamped, tent-plate, and crossed are squared AlN PMUT with 40 μm side, while bridge PMUT measures 40 μm$\times$ 47 μm, these dimensions defined by the cavities are outlined in red in the figure. In addition, the clamped and crossed PMUTs have 8 etching structures out of the PMUT-body, and the last one has two cross slits in the center of 40 μm$\times$2μm. In contrast, tent-plate is clamped only in the corners due to four linear holes (2 μm x 26 μm), and the bridge structure is asymmetric with two opposing linear holes of 2 μm x 40 μm on the edge of the small side. This devices has been discussed in [126], [127], however, some results have been repeated in order to give a more accurate characterization.

Clamped	Tent-plate	Bridge	Crossed
24.7 MHz	20.4 MHz	16.7 MHz	22.9 MHz
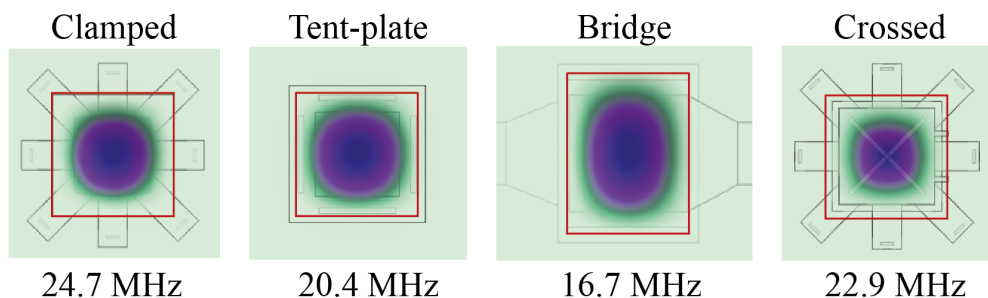
Figure 4.28: FEM Mode shape and frequency of PMUT devices Type I with a pixel size around 40 μm. The cavity is outlined in red.

The tent-plate and bridge structures pretend, as mentioned above, to achieve a more uniform displacement avoiding vibration reduction by a third as happens in a conventional design. Crossed, by your side, is inspired by a microphone of Vesper Technologies [135] where a microphone based on four 90 degrees sections of a squared membrane act as coupled cantilevers and form a cross-shaped slit in between. Based on these considerations, the simulated natural frequencies range from 16 MHz to 25 MHz, see Fig. 4.28. The static displacement reached by the membranes when 1V is applied to them as well as the simulated performance in Fluorinert is shown in

Table 4.13. Comparing the maximum static displacement at the center of the membrane, crossed PMUT exhibits an improvement of $1.3\times$ factor in comparison with the tent-plate, and $3\times$ factor in contrast with the standard clamped PMUT. Comparing to the 80 μm square PMUTs presented in the previous sections, the displacement of the membrane is considerably reduced, taking the lowest value corresponding to the inner electrode of the PMUT type I as a reference, the amplitude at the center of the membrane for the crossed device (the best displacement) drops $1.6\times$ times. Despite this, the frequency is high; therefore, the membrane velocity is comparable with this device (PMUT Type I).

Table 4.13: FEM simulated results of PMUT devices Type I with a pixel size around 40 μm.

Parameters	Clamped	Tent-plate	Bridge	Crossed
f_{air} (MHz)	24.7	20.4	16.7	23
w_0 (pm·V^{-1})	27.2	65.3	46.7	85.1
f_{liquid} (MHz)	12	9.7	7.1	10.1
w_d (pm·V^{-1})	44.2	118.4	103.8	124.5
u (mm·s^{-1}·V^{-1})	3.33	7.22	4.63	7.9

Clamped   Tent-plate   Bridge   Crossed
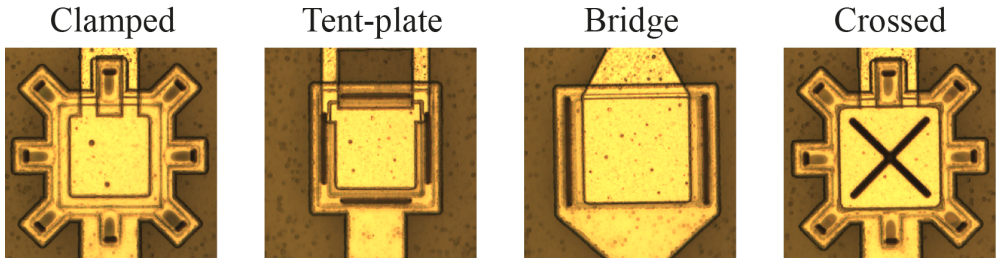
Figure 4.29: Optical images of the PMUT devices Type I with a size around 40 μm.

Figure 4.29 shows the optical images of clamped, tent-plate, bridge, and crossed PMUTs presented in this section. The electrical characterization in the air gives resonance frequencies of 18.5 MHz, 20 MHz, 16 MHz, and 14.5 MHz for clamped, tent-plate, bridge and crossed PMUTs. Considering the simulated and measured frequencies for clamped and crossed PMUTs, there is a significant difference between them due to: (a) the residual stress discussed in previous sections and also, for the crossed (b) the sealing layer penetrating into the slit. To evaluate the influence of the Si_3N_4 layer inside the holes, some FEM simulations were done, where the frequency

dropped considerably down to 20 MHz (no residual stress is considered). Further-
more, this effect affects the static vibration amplitude of the membrane by a $18\times$
factor, impairing the generation of acoustic pressure. For the tent-plate and bridge
PMUTs, seem that the holes in the edge of the cavity relieve stress by preventing a
mismatch between simulation and experimental values.

As a complementary measurement in air, the vibrating amplitudes of the clamped
and the tent-plate PMUTs were measured by a digital holographic MEMS analyzer
from LynceeTec (Lyncée Tec SA, Switzerland), see the set-up in Fig. 4.30a. The
top electrode was driven with 3 cycles at each resonance frequency and the bottom
electrode is grounded. Figure 4.30b shows the displacement at the center of the mem-
brane modifying the input voltages, and the linear fitted curves give the displacement
per volts. From the results an improvement of 72 % is achieved when four linear holes
are implemented in the membrane, demonstrating their effectiveness in the vibration
of the membrane. The 3D surface images when the 10 V_{pp} are applied depict in Fig.
4.30b, the left image corresponds to the tent-plate PMUT and the right to the clamped.

(a) (b)
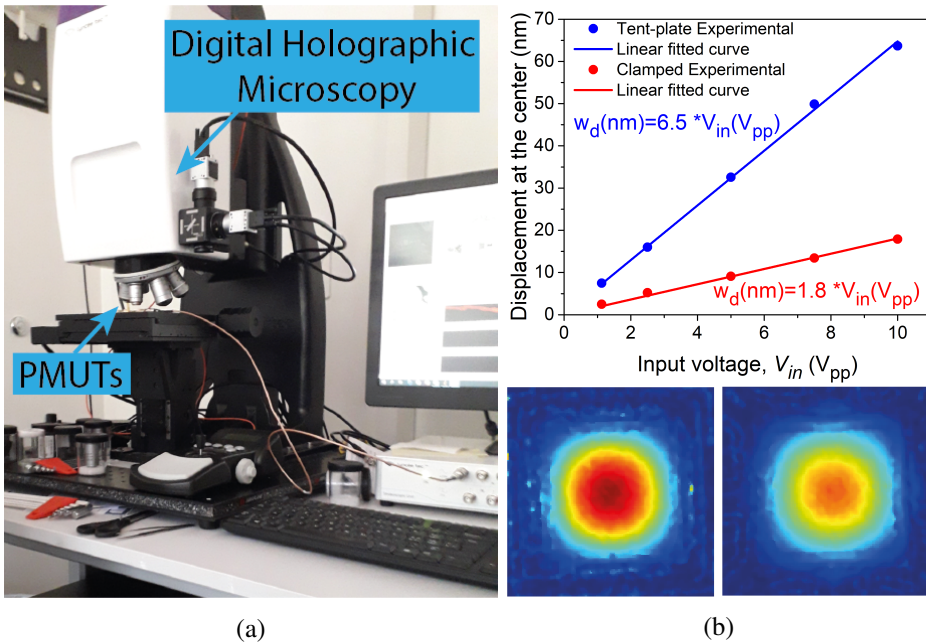
Figure 4.30: Measurements in the air. (a) Lyncée Experimental set-up, and (b) Top: Displace-
ment vs input voltage for the tent-plate and clamped PMUT. Bottom: 3D surface image when
the applied voltage is 10 V_{pp}.

The acoustic characterization in Fluorinert was performed using the HNC-1500

which provides a better signal-to-noise ratio due to the higher sensitivity compared with the HNC-0200, ideal to measure these smaller devices. However, taking into account the expected range of frequencies in liquid (around 10 MHz) for these PMUTs, the pressure will be underestimated because the dimension of the hydrophone's diameter is much larger than a half-wavelength. Despite this, the results allow us to compare them and extrapolated the results in the future if the smaller sensing element is used. On the other hand, to avoid further uncertainty in the measurements, the hydrophone was placed at 3 mm above the PMUT surface, ensuring that it is far enough away from the minimum measurable distance as was explained in Chapter 3. The driving signal in each case consists of four cycles with an amplitude of 22 V_{pp} at the optimized resonance frequency, except for the crossed device whose driving signal is 40 V_{pp}. All measured results are summarized in Table 4.14 where tent-plate and bridge PMUTs exhibits the highest transmitting sensitivities.

Table 4.14: Experimental results of PMUT devices Type I with a pixel size around 40 μm.

Parameters	Clamped	Tent-plate	Bridge	Crossed
f_{air} (MHz)	18.5	20	16	14.5
f_{liquid} (MHz)	7.5	7.4	6.7	6.3
Pressure@3mm (Pa)	31.3	43.6	49.6	26.2
ST (Pa·V^{-1})	242	341	365	133

[1] The amplitude of the driving signal is +40 V_{pp} (Top electrode: +20 V_{pp} and Bottom electrode: -20 V_{pp}.)

The results don't show significant variations as expected from the simulations (see for instance displacement in Table 4.13). This discrepancy between simulation and experimental results is due to the PMUT modeling does not consider the conformality of the different PMUT layers and especially the one related to the passive layer for the tent-plate, bridged, and crossed PMUTs. In addition, the signal acquired by the hydrophone is affected by its high sensing area, being lower than the real one. Despite this, the small PMUTs are very competitive in comparison with the ones published in the literature using AlN as piezoelectric material. For instance, a recently published low-thermal AlN PMUT in liquid operation reports values of 2.93 kPa/V @ 5.5 MHz with an array of 3x20 short-circuited PMUTs [102]. Normalizing this value to a single PMUT, the surface pressure would be 48 Pa/V which is a 7.5× factor lower than the

presented here for the bridged PMUT, demonstrating the capabilities of the presented designs.

Comparing small PMUT devices, the simulations show competitive values compared with the bigger ones, where tent-plate and crossed devices achieve membrane velocities in the same range that the clamped Type I. Despite this, the measured acoustic pressures are unexpectedly low, and one reason is a consequence of the used measurement instruments. In future work, these potential PMUTs will be further characterized to implement systems with improved axial and lateral resolutions and high output pressure levels.

ULTRASONIC SYSTEMS BASED ON PMUT-ON-CMOS ARRAYS

Till now has been discussed how the performance of a single PMUT can be improved. However, in most ultrasonic applications, a single device is insufficient and arrays of various configurations are implemented instead. Many ultrasound systems based on arrays have been the subject of several recent research efforts in order to implement an ultrasound system with a high transmission and reception sensitivities, a small area, and a great axial and lateral resolution. One of these cases is the 65 × 42 PMUT array presented in [34] where circular PMUTs with a diameter of 35 μm are distributed in a hexagonal layout to achieve good mechanical isolation. This system provided an output pressure on a 215 μm thick PDMS layer of 25 kPa which increased to almost 40 kPa if beam-forming techniques are applied, achieving at the end, an ultrasound image of a real fingerprint. In 2017, *Jiang et al.* [19] proposed a 110×56 PMUT array for a fingerprint sensor with a fill factor around a 50%. In this case, the transmit output pressure is 9.4 kPa when a single column was used, while the sensitivity as a sensor was 2 V·MPa⁻¹. Likewise, the capability to reconstruct a fingerprint image based on the epidermis and sub-epidermis layers was demonstrated.

Another array configuration that has aroused great interest in the scientific community is 1-D arrays due to their feasibility in terms of interconnection and low management complexity. *Wang et al.* in 2018 presented a PMUT array with five elements of 3×20 PMUTs each one and, where, the top electrodes of an individual element

were short-circuited [102]. The achieved transmitting sensitivity was 2.93 kPa/V at 5.5 MHz and the receiving sensitivity was 0.5 V·kPa^{-1} (using a commercial charge amplifier with a gain of 10 V/pC). Recently, two PZT 1-D PMUT array for medical imaging were reported in [89], [134]. In the first one, a 128×1 array with a large active area, 26×10.4 mm^2, achieved transmission and reception sensitivities of 430 Pa/V@3 cm and a 190 mV/MPa. The second one, reported in [134], shown a 1D array of 64 elements where the sensitivity as transmitter and as receiver gave 31 kPa/V and 3.2 V/MPa, respectively. These last two systems show competitive performance for ultrasound applications through B-mode imaging demonstration.

Last but not least, annular configurations based on PMUTs have demonstrated the ability to have a good control focusing along the axial direction. *Lu et al.* implemented eight concentric rings where 2 kPa/V pressure sensitivity was achieved with a total aperture of 1.2 mm [28]. Unfortunately, the focusing capability was only demonstrated using FEM simulations. Another annular array based on PMUTs was presented by *Eovino et al.* in [15]. The continuous rings exhibited a great potential in terms of acoustic output pressure and focusing ability compared to typical array designs with a transmitting sensitivity of 3.2 kPa/V in a standard transmission and 12.2 kPa/V focusing at 1.9 mm.

In this chapter, two array configurations will be discussed. The first one consists on a 7x7 PMUTs array connected in columns of 7x1. In contrast, the second array is based on five concentric rings with individual high-frequency PMUTs devices connected across the top electrode. Both of them were fabricated using the MEMS-on-CMOS Silterra fabrication process already discussed, see Chapter 2. As presented in the last chapter with the individual PMUTs, here we intend to characterize the performance as actuators and as sensors. The efficacy of the presented array will be verified through their ability to be implemented in ultrasound imaging systems.

5.1 A 0.5 mm^2 pitch-matched AlN PMUT-on-CMOS ultrasound imaging system

Figure 5.1 depicts the schematic layout and the optical image of the proposed system. Each row is made up of seven square PMUTs Type II with a side length of 80 μm where all top electrodes are connected. The gap in both direction between each device is 25 μm, giving a total area of 0.71×0.71 mm^2. Regarding the CMOS circuitry, the transmission side is composed of three HV Pulser, each shared by two

rows configured symmetrical from the central row, while the readout is only carried out at the central row by a CMOS LNA. Such as in the above-mentioned pulse-echo systems, two low voltage switches were used here to avoid the LNA damage, due to the crosstalk between the transmitter and receiver rows. As it can be seen in the layout, all CMOS circuitry is covered by the PMUT array, making it in a pitch-matched system with a reduced area.
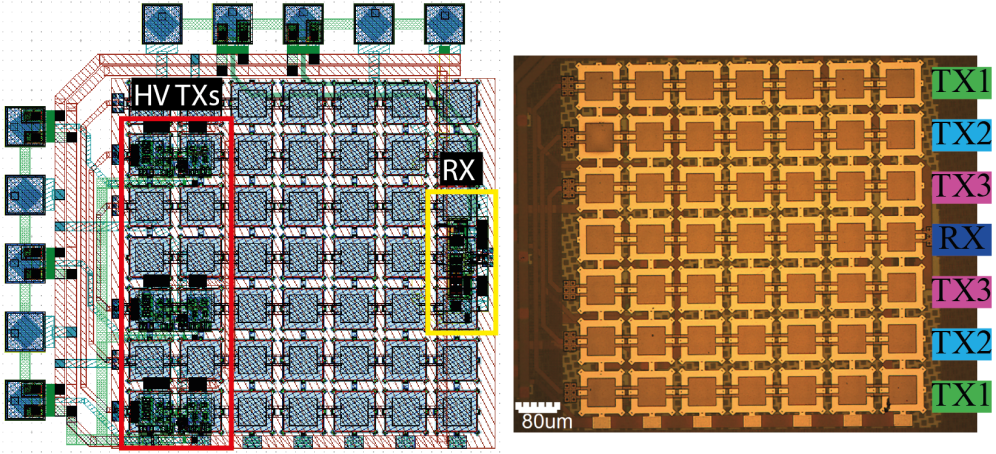
Figure 5.1: (Right) Schematic layout of the PMUT-on-CMOS array with their principal blocks highlighted; in red the HV TXs Pulser and in yellow the LNA amplifier. (Left) Corresponding optical image of the fabricated PMUT-on-CMOS array where rows sharing TX are in the same color and only the central row will receive.

Based on the geometrical specifications, the system can be represented as two sections of three elements. The gap between each section consists in the receiver element size and two pitches, giving an empty distance during the transmission of 130 μm. In each section, every element has a width of 80 μm and a length of 710 μm (7*80 μm+6*25 μm) separated by 25 μm. From the geometric parameters can be determined the fill factor and the influence of grating lobes as undesired lobes. The first one, FF, was defined in Eq. 2.40 and it gives a 78.8 %. This value is 1.5$\times$ higher than the 110$\times$56 presented in [19] and comparable with the 79 % reported in [102]. On the other hand, to assess the presence or absence of grating lobes, the pitch must be compared with the maximum allowable pitch size, $d_{\max}$, that completely eliminates grating lobes, see Eq. 5.1 [136]:

$$d_{max} = \frac{\lambda}{1 + \sin(\theta_s)_{\max}} \frac{N-1}{N} \tag{5.1}$$

where λ is the wavelength, N is the number of elements in the array and θ_s is the steering angle. The configuration of this array (two rows sharing a transmitter circuit) enables only a tuneable focus at its center (no steering is possible), and for this, the θ_s is always zero. Considering this, N equal 7, and λ is 207.6 μm (PMUT Type II resonance frequency, $\approx$ 3.3 MHz and Fluorinert as fluid medium with sound speed of 685 m/s), the value of $d_{\max}$ is 177.9 μm, which is larger than the pitch used here (105 μm), ensuring no grating lobes.

The acoustic performance was simulated with Field II, taking the advantage of the fact that beam pattern modeling is very quick to perform and allows an easy under-standing of the acoustic behavior of the proposed system [95], [96]. Figure 5.2a shows the 2D normalized pressure map at 3.3 MHz from 50 μm to 3 mm along the axial di-rection and from - 1 mm to 1 mm laterally. Unwanted signals appear as side lobes because the criterion for avoiding grating lobes is ensured. Furthermore, from the result, two profiles are performed: (1) an axial profile at the center of the pressure beam (lateral distance = 0 mm), and (2) a lateral profile at the maximum value (axial distance = 717 μm), Fig. 5.2b shows the results. According to this, the near field is close to 717 μm and the beamwidth at - 6 dB gives 334 μm which is equivalent to a resolution of 76 dpi.

(a)	(b)
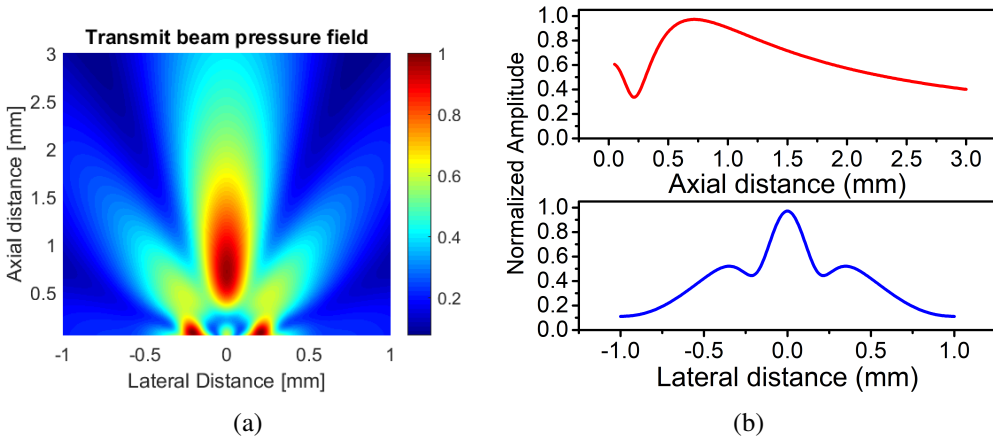
Figure 5.2: Field II simulation results; (a) 2D pressure map, and (b) axial profile at the center (top) and lateral profile at the maximum (bottom).

As mentioned in Chapter 2, in the far-field, the beamwidth (BW) scales as BW $\propto$ 1/D (where D represents the aperture), which means that at the same point a larger array achieves narrow beamwidth. Based on this, the transmission pressure field was simulated under different configurations, as shown in Fig. 5.3, where the receiving

element is gray, the transmitter rows are orange, and the active aperture is outlined in cyan, and from the results the peak amplitude at z = 1 mm and the corresponding -6 dB beamwidth (BW) were extracted. The size of the aperture was modified by increasing the number of the adjacent active rows without empty zones to prevent the effect of grating lobes (pitch $< d_{max}$). The enhancement factor during the transmission (ST improvement) refers to the normalized value with respect to the peak amplitude achieved by the smallest of the apertures (3 elements), see red stars in Fig. 5.3. Note that by increasing the aperture from 3 to 7, the peak pressure is increased by a 2.6× factor, and the beamwidth is reduced by 40 %. Another way to improve the lateral resolution is applying beamforming techniques at distances less than 717 μm (near field when all rows are active), for instance, focusing at 500 μm, the BW is 192.4 μm, being a 42.4 % lower than the achieved in natural focus, and if focused at 300 μm, the BW can be reduced to 157.6 μm.

(a)   (b)
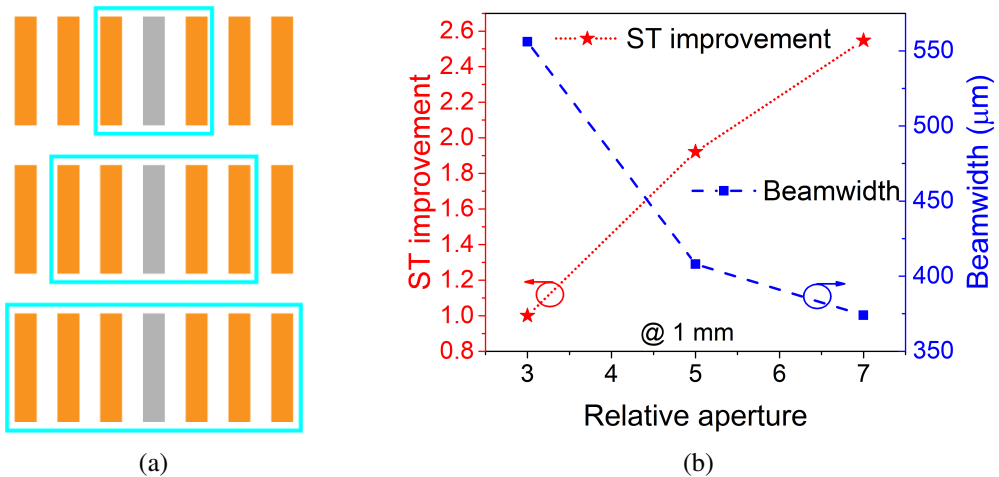
Figure 5.3: Effect of the aperture configuration where (a) shown a schematic representation of the array, and (b) the simulated results (transmission sensitivity improvement, near field, and beamwidth) extracted from Field II at 1 mm.

5.1.1 Experimental results

In order to evaluate the acoustic output pressure, the linear array was immersed in Fluorinert and the hydrophone for ONDA, HNC-0200, was used to acquire the pressure. As stated earlier, there is a minimum measurable distance at which the hydrophone can be placed to ensure a correct pressure measurement. Considering the wavelength ($\lambda = c/f = 685/3.3M = 207.6 \mu m$), the array size (710 μm), and using Fig. 3.6a, the minimum distance gives 1.3 mm and therefore the separation between

the hydrophone and the PMUT surface must be at least this value.

Once the first measurement point was determined, the acoustic output pressure was acquired by raising the hydrophone from 1.3 mm to 2 mm with steps of 100 μm and displaced along the lateral direction from -0.5 mm to 0.5 mm each 50 μm. All Tx rows were driven at the same time with 2 monophasic pulses with 32 V at 3.3 MHz generated by the CMOS circuitry. Figure 5.4a presents the 2D pressure map in this range of distance, which not included the near field point as consequence of the experimental set up. The normalized acoustic field pattern was also simulated in Field II software under the same conditions and the results, outlined in black, were overlaid on the experimental one. According to the comparison, the measurement acoustic pressure agree well with the simulation.

Furthermore, considering a step of 50 μm, Figure 5.4b shows the experimental points along the axial direction and the fitted curve corresponds to the 1/z dependence, giving a normalized pressure of 22.2 kPa$_{pp}$·mm. Note this fitting has been performed at distances higher than 1.3 mm to be sure that the measurement is done properly. To compare the performance as an actuator with other array systems, the normalized output pressure from 1 mm^2 PMUT area at 1.5 mm from its surface when 1 V is applied is computed. From the fitted curve in Fig. 5.4a, the acoustic pressure at 1.5 mm gives 14.8 kPa peak-to-peak and, considering the array area (0.5 mm^2) and 32 V$_{pp}$ driving voltage, the normalized acoustic pressure gives 925 Pa/V/mm^2. The result is 2.7 times higher than the 8×8 AlN PMUT array (@ 9 MHz) reported in [123] and achieves a 16 % improvement compared to the value achieved by one row (which is composed of 56 PMUT elements, more than the 7x6=42 PMUT elements that we have) of the 110×56 AlN array presented in [19].

To measure the receiving sensitivity of the system, all rows were used to transmit and they were driving with the same signal described previously. In the experiment, the Fluorinert thickness was modified to obtain acoustic paths from 1 mm to 7 mm. The peak-to-peak amplitudes were measured by the central row at each distance in a pulse-echo experiment, and the results are shown in Fig. 5.5. The fit was performed from 5 mm since, based on the longest dimension of the receiving element (710 μm) and applying the same concept of the minimum measurable distance, the first valid point should be 4.8 mm. Using both fitted results as $Amplitude(mV_{pp})/P(kPa_{pp})$, the receiving sensitivity gives 2.9 V/MPa, which is three times higher than the 1.5x1.5mm^2 PZT PMUT array [90], and comparable with 19.2x12 mm^2 PZT [134]

(a)　　　　　　　　　　　　(b)
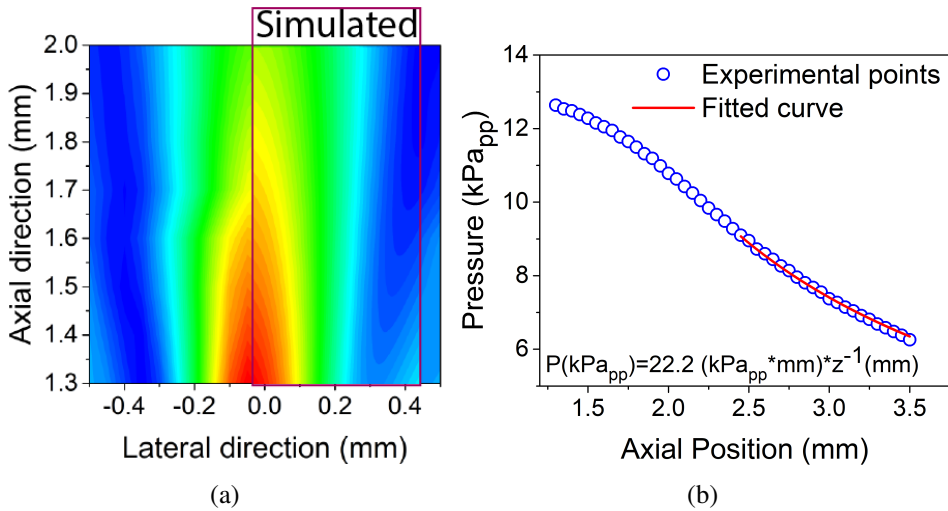
Figure 5.4: Performance as a actuator: (a) 2D measurement pressure map and outlined the Field II simulation results, and (b) Axial dependence of the pressure.
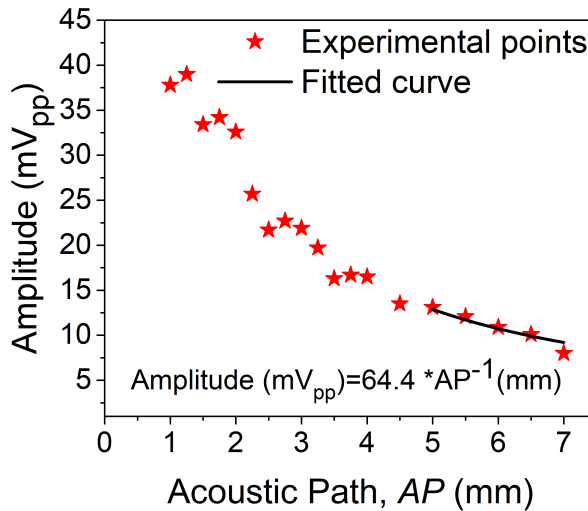
Figure 5.5: Amplitude measured of the received echo versus the acoustic path and its fitting curve.

and 110×56 AlN [19] PMUTs arrays. If the receiving element area is considered (80x710 μm^2), the SR could be increased until 51 V/MPa for a 1 mm².

The functionality of this tiny PMUT array as an ultrasound imaging system was carried out using an earring with a beautiful symbol, "The Tree of Life". This target contains a lot of details making it an interesting pattern. The set-up as well as microscopic images with some critical parts of the object are depicted in Fig. 5.6. Based on the scales of the Tree of Life earring, there are regions with a width of 300

μm that would be good news, if our array is able to solve it. Such as in the previous experiment, two pulses at 3.3 MHz with 32 V were used to actuate the PMUT array immersed in Fluorinert. Before beginning pulse-echo ultrasound imaging, the beam width was measured at 2 mm, that will be the axial position at which the earring will be placed. The result shows a 500 μm 3 dB beamwidth that is in correspondence with the computed and simulated ones, see Fig. 5.6a. The theoretical value is obtained as ($D_{elem} = D_{in} \cdot D_{arX}$ where D_{in} and D_{arX} are defined in Eq. 2.36 and Eq. 2.42, respectively. The level of the side lobes is below the half beamwidth and their behavior is closer to the Field II simulated due to it considers an accurate PMUT distribution.

Finally, the earring was placed at 2 mm above the PMUT surface, and a 5.3 $\times$ 4.8 mm^2 section was manually swept every 50 μm. The received signal when the incoming ultrasound wave comes from the earring/FC-70 interface is shown in Fig. 5.6b in red and the Time-of-Flight of 6 μs corresponds to an acoustic path of 2 mm which was expected. In contrast, the blue curve in Fig. 5.6b is the echo coming from the interface between the air and the fluid, giving a thickness of 3.6 mm. Computing the FFT from the ring-down of this time-response (the blue one) are obtained a peak frequency of 3.37 MHz, a bandwidth at -3 dB of 1.72 MHz, and a Q-factor of 1.95. In addition, considering the peak-to-peak amplitude (11 mV$_{pp}$) and the receiving sensitivity (2.9 V·MPa^{-1}), the pressure over the PMUT surface gives 3.8 kPa (1.34 kPa$_{rms}$). This value ensures the acoustic measurements because the acoustic medium noise represented as $\sqrt{4kTR_{med}\Delta f/S}$ (where k is the Boltzman's constant, T, the temperature (300K); R$_{med}$, the medium acoustic impedance (1.35 MRayls); Δf, bandwidth (1.72 MHz); and S, the array area (0.5 mm^2)) gives 96 mPa$_{rms}$, which can be negligible [137].

Figure 5.8 shows the final ultrasound image, where each value has been normalized with the maximum peak. The 300 μm features of the object are clearly imaged with good contrast, achieving a dynamic range of around 12 dB. This value guarantees the minimal SNR (12 dB) for an accurate fingerprint image [138]. In addition, as a consequence of the imperfections and a possible tilt of the target, the maximum amplitude does not remain constant on the entire earring surface. Table 5.1 summarizes all experimental characterization of the ultrasound system. This system will be presented in IEEE International Ultrasonics Symposium (IUS) 2022 next October as an oral presentation.

Another 7x7 array but using independent actuation of each of the rows (and consequently allowing phased array beam steering) has been designed and also proven
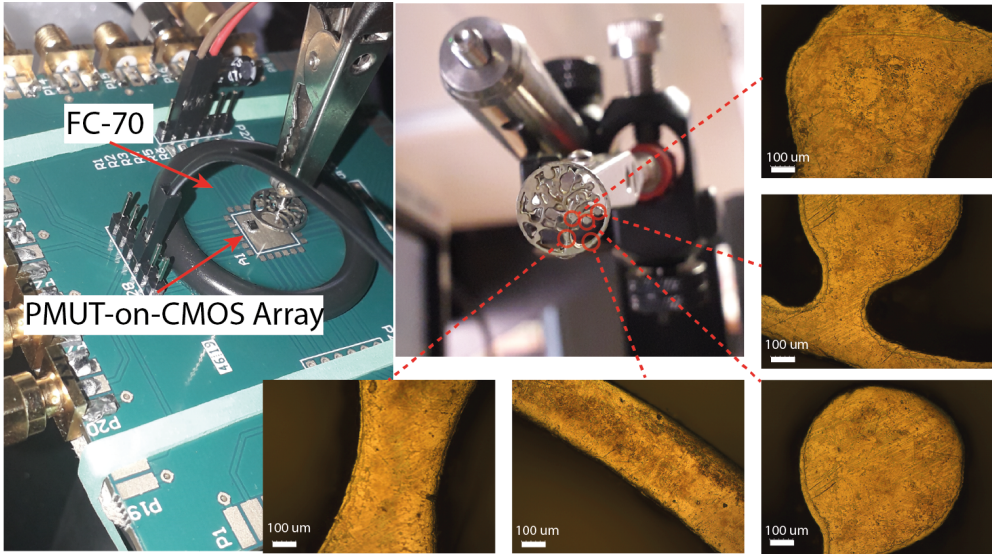
Figure 5.6: Imaging measurement set-up of an earring with a Tree of Life as a symbol as well as details about it.

(a)

(b)
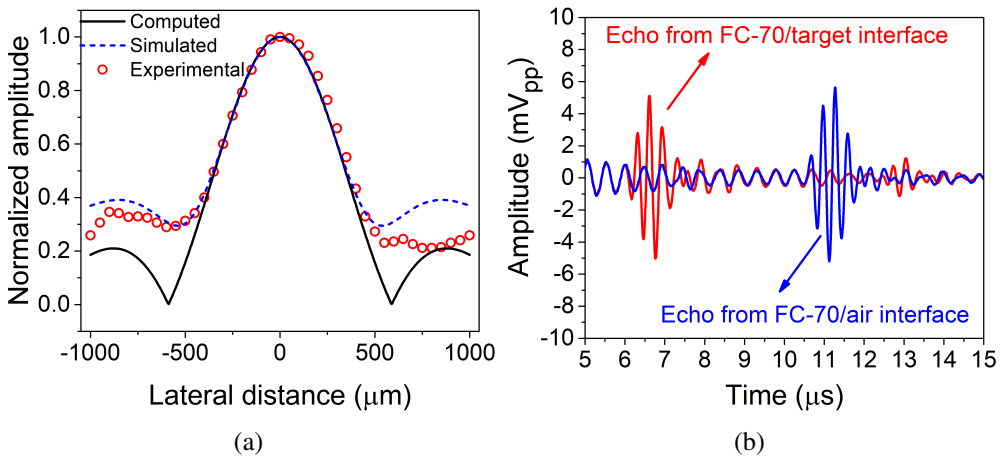
Figure 5.7: (a) Beam pattern in the lateral direction at 2 mm: solid black line: computed, dotted blue line: simulated and red circles: experimental. (b) Pulse-echo time response from the FC-70/earring interface (red line) and FC-70/air interface (blue line).

as an acoustic imager. These results are presented in paper [139]. This linear system consists of 7×7 (where the PMUT in the same row are connected in parallel such as the previous one) AlScN PMUT-on-CMOS elements where each one is connected to an HV Tx Pulser, and the even ones can also receive via an LNA amplifier. With this phased array, a B-mode image with a 16 dB dynamic range, utilizing only one receiving channel without any need of complex data post-processing is demonstrated.
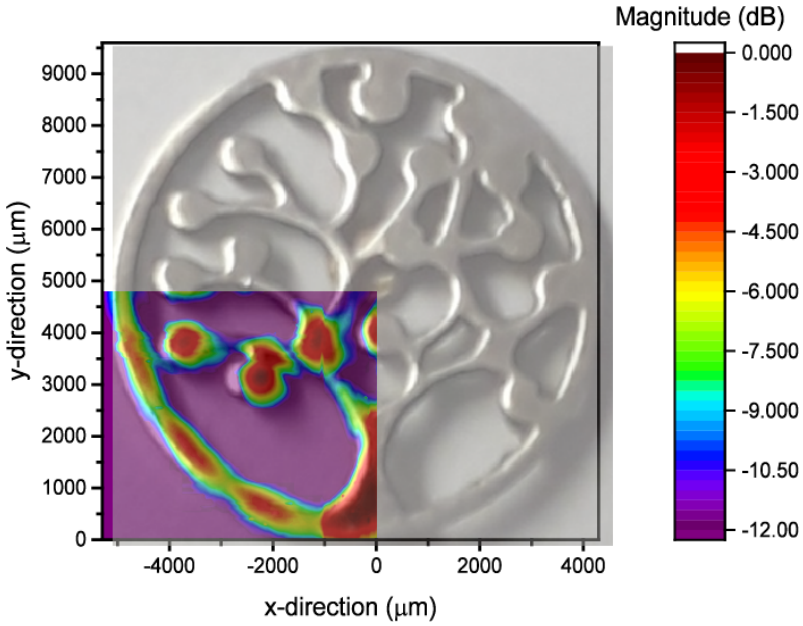
Figure 5.8: Measured pulse-echo ultrasonic image of a section of a Tree of Life earring.

Table 5.1: Ultrasonic imaging sensor based on PMUTs-on-CMOS.

Parameters	Values
Medium	FC-70
Center frequency (MHz)	3.3
Area (mm^2)	0.5
Pitch matched	Yes
Normalized pressure (kPa·mm)	22.2
Pressure@1.5 mm@1 mm^2(Pa·V^{-1}·mm^{-2})	925
V_r (mV·mm^{-1})	64
BW$_{-3dB}$ (MHz)	1.79
SR (V·MPa^{-1})	2.9
Dynamic Range @ 2mm (dB)	12

In addition, the use of a delay and sum algorithm in the reception allows to improve this dynamic range up to 22 dB using 3 PMUTs-on-CMOS channels.

5.2 Multi-element ring array based on minute size PMUTs for high acoustic pressure and tunable focus depth

In this section, two multiple concentric rings arrays composed of several high-frequency piezoelectrical micromachined ultrasound transducers (PMUTs) are presented. Both designs have the same layout (10×10 PMUTs), and each PMUT device has the same dimensions (40 μm), however, there are some differences written in Table 5.2.

Table 5.2: Ring arrays characteristics

Parameters	Ring I[1]	Ring II
Type[2]	II	V
Piezoelectric material	AlN	AlScN
LNA Integrated	No	Yes

[1] This device has been reported in [140].
[2] Details are defined in Table 3.1.

The main advantage of annular arrays is the ability to provide variable focal depth, however, the beam steering is not allowed, so manual scanning is required to create 2D ultrasound images. The focus depth (f_d) can be defined by Eq. 5.2 where S is the transducer area (whatever its shape), λ is the wavelength, f is the frequency, and c is the sound velocity in the propagation medium. Based on this, for the same acoustic medium, a large focal length will be achieved if the S×f product is maximized. Thinking about a continuous ring, if **w** (defined in Fig. 5.9) increases, the active area (S) is larger, but, in this case, the resonance frequency decreases (it is as if it were closer to a circular shape) [71]. An alternative solution is to create, with the same area, multi-element rings where the frequency is set by the individual device. For instance, if the single element is a square device with a side length a, and the width of a continuous ring is equal to the PMUT side, i.e. ($w = a$), a multi-element array reaches frequency 1.6× times greater, and if $w = \sqrt{2}a$ (the width equals square PMUT diagonal), the improvement is 3.3× times [140].

$$F_d = \frac{S}{4\lambda} = \frac{S \times f}{4 \times c} \tag{5.2}$$

Taking into account this, Fig. 5.9 shows an optical image of the proposed ring

array (Ring I) where five continuous rings are overlapping on each channel where D and d are the external and internal radii, respectively, and w is the width of the ring. The concentric configuration is achieved by connecting the top electrodes of each individual PMUT to form irregular polygons. The gap between consecutive elements is 25 μm and width of the side is 40 μm.
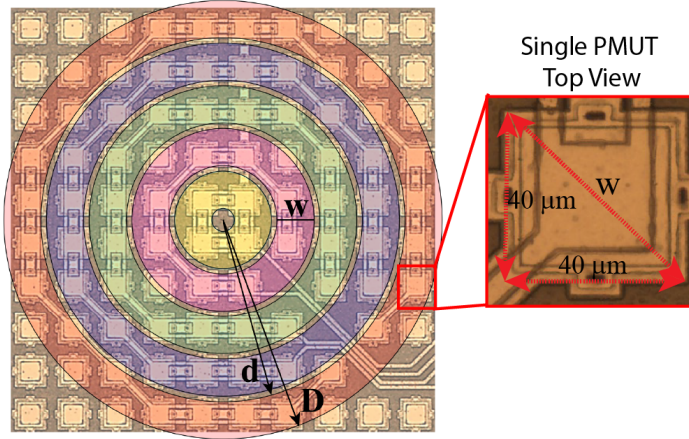
Figure 5.9: (a) Optical image of the multi-element ring array transducer and schematic representation of the continuous rings over it; (b) zoom of the individual 40 μm AlN PMUT. Modified image extracted from [140].

From Eq. 5.2, if the area is the same, the improvement in the focal distance (IF) is given by the frequencies ratios, i.e. f_{multi}/f_{cont}. Taking the simulated frequency in Fluorinert for a continuous annular device (2.3 MHz) with a width equal to 56.6 μm ($\sqrt{(40\mu m)^2 + (40\mu m)^2}$) and a single square PMUT with a 40 μm side (11.3 MHz), the IF gives 4.9, achieving a 1.44 mm maximum focal length when using the entire multi-element ring and a minimum value of 67.4 μm when only the center element is considered. This fact guarantees the ability of the presented multi-element array to focus (without any delays) in a range from 67.4 μm to 1.44 mm; however, by controlling the phase of the driven signal, the focus can be also modified achieving a narrower beamwidth [140]. In [140] can be found more details regarding the theoretical analysis of this configuration.

5.2.1 Ring I Experimental results

The electrical characterization in the air gives a central resonance frequency for the first flexural mode of 17.5 MHz. The crosstalk between rings is also analyzed, being below -56 dB, which ensures minimal interference and therefore guarantees an
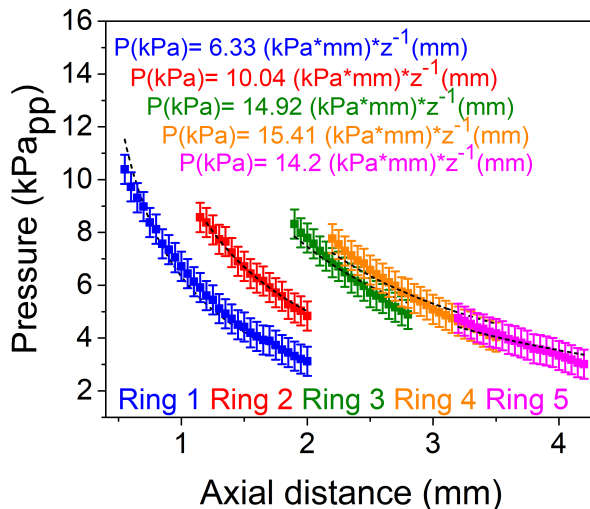
Figure 5.10: Measured pressure driving each ring array individually.

efficient focus of the beam.

On the other hand, the acoustic characterization in Fluorinert was carried out using the HNC-0200 and the initial axial position was determined in each case, giving different values depending on the size of the aperture. Taking into account this, the pressure was measured every 50 μm in the axial direction to perform a fitting curve and then to obtain the normalized pressure with the distance. Figure 5.10 depicts the measured acoustic pressure when each ring array is driven with four sine cycles with 24 V_{pp} at 8.7 MHz. From these results, the global acoustic pressure at 1.2 mm (Field II simulated natural focus) can be extrapolated as the contribution of each ring at this point, giving 50.71 kPa_{pp} [140]. Likewise, the verification as a sensor was carried out through pulse-echo experiments, where the central ring is externally connected to a LNA used previously giving a receiving sensitivity of 441.6 nV/Pa. All characteristic of the proposed multi-element array are summarized in Table 5.3.

Comparing the results with the previous system array (AlN 7×1), a better performance as an actuator is achieved when multiple elements ring array is used. In this sense, the normalized pressure at 1.5 mm with the applied voltage and the area increases 5.2 times, demonstrating the positive influence of high frequency on the membrane velocity and consequently on the output pressure. In contrast, as a sensor, the benefit of the monolithic integration of the linear array with the LNA amplifier allows a decrease in the parasitic capacitance ensuring a high reception sensitivity, being around 6.6 times better. The 1D ultrasound image presented in [140] using

Table 5.3: Characteristic of the ultrasonic multi-element ring array (Ring I) [140].

Parameters	Values
Medium	FC-70
Center frequency (MHz)	8.7
Area (mm^2)	0.35
Normalized pressure (kPa·mm)	60.85
Pressure@1.5 mm@1 mm^2(kPa·V^{-1}·mm^{-2})	4.84
BW$_{-3dB}$ (MHz)	3.4
V_r^1(mV·mm^{-1})	6.45
SR (nV·Pa^{-1})	441

[1] Central Ring is used to receive and Ring 3 to transmit.

a mechanical micrometer scanning system demonstrates the possibility of using this small device in high-performance ultrasound imaging systems.

PDMS measurements

The first measurements with PDMS were performed using this system. In the beginning, a small piece ($\approx$250 μm thickness) was placed on the surface of ring array and the interface with air was used as a reflecting surface, see the experimental setup in Fig. 5.11. Performing a frequency sweep to optimize the amplitude of the received signal, where four sine cycles with 22 V_{pp} are applied, and the maximum value was found about of 11.5 MHz. Figure 5.11a shows the received amplitude by the central ring when ring 3 (blue line) and ring 4 (red line) are used to transmit, and, such as in the above pulse-echo experiments mentioned, an LNA amplifier is externally connected. The measured ToF corresponds with a acoustic distance of 1 mm which is close to 4 times the PDMS thickness. The first bounce on the PDMS surface is not appreciable because the excitation time is greater than the ToF (4/11.5MHz$\approx$348 ns > 250μm/1000=250 ns).

Based on this result, the array was covered by a 600 μm PDMS layer following the process described in Chapter 3. The received echo by the central row is shown in Fig. 5.11b when two rings from the array (ring 3+ring 5) are driven together with 24 V_{pp} four cycles at 11.4 MHz.The first incoming signal from the interface between PDMS-air is appreciable, giving 5 mV$_{pp}$. In addition, if Fluorinert is incorporated, the
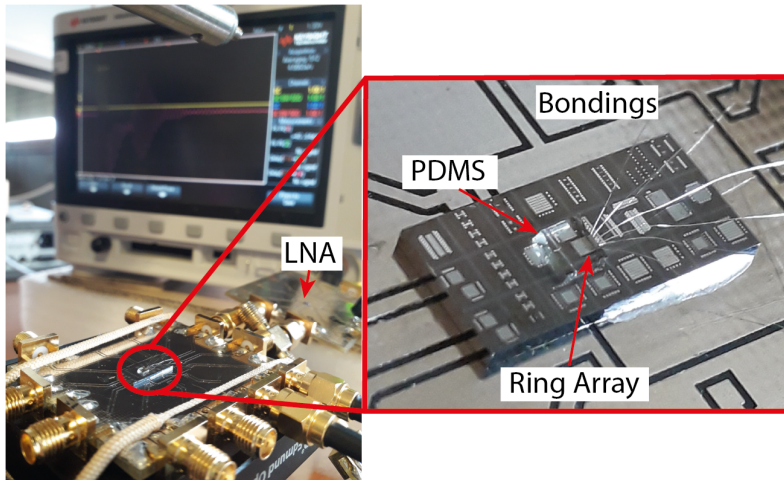
Figure 5.11: Experimental setup to the first acoustic measurements using PDMS.
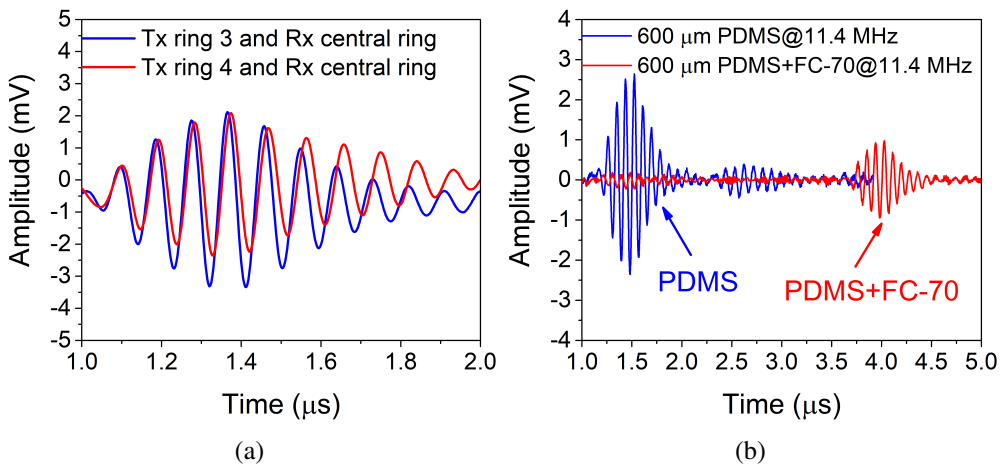
Figure 5.12: Time response received by the central row using PDMS as an acoustic medium where (a) a small piece of PDMS is placed on top of the array using ring 3 and ring 4 to transmit independently, and (b) 600 μm of PDMS is deposited on the ring array using ring 3 and ring 5 to transmit at the same time.

system is able to see the echo coming from the FC-70 air interface. In both cases, the PDMS layer increases the frequency at the expense to decreases the signal amplitude.

5.2.2 Ring II Experimental results

Ring II system has the same PMUT distribution, however, as shown in Fig. 5.13 an LNA amplifier is integrated, and then the received signal by the central ring is improved. In this section, only pulse-echo experiments are implemented to obtain the resonance frequency and characterize the performance of an ultrasound system.

As a first acoustic characterization, the array was immersed in Fluorinert and the air interface was used as a reflecting surface. Each individual ring was driven with 4 sinusoidal cycles with 22 V_{pp} and sweeping from 4.5 MHz to 9 MHz with a step of 0.1 MHz, the optimal received amplitude was found around 6.3 MHz. This value, as expected, is lower than the previous ring, since although the dimensions are the same, the thickness and the materials are different. The time response of the signal received by the central ring when it was driven from ring 5 to ring 2 at 6.3 MHz is shown in Fig. 5.14. The TX Ring number corresponds with the element available to transmit, i.e., Ring 5 is the 4th transmitter ring, Ring 4 corresponds to the 3rd transmitter ring, etc, and the ToF gives an acoustic path of 5 mm. The four vertical lines give the ultrasound wave represented on the right side where the maximum amplitude is reached when Ring 3 is excited, giving almost 2.6 mV_{pp}, which could be increased to 10 mV_{pp} if all the rings are actuated at the same time. The horizontal cross-section has been made at the maximum peak, which is represented in the top side. Taking the value corresponding to the Ring 3, the normalized voltage with the acoustic path gives 13 mV_{pp}·mm. Although the pressure generated by Ring 3 is unknown, the discussed system provides better performance than the previous one, since, for the same input voltage, the received signal is twice as large as Ring I.

Finally, the array covered with 700 μm PDMS immersed in deionized (DI) water was driven with 4 cycles with 22 V_{pp} at 8.6 MHz (ring 2 was not used here).
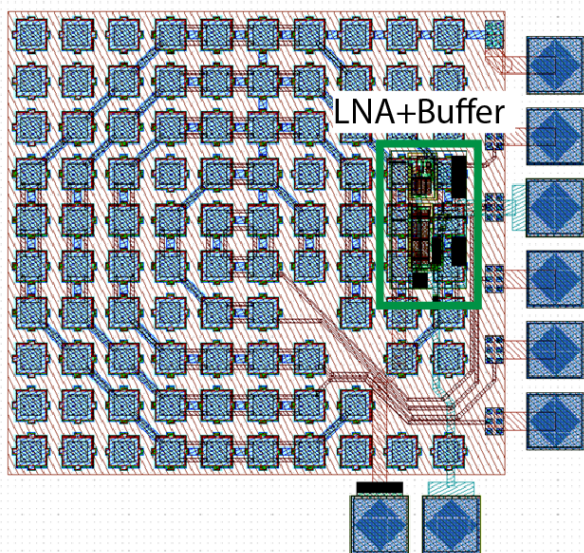
Figure 5.13: Schematic layout of the ring array integrated with an LNA amplifier.
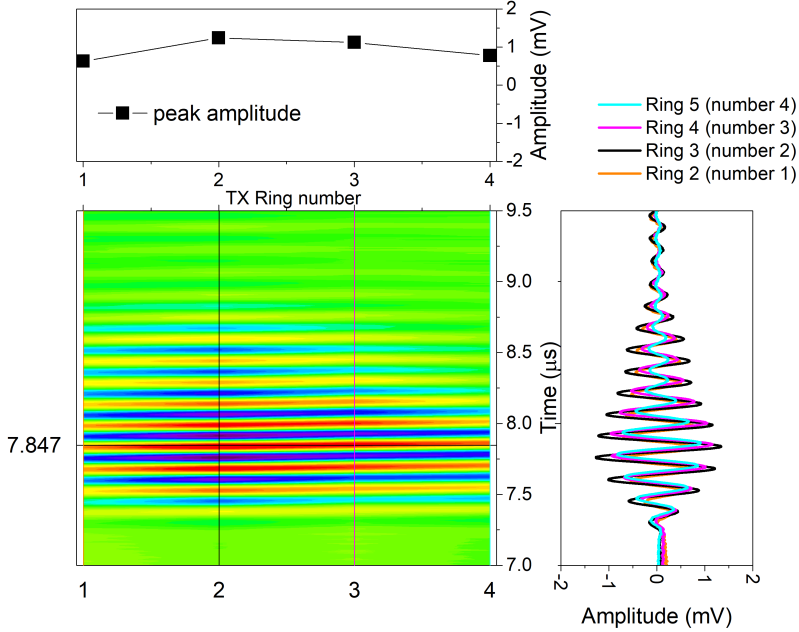
Figure 5.14: Evolution of received signal by each ring channel versus time. The top image corresponds to a cross-section at the maximum amplitude, and the right image is the temporal evolution of each ring.

Figure 5.15b in blue shows, as a reference measurement, the reflected signal at the interface between water and air, where the water thickness computed as $z_{water} = (\frac{ToF}{2} - \frac{h_{PDMS}}{c_{PDMS}})c_{water}$ gives 4.3 mm (with ToF= 7.1 μs; $h_{PDMS} = 700 \mu m$; $c_{PDMS} = 1000 m/s$; $c_{water} = 1500 m/s$). As a next step, a small plastic empty cup was placed into the DI water, causing it to spill out a bit until the thickness was approximately 2.6 mm. Based on the properties of the plastic, (Polypropylene with $c = 2660 m/s$ and $\rho = 890 kg \cdot m^{-3}$ [141]), there is a total reflection if it is empty. However, when filled with water, the reflection coefficient is 22 % at the plastic-water interface and it corresponds to the first magenta echo whose amplitude of 1 mV$_{pp}$ is in agreement with the 22% of the blue one. The second magenta echo is due to the interface between water inside and air, and here the peak-to-peak amplitude should be close to 56 % of that achieved by "PDMS+Water+Plastic cup". In all these results, losses inside the materials are not considered. These experiments open the way to the characterization of different fluids inside the plastic cup without the need to directly immersed the PMUT in the liquid.

The results achieved by these two annular multi-element arrays demonstrate the possibility to obtain high-performance ultrasound imaging systems through mechan-
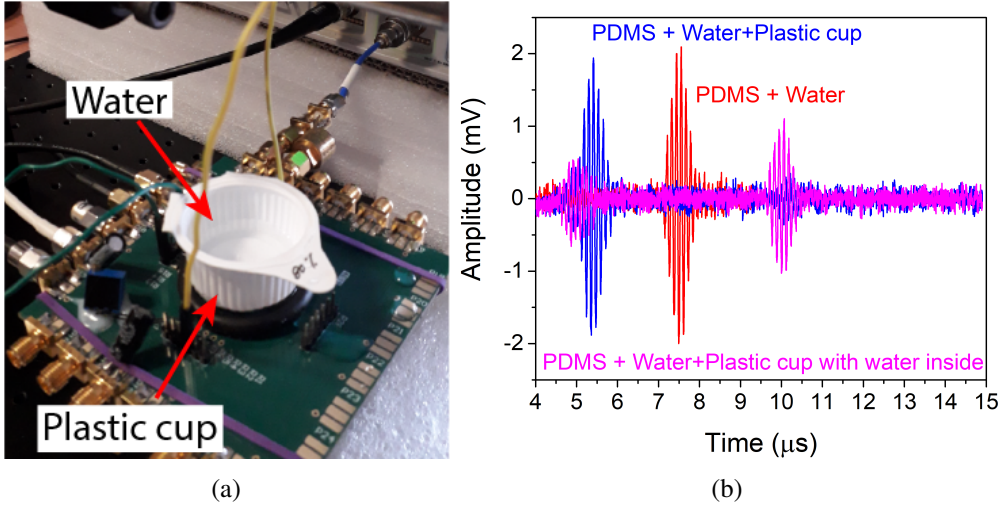
Figure 5.15: Experimental setup of pulse-echo measurements using different media (b) Time-domain responses reflected from different targets.

ical scanning. Furthermore, the capability to detect different materials with a device of small size and low power consumption could be interesting in medical applications to detect muscle disorders, such as hematoma. Additionally, greater focal depth and output pressure can be achieved at the same frequency by increasing the number of rings within the same technology. Focal depth control is interesting in applications to extract information in a 3D scenario, or in applications where different levels of acoustic pressure are needed, for instance in HIFU applications.

CONCLUSIONS

This dissertation has been focused on enhancing the performance of piezoelectric micromachined ultrasonic transducers (PMUTs) by carrying out designs and materials improvements. Individual PMUTs devices are firstly introduced where the theoretical analysis, the modelization, and the FEM simulation allow obtaining different architectures with great potential in terms of acoustic output pressure, frequency, liquid working capacity, and size. PMUT prototypes were fabricated using Silterra's MEMS-on-CMOS fabrication process, and through in-depth characterization, their results as acoustic transducers provide competitive values as actuators and sensors compared to state-of-the-art.

The tent-plate PMUT presented approach avoids the limitations due to the clamped boundary, increasing the movement and consequently the output pressure. The four linear holes on the edge of the cavity modify the clamping boundaries and, being sealed by the passive layer, allow the PMUT not only increases the movement and pressure but also to give the ability to work in a liquid environment. The transmitting sensitivity achieved by this PMUT is around 3.6 kPa/V at 2.1 MHz with a high fractional bandwidth of 89 %.

Furthermore, the benefit of thickness scaling was demonstrated using PMUTs with reduced thicknesses for the piezoelectric and elastic layers. The performance achieved by these thinner PMUTs as transmitters and receivers is better than PMUTs of the same size with the same technology but with greater thicknesses. From the results, thinner PMUT with 0.6 μm AlN thickness and 1 μm Si_3N_4 thicknesses demonstrates higher acoustic pressure production and reception sensitivity. The validation of this PMUT as a pulse-echo system ensures a transmitting and receiving sensitivity of 5.2 kPa/V and 2.05 V/MPa, respectively enhancing the applicability of PMUTs-on-CMOS for ultrasound systems that need to be miniaturized. In addition, the use of AlN with an Sc concentration of 9.5 % instead of pure AlN improved the effective

thin-film piezoelectric coefficient while maintaining compatibility with the CMOS process, which was initially validated considering a PMUT with a piezoelectric thickness of 1.2 μm.

The fusion of thinner layer and AlScN as a two-port pulse-echo system (0.6 μm AlScN thickness and 1 μm Si_3N_4) ensured the best performance as a transmitter and as a sensor with values of 11.9 kPa/V and 3.6 MPa/V. The competitive performance of the aforementioned device allowed the implementation in a novel solution as a single-cell for monitoring fluids density, viscosity, sound velocity, and compressibility exploiting its capability as a resonator and a pulsed-echo ultrasound wave. This device exhibits high density sensitivity, 482 Hz/kg/m^3, with minimum area, 80×80 μm^2 and, where, the signal processing is achieved with the on-chip CMOS front end integrated below the PMUT sensing area.

Apart from stand-alone PMUTs, in this research PMUTs configured as arrays have been implemented. Linear and multi-element annular arrays with areas less than 1 mm^2 were characterized, achieving a good acoustic performance. The presented multi-element ring array eliminates the dependence of acoustic wave frequency on the diameters of the annular array and achieves accurate control of the focus depth (from 67 μm to 1.4 mm), which is 4.9 times greater than that of the equivalent continuous ring array. In addition, the low crosstalk between different rings (levels under -56.8 dB) allows it to be used in modern ultrasound applications where the maximum of the ultrasound beam must be controlled efficiently in the axial direction. Likewise, the pitch-matched linear array could be used for tuneable focus applications, and its ability to image features with a minimum width of 300 μm at a distance of 2 mm was demonstrated.

The appeal of all ultrasound systems validated in this Ph.D. thesis lies in the capability to provide devices with compactness, low power consumption, and high system yield. This validated PMUT-on-CMOS platform opens the way to new high fill factor phased arrayed systems for ultrasonic imaging with high performance and lower cost than the existing ones nowadays. In addition, the validation of the detection capabilities of the systems considering different materials expands their possibilities for diagnostic applications such as muscle disorders (hematoma).

BIBLIOGRAPHY

[1] Donald R Griffin. "Return to the Magic Well : Echolocation Behavior of Bats and Responses of Insect Prey". In: *Bioscience* 51.7 (2001), pp. 555–556.

[2] John L. Butler and Charles H. Sherman. *Transducers and Arrays for Underwater Sound*. new York, USA: Springer, 2016, p. 625.

[3] Iwona Sudoł-Szopińska, Carlo Martinoli, and Marta Panas-Goworska. "History Page : Leaders in MSK Radiology Karl Dussik , 1908 – 1968 : Pioneer of MSK Ultrasonography". In: *Semin. Musculoskelet. Radiol.* 25.01 (2021), pp. 184–185.

[4] Kullervo Hynynen and Ryan M. Jones. "Image-guided ultrasound phased arrays are a disruptive technology for non-invasive therapy". In: *Phys. Med. Biol.* 61.17 (2016), R206–R248.

[5] Weibao Qiu, Ayache Bouakaz, Elisa E. Konofagou, et al. "Ultrasound for the Brain: A Review of Physical and Engineering Principles, and Clinical Applications". In: *IEEE Trans. Ultrason. Ferroelectr. Freq. Control* 68.1 (2021), pp. 6–20.

[6] Yole Développement. *Ultrasound Sensing Technologies for Medical , Industrial , and Consumer Applications 2018 report*. Tech. rep. 2018.

[7] Paul G Newman and Grace S Rozycki. "THE HISTORY OF ULTRASOUND". In: *Surg. Clin. North Am.* 78.2 (1998), pp. 179–195.

[8] Jovana Janjic, Mingliang Tan, Verya Daeichin, et al. "A 2-D Ultrasound Transducer With Front-End ASIC and Low Cable Count for 3-D Forward-Looking Intravascular Imaging: Performance and Characterization". In: *IEEE Trans. Ultrason. Ferroelectr. Freq. Control* 65.10 (2018), pp. 1832–1844.

[9] Ajay Dangi, Sumit Agrawal, Sudhanshu Tiwari, et al. "Ring PMUT array based miniaturized photoacoustic endoscopy device". In: *Photons Plus Ultrasound Imaging Sens. 2019*. Ed. by Alexander A Oraevsky and Lihong V Wang. Vol. 10878. International Society for Optics and Photonics. SPIE, 2019, pp. 46–53.

[10] Jiaqi Wang, Zhou Zheng, Jasmine Chan, et al. "Capacitive micromachined ultrasound transducers for intravascular ultrasound imaging". In: *Microsystems Nanoeng.* 6.1 (2020), pp. 73–86.

[11] Hyunggug Kim, Seongyeon Kim, Nam Suk Sim, et al. "Miniature ultrasound ring array transducers for transcranial ultrasound neuromodulation of freely-moving small animals". In: *Brain Stimul.* 12.2 (2019), pp. 251–255.

[12] Kailiang Chen, Hae-seung Lee, and Charles G Sodini. "A Column-Row-Parallel ASIC Architecture for 3-D Portable Medical Ultrasonic Imaging". In: *IEEE J. Solid-State Circuits* 51.3 (2016), pp. 738–751.

[13] Jihee Lee, Kyoung Rog Lee, Benjamin E. Eovino, et al. "11.1 A 5.37mW/Channel Pitch-Matched Ultrasound ASIC with Dynamic-Bit-Shared SAR ADC and 13.2V Charge-Recycling TX in Standard CMOS for Intracardiac Echocardiography". In: *2019 IEEE Int. Solid- State Circuits Conf. -*. IEEE, 2019, pp. 190–192. ISBN: 9781538685310.

[14] Jihee Lee, Kyoung Rog Lee, Benjamin E. Eovino, et al. "A 36-Channel Auto-Calibrated Front-End ASIC for a pMUT-Based Miniaturized 3-D Ultrasound System". In: *IEEE J. Solid-State Circuits* 56.6 (2021), pp. 1910–1923.

[15] Benjamin E. Eovino, Yue Liang, and Liwei Lin. "Concentric PMUT Arrays for Focused Ultrasound and High Intensity Applications". In: *2019 IEEE 32nd Int. Conf. Micro Electro Mech. Syst.* Seoul, Korea (South): IEEE, 2019, pp. 771–774. ISBN: 9781728116105.

[16] Guo Lun Luo, Yuri Kusano, and David A. Horsley. "Airborne Piezoelectric Micromachined Ultrasonic Transducers for Long-Range Detection". In: *J. Microelectromechanical Syst.* 30.1 (2021), pp. 81–89.

[17] David A. Horsley, Richard J. Przybyla, Stefon E. Shelton, et al. "Piezoelectric Micromachined Ultrasonic Transducers for Range-Finding Applications". In: *2021 5th IEEE Electron Devices Technol. Manuf. Conf. EDTM 2021*. 2021, pp. 2021–2023. ISBN: 9781728181769.

[18] Richard J. Przybyla, Hao Yen Tang, Stefon E. Shelton, et al. "12.1 3D ultrasonic gesture recognition". In: *2014 IEEE Int. Solid-State Circuits Conf. Dig. Tech. Pap.* Vol. 57. San Francisco, CA, USA: IEEE, 2014, pp. 210–211. ISBN: 9781479909186.

[19] Xiaoyue Jiang, Yipeng Lu, Hao-Yen Tang, et al. "Monolithic ultrasound fingerprint sensor". In: *Microsystems Nanoeng.* 3.1 (2017), p. 17059.

[20] Chang Peng, Mengyue Chen, and Xiaoning Jiang. "Under-Display Ultrasonic Fingerprint Recognition with Finger Vessel Imaging". In: *IEEE Sens. J.* 21.6 (2021), pp. 7412–7419.

[21] Kaustav Roy, Harshvardhan Gupta, Vijayendra Shastri, et al. "Fluid Density Sensing Using Piezoelectric Micromachined Ultrasound Transducers". In: *IEEE Sens. J.* 20.13 (2020), pp. 6802–6809.

[22] Kaustav Roy, Kritank Kalyan, Anuj Ashok, et al. "A PMUT Integrated Microfluidic System for Fluid Density Sensing". In: *J. Microelectromechanical Syst.* 30.4 (2021), pp. 642–649.

[23] Jesus Yanez, Arantxa Uranga, and Nuria Barniol. "Fluid compressional properties sensing at microscale using a longitudinal bulk acoustic wave transducer operated in a pulse-echo scheme". In: *Sensors Actuators A Phys.* 334 (2022), p. 113334.

[24] Yole Développement. *Ultrasound Sensing Technologies report*. Tech. rep. 2020.

[25] Joontaek Jung, Wonjun Lee, Woojin Kang, et al. "Review of piezoelectric micromachined ultrasonic transducers and their applications". In: *J. Micromechanics Microengineering* 27.11 (2017).

[26] Yongqiang Qiu, James V. Gigliotti, Margeaux Wallace, et al. "Piezoelectric micromachined ultrasound transducer (PMUT) arrays for integrated sensing, actuation and imaging". In: *Sensors (Switzerland)* 15.4 (2015), pp. 8020–8041.

[27] Benjamin A Griffin, Adam M Edstrand, Sean Yen, et al. "Post-CMOS Compatible Piezoelectric Micro-Machined Ultrasonic Transducers". In: *2018 IEEE Int. Ultrason. Symp.* 2018, pp. 1–4.

[28] Yipeng Lu, Amir Heidari, and David A. Horsley. "A High Fill-Factor Annular Array of High Frequency Piezoelectric Micromachined Ultrasonic Transducers". In: *J. Microelectromechanical Syst.* 24.4 (2015), pp. 904–913.

[29] Harmeet Bhugra and Gianluca Piazza, eds. *Piezoelectric MEMS Resonators*. Switzerland: Springer International, 2017. ISBN: 9783319286860.

[30] Arif S. Ergun, Goksen G. Yaralioglu, and Butrus T. Khuri-Yakub. "Capacitive Micromachined Ultrasonic Transducers: Theory and Technology". In: *J. Aerosp. Eng.* 16.2 (2003), pp. 76–84.

[31] Libo Zhao, Jie Li, Zhikang Li, et al. "A CMUT-based gas density sensor with high sensitivity". In: *J. Micromechanics Microengineering* 29.11 (2019).

[32] Marco Sautto, Alessandro Stuart Savoia, Fabio Quaglia, et al. "A comparative analysis of CMUT receiving architectures for the design optimization of integrated transceiver front ends". In: *IEEE Trans. Ultrason. Ferroelectr. Freq. Control* 64.5 (2017), pp. 826–838.

[33] Mingjun Wang, Yufeng Zhou, and Andrew Randles. "Enhancement of the transmission of piezoelectric micromachined ultrasonic transducer with an isolation trench". In: *J. Microelectromechanical Syst.* 25.4 (2016), pp. 691–700.

[34] Xiaoyue Jiang, Hao-yen Tang, Yipeng Lu, et al. "Ultrasonic Fingerprint Sensor with Transmit Beamforming Based on a PMUT Array Bonded to CMOS Circuitry". In: *IEEE Trans. Ultrason. Ferroelectr. Freq. Control* 64.9 (2017), pp. 1401–1408.

[35] Andreas C. Fischer, Fredrik Forsberg, Martin Lapisa, et al. "Integrating MEMS and ICs". In: *Microsystems Nanoeng.* 1 (2015).

[36] Anshuman Bhuyan, Jung Woo Choe, Byung Chul Lee, et al. "Integrated circuits for volumetric ultrasound imaging with 2-D CMUT arrays". In: *IEEE Trans. Biomed. Circuits Syst.* 7.6 (2013), pp. 796–804.

[37] Kailiang Chen, Byung Chul Lee, Kai E. Thomenius, et al. "A Column-Row-Parallel Ultrasound Imaging Architecture for 3-D Plane-Wave Imaging and Tx Second-Order Harmonic Distortion Reduction". In: *IEEE Trans. Ultrason. Ferroelectr. Freq. Control* 65.5 (2018), pp. 828–843.

[38] Eunchul Kang, Mingliang Tan, Jae Sung An, et al. "A Variable-Gain Low-Noise Transimpedance Amplifier for Miniature Ultrasound Probes". In: *IEEE J. Solid-State Circuits* 55.12 (2020), pp. 3157–3168.

[39] Jaemyung Lim, Coskun Tekes, F. Levent Degertekin, et al. "Towards a Reduced-Wire Interface for CMUT-Based Intravascular Ultrasound Imaging Systems". In: *IEEE Trans. Biomed. Circuits Syst.* 11.2 (2017), pp. 400–410.

[40] Jaemyung Lim, Coskun Tekes, Evren F. Arkan, et al. "Highly Integrated Guidewire Ultrasound Imaging System-on-a-Chip". In: *IEEE J. Solid-State Circuits* 55.5 (2020), pp. 1310–1323.

[41] Christopher B. Doody, Xiaoyang Cheng, Collin A. Rich, et al. "Modeling and characterization of CMOS-fabricated capacitive micromachined ultrasound transducers". In: *J. Microelectromechanical Syst.* 20.1 (2011), pp. 104–118.

[42] David F Lemmerhirt, Xiaoyang Cheng, Robert D White, et al. "A 32×32 Capacitive Micromachined Ultrasonic Transducer Array Manufactured in Standard CMOS". In: *IEEE Trans. Ultrason. Ferroelectr. Freq. Control* 59.7 (2012), pp. 1521–1536.

[43] Pablo Gómez, José Paulino Fernández, and Pablo David García. "Lamb Waves and Dispersion Curves in Plates and its Applications in NDE Experiences Using Comsol Multiphysics". In: *Comsol Conf.* (2011), pp. 1–5.

[44] Jaime Zahorian, Michael Hochman, Toby Xu, et al. "Monolithic CMUT-on-CMOS integration for intravascular ultrasound applications". In: *IEEE Trans. Ultrason. Ferroelectr. Freq. Control* 58.12 (2011), pp. 2659–2667.

[45] Gokce Gurun, Paul Hasler, and F. Levent Degertekin. "Front-end receiver electronics for high-frequency monolithic CMUT-on-CMOS imaging arrays". In: *IEEE Trans. Ultrason. Ferroelectr. Freq. Control* 58.8 (2011), pp. 1658–1668.

[46] David F. Lemmerhirt, Amir Borna, Sushma Alvar, et al. "CMUT-in-CMOS 2D arrays with advanced multiplexing and time-gain control". In: *2014 IEEE Int. Ultrason. Symp.* IEEE, 2014, pp. 582–586. ISBN: 9781479970490.

[47] Gwangrok Jung, Amirabbas Pirouz, Coskun Tekes, et al. "Single-Chip Reduced-Wire CMUT-on-CMOS System for Intracardiac Echocardiography". In: *2018 IEEE Int. Ultrason. Symp.* 2018, pp. 1–4.

[48] Tzu-Hsuan Hsu, Ming-Huang Li, Anurag A. Zope, et al. "A Sub-mW/Pixel Zero-Bias CMUT-in-CMOS Receiver Front-End with TiN Electrode". In: *2020 Jt. Conf. IEEE Int. Freq. Control Symp. Int. Symp. Appl. Ferroelectr.* 2020, pp. 4–7. ISBN: 9781728164304.

[49] Martin Lapisa, Göran Stemme, and Frank Niklaus. "Wafer-level heterogeneous integration for MOEMS, MEMS, and NEMS". In: *IEEE J. Sel. Top. Quantum Electron.* 17.3 (2011), pp. 629–644.

[50] Humberto Campanella. *Acoustic Wave and Electromechanical Resonators: Concept to Key Applications*. Artech, 2010, p. 345. ISBN: 1607839784.

[51] Ira O. Wygant, Xuefeng Zhuang, David T. Yeh, et al. "Integration of 2D CMUT arrays with front-end electronics for volumetric ultrasound imaging". In: *IEEE Trans. Ultrason. Ferroelectr. Freq. Control* 55.2 (2008), pp. 327–341.

[52] Oluwafemi J Adelegan, Zachary A Coutant, Tamzid Ibn Minhaj, et al. "Fabrication of 32 × 32 2D Capacitive Micromachined Ultrasonic Transducer (CMUT) Arrays on a Borosilicate Glass Substrate With Silicon-Through-Wafer Interconnects Using Sacrificial Release Process". In: *J. Microelectromechanical Syst.* 30.6 (2021), pp. 968–979.

[53] Chunkyun Seok, Oluwafemi Joel Adelegan, Ali Onder Biliroglu, et al. "A Wearable Ultrasonic Neurostimulator - Part II: A 2D CMUT Phased Array System with a Flip-Chip Bonded ASIC". In: *IEEE Trans. Biomed. Circuits Syst.* 15.4 (2021), pp. 705–718.

[54] Jonathan M. Rothberg, Tyler S. Ralston, Alex G. Rothberg, et al. "Ultrasound-on-chip platform for medical imaging, analysis, and collective intelligence". In: *Proc. Natl. Acad. Sci. U. S. A.* 118.27 (2021).

[55] Pradeep Dixit and Kimmo Henttinen. "Via Technologies for MEMS". In: *Handb. Silicon Based MEMS Mater. Technol. Second Ed.* Elsevier Inc., 2015, pp. 694–712. ISBN: 9780323312233.

[56]   Viorel Dragoi and Paul Lindner. "Wafer-Bonding Equipment". In: *Handb. Silicon Based MEMS Mater. Technol. Second Ed.* Elsevier Inc., 2015, pp. 648–663. ISBN: 9780323312233.

[57]   J. M. Tsai, M. Daneman, B. Boser, et al. "Versatile CMOS-MEMS integrated piezoelectric platform". In: *2015 Transducers - 2015 18th Int. Conf. Solid-State Sensors, Actuators Microsystems, TRANSDUCERS 2015*. 2015, pp. 2248–2251. ISBN: 9781479989553.

[58]   Y. Lu, H. Tang, S. Fung, et al. "Ultrasonic fingerprint sensor using a piezoelectric micromachined ultrasonic transducer array integrated with complementary metal oxide semiconductor electronics". In: *Appl. Phys. Lett.* 106.26 (2015).

[59]   Hao Yen Tang, Yipeng Lu, Xiaoyue Jiang, et al. "3-D Ultrasonic Fingerprint Sensor-on-a-Chip". In: *IEEE J. Solid-State Circuits* 51.11 (2016), pp. 2522–2533.

[60]   J. Segovia-Fernandez, S. Sonmezoglu, S. T. Block, et al. "Monolithic piezoelectric Aluminum Nitride MEMS-CMOS microphone". In: *TRANSDUCERS 2017 - 19th Int. Conf. Solid-State Sensors, Actuators Microsystems*. 2017, pp. 414–417. ISBN: 9781538627310.

[61]   Ofer Rozen, Scott T. Block, Xuan Mo, et al. "Monolithic MEMS-CMOS ultrasonic rangefinder based on dual-electrode PMUTs". In: *2016 IEEE 29th Int. Conf. Micro Electro Mech. Syst.* 2016, pp. 115–118. ISBN: 9781509019731.

[62]   *SilTerra Malaysia Sdn Bhd*. (Visited on 01/28/2022).

[63]   Mohanraj Soundara Pandian and Arjun Kumar Kantimahanti. *Monolithic integration of PMUT on CMOS*. 2019.

[64]   Stephen D. Senturia. *Microsystem Design*. 1st ed. USA: Springer, Boston, MA, 2001, p. 689. ISBN: 978-0-306-47601-3.

[65]   S Trolier-McKinstry and P Muralt. "Thin Film Piezoelectrics for MEMS". In: *J. Electroceramics* 12.1 (2004), pp. 7–17.

[66]   Katzir Shaul. "Who knew piezoelectricity? Rutherford and Langevin on submarine detection and the invention of sonar". In: *Notes Rec. R. Soc* 66 (2012), pp. 141–157.

[67]   Yuriy Poplavko and Yuriy Yakymenko. "5 - Piezoelectricity". In: *Funct. Dielectr. Electron.* Ed. by Yuriy Poplavko and Yuriy Yakymenko. Woodhead Publishing Series in Electronic and Optical Materials. Woodhead Publishing, 2020, pp. 161–216. ISBN: 978-0-12-818835-4.

[68]   Paul Muralt. "Piezoelectric thin films for mems". In: *Integr. Ferroelectr.* 17.1-4 (1997), pp. 297–307.

[69] Paul Muralt. "Which is the best thin film piezoelectric material?" In: *2017 IEEE Int. Ultrason. Symp.* 2017, pp. 1–3.

[70] Ruochen Lu, Ming Huang Li, Yansong Yang, et al. "Accurate extraction of large electromechanical coupling in piezoelectric MEMS resonators". In: *J. Microelectromechanical Syst.* 28.2 (2019), pp. 209–218.

[71] Robert D. Blevins. *Formulas for natural frequency and mode shape.* Ed. by Van Nostrand Reinhold Co. New York: Litton Educational Publishing, Inc., 1979, p. 492.

[72] Arthur W. Leissa. *Vibration of plates.* 1969.

[73] M. Olfatnia, Z. Shen, J. M. Miao, et al. "Medium damping influences on the resonant frequency and quality factor of piezoelectric circular microdiaphragm sensors". In: *J. Micromechanics Microengineering* 21.4 (2011).

[74] Qingming Chen and Qing Ming Wang. "The effective electromechanical coupling coefficient of piezoelectric thin-film resonators". In: *Appl. Phys. Lett.* 86.2 (2005), pp. 84–87.

[75] "IEEE Standard on Piezoelectricity". In: *ANSI/IEEE Std 176-1987* (1988), 0_1–.

[76] Roy H. Olsson, Khalid Hattar, Sara J. Homeijer, et al. "A high electromechanical coupling coefficient SH0 Lamb wave lithium niobate micromechanical resonator and a method for fabrication". In: *Sensors Actuators, A Phys.* 209 (2014), pp. 183–190.

[77] R. Przybyla et Al. "An ultrasonic rangefinder based on an AlN piezoelectric micromachined ultrasound transducer". In: *SENSORS*. Kona, HI, USA: IEEE, 2010, pp. 2417–2421.

[78] Charles H Sherman and John L Butler. *Transducers and Arrays for Underwater Sound.* 1st ed. New York: Springer, New York, NY, 2007, pp. XIX, 610. ISBN: 9780387329406.

[79] David Horsley, Yipeng Lu, and Ofer Rozen. "Flexural Piezoelectric Resonators". In: *Piezoelectric MEMS Reson.* Ed. by H. Bhugra and G. Piazza. Switzerland: Springer International, 2017. Chap. 6, pp. 153–173. ISBN: 9783319286884.

[80] Nicole E. Weckman and Ashwin A. Seshia. "Reducing dissipation in piezoelectric flexural microplate resonators in liquid environments". In: *Sensors Actuators, A Phys.* 267 (2017), pp. 464–473.

[81] Horace Sir. Lamb. "Vibrations of an Elastic Plate in Contact with Water ." In: *Proc. R. Soc. A Math. Phys. Eng. Sci.* 98.690 (1920), pp. 205–216.

[82] Jonathan J. Bernstein, Stephen L. Finberg, Kenneth Houston, et al. "Micromachined high frequency ferroelectric sonar transducers". In: *IEEE Trans. Ultrason. Ferroelectr. Freq. Control* 44.5 (1997), pp. 960–969.

[83] Y. Kozlovsky. "Vibration of plates in contact with viscous fluid: Extension of Lamb's model". In: *J. Sound Vib.* 326.1-2 (2009), pp. 332–339.

[84] D T Blackstock. *Fundamentals of Physical Acoustics*. New York: John Wiley & Sons, 2000, p. 568. ISBN: 0471319791.

[85] Lawrence E. Kinsler, Austin R. Frey, Alan B. Coppens, et al. *Fundamentals of Acoustics*. 4th. John Wily & Sons, Inc., 2000.

[86] Olympus. *Introduction to Phased Array Ultrasonic Technology applications*. ISBN: 097359330X.

[87] SIEMENS. *Sound Fields: Fre versus Diffuse Field, Near versus Far Field*.

[88] Xiaoyue Jiang, Hao Yen Tang, Yipeng Lu, et al. "Monolithic 591×438 DPI ultrasonic fingerprint sensor". In: *Proc. IEEE Int. Conf. Micro Electro Mech. Syst.* 2016-Febru.January (2016), pp. 107–110.

[89] Sina Sadeghpour, Marcus Ingram, Chen Wang, et al. "A 128x1 Phased Array Piezoelectric Micromachined Ultrasound Transducer (pMUT) for Medical Imaging". In: *2021 21st Int. Conf. Solid-State Sensors, Actuators Microsystems*. 2021, pp. 34–37.

[90] Xiaoyue Jiang, Vincent Perrot, Francois Varray, et al. "Piezoelectric Micromachined Ultrasonic Transducer for Arterial Wall Dynamics Monitoring". In: *IEEE Trans. Ultrason. Ferroelectr. Freq. Control* 69.1 (2022), pp. 291–298.

[91] Yuri Kusano, Guo Lun Luo, and David A. Horsley. "Spurious Mode Free Hexagonal PMUT Array". In: *2019 20th Int. Conf. Solid-State Sensors, Actuators Microsystems Eurosensors XXXIII, TRANSDUCERS 2019 EUROSENSORS XXXIII*. IEEE, 2019, pp. 238–241. ISBN: 9781728120072.

[92] N M Tole and H Ostensen. *Basic Physics of Ultrasonographic Imaging*. Who/Diagnostic Imaging and Laboratory Technology Series. World Health Organization, 2005. ISBN: 9789241592994.

[93] Olympus. *Ultrasonic Transducers Technical Notes Basic*. Tech. rep. 2006.

[94] Sweden COMSOL AB, Stockholm. *COMSOL Multiphysics*.

[95] J. A. Jensen and N. B. Svendsen. "Calculation of pressure fields from arbitrarily shaped, apodized, and excited ultrasound transducers". In: *Ultrason. Ferroelectr. Freq. Control. IEEE Trans.* 39.2 (1992), pp. 262–267.

[96] Jørgen Arendt Jensen. "Field: A program for simulating ultrasound systems". In: *Med. Biol. Eng. Comput.* 34.SUPPL. 1 (1996), pp. 351–352.

[97] Arantxa Uranga, Guillermo Sobreviela, Eloi Marigó, et al. "ABOVE-IC 300 MHZ AlN SAW OSCILLATOR". In: *2017 19th Int. Conf. Solid-State Sensors, Actuators Microsystems*. Kaohsiung, 2017, pp. 1927–1930. ISBN: 9781538627327.

[98]   J Muñoz, F Torres, A Uranga, et al. "Monolithical AlN PMUT on Pre- Processed CMOS Substrate". In: *2018 IEEE Int. Freq. Control Symp.* Olympic Valley, USA, 2018, pp. 1–3. ISBN: 9781538632147.

[99]   Mohanraj Soundara Pandian, Eloi Marigo Ferrer, Wee Song Tay, et al. "Thin film piezoelectric devices integrated on CMOS". In: *Proc. 2016 Symp. Piezoelectricity, Acoust. Waves Device Appl. SPAWDA 2016*. Xi'an, China: IEEE, 2016, pp. 167–170. ISBN: 9781509011896.

[100] Eyglis Ledesma, Ivan Zamora, Arantxa Uranga, et al. "9.5 % Scandium Doped ALN PMUT Compatible with Pre-Processed CMOS Substrates". In: *Proc. IEEE Int. Conf. Micro Electro Mech. Syst.* 2021, pp. 887–890. ISBN: 9781665419123.

[101] Guo-lun Luo, Yuri Kusano, and David Horsley. "Immersion PMUTs Fabricated with a Low Thermal- Budget Surface Micromachining Process". In: *2018 IEEE Int. Ultrason. Symp.* Kobe, Japan: IEEE, 2018, pp. 4–7. ISBN: 9781538634257.

[102] Qi Wang, Guo Lun Luo, Yuri Kusano, et al. "Low Thermal Budget Surface Micromachining Process for Piezoelectric Micromachined Ultrasonic Transducer Arrays With in-Situ Vacuum Sealed Cavities". In: *Hilt. Head Work. 2018 A Solid-State Sensors, Actuators Microsystems*. San Diego, USA, 2018, pp. 245–248. ISBN: 9781940470030.

[103] Iván Zamora, Eyglis Ledesma, Arantxa Uranga, et al. "Monolithic Single PMUT-on-CMOS Ultrasound System with +17 dB SNR for Imaging Applications". In: *IEEE Access* 8 (2020), pp. 142785–142794.

[104] 3M Company. *3M ™ Fluorinert ™ Electronic Liquid FC-70 Product description*. Tech. rep. 2019, pp. 1–4.

[105] L.S. Starrett Company. *Catalog 33 - Section 1 - Micrometers*. (Visited on 12/20/2021).

[106] Iván Zamora, Eyglis Ledesma, Arantxa Uranga, et al. "Miniaturized 0.13-μm CMOS Front-End Analog for AlN PMUT Arrays". In: *Sensors* 20.4 (2020), p. 1205.

[107] Keith A. Wear, Anant Shah, and Christian Baker. "Correction for Hydrophone Spatial Averaging Artifacts for Circular Sources". In: *IEEE Trans. Ultrason. Ferroelectr. Freq. Control* 67.12 (2020), pp. 2674–2691.

[108] Robert A Smith. "Are hydrophones of diameter 0 . 5 mm small enough to characterise diagnostic ultrasound equipment ?" In: *Phys. Med. Biol.* 34 (1989), pp. 1953–1607.

[109] Onda Coorporation. *HNC Hydrophones*. Tech. rep. 2015, pp. 1–2.

[110] Onda Corporation. *Hydrophone Handbook*. CA,USA, 2015. (Visited on 06/08/2021).

[111] Optel. *OPTEL Ultrasonic Technology*. (Visited on 05/20/2022).

[112] Hao Yen Tang, Yipeng Lu, Stephanie Fung, et al. "Integrated ultrasonic system for measuring body-fat composition". In: *Dig. Tech. Pap. - IEEE Int. Solid-State Circuits Conf.* 58 (2015), pp. 210–211.

[113] Ziyi Liu, Shinya Yoshida, Toshiaki Horie, et al. "Feasibility study of ultrasonic biometrics based on finger vessel imaging by epitaxial-PZT/Si piezoelectric micromachined ultrasonic transducer". In: *Sensors Actuators, A Phys.* 312 (2020), p. 112145.

[114] J. Xie H. Ding, S. Akhbari, B. E. Eovino, Y. Wu and L. Lin. "Ultrasonic imaging of muscle-like phantoms using bimorph pmuts toward wearable muscle disorder diagnostics". In: *2018 IEEE Micro Electro Mech. Syst.* Belfast, 2018, pp. 396–399. ISBN: 9788578110796. arXiv: `arXiv:1011.1669v3`.

[115] Christopher Y. Cheng, Ajay Dangi, Liqiang Ren, et al. "Thin Film PZT-Based PMUT Arrays for Deterministic Particle Manipulation". In: *IEEE Trans. Ultrason. Ferroelectr. Freq. Control* 66.10 (2019), pp. 1605–1615.

[116] Guo Lun Luo and David A. Horsley. "Piezoelectric Micromachined Ultrasonic Transducers with Corrugated Diaphragms Using Surface Micromachining". In: *2019 20th Int. Conf. Solid-State Sensors, Actuators Microsystems Eurosensors XXXIII (TRANSDUCERS EUROSENSORS XXXIII).* Berlin, Germany: IEEE, 2019, pp. 841–844. ISBN: 9781728120072.

[117] A Guedes, S Shelton, R Przybyla, et al. "Aluminum nitride pMUT based on a flexurally-suspended membrane". In: *2011 16th Int. Solid-State Sensors, Actuators Microsystems Conf.* Beijing, China: IEEE, 2011, pp. 2062–2065. ISBN: 9781457701566.

[118] Tao Wang, Renshi Sawada, and Chengkuo Lee. "A piezoelectric micromachined ultrasonic transducer using piston-like membrane motion". In: *IEEE Electron Device Lett.* 36.9 (2015), pp. 957–959.

[119] Yue Liang, Benjamin Eovino, and Liwei Lin. "Piezoelectric Micromachined Ultrasonic Transducers With Pinned Boundary Structure". In: *J. Microelectromechanical Syst.* 29.4 (2020), pp. 585–591.

[120] Sina Akhbari, Firas Sammoura, Chen Yang, et al. "Bimorph pMUT with dual electrodes". In: *2015 28th IEEE Int. Conf. Micro Electro Mech. Syst.* 2015, pp. 928–931.

[121] Yipeng Lu, Qi Wang, and David A. Horsley. "Piezoelectric micromachined ultrasonic transducers with increased coupling coefficient via series transduction". In: *2015 IEEE Int. Ultrason. Symp. IUS 2015.* Taipei, Taiwan: IEEE, 2015, pp. 1–4. ISBN: 9781479981823.

[122] Sina Akhbari, Arne Voie, Zhikang Li, et al. "Dual-electrode bimorph pmut arrays for handheld therapeutic medical devices". In: *2016 IEEE 29th Int. Conf. Micro Electro Mech. Syst.* 2016, pp. 1102–1105.

[123] Qi Wang, Yipeng Lu, Sergey Mishin, et al. "Design, Fabrication and Characterization of Scandium Aluminum Nitride Based Piezoelectric Micromachined Ultrasonic Transducers". In: *J. Microelectromechanical Syst.* 26.5 (2017), pp. 1132–1139.

[124] Yuri Kusano, Guo-Lun Luo, David Horsley, et al. "36% Scandium-doped Aluminium Nitride Piezoelectric Micromachined Ultrasonic Transducers". In: *2018 IEEE Int. Ultrason. Symp.* Kobe, Japan: IEEE, 2018, pp. 1–4. ISBN: 978-1-5386-3425-7.

[125] Eyglis Ledesma, Iván Zamora, Francesc Torres, et al. "Squared PMUT with enhanced pressure sensitivities". In: *Eurosensors 2018*. Graz, Austria: MDPI, 2018, p. 925.

[126] Eyglis Ledesma, Vassil Tzanov, Iván Zamora, et al. "AlN PMUT with crossed-cavity for better acoustic pressure outputs in liquid at high frequency". In: *2019 20th Int. Conf. Solid-State Sensors, Actuators Microsystems Eurosensors XXXIII (TRANSDUCERS EUROSENSORS XXXIII)*. Berlin, Germany: IEEE, 2019, pp. 825–828. ISBN: 9781538681046.

[127] E. Ledesma, I. Zamora, V. Tzanov, et al. "Liquid operable AlN PMUT with high output pressure capabilities". In: *2019 IEEE Int. Ultrason. Symp.* Glasgow, United Kingdom: IEEE, 2019, pp. 251–254. ISBN: 9781728145952.

[128] Eyglis Ledesma, Ivan Zamora, Arantxa Uranga, et al. "Monolithic PMUT-on-CMOS Ultrasound System for Single Pixel Acoustic Imaging". In: *Proc. IEEE Int. Conf. Micro Electro Mech. Syst.* 2021, pp. 394–397. ISBN: 9781665419123.

[129] P. Muralt and J. Baborowski. "Micromachined ultrasonic transducers and acoustic sensors based on piezoelectric thin films". In: *J. Electroceramics* 12.1-2 (2004), pp. 101–108.

[130] M. Olfatnia, T. Xu, L. S. Ong, et al. "Investigation of residual stress and its effects on the vibrational characteristics of piezoelectric-based multilayered microdiaphragms". In: *J. Micromechanics Microengineering* 20.1 (2010).

[131] Glenn Ross, Hongqun Dong, Cyril Baby Karuthedath, et al. "The impact of residual stress on resonating piezoelectric devices". In: *Mater. Des.* 196 (2020), p. 109126.

[132] Arman Hajati, Dimitre Latev, Deane Gardner, et al. "Three-dimensional micro electromechanical system piezoelectric ultrasound transducer". In: *Appl. Phys. Lett.* 101.25 (2012).

[133] Tao Wang and Chengkuo Lee. "Zero-Bending Piezoelectric Micromachined Ultrasonic Transducer (pMUT) With Enhanced Transmitting Performance". In: *J. Microelectromechanical Syst.* 24.6 (2015), pp. 2083–2091.

[134] Alessandro S. Savoia, Marco Casavola, Enrico Boni, et al. "Design, Fabrication, Characterization, and System Integration of a 1-D PMUT Array for Medical Ultrasound Imaging". In: *2021 IEEE Int. Ultrason. Symp.* IEEE, 2021, pp. 1–3. ISBN: 9781665403559.

[135] Inc. Vesper Technologies. *Vesper's Disruptive*. (Visited on 2018).

[136] Shi-Chang Wooh and Yijun Shi. "Optimum beam steering of linear phased arrays". In: *Wave Motion* 29.3 (1999), pp. 245–265.

[137] I O Wygant, X Zhuang, D T Yeh, et al. "An Endoscopic Imaging System Based on a Two-Dimensional CMUT Array : Real-Time Imaging Results". In: *IEEE Ultrason. Symp.* Rotterdam, The Netherlands: IEEE, 2005, pp. 792–795. ISBN: 078039383X.

[138] H. Tang, Y. Lu, S. Fung, et al. "Pulse-echo ultrasonic fingerprint sensor on a chip". In: *2015 Transducers - 2015 18th Int. Conf. Solid-State Sensors, Actuators Microsystems, TRANSDUCERS 2015*. 2015, pp. 674–677. ISBN: 9781479989553.

[139] I. Zamora, E. Ledesma, A. Uranga, et al. "Phased array based on AlScN Piezoelectric Micromachined Ultrasound Transducers monolithically integrated on CMOS". In: *IEEE Electron Device Lett.* 43.7 (2022), pp. 1113–1116.

[140] Eyglis Ledesma, Iván Zamora, Arantxa Uranga, et al. "Multielement ring array based on minute size pmuts for high acoustic pressure and tunable focus depth". In: *Sensors* 21.14 (2021).

[141] NDTnet. *Plastic Material's acoustic properties*. 1997.

Appendices

Tent-plate AlN PMUT with a piston-like shape under liquid operation

Eyglis Ledesma, Iván Zamora, Arantxa Uranga, and Núria Barniol

Abstract— In this work, a waterproof tent-plate piezoelectric micromachined ultrasonic transducer (PMUT) with enhanced performance as actuator and sensor in comparison with standard clamped PMUT is presented. The squared AlN PMUT has four linear holes that are sealed by the passive layer allowing to increase the movement and giving the capability to work in liquid environment. The dimension of the holes was optimized to increase the PMUT displacement at least twice in relation with the regular clamped device. The acoustic performance of the PMUT was simulated in COMSOL Multiphysics and the results were experimentally verified under liquid operation. The experimental transmitting sensitivity, 3.9 kPa/V, as well as the sensor sensitivity, 13.4 V/MPa, provide a 2x factor improvement in contrast with the clamped PMUT with competitive values. Additionally, the presented tent-plate PMUT provides advantages in relation with the area, cost, power consumption and imaging quality thanks to the capability to be monolithically integrated over CMOS substrates.

Index Terms—MEMS-on-CMOS, piezoelectric micromachined ultrasonic transducer (PMUT), receiving sensitivity, transmitting sensitivity.
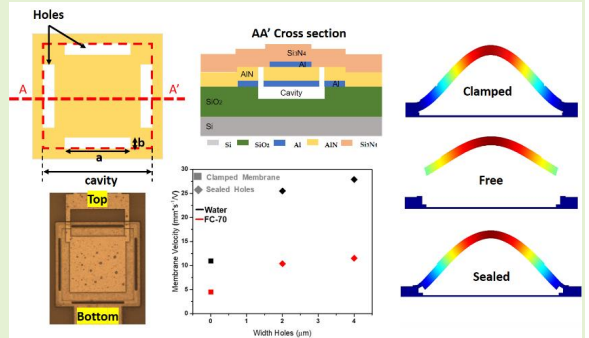
I. Introduction

ULTRASOUND is a non-invasive diagnostic tool widely used in a large number of applications: from medical imaging, non-destructive testing in industrial applications to biometric applications as fingerprints or gesture recognition systems [1], [2]. In this sense, Micromachined Ultrasonic Transducers (MUTs) appear as a promising solution due to small size, low cost, possibility to be integrated with CMOS circuitry and good acoustic impedance matching in comparison with conventional ultrasonic transducers [3]–[5].

MUTs are basically flexural membranes with micrometric size classified depending on the actuation principle in capacitive (CMUTs) and piezoelectric (PMUTs). Comparing both, PMUTs require lower power consumption without the need of a polarization voltage and reduce the fabrication complexity without the need of different gaps in the membrane for actuation or sensing and consequently with a reduction on the cost of fabrication. Taking into account these

advantages and considering AlN as the piezoelectric material with the possibility to be deposited at low temperatures and to be integrated over CMOS technology, several PMUTs designs have been presented in the state-of-the-art to obtain an enhancement in the individual or arrayed PMUTs performance [6]–[8].

PMUTs are capable to work as transmitter and receiver due to inverse and direct piezoelectric effect. If the membrane is excited by an AC signal at the resonance frequency, a sound wave will be generated due to the membrane deflection. As receiver, an incident pressure on the PMUT surface also causes a membrane deflection, producing an electrical charge between both electrodes which can be transduced to a voltage proportional to the input acoustic pressure.

As an actuator, the output pressure is one of the most important parameters to consider in the PMUT design because it is directly related with the image quality. The general expression is defined by (1) [9]:

$$p = j\frac{P_0 R_0}{r} D(\theta) e^{j(wt-kr)},\qquad(1)$$

where P_0 is the surface pressure, R_0 is the Rayleigh distance (R_0=PMUT surface/wavelength) and D is the directivity. Considering (1), the on-axis pressure in the far field at a distance z, can be expressed by (2) where ρ_0 is the medium density, c_0 its the sound velocity, u_0 is the membrane velocity (u_0=2πfd_s), λ is the wavelength, d_s is the dynamic membrane displacement, f is the resonance frequency and A is the PMUT surface:

$$p(z) = \frac{P_0 R_0}{z} = \frac{(\rho_0 c_0 u_0)A}{z\lambda} = \frac{\rho_0 2\pi d_s f^2 A}{z}, \qquad (2)$$

From this equation it can be stated that a good PMUT candidate must have high frequency, high displacement and high area. For clamped PMUT, an effective area of 1/3 the real area is normally assumed diminishing by 1/3 the efficiency as actuator in comparison with the standard piston-like PMUTs [9], [10]. Similar enhancement can be expected considering the sensing capability of a PMUT with a piston-like behavior instead of a flexural clamped PMUT. Recently, some researches have been focusing their attention in achieving high levels of output pressure to improve the signal to noise ratio and consequently the quality of the image with small high frequency PMUTs devices with this. The modifications in the PMUT design are aimed to obtain a piston-like movement instead of a conventional clamped device [10]–[14]. Some of these works have the limitation to be used only in airborne applications.

Another aspect to be considered is related with the need to construct an arrayed PMUTs systems to enhance the pressure level and allow electronic beam steering and beam focusing, maintaining a relative high frequency with small single PMUT devices [15]. In this arrayed PMUT systems, higher fill-factor implies better performance system. Defining the fill-factor as the ratio between active area (PMUT area) and total area (which also considers the gap between PMUT devices), it is clear than squared PMUTs in comparison with circular PMUTs could derive in higher fill factors [1], [16].

This work proposes squared PMUT devices with partial free boundaries, capable to achieve higher level of acoustic output pressure and great reception sensitivity in liquid environment compared with its counterpart clamped membranes and with the state-of-the-art. FEM simulations predict the mechanical and acoustic behavior allowing to define the new PMUT device. Comparison with the experimental results, achieves a good correlation between them. The proposed device has been fabricated using AlN with the MEMs-on-CMOS process from Silterra that allow the monolithic integration with CMOS substrates [8], [14], [16].

II. PMUT DESIGN

Fig. 1a shows the proposed device, called "tent-plate" due to it is only clamped in the corners. The device is a squared AlN PMUT with 80 μm side and has four symmetric rectangular holes in each of the sides. These holes are located at the edge of the cavity as it is depicted in Fig. 1a. The dimensions of the holes, a, length and b, width will be changed while the cavity is kept equal to 80 μm side in all the designs. The holes are used to modify the boundary conditions avoiding a fully-clamped structure, increasing the effective area and membrane displacement. Additionally, these holes are also used for the membrane releasing. A 1.5 μm Si_3N_4 elastic layer is deposited as the last step with a low temperature Plasma Enhanced Chemical Vapor Deposition (PECVD) process. This passive layer is also in charge to seal the holes and allow liquid operation, not requiring any other layer as PDMS deposition like in [17] or additional processes
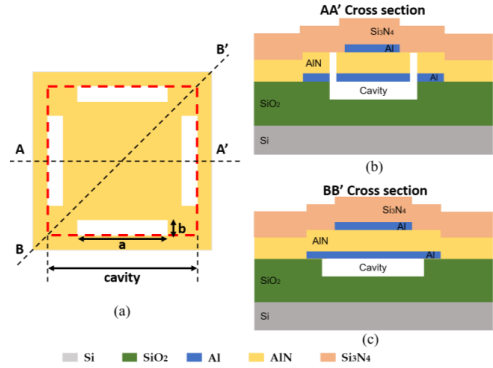
Fig. 1. Schematic model of the tent-plate PMUT: (a) Top view (the holes go through AlN); (b) AA' Cross section (the holes are at the edge of the cavity); (c) BB' Cross section (the corners are clamped).

[18]. The electrodes are aluminum with thicknesses of 0.4 μm for bottom electrode and 0.35 μm for top electrode. The thickness of the AlN piezoelectric layer deposited by Physical Vapor Deposition (PVD) is 1.3 μm [19]. Fig. 1b and 1c show cross-section profiles of the PMUT device. Table I summarizes the principal geometric parameters and properties of the materials used in the simulations. The AlN piezoelectric coefficient used in COMSOL simulations, *d31*, is -1.92 pC/N.

FEM simulations were done in COMSOL Multiphysics to stablish optimal dimensions for the linear holes and maximize displacement, frequency and effective area in relation with the clamped PMUT. Besides, the acoustic behavior in liquid environment, specifically in Fluorinert (FC-70), was obtained and compared with the experimental results.

The linear holes dimensions have been chosen according with the simulation to optimize the natural frequency and membrane displacement. The dimensions were chosen taking into account that the top metal electrode must be contacted through the corners and to guarantee symmetry on all four anchors to obtain the same pressure distribution in the plane. Fig. 2 shows the variation of the resonance frequency for the first flexural mode and the static displacement at the center of the membrane when the dimensions of the holes are changed. According with these results if the width of the holes, b, increases for the same length, a, the displacement increases but the resonance frequency decreases.

TABLE I
PARAMETERS USED IN COMSOL TO MODEL THE TENT-PLATE PMUT.

PMUT Layer	Material	Young's modulus (GPa)	Density (kg/m³)	Side (μm)	Thickness (μm)
Passive Layer	Si_3N_4	250	3100	100	1.5
Top Electrode	Al	70	2700	56.6	0.35
Piezoelectric Layer	AlN	345	3300	100	1.3
Bottom Electrode	Al	70	2700	86	0.4
Cavity	-	-	-	80	1.6
Substrate	SiO_2	70	2200	100	2
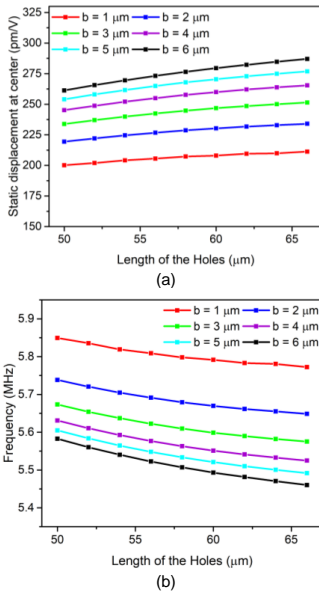
Fig. 2. FEM simulation of tent-plate PMUT with different dimensions of the holes: (a) Dependence of the static displacement with the dimensions of the holes; (b) Dependence of the resonance frequency with the dimensions of the holes.

To choose the holes dimensions, it is important to take into account that the passive layer, Si_3N_4, is conformally deposited over all the PMUT (as it is depicted in Fig. 1b). In this sense, the size of the hole, specifically its width, b, must be chosen small enough to avoid the penetration of the Si_3N_4 layer until the cavity which would convert the tent-plate PMUT to a standard clamped PMUT with smaller size, avoiding any of the abovementioned benefits (higher displacement). Fig. 3 shows a qualitative assessment of the effective area contribution for the first flexural mode shape for the clamped-PMUT, the free tent-plate PMUT (when holes are not covered with the passive layer), the sealed tent-plate PMUT and a piston baffled PMUT. From this Fig. 3, it can be qualitatively appreciated that the free tent-plate PMUT will
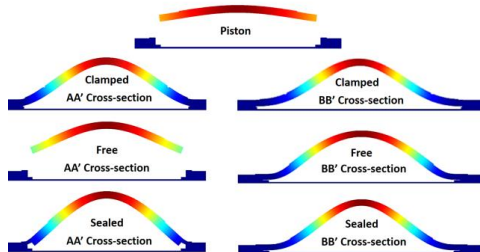
Fig. 3. COMSOL FEM mode shape for the first flexural mode in air. Cross section for the piston, clamped, free and sealed PMUT considering the same cross-sectional profiles AA', BB' from Fig 1.

present a closer mode shape to a piston baffled in comparison with a clamped PMUT. Additionally, the benefit of the passive layer sealing the holes and allowing liquid operation, comes with a moderate degradation of the maximum achievable displacement of the sealed tent-plate PMUT in comparison with the free tent-plate PMUT.

For a clamped PMUT, the maximum static displacement at the center of membrane is around 100 pm/V and the resonance frequency is 7.12 MHz. Considering this, the dimensions of the holes were chosen to increase the membrane displacement at least twice in respect the clamped PMUT affecting the frequency less than 1.5x factor in relation with the clamped device. Picking 2 μm width (as a trade-off to avoid holes filling with Si_3N_4 layer and preserve the modification in the boundary conditions), the length of the holes was optimized (considering also the top electrode needs to be connected to the substrate), see Fig. 4a, being the best option 54 μm, where both parameters are maximized. To see the behavior of the PMUT as sensor, the terminal voltage was acquired when 100 Pa were applied uniformly over PMUT surface. Taking into account that for a clamped device the normalized electric voltage at the center of membrane is around -1.1 V/MPa, choosing 54 μm length ensures 1.85x factor improvement, see Fig. 4b (red). The simulated performance as actuator (volume velocity: membrane velocity*Area) and sensor (normalized terminal voltage) is summarized in Fig. 4b.

The dimension of the top electrode was optimized to guarantee the maximal energy transformation between electrical and mechanical domain which will happen when
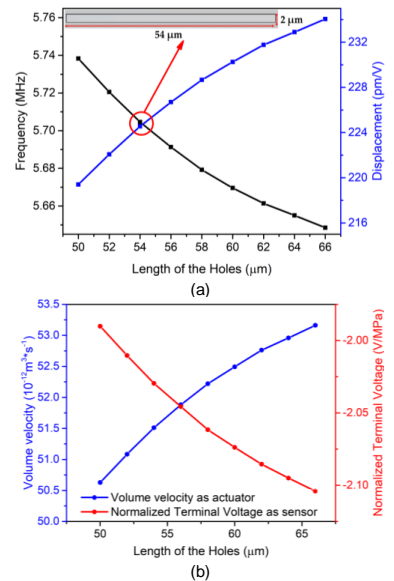
Fig. 4. FEM simulations of: (a) Eigenvalue frequency (left axis, black) and static displacement (right axis, blue); (b) Volume velocity (left axis, blue) and normalized terminal voltage (right axis, red); both a) and b) as a function of the linear hole length (with a 2 μm hole width).

the electrical-mechanical coupling coefficient is maximum. This electrical-mechanical coupling coefficient, η, can be computed using (3)-(4) where $e_{31,f}$ is the effective piezoelectric coefficient, z_p is the distance from the mid-plane of piezoelectric layer to the neutral axis, $\gamma=$ top_electrode_size/cavity_size and $\varphi_{11}(\bar{x},\bar{y})$ is the mode shape of the resonator (where $\bar{x}= x/l$, and $\bar{y}= y/l$) [20].

$$\eta = \frac{1}{2}e_{31,f}\, \bar{z}_p I_{piezo} \qquad (3)$$

$$I_{piezo} = \int_{-\gamma/2}^{\gamma/2}\int_{-\gamma/2}^{\gamma/2}\left[\frac{d^2\varphi(\bar{x},\bar{y})}{d\bar{x}^2} + \frac{d^2\varphi(\bar{x},\bar{y})}{d\bar{y}^2}\right]d\bar{x}d\bar{y} \qquad (4)$$

Considering the mode shape for the first flexural mode for a square plate, $\varphi_{11}(\bar{x},\bar{y}) = (1-4\bar{x}^2)^2(1-4\bar{y}^2)^2$, and substituting (4) in (3), the electrical-mechanical coupling coefficient for squared plate can be expressed by (5):

$$\eta = 16e_{31,f}\,\bar{z}_p\left[\gamma^2(\gamma^2-1)(\frac{\gamma^4}{5}-\frac{2\gamma^2}{3}+1)\right] \qquad (5)$$

For $\gamma=0.65$ maximal energy transformation ($d\eta/d\gamma=0$) is achieved, which is very close to the expected value for circular PMUT ($\gamma=\sqrt{2}/2=0.707$). Taking to account this and considering the influence of the holes in the mode shape, the top electrode side should be between 52 µm and 57 µm.

To validate this, the normalized static displacement was obtained changing the top electrode side. The maximum value
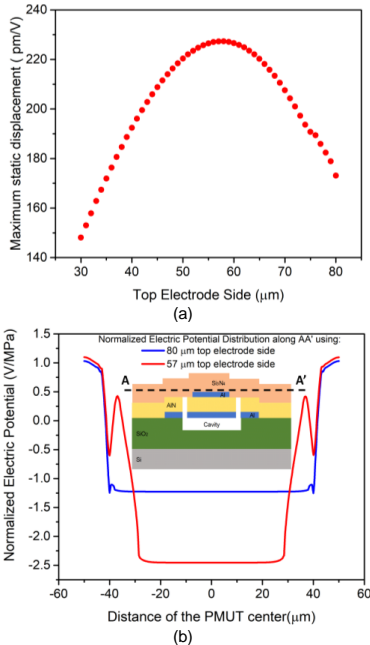
Fig. 5. FEM simulation changing the side of the top electrode using the holes dimension selected previously: (a) Maximum static displacement applying 1 V; (b) Normalized electric potential using 80 µm top electrode (blue) and 57 µm top electrode (red).

(a)   (b)
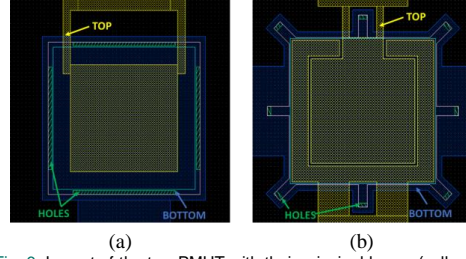
Fig. 6. Layout of the two PMUT with their principal layers (yellow is top electrode, blue is bottom electrode and green the holes): (a) Tent-plate PMUT; (b) Clamped PMUT.

is around 224 pm/V and the top side in this case 56.6 µm, like was expected, see Fig. 5a. Fig. 5b corresponds with the distribution of the normalized electric potential (V/MPa) of the PMUT as sensor at AA' (along the 80 µm side cavity) when the top electrode side is 57 µm and 80 µm respectively. The AA' position is 0.5 µm over piezoelectric layer to avoid the holes and consequently the discontinuities due to them. When the electrode size is 80 µm side, the distribution is more uniform in comparison with 57 µm side due to the electrode covers all plate. Taking the maximum value, using 57 µm side the electric potential is 2 times higher, demonstrating the importance to optimize the electrode side.

Fig. 6a, shows the final layout of the tent-plate where due to the wire connection, the final length of the linear holes is 54 µm and the electrodes size is 56.6 µm. Fig. 6b shows a standard clamped device used as reference to be compared with the tent-plate PMUT. This reference PMUT is a fully clamped squared AlN PMUT with 80 µm side with the same fabrication process than the tent-plate PMUT and fabricated simultaneously. As it is shown in Fig. 6b it has two optimized top electrodes for differential measurements but in this work only the inner electrode has been used for fair comparison with the tent-plate PMUT. Eight little holes out of the PMUT-body are used to etch the cavity.

Finally, the mode shapes for the tent-plate PMUT (free and sealed) is compared with the conventional PMUT (Fig. 7). To compare the effective area (Ae) of the PMUTs with the piston, the displacement at -6 dB was used as reference. For the tent-
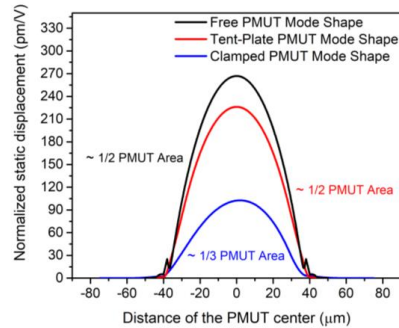
Fig. 7. Normalized static displacement of the PMUT in x direction: free tent-plate (black curve), sealed tent-plate (red curve) and clamped (blue curve).

plate (free and sealed) the movement is closer to a piston and the area in movement is approximately 1/2 of the total area. However, as it is expected, for the clamped the effective area is around 1/3 of the total and describes a gaussian mode shape. Moreover, comparing the displacement at the center of the membrane, sealed tent-plate achieves 2.2x factor improvement in relation with the clamped PMUT. Small asymmetry in the mode shape for the clamped device can be appreciated in this Fig. 7 (blue), consequence of the single site connection of the top electrode as shown in Fig. 6b.

These static simulations in air allow to conclude that tent-plate PMUTs should produce higher output pressure in comparison with the conventional PMUT. Dynamic simulations in liquid environment will allow to estimate acoustic pressure levels, giving data for comparison with experimental results and quantitative demonstration of this acoustic pressure enhancement.

Dynamic simulations

The membrane velocity (defined in Eq. 1) for a tent-plate with two different linear hole widths, 2 μm and 4 μm, and clamped PMUT was computed using the FEM simulator results in FC-70 (density, ρ= 1940 kg/m^3 and the sound velocity, c = 689 m/s) and water (density, ρ= 1000 kg/m^3 and the sound velocity, c = 1500 m/s), see Fig. 8. The membrane velocity has been normalized with the applied voltage (20Vpp in this case). From this image it can be concluded that, there is a clear improvement in the displacement and consequently in the velocity for the tent-plate PMUT in contrast with the clamped PMUT, being 2.3x factor better (considering the velocity at the center of the membrane and 2 μm width). Due to the devices don't move like a piston, it is necessary to consider the effective area, defined at -6 dB, being for tent-plate 1/2 and for clamped 1/3 part of the total area, then the final normalized membrane velocity for the tent-plate will be 3.5x factor better than the standard clamped PMUT. Table II summarizes the simulated results in FC-70 for the tent-plate with 2μm width and the clamped device for a clear comparison.

All obtained results with the dynamic FEM simulation are in correspondence with the previous ones, demonstrating the positive influence of the holes to increase the movement of the membrane.

Finally, the time-domain simulations were done to
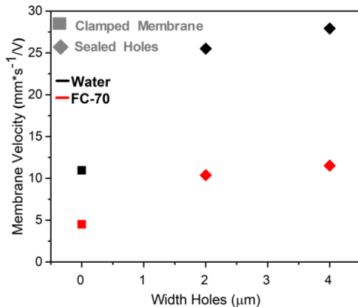
Fig. 8. Membrane velocity per volt (mm*s^{-1}/V) for different width holes excited with 1 V in water and FC-70.

TABLE II
SIMULATION RESULTS OF DISPLACEMENT-FREQUENCY RESPONSE FC-70. COMPARISON BETWEEN TENT-PLATE (2 μM LINEAR HOLE WIDTH) AND CLAMPED PMUT.

Device	Frequency (MHz)	Displacement at center (pm)	Normalized membrane velocity (mm/s*V^{-1})
Tent-plate	2.175	758	10.4
Clamped	2.75	261	4.51

characterize the PMUT performance as actuator and as sensor in FC-70, see Fig. 9.

The acoustic pressure was generated driving the PMUT with 2 cycles at 2.2 MHz with 20 Vpp. The signal was acquired 1 mm over its surface giving around 1.6 kPa peak-to-peak, see Fig. 9a. Also, the transmitted sensitivity (ST) or normalized surface pressure, is defined by P_0/V, where P_0 is the surface pressure (see Eq. 2) and V the applied voltage. With the Rayleigh distance (20.4 μm), which corresponds to an 80 μm side squared PMUT at 2.2 MHz in FC-70, the simulated pressure at 1 mm (1.6 kPa) and the applied voltage (20 Vpp), a 3.9 kPa/V transmitted sensitivity is obtained from the FEM simulations. The quality factor (Q) was computed using the ringdown for the acoustic simulation giving 2.1. For comparison, clamped PMUT was simulated with the same excitation signal but the frequency in this case is 2.75 MHz, the acquired pressure at 1 mm is 990 Pa peak-to-peak, being
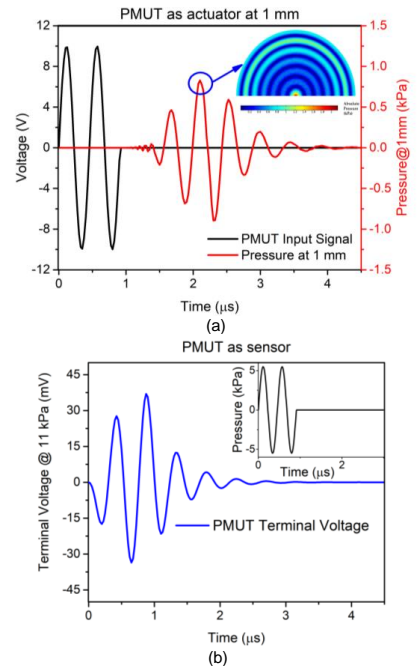
Fig. 9. Time domain simulation of the tent-plate PMUT in FC-70: (a) Pulse-echo response at 1 mm where black is the actuation signal and red the echo measured 1 mm over PMUT surface. Inset: pressure profile at 2.1 μs along the 1mm axial direction; (b) PMUT as sensor: voltage in the terminal when 11 kPa @ 2.2 MHz are applied. Inset: Pressure applied (11 kPa) over PMUT surface.

the surface pressure 1.9 kPa/V and the Q-factor 2.4. These results allow us to conclude that tent-plate PMUT is capable to generate 2x times output pressure that the conventional device, close to predicted when the holes dimensions where selected. Inset of Fig. 9a corresponds with the pressure profile at 2.1 µs along the 1mm axial direction. The last blue semicircle gives around 800 Pa and it is the maximum peak in the echo time response as it is shown.

The performance as sensor is analyzed too, and to do it 2 cycles at 2.2 MHZ with 11 kPa peak-to-peak is applied over PMUT surface, see Fig.9b Inset. The generated peak-to-peak voltage gives 70 mV, see Fig. 9b, and the sensitivity as sensor (SR) was computed as V_{PMUT}/P_A where V_{PMUT} is the voltage in the PMUT terminals and P_A is the applied pressure on the surface, obtaining 6.4 V/MPa.

III. EXPERIMENTAL RESULTS

To validate simulated results, the same designs were used experimentally. The optical images of the proposed PMUTs are showed in Fig. 10.

A. Electrical Characterization in air

Tent-plate PMUT was electrically characterized in air using a manual probe table and network analyzer where top electrode was used as input and the bottom electrode as output, see the set-up in Fig. 11 (Upper Inset). The electrical equivalent circuit is shown in Fig. 11 (Lower Inset) where C_0 is the static capacitance obtained from the physical PMUT layout (196 fF), C_p is the parasitic capacitance (59 fF), C_m, L_m and R_m are the motional capacitance, inductance and resistance, being 0.12 fF, 8.64 H and 0.68 MΩ respectively. The measured resonance frequency (fr) is 4.9 MHz. The results are shown in Fig. 11 where the electrical measure and the obtained fitted curve, demonstrate a good correlation. The equivalent electrical components have been used to obtain the quality factor (Q) in air, giving 392. The electromechanical coupling factor (k_t^2) was computed using (6) where f_s is the series resonance and f_p is the parallel resonance, giving 1 %. This value is lower than clamped device, 1.6 % [21], due to in the clamped PMUT, the electrical measure has been done between the two top electrodes, with a corresponding much lower C_0.

$$k_t{}^2 = \frac{\pi^2}{4}\left[\frac{f_p - f_s}{f_s}\right] \qquad (6)$$

B. Acoustic Characterization in liquid

The acoustic characterization as actuator were done in FC-70 ($\rho_0 = 1940$ kg/m^3 and $c_0 = 694$ m/s) using two commercial hydrophones from ONDA (HNC-1500 and HNC-0200), the set-
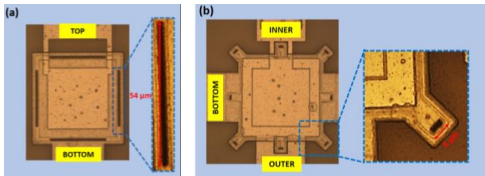
Fig. 10. Optical Images of the PMUTs where blue squares are drawn over the holes in each design: (a) Tent-plate PMUT; (b) Clamped PMUT.
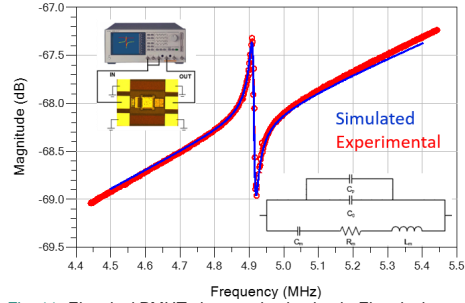
Fig. 11. Electrical PMUT characterization in air: Electrical measure at the resonance frequency (red) and fitted curve due to C_0, C_p, C_m, L_m and R_m (blue) obtained. Upper Inset: Set-up. Lower Inset: Electrical model of the tent-plate PMUT considering the static capacitance in parallel with the parasitic capacitance and motional branch.

up is shown in Fig. 12a. Tent-plate PMUT was driven with 2 cycles at 2.1 MHz with 22 Vpp and the signal was measured at 1 mm over the PMUT surface (see set-up in Fig. 12a) which corresponds to unidirectional time-of-flight of 1.45 µs after the pulse was generated. Fig. 12b (Inset) shows the echo response using HNC-0200. The sensitivity of the hydrophone in FC-70 was computed considering the hydrophone calibration in water and the acoustic impedances ratio (Senstivity$_{FC70}$ = Z_{FC70}/Z_{H2O}*Sensitivity$_{H2O}$ where Z_{FC70} and Z_{H2O} are the acoustic impedance for FC-70 and water respectively). Using the
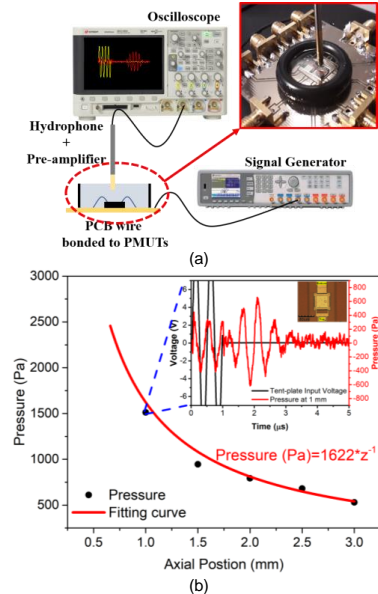
Fig. 12. (a) Set-up for acoustic PMUT characterization as actuator in liquid; (b) Acoustic pressure measurements at different axial positions from the PMUT. Red curve shows the fitting assuming 1/z pressure dependence. Inset: Unidirectional pulse-echo response measures at 1 mm over PMUT, in black excitation signal and red echo for the tent-plate PMUT.

acquired voltage and considering the sensitivity in FC-70, the pressure at 1 mm is 1.5 kPa peak-to-peak. According with (2) and considering 19.4 μm Rayleigh's distance, the surface pressure (P_0) was computed, giving 85.8 kPa. Normalizing with the applied voltage (22 Vpp), the transmitting (ST) is 3.9 kPa/V, demonstrating a good correspondence between simulation and experimental measures.

The acoustic pressure was measured at different heights over PMUT surface and the results are shown in Fig. 12b. The acquired pressure amplitudes were fitted assuming that the pressure in far field decay 1/z, where z is the axial position, obtaining $1622*z^{-1}$. Normalizing it with the Rayleigh distance (~19.4 μm) and the applied voltage, the output normalized surface pressure is 3.8 kPa/V, very close to the simulated one and the previously obtained experimentally.

Clamped PMUT was also measured in FC-70 under the same experimental conditions to compare, as was done in the FEM simulation. The hydrophone was at 1 mm over PMUT and the excitation signal is two cycles with 22 Vpp at 2.4 MHz. The acquired pressure is 850 Pa peak-to-peak, and the normalized surface pressure is 1.9 kPa/V. The results shown a considerable improvement with the tent-plate in the transmitting acoustic pressure, achieving 3.9/1.9=2x factor better, in relation with its counterpart clamped device, demonstrating the benefit to use this design.

Other complementary acoustic measures as actuator in FC-70 were done using the hydrophone HNC-1500, see Fig. 13, which provides a better signal-to-noise ratio due to the higher sensitivity compared with the HNC-0200. The time domain response at 3 mm from the PMUT surface is shown (black). Due to the large signal-to-noise ratio obtained with this hydrophone, the Fast Fourier Transform from the ring down time domain response, was computed giving a resonance frequency f= 1.9 MHz, close to the expected, and a bandwidth at -3 dB (BW) of 1.24 MHz (red). In liquid, the main energy dissipation of the PMUTs is due to medium losses and for this $Q_{total} \sim Q_{medium}$ [22]. Considering this, the quality factor in FC-70 is Q=f/BW=1.5. The fractional bandwidth at -6 dB for the proposed device is 89 %, higher compared with most of the

PMUTs reported [1], [17], [23], and only comparable in case of using PDMS as acoustic coupling material with the liquid [17].

An acoustic field characterization was also performed (Fig. 14). The acoustic pressure was acquired lifting the HNC-1500 hydrophone and displacing it in x-direction and y-direction respectively using a 3-axis micrometric manual system as it is

(a)

(b)

(c)
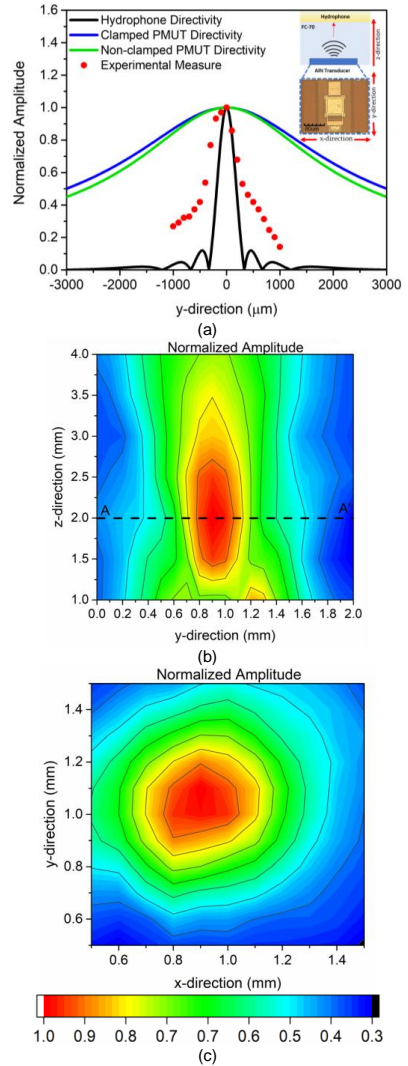
Fig. 14. Acoustic measurements using HNC-1500 hydrophone: (a) Acoustic beam-pattern at AA' with the lateral position shifted to 0 to see the width of the acoustic beam at 2 mm. In black the HNC1500 hydrophone directivity, blue the clamped PMUT field, green the non-clamped PMUT field and red the experimental measures. Inset: Experimental set-up; (b) 2D measured acoustic field in y-z plane; (c) 2D measured acoustic pattern in x-y plane at 2 mm over PMUT surface, the coordinates are selected around the maximum point.

Fig. 13. Time-domain response measured with the hydrophone situated over the PMUT (black line corresponding to bottom-left axis). The echo starts at 4,35 μs which corresponds to the 3 mm distance. Red line (corresponding with top-right axis) shows the FFT from ring down time-domain response.

showed in Fig. 14a (Inset). The step used in x and y is 100 μm and in the axial direction is 500 μm. Fig. 14a presents the simulated beam pattern for the PMUT, clamped (blue) and non-clamped (green), and hydrophone (black) at 2 mm where the acoustic beam width at -6 dB for the PMUTs are between 5 and 6 mm. The experimental measurements at the same axial position (AA' cut in Fig. 14b) is also shown in Fig. 14a (points in red), where the maximum peak-to-peak pressure is 811 Pa. Note how the acquired signal has practically the same behavior than the hydrophone directivity. Fig. 14b shows the 2D measured acoustic field (normalized acoustic pressure) in y-z plane. At the axial position of z= 2 mm, the acoustic pressure was acquired around the maximum point to pattern the 2D acoustic field as it is shown in Fig. 14c.

All results are affected by the HNC-1500 hydrophone's directivity due to its aperture size is bigger than half-wavelength of the sound wave at 2.1 MHz [24]. To correct this effect, the definition of the directivity for the hydrophone proposed in [25] can be used to deconvolve and obtain the real pattern for the PMUT. The acoustic beam width at 2 mm will be around 6 mm according with the simulated profiles shown in Fig. 14a. Note that this beam width can be decreased with an arrayed PMUT system, allowing beam forming for focusing.

The acoustic characterization as sensor were also done in FC-70 using a commercial transducer from OPTEL. The transducer was excited with 4 cycles at 2.1 MHz with 22 Vpp and it has been previously calibrate obtaining at 3 mm and at the same frequency in FC-70, 11 kPa. The generated signal in the electrodes due to the applied pressure was acquired by the oscilloscope using different cable lengths between them, see Fig. 15. The inset shows 1.70 mVpp when the cable length is 5 cm, giving received sensitivity around 155 mV/MPa. For comparison, clamped PMUT was also characterized as sensor in the same conditions and the acquired signal was 0.94 mVpp. Considering this, the applied pressure in this case is around 14 kPa (OPTEL calibration at 2.4 MHz)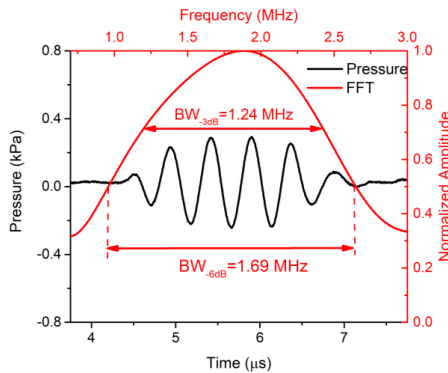, the received sensitivity is 67 mV/MPa; a 57 % lower than tent-plate PMUT. However, it is necessary to consider all parasitic capacitances that affect the measure to obtain the intrinsic PMUT sensitivity as sensor [25] defined by (7) as S_{R_EOC}:

$$S_R = S_{R\_EOC} * \frac{C_{PMUT}}{C_{PMUT} + C_W + C_{OSC} + C_{SET}} \qquad (7)$$

S_{R_EOC} is the PMUT's "End-of-cable Open circuit sensitivity", $C_{PMUT}=C_0+C_p=255$ fF is the capacitance obtained through the electric characterization (see Fig. 11); C_w is the capacitance due to the used cable between PMUT and oscilloscope, being in our case 96 pF/m; C_{osc} is the input capacitance of the oscilloscope, 14 pF; and C_{SET} is the capacitance due to the printed circuit board and connectors, 3 pF. Considering these values, the S_{R_EOC} is 13.4 V/MPa. Fig. 15 shows the degradation in the received signal when the cable length (and consequently parasitic capacitance) between tent-plate PMUT and oscilloscope increases, demonstrating the importance to reduce the parasitic capacitances which will be minimized through the monolithical integration on CMOS circuitry allowing much better signal-to-noise ratios.

The obtained results in this work show the positive influence of the linear holes to improve the PMUT performance as actuator and as sensor in comparison with the conventional clamped device. Table III summarizes a comparison between the performance of tent-plate PMUT and other AlN and ScAlN devices reported in the state-of-the-art which are operated in liquid. Note that PMUTs with some corrugated surfaces or piston-like shapes like the ones presented in references [10], [12], [13] are not operated under liquid environment and

TABLE III
COMPARISON WITH PMUTs IN LIQUID[1] AS ACTUATOR AND AS SENSOR.

Ref	ST kPa/V	SR V/MPa	PMUT Config. /Size	Single/ Array	Process/ Comments
This work	3.9	13.4	Squared tent-plate/ 80μmx80μm	Single	AlN-on-CMOS
This work	1.9	7.6	Squared clamped/ 80μmx80μm	Single	AlN-on-CMOS
[1]	2.95	2	Rectangular/ 30μmx43μm	Array 1x56.	AlN//Array 110x56
[18]	2.93	510[2]	Squared/ 50μmx50μm	Array 3x20.	AlN/CMOS compatible
[26]	2.8	-	Concentric Rings/ 2.6mm aperture	Array 5rings	AlN // Ring array.
[27]	1.38	-	Rectangular/ 30μmx43μm	Single[3]	AlN//Array 110x56
[28]	1.1	-	Circular/ 40μm radius	Single	AlN-on-CMOS
[29]	0.7[4]	-	Circular/ 50- and 40-μm	Array 7x7	ScAlN
[23]	0.04[5]	-	Circular/ 50μm radius	Array 23x23.	AlN- on glass substrate

[1] Liquid is FC-70 in all cases except in ref [26] that uses mineral oil.
[2] In reception 10 V/pC charge amplifier was used.
[3] Extrapolated from array.
[4] Pressure measured at 1.7 mm (assuming that it is equivalent to their R_0 distance [29]).
[5] Pressure measured at 10 μs (equivalent to their R_0 distance [29]).

Fig. 15. Time domain characterization as sensor in FC-70. Dependence between received signal and cable length using tent-plate PMUT. Inset: Echo response, in black excitation signal and red measured signal by the electrodes when the OPTEL is placed 3 mm over PMUT surface.

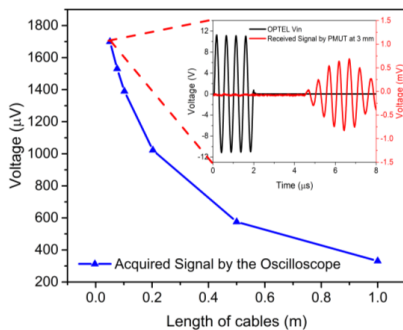consequently, they are not included in Table III. It can be stated that tent-plate achieves high levels of transmitting sensitivity (ST in kPa/V) compared with arrays of PMUTs. Taking the best reported transmitting sensitivity and normalized it respect to the PMUTs number (56 PMUT), tent-plate PMUT achieve an improvement of 72x factor. In relation with the sensitivity as sensor, tent-plate PMUT achieve around 13.4 V/MPa without any amplifier, being 6.7x factor higher than the array PMUT (without circuitry) proposed in [1].

IV. Conclusions

The FEM simulation in COMSOL Multiphysics and the experimental characterization of the tent-plate PMUT allow us to demonstrate the positive influence of the linear holes in the PMUT performance. The Si_3N_4 layer acts as passive layer while contributes to seal the cavity, and liquid-proofing protection. The limitations due to the clamped boundary are eliminated with the tent-plate device, increasing the movement and consequently the output pressure. The fractional bandwidth for the proposed device is 89 %. Unlike other non-clamped PMUTs, the fabricated tent-plate achieves a transmitting sensitivity of 3.9 kPa/V in FC-70 and 13.4 V/MPa as reception sensitivity.

Acknowledgment

References

[1] X. Jiang *et al.*, "Monolithic ultrasound fingerprint sensor," *J. Microsystems Nanoeng.*, vol. 3, 2017.

[2] R. J. Przybyla, H. Y. Tang, S. E. Shelton, D. A. Horsley, and B. E. Boser, "12.1 3D ultrasonic gesture recognition," in *2014 IEEE International Solid-State Circuits Conference Digest of Technical Papers (ISSCC)*, 2014, vol. 57, pp. 210–211.

[3] Y. Lu, H. Tang, S. Fung, B. E. Boser, and D. A. Horsley, "Pulse-Echo Ultrasound Imaging Using an AlN Piezoelectric Micromachined Ultrasonic Transducer Array With Transmit Beam-Forming," *J. Microelectromechanical Syst.*, vol. 25, no. 1, pp. 179–187, 2016.

[4] Y. Qiu *et al.*, "Piezoelectric micromachined ultrasound transducer (PMUT) arrays for integrated sensing, actuation and imaging," *Sensors*, vol. 15, no. 4, pp. 8020–8041, 2015.

[5] B. T. Khuri-Yakub and Ö. Oralkan, "Capacitive micromachined ultrasonic transducers for medical imaging and therapy," *J. Micromechanics Microengineering*, vol. 21, no. 5, 2011.

[6] J. Jung, W. Lee, W. Kang, E. Shin, J. Ryu, and H. Choi, "Review of piezoelectric micromachined ultrasonic transducers and their applications," *J. Micromechanics Microengineering*, vol. 27, no. 11, 2017.

[7] D. A. Horsley *et al.*, "Piezoelectric micromachined ultrasonic transducers in consumer electronics: The next little thing?," in *2016 IEEE 29th International Conference on Micro Electro Mechanical Systems (MEMS)*, 2016, pp. 145–148.

[8] E. Ledesma *et al.*, "AlN PMUT with crossed-cavity for better acoustic pressure outputs in liquid at high frequency," in *2019 20th International Conference on Solid-State Sensors, Actuators and Microsystems & Eurosensors XXXIII (TRANSDUCERS & EUROSENSORS XXXIII)*, 2019, pp. 825–828.

[9] D. T. Blackstock, *Fundamentals of Physical Acoustics*. New York: John Wiley & Sons, 2000.

[10] G. L. Luo and D. A. Horsley, "Piezoelectric Micromachined Ultrasonic Transducers with Corrugated Diaphragms Using Surface Micromachining," in *2019 20th International Conference on Solid-State*

Sensors, Actuators and Microsystems & Eurosensors XXXIII (TRANSDUCERS & EUROSENSORS XXXIII), 2019, pp. 841–844.

[11] A. Guedes, S. Shelton, R. Przybyla, I. Izyumin, B. Boser, and D. A. Horsley, "Aluminum nitride pMUT based on a flexurally-suspended membrane," in *2011 16th International Solid-State Sensors, Actuators and Microsystems Conference*, 2011, pp. 2062–2065.

[12] T. Wang, R. Sawada, and C. Lee, "A piezoelectric micromachined ultrasonic transducer using piston-like membrane motion," *IEEE Electron Device Lett.*, vol. 36, no. 9, pp. 957–959, 2015.

[13] Y. Liang, B. E. Eovino, and L. Lin, "Pinned Boundary Piezoelectric Micromachined Ultrasonic Transducers," in *2019 IEEE 32nd International Conference on Micro Electro Mechanical Systems (MEMS)*, 2019, pp. 791–794.

[14] E. Ledesma *et al.*, "Liquid operable AlN PMUT with high output pressure capabilities," in *2019 IEEE International Ultrasonics Symposium (IUS)*, 2019, pp. 251–254.

[15] X. Jiang *et al.*, "Ultrasonic Fingerprint Sensor with Transmit Beamforming Based on a PMUT Array Bonded to CMOS Circuitry," *IEEE Trans. Ultrason. Ferroelectr. Freq. Control*, vol. 64, no. 9, pp. 1401–1408.

[16] E. Ledesma *et al.*, "AlN piezoelectric micromachined ultrasonic transducer array monolithically fabricated on top of pre-processed CMOS substrates," in *2019 20th International Conference on Solid-State Sensors, Actuators and Microsystems & Eurosensors XXXIII (TRANSDUCERS & EUROSENSORS XXXIII)*, 2019, pp. 655–658.

[17] G. Luo, Y. Kusano, and D. Horsley, "Immersion PMUTs Fabricated with a Low Thermal- Budget Surface Micromachining Process," in *2018 IEEE International Ultrasonics Symposium (IUS)*, 2018, pp. 4–7.

[18] Q. Wang, G. L. Luo, Y. Kusano, and D. A. Horsley, "Low Thermal Budget Surface Micromachining Process for Piezoelectric Micromachined Ultrasonic Transducer Arrays With in-Situ Vacuum Sealed Cavities," in *Hilton Head Workshop 2018: A Solid-State Sensors, Actuators and Microsystems*, 2018, pp. 245–248.

[19] M. S. Pandian *et al.*, "Thin film piezoelectric devices integrated on CMOS," in *Proceedings of the 2016 Symposium on Piezoelectricity, Acoustic Waves and Device Applications, SPAWDA 2016*, 2016, pp. 167–170.

[20] H. Bhugra and G. Piazza, Eds., "Piezoelectric MEMS Resonators," in *Microsystems and Nanosystems*, Switzerland: Springer International, 2017.

[21] E. Ledesma *et al.*, "Squared PMUT with enhanced pressure sensitivities," in *Eurosensors 2018*, 2018, p. 925.

[22] M. Olfatnia, Z. Shen, J. M. Miao, L. S. Ong, T. Xu, and M. Ebrahimi, "Medium damping influences on the resonant frequency and quality factor of piezoelectric circular microdiaphragm sensors," *J. Micromechanics Microengineering*, vol. 21, no. 4, 2011.

[23] G. L. Luo *et al.*, "High fill factor piezoelectric micromachined ultrasonic transducers on transparent substrates," in *2017 19th International Conference on Solid-State Sensors, Actuators and Microsystems (TRANSDUCERS)*, 2017, pp. 1053–1056.

[24] S. Umchid, "Spatial Averaging Correction for Ultrasound Hydrophone Calibrations," *Int. J. Appl. Biomed. Eng.*, vol. 9, no. 1, pp. 33–38, 2016.

[25] ONDA Corporation, *Hydrophone Handbook*. CA,USA, 2015.

[26] B. E. Eovino, Y. Liang, and L. Lin, "Concentric PMUT Arrays for Focused Ultrasound and High Intensity Applications," in *2019 IEEE 32nd International Conference on Micro Electro Mechanical Systems (MEMS)*, 2019, pp. 771–774.

[27] X. Jiang *et al.*, "Inter-element coupling effects in pulse-echo ultrasonic fingerprint sensors," in *2017 IEEE 30th International Conference on Micro Electro Mechanical Systems (MEMS)*, 2017, pp. 1192–1195.

[28] J. Muñoz, F. Torres, A. Uranga, V. Tzanov, and N. Barniol, "Monolithical AlN PMUT on pre-processed CMOS substrate," *IEEE Int. Freq. Control Symp.*, pp. 4–5.

[29] Q. Wang, Y. Lu, S. Mishin, Y. Oshmyansky, and D. A. Horsley, "Design , Fabrication and Characterization of Scandium Aluminum Nitride Based Piezoelectric Micromachined Ultrasonic Transducers," *J. Microelectromechanical Syst.*, vol. 26, no. 5, pp. 1132–1139, 2017.

MDPI

Article

Enhancing AlN PMUTs' Acoustic Responsivity within a MEMS-on-CMOS Process

Eyglis Ledesma [ID]**, Ivan Zamora** [ID]**, Arantxa Uranga** [ID]**, Francesc Torres** [ID] **and Núria Barniol *** [ID]

Departament d'Enginyeria Electrònica, Universitat Autònoma de Barcelona, 08193 Bellaterra, Spain; eyglis.ledesma@uab.es (E.L.); ivan.zamora@uab.es (I.Z.); arantxa.uranga@uab.es (A.U.); francesc.torres@uab.cat (F.T.)
* Correspondence: nuria.barniol@uab.cat

Abstract: In this paper, guidelines for the optimization of piezoelectrical micromachined ultrasound transducers (PMUTs) monolithically integrated over a CMOS technology are developed. Higher acoustic pressure is produced by PMUTs with a thin layer of AlN piezoelectrical material and Si_3N_4 as a passive layer, as is studied here with finite element modeling (FEM) simulations and experimental characterization. Due to the thin layers used, parameters such as residual stress become relevant as they produce a buckled structure. It has been reported that the buckling of the membrane due to residual stress, in general, reduces the coupling factor and consequently degrades the efficiency of the acoustic pressure production. In this paper, we show that this buckling can be beneficial and that the fabricated PMUTs exhibit enhanced performance depending on the placement of the electrodes. This behavior was demonstrated experimentally and through FEM. The acoustic characterization of the fabricated PMUTs shows the enhancement of the PMUT performance as a transmitter (with 5 kPa V^{-1} surface pressure for a single PMUT) and as a receiver (12.5 V MPa^{-1}) in comparison with previously reported devices using the same MEMS-on-CMOS technology as well as state-of-the-art devices.

Keywords: PMUT; ultrasound; CMOS; MEMS-on-CMOS; acoustic responsivity; AlN; piezoelectric transducers; PMUT-on-CMOS

check for
updates

1. Introduction

Currently, there is a growing demand for miniaturized devices capable of producing and sensing ultrasonic signals in a very efficient manner. There is a broad range of applications that use ultrasonics due to its non-invasive approach and small size including: minimally invasive intravascular medical imaging [1], ultrasonic powering of miniaturized implantable medical devices for in vivo and in situ physiological monitoring [2,3], systems for selective neural stimulation with an ultrasound signal [4], and fingerprints for biometric identification [5]. Some of these applications demand compact, minute systems. Piezoelectrical micromachined ultrasound transducers (PMUTs), based on out-of-plane micrometric flexural membranes are devices that can meet these requirements, thus replacing bulky piezoceramics that are difficult to compact, and result in low yield of the fabricated devices due to fabrication complexity. PMUTs composed of a multilayer laminate structure where at least one layer is made of a piezoelectric material, benefit from the robust fabrication processes used in MEMS technology, and provide high yields and scalable designs [6–9]. Moreover, PMUTs monolithically fabricated over pre-processed CMOS wafers enhance the obtention of very compact systems, are highly programmable if required and exhibit a high fabrication yield. Despite these benefits, some constraints due to the poor compatibility of PMUTs with the CMOS process, can limit the performance of ultrasonic signal processing. In addition, the CMOS process is limited to technologies that allow electrical contact from its last metal layer to the MEMS device within a specific post-process. Up until now, most of the reported PMUTs over CMOS are based on two-wafer bonding processes, in which the wafer with the PMUT (either AlN or PZT) is bonded to a CMOS wafer with analog

front-end circuitry [10–13]. Despite the feasibility of this approach, the complexity of the bonding process and the limitations of the achievable fill factor impose some limitations. So far, we have already presented a system with AlN PMUTs monolithically integrated with a dedicated analog front-end circuitry for a single-pixel ultrasonic transducer [14,15]. Although we have demonstrated the viability and workability of this approach, in this paper we develop some guidelines for the optimization of the PMUTs over the CMOS and compare the results with previous ones.

The paper is divided into four sections. Section 2 presents the main parameters for the optimization of the acoustic pressure output and mechanical simulations to determine the optimal parameters of the PMUT layers. Section 3 is dedicated to the experimental electrical and acoustic characterization of the PMUTs to establish the device's performance. In Section 4, a discussion and a comparison with the state-of-the-art PMUTs are provided.

2. Materials and Methods: Optimization of PMUT Transducer

PMUTs can act as acoustic transmitters and acoustic receivers. If an electrical field is applied at both sides of the membrane, a transverse stress due to the inverse piezoelectrical effect at the piezoelectrical layer is produced and bending of the membrane out-of-plane is achieved, thus producing acoustic output pressure in the media (transmitter). If an input acoustic field is applied to the membrane, it will be bent and produce a transverse stress on the piezoelectrical layer; consequently, some electrical field is produced at the sides of the membrane due to the direct piezoelectrical effect of the piezoelectrical layer (receiver). For efficient production of the acoustic or electrical signal as a transmitter or a receiver, the membrane should be excited in its first out-of-plane flexural resonant mode, which relates the dimensions, layers, and materials of the PMUT with the desired resonant frequency [16]. In this paper we focus on PMUTs working in a liquid environment in the MHz range.

To optimize the size and thickness of PMUT devices (maximum acoustic pressure output as a transducer and maximum electrical signal as a receiver), it is convenient to define a cost function or figure of merit to be optimized. For this purpose, we have defined a figure of merit (FoM) as the product of the generated output acoustic pressure, P, and generated voltage at the PMUTs electrodes, V_r. This FoM should be maximized to enhance the PMUT's performance. Both parameters, P and V_r, are analyzed below.

The axial pressure amplitude at a distance z, P(z), in the far field region ($z > R_0$, being R_0, Rayleigh distance = S/λ, where S is the PMUT surface and λ is the wavelength of the acoustic signal in the propagation media, $\lambda = c/f_0$, f_0 = resonance frequency, c = sound speed) is given by Equation (1), where P_0 is the pressure at the surface of the PMUT [16]. This pressure P_0 is proportional to the membrane velocity, $u_0 = 2\pi d_0 f_0$ (where d_0 is the membrane displacement) and the acoustic impedance of the media, $Z_0 = \rho_{med}c$ (where ρ_{med} is the mass density of the acoustic media).

$$P(z)_{\text{far field}} = P_o R_o/z = u_0 Z_0 S/\lambda/z = u_0 f_0 \rho_{med} S/z = 2\pi d_0 (f_0)^2 \rho_{med} S/z \qquad (1)$$

According to Equation (1), high resonance frequencies and large membrane displacements will benefit the acoustic pressure output of equal sized PMUTs. The membrane displacement for a PMUT is directly related to the elastic constant, k_m, of the structure and the electro-mechanical coupling factor, η (as shown in Equation (2), where V_{in} is the actuation voltage applied between the top and bottom electrodes). Thin structures will produce larger displacement at the expense of resonating with smaller frequency because these structures will have smaller elastic constants. Analogously, when an acoustic pressure, P_a, is applied over the PMUT membrane, the output voltage between the top and bottom electrodes of the membrane, V_r, will be proportional to the membrane displacement, d_r (where r refers to receiver) according to Equation (3). In both cases it is necessary to compute the electro-mechanical coupling factor, η (Equation (4)) [16], which will quantify the conversion efficiency between the applied or received voltage and the membrane displacement. Because the PMUT is resonating, the dynamic displacement of

the membrane, $d = Q \times d_0$ should be used, where Q is the resonator quality factor. Both displacements, static and dynamic, will be in the same range due to the high damping in the liquid environment, which reduces the Q factor to values between 1 and 3, as will be shown in the Experimental section, and it is also reported in [17].

$$d_0 = \eta V_{in}/k_m \tag{2}$$

$$d_r = P_a S/k_m, \tag{3}$$

$$V_r = d_r k_m/\eta = P_a S/\eta$$

$$\eta = 0.5 e_{31,f} z_p I_{piezo} \tag{4}$$

In Equation (4), $e_{31,f}$ is the transverse effective piezoelectrical coefficient of the piezo-electrical layer, z_p is the distance from the mid-plane of the piezoelectric layer to the neutral axis, which depends on the multilayer lattice structure and I_{piezo} is an integral that depends on the mode shape and electrode size, which equals 5.73 for an optimized inner electrode in a square membrane [18].

The resonance frequency, f_{01}, Equation (5), in a multilayered membrane depends on the resonance mode, $\lambda_{01}^2 = 35.99$ for the first out-of-plane flexural mode in square-shaped membranes [19], the membrane side, a, the flexural rigidity, D, given in Equation (6) and on the mass per unit area or surface density, μ, Equation (7). Although the membrane resonance frequency will depend linearly on the thickness, and inversely on the square of the size of the membrane, it is difficult to analyze the dependence of the resonance frequency on thickness variations in multilayered membranes with different physical properties (i.e., plate modulus, E_{11}, and mass density, ρ) [16].

$$f_{01} = \frac{\lambda_{01}^2}{2\pi a^2} \sqrt{\frac{D}{\mu}}, \tag{5}$$

$$D \approx \frac{1}{3} \cdot \sum_{n=1}^{N} E_{11,n} \cdot (\overline{h_n}^3 - \overline{h_{n-1}}^3), \tag{6}$$

where $\overline{h_n} = h_n - Z_{NA}$, is the distance from the top of the n-th layer to the neutral axis, Z_{NA} and h_n is the relative height between the bottom device and the top of the n-th layer.

$$\mu_n = \sum_{n=1}^{N} t_n \cdot \rho_n \tag{7}$$

where t_n is the thickness of the n-th material layer.

Due to the complexity of the multilayer laminate structure for analytical computation of the above equations, finite element models (FEM) were used to evaluate the performance of the PMUT parameters of interest: displacement, d_0; frequency, f_0; membrane velocity u_o and output voltage, V_r; and the defined figure of merit, FoM = P * V_r.

In the MEMS-on-CMOS technology considered [20,21], the PMUT is composed of four layers of different materials: AlN for the piezoelectrical layer, Si_3N_4 as the elastic layer, and Al for the top and bottom electrodes. Figure 1 shows the schematic cross section of the PMUT with two top electrodes: an inner or central electrode (CENT) and outer or ring electrode (RING), and one bottom electrode (BOT).

In a first approximation, an axisymmetric model of a circular PMUT was assumed and mechanic–acoustic simulations were done by means of the COMSOL finite element software. The thickness of the Si_3N_4 passive layer as well as the AlN piezoelectrical layer was swept from 1 to 2 μm and 0.5 to 1.5 μm, respectively, to obtain an enhanced acoustic performance in an equal-sized PMUT. The physical parameters for each of the PMUT's layers used in the model are listed in Table 1. In the simulations, the PMUT was immersed in a liquid medium, in this case FC-70, in accordance with the experimental characterization discussed in the next sections.

(a)

(b)
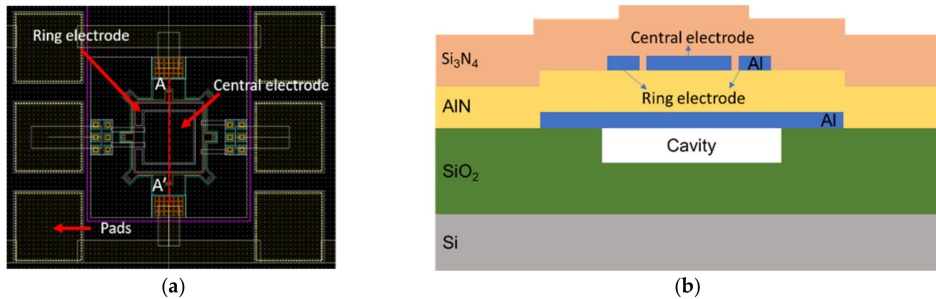
Figure 1. (**a**) Layout of the 80 μm × 80 μm square AlN PMUT with two top electrodes, (**b**) AA' cross-section of AlN PMUT.

Table 1. Material properties and thicknesses used in COMSOL-FEM simulations.

PMUT Layer	Properties			Geometric Dimensions	
	Mat.	Young's Modulus (GPa)	Density (kg m^{-3})	Side (μm)	Thickness (μm)
Substrate	SiO$_2$	70	2200	100	2
Bottom Electrode (BOT)	Al	70	2700	86	0.4
Piezoelectric	AlN [1]	279	3230	100	0.5 to 1.5
Top Electrode (CENT)	Al	70	2700	56.6	0.35
Top Electrode (RING)				External side: 77 Internal side: 60.6	0.4
Passive	Si$_3$N$_4$	250	3100	100	1 to 2

[1] The piezoelectric coefficients e_{33} and e_{31} used in COMSOL are 1.55 C m^{-2} and -0.6 C m^{-2}, respectively.

In Figure 2, the resonance frequency and normalized displacement as a function of the piezoelectrical layer thickness is shown (with a passive layer of Si$_3$N$_4$ with a thickness of 1.5 μm). As expected, thinner membranes produce larger displacements at the expense of lower resonant frequencies. In fact, resonance frequency is linearly dependent on the membrane thicknesses as is inferred from Equation (5) [22]. The dependence of resonance frequency and normalized displacement (in terms of applied voltage) as a function of the AlN and Si$_3$N$_4$ layer thicknesses are shown in Figure 3. This figure shows that the variation in the displacement is greater than a factor of ×77 (from 34 nm V^{-1} at minimum thicknesses to 0.44 nm V^{-1} at maximum thicknesses) while the variation in frequency does not change by more than a factor of ×3.3 (from 3.14 MHz at the maximum thicknesses to 0.95 MHz at the minimum). Accordingly, it is expected that the output pressure is maximum with the minimum thickness since the sound pressure depends on the normalized displacement and the square frequency (see Equation (1)).

On the other hand, we are also interested in the PMUT as a receiver, thus we also simulated the normalized output voltage at the central top electrode when an acoustic pressure is applied on the PMUT surface (Figure 4). In all these simulations, the size of the top central electrode was optimized to have the maximum out-of-plane membrane displacement [18], and it was fixed for all the thicknesses. As shown in Figure 4, a maximum terminal voltage was generated at an AlN thickness close to 0.8 μm and Si$_3$N$_4$ thickness of 1 μm (black curve).

Once the main parameters involved in the PMUT performance as transmitter and receiver have been obtained, the figure of merit can be computed. For this computation we assumed that the acoustic pressure is proportional to $d_0 \times f^2$, considering equal sized PMUTs according to Equation (1). In Figure 4b, the computed FoM = $d_0 \times f^2 \times V_r$ defines an optimal point with an AlN thickness close to 0.6 μm and with a Si$_3$N$_4$ thickness of 1 μm.
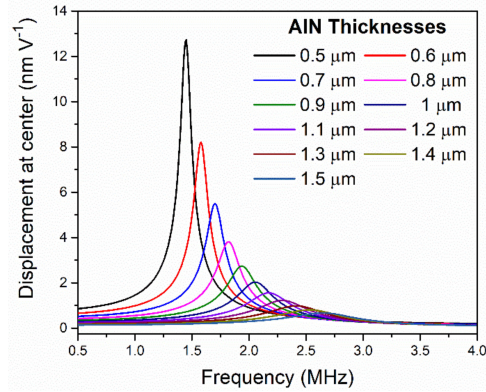
Figure 2. Simulated frequency response of the PMUT immersed in liquid with different AlN layer thicknesses. The normalized displacement in respect to the applied voltage is shown.
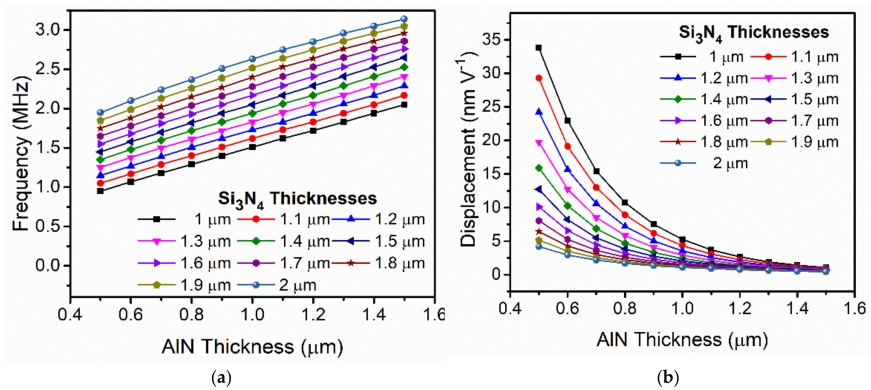
Figure 3. Simulated resonance frequency (**a**) and normalized dynamic displacement (**b**) of an equal-sized PMUT sweeping the AlN layer thicknesses and for different Si_3N_4 layer thicknesses as parameters in a liquid environment.
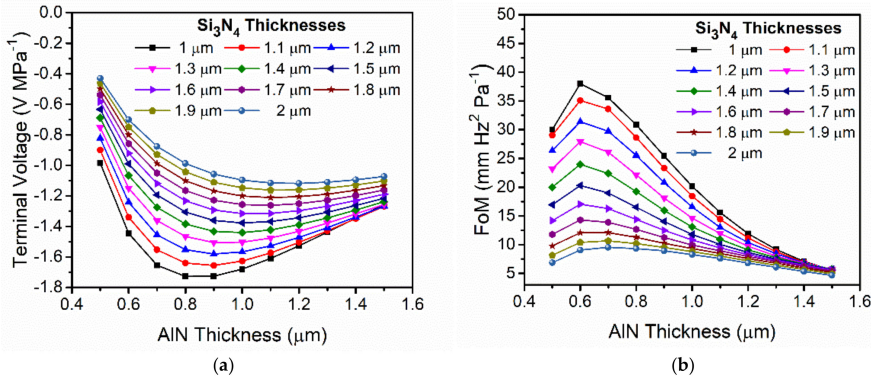
Figure 4. (**a**) Simulated normalized terminal voltage when an acoustic pressure is applied over the surface in a liquid environment. (**b**) Computed FoM = $d_0 \times f^2 \times V_r$. Equal-sized PMUTs were considered.

Once the optimal thicknesses for the piezoelectrical layer, AlN, and the passive layer, Si_3N_4 were defined, a theoretical comparison of the PMUT static behavior as a transmitter considering the two top electrodes was done. Figure 5 shows the comparison between two piezoelectrical layer thicknesses with a fixed passive layer thickness (Si_3N_4, 1.5 μm) in terms of normalized displacement as a function of the inner electrode side. Excitation of the membrane with the inner or the outer electrode achieves different deflections of the membrane because the outer electrode width is reduced from the optimal one, to incorporate the required gap between the inner and outer electrodes (2 μm) and the distance between the cavity and metal layer according to the technological rules for the PMUT fabrication (see schematic of the PMUT layout in the inset in Figure 5). From this static displacement, the displacement achieved with the 0.6 μm AlN was almost three times larger than with a thicker 1.3 μm AlN thickness, as expected.
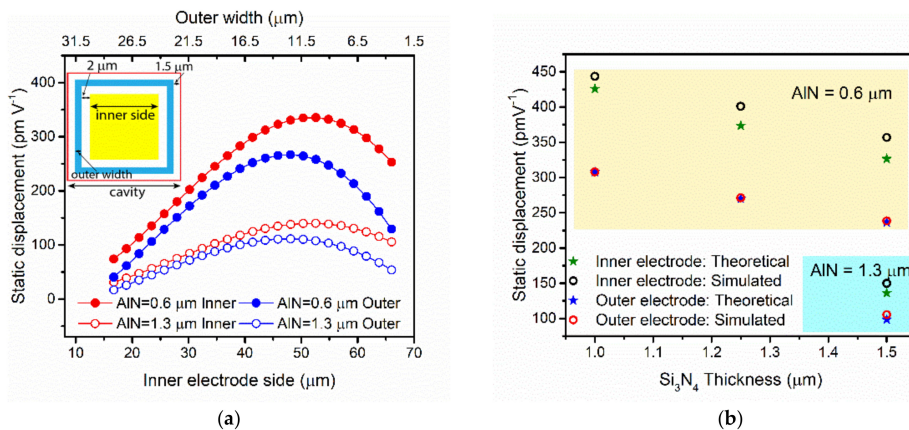
Figure 5. (**a**) Theoretical static displacement for two different AlN thicknesses actuating the PMUT with the inner (yellow square in the PMUT schematic top-view inset) or outer (blue ring in the inset) electrodes. Full circles indicate the 0.6 mm AlN layer, while empty circles correspond to the 1.3 mm AlN layer. (**b**) Theoretical and simulated static displacement for the proposed devices with different material layer thicknesses.

Finally, to predict more realistic PMUT behaviors, 3D COMSOL simulations considering all the geometric layout and material's layer thicknesses for the PMUT were performed. Figure 5b shows good agreement between the theoretical values computed for both electrodes: there is no difference between the theoretical and simulation results for the static displacement when the actuation is made using the outer electrodes and with a small difference with the inner electrode. From Figure 5b, it is also clear that bigger displacements are obtained with inner electrode actuation, with this difference being higher in the 0.6 μm AlN PMUT (yellow area). The main PMUT characteristics in liquid for the different proposed thicknesses are quantified in Table 2.

Several conclusions can be extracted from the results shown in Table 2. Thinner passive layers enhance the performance as a sensor but slightly decrease the output achievable pressure, mainly due to the decrease in the resonance frequency (note that the output pressure depends quadratically on the frequency according to Equation (1)). Despite the decrease in the output pressure, the FoM (considering both transmitting and receiving PMUT system) is higher for thinner PMUTs. Moreover, the performance of thicker PMUTs (i.e., 1.3 μm AlN + 1.5 μm Si_3N_4, was also simulated, obtaining: f = 2.48 MHz, d = 450 pm V^{-1}, V_r = 1.34 V MPa^{-1} (normalized voltage at inner electrode), corresponding to a FoM less than 3.71 Hz^2 m kPa^{-1}), which is a factor of ×2.2 lower than that reported in the first column of Table 2, which clearly highlights the benefits of using thinner piezoelectrical layers.

Table 2. Simulated performance for different Si_3N_4 layer thicknesses for a PMUT with 0.6 μm AlN piezoelectrical layer using the inner or outer electrodes in liquid.

Si_3N_4 Thickness	1 μm		1.25 μm		1.5 μm	
Electrode	**Inner**	**Outer**	**Inner**	**Outer**	**Inner**	**Outer**
Frequency, f (MHz)	1.36		1.58		1.8	
Displacement, d (pm V^{-1})	2309	1539	1809	1175	1431	914
$d \times f^2$ (m V^{-1} Hz^2)	4271	2846	4516	2933	4636	2961
Terminal voltage [a], Vr (V MPa^{-1})	1.91	1.78	1.73	1.55	1.54	1.35
FoM (Hz^2 m kPa^{-1})	8.15	5.06	7.81	4.55	7.14	3.99

[a] Normalized value when 1 Pa is applied over PMUT surface.

3. Experimental Results

3.1. PMUTs Fabrication and Electrical Characterization

According to the optimized piezoelectrical layer thickness (0.6 μm AlN), a set of PMUTs with three Si_3N_4 thicknesses (1 μm, 1.25 μm and 1.5 μm) were fabricated using the MEMS-on-CMOS SilTerra technology. The results were compared with a previously fabricated PMUT with a 1.3 μm AlN piezoelectric material [18]. The MEMS-on-CMOS process from Silterra [20,21], basically consists of: (a) deposition and patterning of an stack of Al metal electrodes (top and bottom) and a physical vapor deposited AlN layer on top of the last CMOS layer; (b) releasing of the membrane through pre-defined holes around the PMUT structure; and (c) deposition of the Si_3N_4 elastic layer deposited with a low temperature plasma-enhanced chemical vapor deposition (PECVD) process, which allows the holes to be sealed for liquid operation.

Next, the electrical characterization in air was performed and compared with COMSOL and the analytical expression of the resonance frequency. Figure 6 corresponds to the experimental frequency response for the PMUT with 0.6 μm AlN and 1.25 μm Si_3N_4 thicknessess, an optical image is shown as an inset in the characterization set-up (Figure 6a).

From Figure 6b, an effective electromechanical coupling factor, $k_{eff}^2 = 1.14\%$ was computed according to Equation (8) [23,24], between the inner and outer electrodes where $f_s = 4.866$ MHz (resonance) and $f_p = 4.894$ MHz (antiresonance or parallel resonance). In Table 3, the resonance frequencies for the three squared PMUTs are shown together with those computed by Equation (5), and the FEM simulated ones, and show a good match.

$$k_{eff}^2 = (f_p^2 - f_s^2)/f_p^2 \tag{8}$$

(**a**)   (**b**)
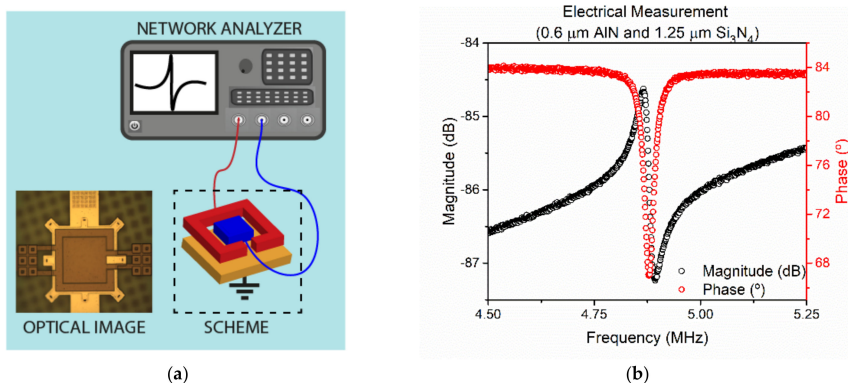
Figure 6. (**a**) Schematic set-up for the electrical characterization in air and (**b**) frequency response (magnitude and phase) for the PMUT with 0.6 μm AlN and 1.25 μm Si_3N_4 in air.

Table 3. Resonance frequencies in air for the PMUTs with different layer thicknesses.

Layer Thickness		Resonance Frequency (MHz)		
AlN (µm)	Si$_3$N$_4$ (µm)	Experimental	COMSOL	Analytical
0.6	1	4.47	4.19	4.18
0.6	1.25	4.87	4.67	4.69
0.6	1.5	5.21	5.14	5.20

3.2. Acoustic Characterization

The PMUTs were characterized as an acoustic transmitter and receiver in a liquid environment (FC-70, sound speed c = 689 m s^{-1} and mass density, ρ = 1940 kg m^{-3}). As transmitters, the PMUTs were driven by four cycles of a 22V$_{pp}$ harmonic signal generated by the signal generator (Keysight 81150A, Sunnyvale, CA, USA). Both top electrodes (inner and outer) were independently polarized for a complete characterization with the bottom electrode grounded. The acoustic pressure was measured with a commercial hydrophone from ONDA, Sunnyvale, CA, USA (HNC-1500) and displayed on an oscilloscope (Keysight DSOX3054A, Sunnyvale, CA, USA). Frequency and hydrophone micrometric positioning over the PMUT were manually tuned to maximize the receiving signal. Note that for liquid operation, the added mass loading effect should be considered [25], which will lower the resonance frequency from the 4–5 MHz found in air to the 1–2 MHz range as expected from the results shown in Figure 3.

The signals received by the hydrophone exciting the PMUT with 0.6 µm AlN and 1.25 µm Si$_3$N$_4$ thicknessess at 1.6 MHz are shown in Figure 7. Unexpectedly, driving the inner electrode (Figure 7a) produces lower amplitude signals than driving the outer electrode (Figure 7b). FEM simulations from the previous section predicted the contrary as the size of the electrodes are complementary and were chosen to maximize the movement. This behavior can be attributed to the additional curvature produced on the PMUT surface by the residual stress from the piezoelectric, passive layer and electrodes during the fabrication. The physical characterization of the surface profiles of the PMUTs using a surface profilometer confirmed that thinner membranes are more prone to bending (Figure 8) [26,27]. The maximum central height for the 0.6 µm AlN and 1.25 µm Si$_3$N$_4$ thicknessess was 1 µm (see Figure 8) while the same feature decreased to 200 nm in the case of 1.3 µm AlN and 1.5 µm Si$_3$N$_4$. Several FEM simulations were done with same-sized membranes with two top electrodes and two different curvatures (maximum central heights of 1 µm and 400 nm). Figure 9 shows the simulated displacements, which are higher when the outer electrode is driven in both cases and with higher movement when the central height is bigger, which is in line with the obtained voltage amplitudes shown in Figure 7.

Table 4 summarizes the performance of the fabricated PMUTs. The output pressure was measured at 2 mm using the HNC-0200 ONDA hydrophone considering its sensitivity at the operation frequency and under the same voltage driving conditions (four cycles and 22 Vpp). From the normalized acoustic pressure in respect to applied voltage, the normalized surface pressure (P$_0$ = P × distance/R$_0$, where R$_0$ is the Rayleigh distance already defined) can be calculated. This normalized surface pressure is an important parameter for the assessment of the performance of the presented PMUTs as transmitters and allows the comparison with the state-of-the-art PMUTs, as will be discussed in Section 4. As expected, thinner PMUTs with 0.6 µm AlN result in higher surface pressure, being almost a factor of 2 in comparison with the thicknesses used in previous works using the same technology. In addition, the influence on the achieved surface pressure is weakly related to the Si$_3$N$_4$ layer thicknesses.

(**a**) (**b**)
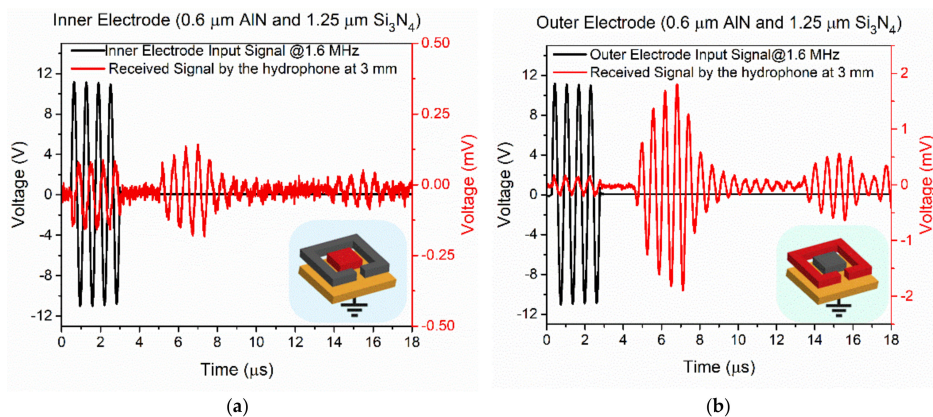
Figure 7. Time response of the acoustic signal produced by the 0.6 μm AlN and 1.25 μm Si_3N_4 thicknesses PMUT driving (**a**) the inner electrode, and (**b**) the outer electrode (in both cases, the bottom electrode is grounded). Left axis is the applied voltage to the PMUT (black), right axis is the voltage received by the hydrophone (red). Two echoes were taken with the hydrophone situated at 3 mm over the PMUT surface.

(a) (b)
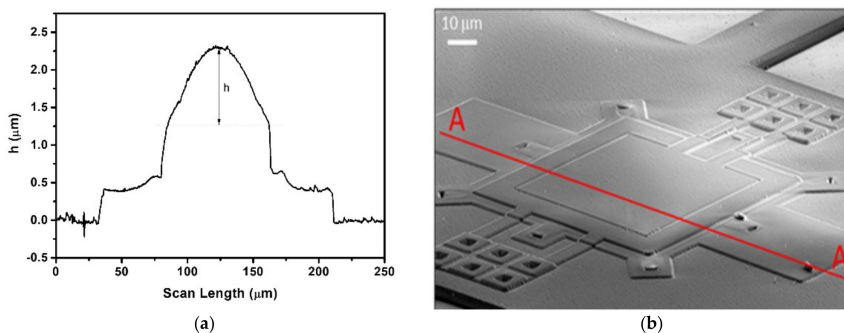
Figure 8. (**a**) Profile for curvature characterization of the 0.6 μm AlN and 1.25 μm Si_3N_4 PMUT over the red line in the (**b**) SEM image, showing a h = 1 μm height in the middle of the membrane.

(**a**) (**b**)
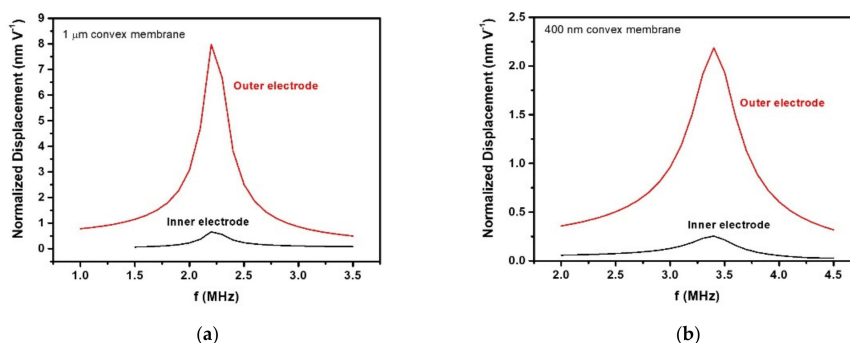
Figure 9. FEM simulations to compare displacement as a function of the driving electrode (inner or outer) when a convex membrane with a maximum height at the center equal to 1 μm (**a**) and 400 nm (**b**) was considered.

Table 4. Experimental performance characterization of the PMUT as an ultrasound transmitter and receiver using the outer electrode for electrical actuation/sensing. The last column shows computed FoM.

Layer Thickness		Frequency (MHz)	Normalized Pressure @ 2 mm (Pa V^{-1})	P_0, Normalized Surface Pressure (kPa V^{-1})	V_r, Received Voltage (mV$_{pp}$)	FoM P_0 V_r (Pa)
AlN (µm)	Si$_3$N$_4$ (µm)					
0.6	1	1.5	33.8	4.9	2.8	13.7
0.6	1.25	1.6	36.2	4.8	2.5	12
0.6	1.5	2	33.4	3.6	2	7.2
1.3	1.5	2.4	27.4 *	2.4	<1	<2.4

* PMUT driving voltage in this case was a 32 Vpp squared signal instead of 22 V$_{pp}$ sine signal.

The PMUTs devices were also characterized as sensors using a commercial ultrasound transducer (OPTEL) at a 3 mm distance in the liquid environment. The transducer was excited with four cycles at the central resonance frequency of each of the PMUTs, with four cycles and 22 V$_{pp}$. The generated signal in the outer electrode directly acquired by the oscilloscope is shown in Figure 10 for the case of a 0.6 µm AlN and 1.25 µm Si$_3$N$_4$ PMUT. The same measurements under the same conditions were done for all the PMUTs to complete the comparison (Table 4, Received voltage column). The amplitudes decrease for thicker piezoelectric layers, with a weak dependence in respect to the thickness of the passive layer as was already seen in the simulations. Finally, the FoM was computed in this table, and demonstrated better performance for the thin PMUTs as was already predicted by the FEM simulations.
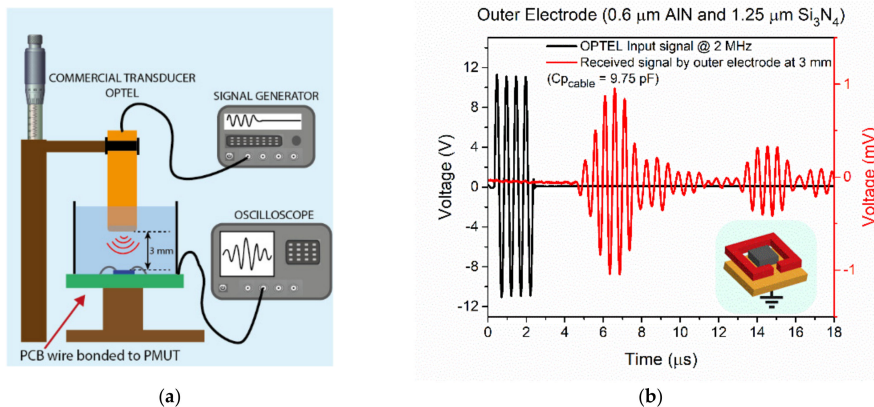
Figure 10. (**a**) Schematic set-up for the acoustic characterization as sensor and (**b**) characterization of the transient signal received by the 0.6 µm AlN and 1.25 µm Si$_3$N$_4$ PMUT acting as an acoustic sensor when a commercial ultrasound transducer is used.

4. Discussion and Conclusions

As was shown in the previous sections, the presented PMUTs with reduced thicknesses for the piezoelectrical and elastic layer, achieve better performance as transmitters as well as receivers in comparison to PMUTs of equal size with the same technology but larger thicknesses. In this section, we compare the PMUTs' performance with several recently published papers on PMUTs. For convenience, the receiving sensitivity will be used. The receiving sensitivity is computed considering the calibration of the used ultrasound transducer at distances of 3 mm and 2 MHz [18].

A summary is given in Table 5. In comparing the same technological process, which follows a MEMS-on-CMOS process and exactly the same PMUT layout [18], the presented

PMUTs exhibit bigger transmission and receiving sensitivities, with an overall x4 enhancement factor. This enhancement was also demonstrated in comparison with other PMUTs based on AlN, either with CMOS compatible processes [28] for the fabrication of PMUTs together with CMOS circuitry or with non-CMOS compatible processes [5] in which complex bonding between PMUT devices and CMOS circuitry are required. On the other hand, the presented PMUTs offer lesser performance in comparison with PZT devices [29] as transmitters, due to the high piezoelectrical constant of this material [6]. Despite this, the FoM is only a factor of $\times 1.8$ smaller, which can be overcome by considering the compactness of the system due to the monolithic integration with the CMOS circuitry in our process. Note also that only simulated results are given for the receiver sensitivity in the case in [29]. In summary, the thinner PMUT with 0.6 μm AlN thickness and 1 μm Si_3N_4 thicknesses presented in this work, demonstrates higher acoustic pressure production along with higher receiver sensitivity, and enhances the applicability of PMUTs on CMOS for ultrasound systems that need to be miniaturized.

Table 5. Comparison of PMUT performance in liquid operation.

Parameters	[5] 2017	[28] 2018	[29] 2018	[18] 2020	This Work
Transducer	AlN 30 μm × 43 μm	AlN 50 μm × 50 μm	PZT 80 μm × 80 μm	AlN [a] 80 μm × 80 μm	AlN 80 μm × 80 μm
Array/single	Array 1 × 56	Array 3 × 20	Single	Single	Single
Process	Bonded-to-CMOS	CMOS compatible	Bonded-to-CMOS	MEMS-on-CMOS	MEMS-on-CMOS
ST (kPa V^{-1})	2.95	2.93	27 [b]	1.9	4.9
SR (V MPa^{-1})	2 [c]	510 [d]	4 [e]	7.6	12.5
FoM ($\times 10^3$)	5.9		108	14.4	61

[a] Clampled-clamped square PMUT (same layout as presented here). [b] Estimated according to the data provided in [29] and considering ST = P × distance/R_0 = 27 kPa V^{-1} if experimental data are used (extracted from [29]: Pressure = 8 kPa/30 V = 0.3 kPa V^{-1}, distance = 5 mm, and R_0 = $(80 \, \mu m)^2/\lambda$ = 55.6 μm where λ = c/f = 1500 m s^{-1}/13 MHz = 115 μm). [c] Value obtained together with the custom CMOS ASIC [5]. [d] In reception 10 V pC^{-1} charge amplifier was used [28]. [e] PZFlex simulations [29].

References

1. Wang, J.; Zheng, Z.; Chan, J.; Yeow, J.T.W. Capacitive micromachined ultrasound transducers for intravascular ultrasound imaging. *Microsyst. Nanoeng.* **2020**, *6*, 73. [CrossRef] [PubMed]
2. Shi, C.; Andino-Pavlovsky, V.; Lee, S.A.; Costa, T.; Elloian, J.; Konofagou, E.E.; Shepard, K.L. Application of a sub-0.1-mm^3 implantable mote for in vivo real-time wireless temperature sensing. *Sci. Adv.* **2021**, *7*, 1–10. [CrossRef] [PubMed]
3. Hosseini, S.; Laursen, K.; Rashidi, A.; Mondal, T.; Corbett, B.; Moradi, F. S-MRUT: Sectored-Multiring Ultrasonic Transducer for Selective Powering of Brain Implants. *IEEE Trans. Ultrason. Ferroelectr. Freq. Control* **2021**, *68*, 191–200. [CrossRef] [PubMed]

4. Seok, C.; Adelegan, J.O.; Biliroglu, A.O.; Yamaner, F.Y.; Oralkan, O. Wearable Ultrasonic Neurostimulator—Part II: A 2D CMUT Phased Array System with a Flip-Chip Bonded ASIC. *IEEE Trans. Biomed. Circuits Syst.* **2021**, *15*, 705–718. [CrossRef] [PubMed]

5. Jiang, X.; Lu, Y.; Tang, H.Y.; Tsai, J.M.; Ng, E.J.; Daneman, M.J.; Boser, B.E.; Horsley, D.A. Monolithic ultrasound fingerprint sensor. *Microsyst. Nanoeng.* **2017**, *3*, 1–8. [CrossRef] [PubMed]

6. Jung, J.; Lee, W.; Kang, W.; Shin, E.; Ryu, J.; Choi, H. Review of piezoelectric micromachined ultrasonic transducers and their applications. *J. Micromech. Microeng.* **2017**, *27*, 113001. [CrossRef]

7. Sun, C.; Shi, Q.; Yazici, M.C.; Kobayashi, T.; Liu, Y.; Lee, C. Investigation of Broadband Characteristics of Multi-Frequency Piezoelectric Micromachined Ultrasonic Transducer (MF-pMUT). *IEEE Sens. J.* **2019**, *19*, 860–867. [CrossRef]

8. Wang, H.; Yang, H.; Jiang, H.; Chen, Z.; Feng, P.X.-L.; Xie, H. A multi-frequency PMUT array based on ceramic PZT for endoscopic photoacoustic imaging. In Proceedings of the 2021 21st International Conference on Solid-State Sensors, Actuators and Microsystems (Transducers), Orlando, FL, USA, 20–24 June 2021. [CrossRef]

9. Sadeghpour, S.; Ingram, M.; Wang, C.; D'Hooge, J.; Kraft, M. A 128x1 phased array piezoelectric micromachined ultrasound transducer (PMUT) for medical imaging. In Proceedings of the 2021 21st International Conference on Solid-State Sensors, Actuators and Microsystems (Transducers), Orlando, FL, USA, 20–24 June 2021. [CrossRef]

10. Jiang, X.; Tang, H.-Y.; Lu, Y.; Ng, E.J.; Tsai, J.M.; Boser, B.E.; Horsley, D.A. Ultrasonic Fingerprint Sensor with Transmit Beamforming Based on a PMUT Array Bonded to CMOS Circuitry. *IEEE Trans. Ultrason. Ferroelectr. Freq. Control* **2017**, *64*, 1401–1408. [CrossRef] [PubMed]

11. Lu, Y.; Tang, H.; Fung, S.; Wang, Q.; Tsai, J.M.; Daneman, M.; Boser, B.E.; Horsley, D.A. Ultrasonic fingerprint sensor using a piezoelectric micromachined ultrasonic transducer array integrated with complementary metal oxide semiconductor electronics. *Appl. Phys. Lett.* **2015**, *106*, 263503. [CrossRef]

12. Lee, J.; Lee, K.-R.; Eovino, B.E.; Park, J.H.; Liang, L.Y.; Lin, L.; Yoo, H.-J.; Yoo, J. A 36-Channel Auto-Calibrated Front-End ASIC for a pMUT-Based Miniaturized 3-D Ultrasound System. *IEEE J. Solid-State Circuits* **2021**, *56*, 1910–1923. [CrossRef]

13. Costa, T.; Shi, C.; Tien, K.; Elloian, J.; Cardoso, F.A.; Shepard, K.L. An Integrated 2D Ultrasound Phased Array Transmitter in CMOS with Pixel Pitch-Matched Beamforming. *IEEE Trans. Biomed. Circuits Syst.* **2021**, *15*, 731–742. [CrossRef] [PubMed]

14. Zamora, I.; Ledesma, E.; Uranga, A.; Barniol, N. Monolithic Single PMUT-on-CMOS Ultrasound System with +17 dB SNR for Imaging Applications. *IEEE Access* **2020**, *8*, 142785–142794. [CrossRef]

15. Ledesma, E.; Zamora, I.; Uranga, A.; Barniol, N. Monolithic PMUT on CMOS ultrasound system for single pixel acoustic imaging. In Proceedings of the 2021 IEEE 34th International Conference on Micro Electro Mechanical Systems (MEMS), Gainesville, FL, USA, 25–29 January 2021.

16. Horsley, D.; Lu, Y.; Rozen, O. Flexural Piezoelectric Resonators. In *Piezoelectric MEMS Resonators*; Bhugra, H., Piazza, G., Eds.; Microsystems and Nanosystems; Springer International Publishing: Cham, Switzerland, 2017; pp. 153–167. [CrossRef]

17. Wang, X.-B.; He, L.-M.; Ma, Y.-C.; Liu, W.-J.; Xu, W.-J.; Ren, J.-Y.; Riaud, A.; Zhou, J. Development of Broadband High-Frequency Piezoelectric Micromachined Ultrasonic Transducer Array. *Sensors* **2021**, *21*, 1823. [CrossRef] [PubMed]

18. Ledesma, E.; Zamora, I.; Uranga, A.; Barniol, N. Tent-plate AlN PMUT with a piston-like shape under liquid operation. *IEEE Sens. J.* **2020**, *20*, 11128–11137. [CrossRef]

19. Blevins, R.D. Formulas for Natural Frequency and Mode Shape. Van Nostrand Reinhold Co., Ed.; Litton Educational Publishing, Inc.: New York, NY, USA, 1979.

20. Silterra. MEMS-on-CMOS. Available online: www.silterra.com (accessed on 10 October 2021).

21. Soundara Pandian, M.; Ferrer, E.M.; Tay, W.S.; Madhaven, V.; Kantimahanti, A.K.; Sobreviela, G.; Uranga, A.; Barniol, N. Thin film piezoelectric devices integrated on CMOS. In Proceedings of the 2016 Symposium on Piezoelectricity, Acoustic Waves, and Device Applications (SPAWDA), Xi'an, China, , 21–24 October 2016; pp. 167–170.

22. Lu, Y.; Heidari, A.; Horsley, D.A. A High Fill-Factor Annular Array of High Frequency Piezoelectric Micromachined Ultrasonic Transducers. *J. Microelectromech. Syst.* **2015**, *24*, 904–913. [CrossRef]

23. *IEEE Standard on Piezoelectricity, Standard 3237638 and 176-1987*; IEEE Ultrasonics and Frequency Control Society: New York, NY, USA, 1987; Available online: https://ieeexplore.ieee.org/document/26560 (accessed on 10 October 2021).

24. Lu, R.; Li, M.-H.; Yang, Y.; Manzaneque, T.; Gong, S. Accurate Extraction of Large Electromechanical Coupling in Piezoelectric MEMS Resonators. *J. Microelectromech. Syst.* **2019**, *28*, 209–218. [CrossRef]

25. Ledesma, E.; Zamora, I.; Uranga, A.; Barniol, N. Multielement Ring Array Based on Minute Size PMUTs for High Acoustic Pressure and Tunable Focus Depth. *Sensors* **2021**, *21*, 4786. [CrossRef] [PubMed]

26. Wang, T.; Lee, C. Zero-Bending Piezoelectric Micromachined Ultrasonic Transducer (pMUT) With Enhanced Transmitting Performance. *J. Microelectromech. Syst.* **2015**, *24*, 2083–2091. [CrossRef]

27. Hajati, A.; Latev, D.; Gardner, D.; Hajati, A.; Imai, D.; Torrey, M.; Schoeppler, M. Three-dimensional micro electromechanical system piezoelectric ultrasound transducer. *Appl. Phys. Lett.* **2012**, *101*, 253101. [CrossRef]

28. Wang, Q.; Luo, G.; Kusano, Y.; Horsley, D.A. Low thermal budget surface micromachining process for piezoelectric micromachined ultrasonic transducer arrays with in-situ vacuum sealed cavities. In Proceedings of the Hilton Head Workshop 2018: A Solid-State Sensors, Actuators and Microsystems Workshop, Hilton Head Island, SC, USA, 3–7 June 2018; pp. 245–248.

29. Tan, M.; Chen, C.; Chen, Z.; Janjic, J.; Daeichin, V.; Chang, Z.-Y.; Noothout, E.; Van Soest, G.; Verweij, M.D.; De Jong, N.; et al. A front-end ASIC with high-voltage transmit switching and receive digitization for 3-D forward-looking intravascular ultrasound imaging. *IEEE J. Solid-State Circuits* **2018**, *53*, 2284–2297. [CrossRef]

Single-Cell system using monolithic PMUTs-on-CMOS to monitor fluid hydrodynamic properties

Eyglis Ledesma, Iván Zamora, Jesús Yanez, Arantxa Uranga, and Núria Barniol*
eyglis.ledesma@uab.cat; ivan.zamora@uab.cat; jyaneso@gmail.com; arantxa.uranga@uab.cat; nuria.barniol@uab.cat

Department of Electronics Engineering, Universitat Autònoma de Barcelona, 08193 Bellaterra, Spain
Correspondence to: Núria Barniol; Phone: +34-93-581-13-61

Abstract

In this work, a single cell capable of monitoring fluid density, viscosity, sound velocity, and compressibility with a compact and small design is presented. The fluid measurement system is formed by a two-port AlScN piezoelectric micromachined ultrasonic transducer (PMUT) with an 80 μm length monolithically fabricated with a 130 nm complementary metal oxide semiconductor (CMOS) process. The electrode configuration allows the entire system to be implemented in a single device, where one electrode is used as an input and the other as an output. Experimental verification was carried out exploiting the features of piezoelectric devices such as resonators and acoustic transducers, where a frequency shift and amplitude variation are expected because of a change in density and viscosity. A sensitivity of 482±14 Hz/kg/m^3 demonstrates the potential of the system compared to other dual electrode PMUTs. In addition, according to the acoustic measurement, the sound velocity, fluid compressibility, and viscosity coefficient can be extracted, which, to the best of our knowledge, is novel in these PMUT systems.

Introduction

The characterization of liquid properties is becoming progressively more popular in an increasing number of fields: for example, in the quality assessment in industrial applications, i.e., lubricants [1], [2]; in fermentation processes [3], and in health care applications (i.e., the use of blood density and viscosity changes as an indication of heart disease [4]). In most of these cases, tiny-sized devices that require small amounts of liquid and provide a fast response are desirable, points in which microelectromechanical systems (MEMS) excel. MEMS resonant devices have been widely used as a useful alternative in processes requiring online and insitu monitoring [4]–[11].

There are three main techniques for extracting liquid parameters with MEMS devices: a) using resonators and evaluating the change in the resonance frequency and resonator quality factor due to the influence of the liquid surrounding the resonator, which modifies the resonant performance (mass added virtual factor [11]–[14]); b) using acoustic devices (SAW devices, quartz microbalances, and FBARs), to measure changes in the frequency response [15], [16] or in a pulse-echo system [17] due to a change in the acoustic impedance load, which depends on the liquid under test; and c) using acoustic devices that generate a pressure wave and characterize its propagation and sound attenuation inside the liquid [2], [15]. These three techniques allow the characterization of some but not all parameters. For instance, a) facilitates the characterization of density and viscosity but does not determine the sound velocity or compressibility of the liquid; b) is limited by surface changes being important for shear viscosity evaluation [2]; and c) can extract liquid properties such as sound speed and longitudinal viscosity if the density has been previously determined. Numerous examples using the three approaches can be found in the literature. Following approach a), resonant MEMS devices including plates [14], membranes [12], [13], microcantilevers under different resonant modes such as torsional [18], microbeam arrays [19] and suspended channel resonators [9] have been used as density sensors, using most of them Newtonian fluids with low viscosity of 10 cP. Capacitive and piezoelectric micromachined ultrasound transducers (CMUTs and PMUTs) have also been used as plate flexural resonators for density-viscosity sensing, providing very compact systems on the micrometer scale. In 2016 [20], a system of two CMUTs was used to extract the dynamic viscosity of fluids with high values (from 30 cP to 100 cP) through acoustic measurements. Here, the CMUT was used as an ultrasound device in pulse-echo operation mode, acquiring the time response and computing the FFT to determine the change in resonance frequency, which is a footprint of the liquid damping on the resonator (due to the added virtual mass from the liquid over the resonator [11], [13], [15]). Unfortunately, the change in mass density was not discussed, and consequently clear interpretation of the cross sensitivity between density and viscosity was not evaluated.

Other alternatives based in the same operation principle have recently emerged; these methods use piezoelectric micromachined ultrasonic transducers (PMUTs), which require lower driving voltages than CMUTs facilitating their integration into microfluidic systems. One presented in [21], is a PMUT-fluid-PMUT system with a sensitivity of 292.6 Hz/kg/m^3 when the PMUT side is 250 μm. However, a pair of PMUTs are needed and, only low viscosity fluids can be measured. To overcome these drawbacks, in [22], an array is presented where the individual element is a dual electrode PMUT that facilitates detection of the density change at the expense of decreasing sensitivity (26.3 Hz/kg/m^3 , which is still in the range of the human blood density).

A different approach is followed with CMUT devices in [23], using an array of independently driven CMUTs that can produce either standing surface waves in the fluid (approach b) or longitudinal acoustic waves (approach c) depending on the array driving. From both kinds of actuation, the system is capable of

determining several fluid properties such as density, shear viscosity, and sound velocity, although only shear viscosity at low values is demonstrated experimentally.

In this work, it is demonstrated that a single AlScN PMUT-on-CMOS with two top electrodes could be an excellent alternative, as a minute device capable of determining fundamental mechanical properties of fluids such as density, viscosity, sound velocity and compressibility. The main contribution of the work is exploiting the integrated system as a resonator or as an acoustic transducer through a pulse-echo system with a combination of approaches a) and c) described above. In this way, a single-cell system can unequivocally sense the density, acoustic viscosity, sound velocity, and compressibility of the fluid being tested, offering added value compared to the state-of-the-art. The single-cell can detect these properties for high density liquids (i.e., Fluorinert (FC-70)), or those with viscosity over 10 cP such as 100 % glycerol, with a density sensitivity of 482±14 Hz/kg/m^3. Moreover, the presented system is monolithically integrated over a preprocessed CMOS substrate with the adequate circuitry for PMUT driving and sensing. Different from our previous works [24], [25], in this paper AlN doped with Sc is used as the piezoelectric material, providing benefits in terms of piezoelectric transduction coefficients [26]. This single-cell or lab-on-chip for liquid characterization could be easily integrated in a microfluidic cell or hand-held devices of small size, which will make it competitive with respect to other systems [2], [21], [22].

Materials and Methods

The presented PMUT is a two-port device fabricated using the MEMS-on-CMOS process of Silterra [24], [27]. As shown in Fig. 1a-b, it consists in a unimorph square structure with an 80 μm side, in which one electrode is used as a transmitter and the other as a receiver. A 0.6 μm AlN with 9.5% Sc piezoelectric layer ($Sc_{9.5\%}Al_{90.5\%}N$) is sandwiched between two top Al electrodes (0.35 μm thick) and one Al bottom electrode (0.4 μm thick). Based on the piezoelectric coefficients (see Table 1 footnote), an improvement in the transduction efficiency is expected compared to that of pure AlN, as shown in [26]. Finally, the PMUT device is covered by 1 μm Si_3N_4, which acts as an elastic layer and seals the cavity. The AlScN layer is deposited by physical vapor deposition while the Si_3N_4 layer is deposited with low temperature plasma enhanced chemical vapor deposition (PECVD) process [28]. All material properties used in theoretical analysis are summarized in Table 1.

The final AlScN PMUT system is monolithically fabricated over the CMOS circuitry integrated in a 130 nm high voltage CMOS [29], where the outer top electrode is used to generate the acoustic pressure, driven by a high voltage pulser CMOS circuit, while the inner electrode receives the incoming ultrasound wave, which is amplified by a low noise amplifier (LNA) [24], [30]. Low voltage switches are used to isolate the transmitter from the receiver. Figure 1d shows an optical image of the PMUT-on-CMOS system presented and its corresponding layout, highlighting the transmitter side (HV pulser), the receiver (LNA+buffer) and the PMUT device.
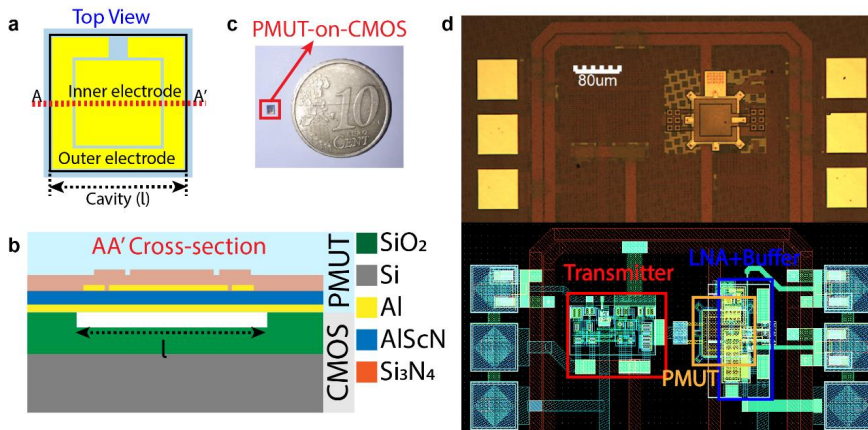
Fig. 1: Two-port PMUT device. a Schematic PMUT-on-CMOS design top view. **b** AA' cross-section. (Layers are not to scale). **c** Photograph of the PMUT-on-CMOS devices in comparison with a 10 cents coin. **d** Optical image (top) and schematic layout (bottom) of the PMUT-on-CMOS device. The principal blocks are highlighted in the layout.

Table 1: PMUT material properties

Layer	Material	Young's modulus (GPa)	Density (kg/m^3)	Poisson's ratio
Substrate	SiO$_2$	70	2200	0.17
Bottom electrode	Al	70	2700	0.35
Piezoelectric	AlScN[1]	250	3520	0.31

Top electrode	Al	70	2700	0.35
Passive	Si₃N₄	250	3100	0.23

[1] Piezoelectric coefficient for $Sc_{9.5\%}Al_{90.5\%}N$: e_{31}= -1.25 C/m² and e_{33} = 1.75 C/m² [26].

The natural frequency of a PMUT is defined by Eq. 1, where the value is determined by its physical characteristics: λ_{ij}^2 depends on the vibration mode, the shape and the boundary conditions (λ_{ij}^2 = 35.99 for the first mode corresponding to a square clamped PMUT), l is the PMUT side length, μ is the mass per unit area, and D is the flexural rigidity [31].

$$f_{air} = \frac{\lambda_{ij}^2}{2\pi \cdot l^2} \sqrt{\frac{D}{\mu}} \qquad i=1,2, \dots \; j=1,2, \dots \qquad (1)$$

On the other hand, when the PMUT is in contact with a fluid, the resonance frequency is affected by the medium properties, which add extra mass, causing a drop in frequency; see Eq. 2. This parameter is known as added virtual mass (β) [13]. It was first determined by Lamb [32] according to Eq. 3, where the fluid is considered inviscid, and only its density (ρ_{liquid}) causes an increase in β and consequently a decrease in the frequency for the same device. The coefficient Γ changes depending on the PMUT shape, being 0.342 for a square clamped device [33].

$$f_{liquid} = \frac{f_{air}}{\sqrt{1+\beta}} \qquad (2)$$

$$\beta = \Gamma \frac{\rho_{liquid} \cdot l}{\mu} \qquad (3)$$

However, viscosity is a relevant property of fluids, so it is important to know the reaction of the transducer at high values of dynamic viscosity ($\eta \gg 10$ cP). An extension of the Lamb's model was presented by Kozlovsky in [34] where the effect of the viscosity is included in the added virtual mass through ξ; see Eq. 4. Based on Eq. 5, this nondimensional parameter (ξ) depends on the PMUT side length (l), the kinetic viscosity ($\upsilon=\eta/\rho_{liquid}$), and the angular frequency (ω) in the liquid environment. In addition, Kozlovsky's model, unlike Lamb's model, considers Newtonian viscous fluids, allowing quantification of the viscosity contribution to the resonance frequency. In fact, based on Eq. 4 and 5, a direct relationship between the viscosity and the thickness of the membrane can be extracted ($\xi \propto (fl^2)^{-1/2} \propto h^{-1/2}$), which shows how the viscosity acquires more importance in thin devices [34]. Furthermore, comparing the added virtual mass for both methods, using Kozlovsky's model, lower frequencies are reached if the viscosity in the liquid increases.

$$\beta = 0.342 \frac{\rho_{liquid} \cdot l}{\mu} (1 + 1.057\xi + O(\xi^3)) \qquad (4)$$

$$\xi = \sqrt{\frac{\upsilon}{\omega \cdot l^2}} \qquad (5)$$

In addition to a resonance frequency shift, resonant MEMS devices in liquid suffer from high damping due to the fluid media. This damping is related to the following: (a) the acoustic radiation or mass loading effect, which is proportional to β (see Eq. 6a and 6b where ρ_p is the PMUT mass density, h is the total PMUT thickness, and c_{liquid} is the sound velocity in the liquid), and (b) viscous losses (Eq. 7) [11], [13]. Both parameters must be considered in the resonator behavior of the PMUT immersed in a fluid.

$$Q_{ar} = \frac{\pi \cdot f_{liquid}}{\alpha} \qquad (6a)$$

$$\alpha = \frac{5\pi^2}{9} \frac{\cdot \rho_{liquid}}{\rho_p} \frac{f_{liquid}^2 \cdot l^2}{(1+\beta) \cdot h \cdot c_{liquid}} \qquad (6b)$$

$$Q_{vis} = \frac{0.95}{\xi} \left(\frac{1}{\beta} + 1\right) \qquad (7)$$

Considering the PMUT device characteristics, theoretical analysis was carried out using six different water-glycerol mixtures at 29 °C, where the density varies almost linearly throughout the range but the viscosity strongly increases for the last three mixtures from 7.56 cP to 648.2 cP; all properties are summarized in Table 2. As a first step, the resonance frequency for the first flexural mode in air was obtained, which equaled 3.99 MHz. Then, in a liquid environment, the resonance frequency was computed according to both approaches, Lamb and Kozlovsky; see Fig. 2a. The results demonstrate that resonance frequency decreases if the percentage of glycerol increases. Furthermore, according to Kozlovsky's model, if the viscosity increases (from 80%) the frequency is even lower, demonstrating the effect of the viscosity. Finally, to obtain the PMUT sensitivity to detect the density change, a linear fit was applied (considering Lamb's model), giving 1.61 kHz/%, which translated in terms of density to 628 Hz/kg/m³. Note that the parameter ξ must be smaller than 1 to apply Eq. 4, which is fulfilled in our case despite the small size of the PMUT device.

Table 2: Water-glycerol mixtures properties

Property	Glycerol weight percent (%)					
	0	20	40	60	80	100

Density (kg/m³)[1]	1000	1045.3	1110	1151.1	1205.5	1254
Viscosity (cP)[2]	0.89	1.38	2.78	7.56	36.4	648.2

[1]: Extracted from [14] [35].
[2]: Computed taking into account the approach presented in [36].

(a)   **(b)**
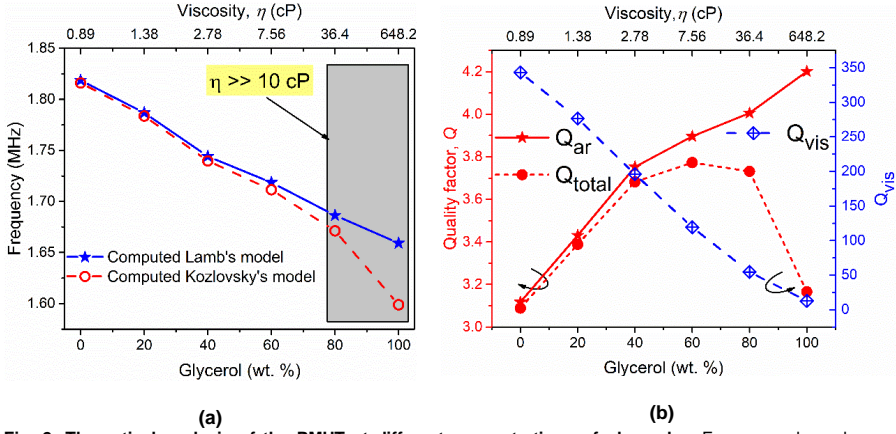
Fig. 2: Theoretical analysis of the PMUT at different concentrations of glycerol. a Frequency dependence considering Lamb's model (blue stars) and Kozlovsky's model (red circles). **b** Contribution of the acoustic radiation (Q_{ar} red stars and solid line, left axis) and viscosity (Q_{vis} blue squares, right axis) to the global Q-factor (Q_{total} red points and dash line, left axis).

In relation to the damping, Fig. 2b depicts the quality factor due to the acoustic radiation (Eq. 6a), the damping due to viscosity (Eq. 7), and the global Q factor ($Q_{total}^{-1}=Q_{ar}^{-1}+Q_{vis}^{-1}$). According to the values in Table 2, the acoustic radiation losses are much greater than the viscous losses until viscosity values are above 10 cP. Consequently, for low viscosity liquids, the global resonator Q-factor (Q_{total}) is almost independent of the viscosity. In the case of high viscosity, this term has a clear influence, with it being difficult to extract the viscosity from the evaluation of the global quality factor due to its reduced value and small variation: the change in the global quality factor, Q_{total}, ranges from 3.75 to 3.1 (x0.82 factor), while the Q for viscosity, Q_{vis}, changes between 110 to 10 (x0.09 factor) for viscosities between 10 cP and 1000 cP. Because of this, it is not possible to evaluate the effects of the viscosity through the measurement of the PMUT resonator frequency response.

Up to now, the influence of only density and viscosity on the frequency response of the PMUT as a resonator (frequency shift and damping with the evaluation of the quality factor, Q) has been analyzed. Considering the PMUT as an acoustic source in a pulse-echo configuration by changing the travel distance inside the liquid, parameters such as sound velocity and acoustic attenuation can be measured with the time-of-flight and amplitude of the received signal respectively. In relation with the acoustic attenuation and considering the longitudinal or acoustic viscosity, η, the damping viscosity coefficient is given by Eq. 8 [15], [37], [38],

$$\alpha_{p,visc} \approx \frac{2 \cdot \pi^2 \cdot f_{liquid}^2 \cdot \eta}{\rho_{liquid} \cdot c_{liquid}^3} \qquad (8)$$

where f_{liquid} corresponds to the resonance frequencies in the liquid, ρ_{liquid} and c_{liquid} are the density and the sound velocity in the liquid environment, respectively. Note the quadratic dependence of this acoustic damping with the frequency.

Results and discussion

Fluid characterization using the PMUT as a resonator

A lock-in amplifier (HF2LI, Zurich Instruments, Switzerland) was used to electrically characterize a simple PMUT device (without any CMOS circuitry connected) wire bonded to a PCB. To find the peak resonance and its amplitude, a frequency sweep was performed according to the theoretical values driving one top electrode with a 10 V continuous wave. The other top electrode was used to detect the frequency change, while the bottom electrode was grounded. Finally, an O-ring with 30 mm diameter was used to confine the liquid over PMUT surface; the set-up is shown in Fig. 3a. The fluid test was experimentally performed not only with the water-glycerol mixtures described in Table 2 but also with liquids such as Fluorinert (FC-70)

(3M with ρ_{liquid}= 1940 kg/m^3, η= 24 cP), and elastic materials such as PDMS (10:1, Sylgard 184 Silicone Elastomer with ρ= 980 kg/m^3) were included.

Several samples were used during the experiment, and before immersing the PMUTs in a liquid environment, they were electrically characterized in air using the same set-up. Based on the theoretical value of the frequency for the first mode, a sweep around 4 MHz with a span of 1 MHz was used. A mean resonance frequency of 4.42 MHz with a standard deviation of 0.13 MHz was obtained. Because of this dispersion and to achieve an easy comparison, the resonant frequency (theoretical and measured) in the fluid was normalized with its value in the air (f_{media}/f_{air}) for the same device. Figure 3b includes the theoretical results considering Lamb's and Kozlovsky's models as well as the measured values. As expected, the resonance frequency decreases when the medium density increases. Furthermore, regarding the last point of the water-glycerol mixtures (100% glycerol), the experimental frequency shifts according to Kozlovsky's model, demonstrating the PMUT's capability to detect fluids with high viscosity values. Additionally, note how the density plays an important role in the mass loading (β), achieving the highest value when FC-70 is used (lower frequency), even though this sample has 27 times lower viscosity than 100% of glycerol. To evaluate the sensitivity as demonstrated in [22], the experimental data points were fitted (excluding 100% glycerol due to its high viscosity). The curve fitted using f_{media}/f_{air} is a linear function with a slope of -1.089e-4 [1/kg/m^3] and intercept of 0.55; see Fig. 3b inset. An R-squared value of 0.94 indicates that the presented two-port PMUT can work effectively as a density sensor. According to the mean frequency in the air (f_{air}= 4.42 MHz$\pm$0.13 MHz), the density sensitivity is 482$\pm$14 Hz/kg/m^3, and the resonance frequency range in the used liquids ranges from 1.5 MHz to 2 MHz. The error here was computed by transferring the dispersion in the electrical measurement in the air (0.13 MHz) to the liquid according to Eq. 2, with a 3% variation from the center frequency.
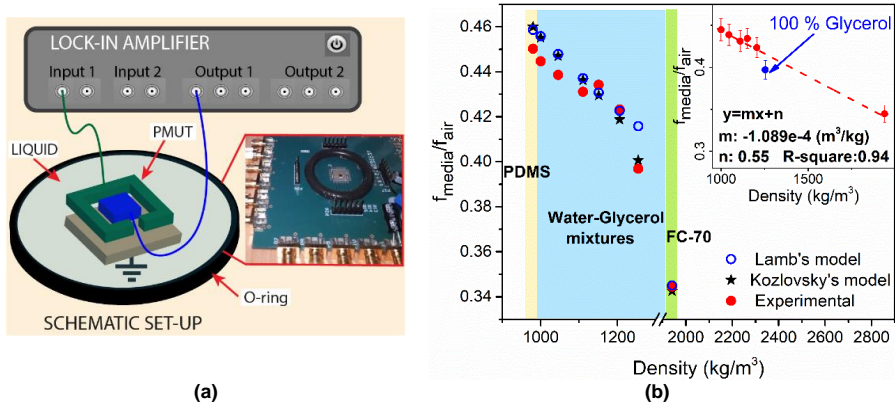
Fig. 3: PMUT as a resonator. a Experimental set-up for the electrical characterization using a lock-in amplifier. Inset: Photograph of the set-up. **b** Normalized frequency in different acoustic media considering theoretical (blue circles-black stars) and experimental results (red points). Each material is identified by one color; PDMS: yellow, water-glycerol mixtures: blue, and FC-70: green. Inset: Fitted curve excluding 100% glycerol.

Table 3 shows a comparison between different PMUTs systems as density sensors. Taking the highest sensitivity [21], our PMUT achieves 1.6x improvement with a single and compact device. Furthermore, in comparison with other PMUTs, the AlScN PMUT reaches better sensitivity (2.5x that of [39] and 18.3x that of [22]) with a smaller area.

Table 3: Comparison of PMUTs as density sensors

Parameters	2020 [39]	2020 [21]	2021 [22]	This work
Piezoelectric layer	PZT	PZT	PZT	AlScN
TX/RX same chip	Yes	No	Yes	Yes
PMUT size (μm)	500	250	750	80
Sensitivity (Hz/kg/m^3)	191	292.6	26.3	482

Fluid characterization using the PMUT as a pulse-echo system

Fluid Density: Experimental verification was done by immersing the device first in FC-70 and then in 100% glycerol, due to their high density and viscosity, respectively. The air-liquid interface was used as a reflecting surface, and its thickness was adjusted to ensure a time of flight values close to 11 μs in FC-70

and 7 μs in 100% glycerol. To generate the acoustic pressure, the HV transmitter circuit was configured to excite the outer electrode with two cycles of 32V amplitude.

A frequency sweep was carried out in the PMUT in the pulse-echo experiment to identify the resonance frequency (maximum received signal) in each liquid environment. The signal (peak-to-peak amplitude) received by the inner electrode is shown in Fig. 4a. The maximum amplitudes are achieved at 1.49 MHz and 1.71 MHz when FC-70 and 100% glycerol are used, respectively, values close to the electrical measurements (1.54 MHz using FC-70 and 1.81 MHz using 100% glycerol) allowing the determination the density values. In addition, the maximum amplitude for FC-70 is higher than that for 100% glycerol, which is expected for two main reasons: (a) the speed of sound in 100% glycerol is almost 3 times higher, and therefore, the interface liquid-air is further away, and (b) the viscosity coefficient is higher in 100% glycerol than in FC-70 which increases the signal attenuation.

Sound velocity: The inset of Figure 4b shows the schematic setup used to determine the sound velocity in different liquids concentrations. As shown, a piece of silicon wafer (Si-wafer) was used as a reflecting surface, and it was positioned at a base point z_1. Through a manual micrometer system, the Si-wafer was lifted in increments of 50 μm until it was displaced 1 mm from its original position. Finally, the acoustic pressure was generated by the outer electrode, driven with two cycles with 32 V at the frequency previously determined.

To estimate the sound velocity, cross-correlation was used to obtain the difference in time between the base point and the point of interest. Each time-distance pair was plotted. Figure 4b shows the values, and the slope of a linear fit allows the determination of the sound velocity (c), giving 676±4.5 m/s in FC-70 and 1903±31.2 m/s in 100% glycerol in accordance with the reported values [40]. The uncertainty in the sound velocity estimation can be analyzed through the standard deviation (σ_c), defined by Eq. 9, where σ_z is the micropositioner accuracy $\pm$ 2 μm [41] and σ_t depends on the sampling frequency (250 MHz for 100% glycerol and 200 MHz for FC-70) giving 4 ns and 5 ns, respectively.

$$\sigma_c = \sqrt{(\frac{dc}{dz} \cdot \sigma_z)^2 + (\frac{dc}{dt} \cdot \sigma_t)^2} \tag{9}$$
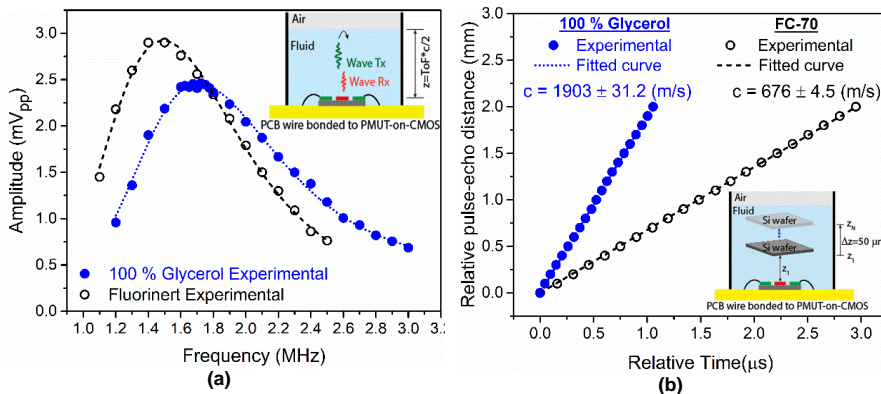
Fig. 4: PMUT as a pulse-echo system. **a** Frequency response considering 100% glycerol (blue points) and FC-70 (black circles). The time of flight (ToF) is 7 μs and 11 μs, respectively. **b** Experimental relative distance-time curves to estimate sound velocity in 100% Glycerol (blue point) and FC-70 (black circles). Insets: schematic setups for the frequency response and the sound velocity estimation.

Compressibility: This is an important mechanical property in liquids that indicates a relative change in volume because of a change in pressure, and it can be defined as the inverse of the bulk modulus ($K=c^2 \cdot \rho_{liquid}$). The fluids being tested, in this case, were the six proposed concentrations of water and glycerol shown in Table 2. The sound velocity was obtained considering the same procedure mentioned above but, unlike the previous section, here, the surface of the PMUT was covered with a 200 μm layer of PDMS (10:1, Sylgard 184 Silicone Elastomer) to isolate the wire-bonding and provide good performance during all experiments.

Figure 5a (left axis) shows the experimental sound velocity obtained (red points) as well as the reported values in [35] (green stars). The estimated sound velocity without PDMS is also included for 100% glycerol (purple circle), indicating that the PDMS layer does not affect the performance of the PMUT device. On the other hand, the right axis of Fig. 5a shows the compressibility variation for the same density range and its inaccuracy regarding sound velocity (inaccuracy computed as $2(\rho_{liquid}c^3)^{-1}\sigma_c$, where c is the obtained sound velocity, ρ_{liquid} is the density, and σ_c is the standard deviation of the sound velocity). Note that, as expected, an increase in the sound velocity causes lower compressibility values. In addition, based on the reported

values in the literature at a temperature close to the one used here (29 °C), the obtained compressibility shows a good correspondence with [17], [42], which demonstrates the high potential of the proposed device.

Viscosity: The acoustic losses of the same six water glycerol mixtures were also studied. To carry out this experiment, the acoustic path (AP) was modified every 100 μm (2*Δz) using the same Si-wafer as a reflecting surface; see the set-up in the Fig. 4b inset. Losses as a consequence of liquid damping have been studied in [40], [43] where the propagation waves were considered planar waves and then, only losses caused by the fluid properties affected the signal amplitude. The radiation patterns of small sized PMUTs, such as the one in this work, are almost omnidirectional [44], and in consequence, the decrease in amplitude is due to the acoustic path (spherical acoustic wave) and the acoustic medium losses due to the viscosity [45]. Considering this, the signal received by the inner electrode is not only reduced by 1/AP but also exponentially decays due to viscous losses ($e^{-\alpha_{p,visc}\cdot AP}$; where $\alpha_{p,visc}$ is defined in Eq. 8). To see the influence of this second term, the product of the peak-to-peak amplitude (*Amp*) and acoustic path (*AP*) was used (Eq. 10).

$$Amp\left(mV_{pp}\right)\cdot AP(mm) = e^{-\alpha_{p,visc}\cdot AP} \tag{10}$$

Figure 5b shows the experimental points for water (red triangles), 100% glycerol (blue points), and FC-70 (green squares). Measurements were made with the PMUT-on-CMOS covered by 200 μm PDMS (for water and glycerol mixtures) to preserve wire bonding during the experiments. The base point in the acoustic path (*AP*) was determined with AP=2*(z_1 +h_{PDMS}) and z_1= (ToF/2- h_{PDMS}/c_{PDMS})*c_{liquid} (where *ToF*=7 μs is the time of flight, c_{liquid} is the sound velocity shown in Fig. 5a, and h_{PDMS}= 200 μm and c_{PDMS}= 1000 m/s correspond to the thickness and sound velocity of the PDMS). Considering this, the first the acoustic path in water is 10.2 mm, and that in 100% glycerol is 13 mm. When FC-70 is used, the PMUT is not covered with PDMS (h_{PDMS}= 0 μm), and the ToF is 11 μs, giving an acoustic path of 7.4 mm. To see the influence of viscosity on acoustic losses, an exponential adjustment was performed according to Eq. 10. The coefficient $\alpha_{p,visc}$ was computed using Eq. 8, giving 0.021 m⁻¹, 4.76 m⁻¹, and 1.85 m⁻¹ for water, 100% glycerol, and FC-70, respectively. These curves are represented by dotted lines on the same graphs. Despite there being some dispersion in the experimental points, they show the same trend as the theoretical fit, demonstrating the ability of the PMUT to estimate viscosity.

(a)   **(b)**
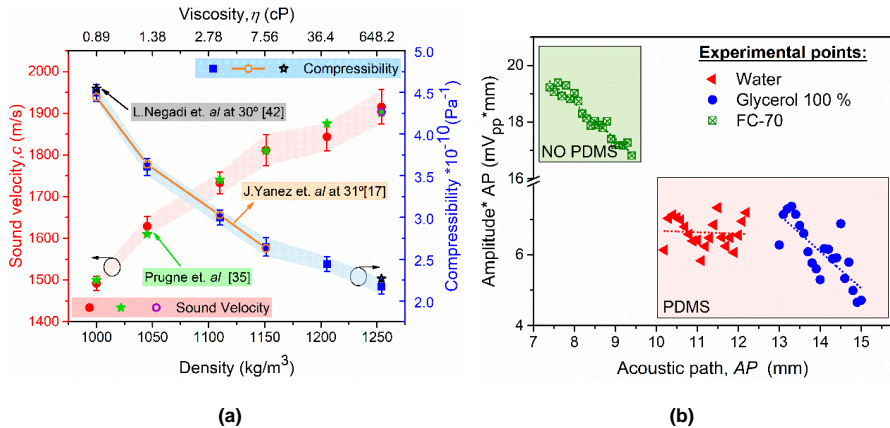
Fig. 5: a Left axis (red): Sound velocity versus density-viscosity corresponding to water-glycerol mixtures (red points) and data published in [35] (green stars); the sound velocity without PDMS is included (purple circle). Right axis (blue): Compressibility estimation and data published in [17] (orange circles and line) and in [42] (black stars). **b** Pulse-echo amplitude versus acoustic path (AP) with the PMUT immersed in FC-70 (green squares), water (red triangles), and 100% glycerol (blue points). The dotted curves consider the viscosity losses, $\alpha_{p,visc}$, giving 0.021 m⁻¹, 4.76 m⁻¹, and 1.85 m⁻¹ for water, 100% glycerol, and FC-70, respectively

Conclusions

In this article the capabilities of a single AlScN PMUT-on-CMOS for monitoring density, viscosity, sound velocity, and compressibility of fluids are demonstrated. Based on the PMUT behavior, two approaches are presented to characterize different fluids. First, working as a resonator, a change in the liquid density causes a decrease in the resonance frequency, with a sensitivity of 482±14 Hz/kg/m³. Second, the propagation of an acoustic wave allows the determination of not only the density but also the sound velocity, which allows the compressibility of the fluid to be characterized. Furthermore, the effect of viscosity is seen in the incoming

ultrasonic wave, where the theoretical viscosity coefficient adjusts for the exponential decrease in amplitude. Experimental verification shows that this tiny device, manufactured monolithically on a CMOS substrate, is an excellent candidate for a single measurement cell unit for use in microfluidic systems that require the characterization of the properties of small quantities of fluids. Integrated CMOS circuitry with further signal processing can be easily upgraded to provide smart solutions for demanding industrial and biomedical applications, with constraints on area, power consumption and cost.

References

[1] G. Nicholas, B. P. Clarke, and R. S. Dwyer-Joyce, "Detection of lubrication state in a field operational wind turbine gearbox bearing using ultrasonic reflectometry," *Lubricants*, vol. 9, no. 1, pp. 1–22, 2021.

[2] A. P. V. Egas *et al.*, "Speed of sound and derived thermodynamic properties of glycerol," *J. Chem. Thermodyn.*, vol. 156, p. 106367, 2021.

[3] J. Toledo, V. Ruiz-Díez, J. Velasco, J. Hernando-García, and J. L. Sánchez-Rojas, "3D-Printed Liquid Cell Resonator With Piezoelectric Actuation for in-Line Density-Viscosity Measurements," *Sensors*, vol. 21, no. 22, 2021.

[4] H. J. Kim *et al.*, "Piezoelectric layer embedded-microdiaphragm sensors for the determination of blood viscosity and density," *Appl. Phys. Lett.*, vol. 105, no. 15, 2014.

[5] B. Jakoby *et al.*, "Miniaturized sensors for the viscosity and density of liquids - Performance and issues," *IEEE Trans. Ultrason. Ferroelectr. Freq. Control*, vol. 57, no. 1, pp. 111–120, 2010.

[6] B. Jakoby and M. J. Vellekoop, "Physical sensors for liquid properties," *IEEE Sens. J.*, vol. 11, no. 12, pp. 3076–3085, 2011.

[7] R. Paxman, J. Stinson, A. Dejardin, R. A. Mckendry, and B. W. Hoogenboom, "Using Micromechanical Resonators to Measure Rheological Properties and alcohol content of model solutions and commercial beverages," *Sensors (Switzerland)*, vol. 12, no. 5, pp. 6497–6507, 2012.

[8] O. Cakmak, E. Ermek, H. Urey, G. G. Yaralioglu, and N. Kilinc, "MEMS based blood plasma viscosity sensor without electrical connections," in *Proceedings of IEEE Sensors*, 2013.

[9] M. F. Khan *et al.*, "Online measurement of mass density and viscosity of pL fluid samples with suspended microchannel resonator," *Sensors Actuators, B Chem.*, vol. 185, pp. 456–461, 2013.

[10] X. Lu, L. Hou, L. Zhang, Y. Tong, G. Zhao, and Z. Y. Cheng, "Piezoelectric-excited membrane for liquids viscosity and mass density measurement," *Sensors Actuators, A Phys.*, vol. 261, pp. 196–201, 2017.

[11] N. E. Weckman and A. A. Seshia, "Reducing dissipation in piezoelectric flexural microplate resonators in liquid environments," *Sensors Actuators, A Phys.*, vol. 267, pp. 464–473, 2017.

[12] C. Ayela and L. Nicu, "Micromachined piezoelectric membranes with high nominal quality factors in newtonian liquid media: A Lamb's model validation at the microscale," *Sensors Actuators, B Chem.*, vol. 123, no. 2, pp. 860–868, 2007.

[13] M. Olfatnia, Z. Shen, J. M. Miao, L. S. Ong, T. Xu, and M. Ebrahimi, "Medium damping influences on the resonant frequency and quality factor of piezoelectric circular microdiaphragm sensors," *J. Micromechanics Microengineering*, vol. 21, no. 4, 2011.

[14] S. Cerimovic, R. Beigelbeck, H. Antlinger, J. Schalko, B. Jakoby, and F. Keplinger, "Sensing viscosity and density of glycerol-water mixtures utilizing a suspended plate MEMS resonator," *Microsyst. Technol.*, vol. 18, no. 7–8, pp. 1045–1056, 2012.

[15] R. Beigelbeck, H. Antlinger, S. Cerimovic, S. Clara, F. Keplinger, and B. Jakoby, "Resonant pressure wave setup for simultaneous sensing of longitudinal viscosity and sound velocity of liquids," *Meas. Sci. Technol.*, vol. 24, no. 12, 2013.

[16] Y. Lu, M. Zhang, H. Zhang, Y. Jiang, H. Zhang, and W. Pang, "Microfluidic Bulk-Modulus Measurement by a Nanowavelength Longitudinal-Acoustic-Wave Microsensor in the Nonreflective Regime," *Phys. Rev. Appl.*, vol. 11, no. 4, p. 1, 2019.

[17] J. Yanez, A. Uranga, and N. Barniol, "Fluid compressional properties sensing at microscale using a longitudinal bulk acoustic wave transducer operated in a pulse-echo scheme," *Sensors Actuators A Phys.*, vol. 334, p. 113334, 2022.

[18] L. Zhao *et al.*, "A mems resonant sensor to measure fluid density and viscosity under flexural and torsional vibrating modes," *Sensors (Switzerland)*, vol. 16, no. 6, 2016.

[19] S. Marquez, M. Álvarez, D. Fariña Santana, A. Homs-Corbera, C. Domínguez, and L. M. Lechuga, "Array of Microfluidic Beam Resonators for Density and Viscosity Analysis of Liquids," *J. Microelectromechanical Syst.*, vol. 26, no. 4, pp. 749–757, 2017.

[20] Y. Hongbin, L. Liang, and A. G. Yuandong, "Capacitive micromachined ultrasonic transducer (CMUT) based micro viscosity sensor," *Sensors Actuators, B Chem.*, vol. 227, pp. 346–351, 2016.

[21] K. Roy *et al.*, "Fluid Density Sensing Using Piezoelectric Micromachined Ultrasound Transducers," *IEEE Sens. J.*, vol. 20, no. 13, pp. 6802–6809, 2020.

[22] K. Roy, K. Kalyan, A. Ashok, V. Shastri, and R. Pratap, "A PMUT Integrated Microfluidic System for Fluid Density Sensing," *J. Microelectromechanical Syst.*, vol. 30, no. 4, pp. 642–649, 2021.

[23] M. Thränhardt, P. C. Eccardt, H. Mooshofer, P. Hauptmann, and L. Degertekinz, "A resonant CMUT sensor for fluid applications," in *Proceedings of IEEE Sensors*, 2009, pp. 878–883.

[24] I. Zamora, E. Ledesma, A. Uranga, and N. Barniol, "Monolithic Single PMUT-on-CMOS Ultrasound System with +17 dB SNR for Imaging Applications," *IEEE Access*, vol. 8, pp. 142785–142794, 2020.

[25] E. Ledesma, I. Zamora, A. Uranga, F. Torres, and N. Barniol, "Enhancing AlN PMUTs Acoustic Responsivity within a MEMS-on-CMOS Process," *Sensors*, vol. 21, no. 24, 2021.

[26] E. Ledesma, I. Zamora, A. Uranga, and N. Barniol, "9.5 % Scandium Doped ALN PMUT Compatible with Pre-Processed CMOS Substrates," in *Proceedings of the IEEE International Conference on Micro Electro Mechanical Systems (MEMS)*, 2021, pp. 887–890.

[27] E. Ledesma, I. Zamora, A. Uranga, and N. Barniol, "Multielement ring array based on minute size pmuts for high acoustic pressure and tunable focus depth," *Sensors*, vol. 21, no. 14, 2021.

[28] M. S. Pandian *et al.*, "Thin film piezoelectric devices integrated on CMOS," in *Proceedings of the 2016 Symposium on Piezoelectricity, Acoustic Waves and Device Applications, SPAWDA 2016*, 2016, pp. 167–170.

[29] "SilTerra Malaysia Sdn Bhd," *web.* [Online]. Available: https://www.silterra.com/technology/technology#section03. [Accessed: 28-Jan-2022].

[30] E. Ledesma, I. Zamora, A. Uranga, and N. Barniol, "Monolithic PMUT-on-CMOS Ultrasound System for Single Pixel Acoustic Imaging," in *Proceedings of the IEEE International Conference on Micro Electro Mechanical Systems (MEMS)*, 2021, pp. 394–397.

[31] R. D. Blevins, *Formulas for natural frequency and mode shape.* New York: Litton Educational Publishing, Inc., 1979.

[32] Horace Lamb, "On the vibrations of an elastic plate in contact with water," *Proc. R. Soc. Lond. A vol.* 98, pp. 205–216,1920.

[33] J. J. Bernstein *et al.*, "Micromachined high frequency ferroelectric sonar transducers," *IEEE Trans. Ultrason. Ferroelectr. Freq. Control*, vol. 44, no. 5, pp. 960–969, 1997.

[34] Y. Kozlovsky, "Vibration of plates in contact with viscous fluid: Extension of Lamb's model," *J. Sound Vib.*, vol. 326, no. 1–2, pp. 332–339, 2009.

[35] C. Prugne, J. Van Est, B. Cros, G. Lévêque, and J. Attal, "Measurement of the viscosity of liquids by near-field acoustics," *Meas. Sci. Technol.*, vol. 9, no. 11, pp. 1894–1898, 1998.

[36] N. Cheng, "Formula for the Viscosity of a Glycerol-Water Mixture," *Ind. Eng. Chem. Res.*, vol. 47, no. 9, pp. 3285–3288, 2008.

[37] P. Hauptmann, R. Lucklum, A. Piittmer, and B. Henning, "Ultrasonic sensors for process monitoring and chemical analysis : state-of-the-art and trends," vol. 67, no. 97, pp. 32–48, 1998.

[38] J. Holmes, G. Parker, and W. Povey, "Temperature dependence of bulk viscosity in water using acoustic spectroscopy," *J. Phys. Conf. Ser.*, vol. 269, no. 1, 2011.

[39] K. Roy, A. Mandal, A. Ashok, H. Gupta, V. Shastri, and R. Pratap, "A Single Cell PMUT as a Bio-Fluid Density Sensor," in *2020 IEEE International Ultrasonics Symposium, IUS*, 2020, vol. 2020-Septe, no. c, pp. 1–4.

[40] M. S. Hossain, B. Pal, and P. K. Mukhopadhyay, "Ultrasonic Characterization of Newtonian and Non-newtonian Fluids," *Univers. J. Phys. Appl.*, vol. 12, no. 3, pp. 41–46, 2018.

[41] L.S. Starrett Company, "Catalog 33 - Section 1 - Micrometers," *https://www.starrett.com/.* [Online]. Available: https://www.starrett.com/vdoc/Catalog 33 - Section 1 - Micrometers. [Accessed: 20-Dec-2021].

[42] L. Negadi *et al.*, "Effect of temperature on density, sound velocity, and their derived properties for the binary systems glycerol with water or alcohols," *J. Chem. Thermodyn.*, vol. 109, pp. 124–136, 2017.

[43] F. Behroozi, J. Smith, and W. Even, "Stokes' dream: Measurement of fluid viscosity from the attenuation of capillary waves," *Am. J. Phys.*, vol. 78, no. 11, pp. 1165–1169, 2010.

[44] Y. Lu, A. Heidari, and D. A. Horsley, "A High Fill-Factor Annular Array of High Frequency Piezoelectric Micromachined Ultrasonic Transducers," *J. Microelectromechanical Syst.*, vol. 24, no. 4, pp. 904–913, 2015.

[45] L. E. Kinsler, A. R. Frey, A. B. Coppens, and J. V. Sanders, *Fundamentals of Acoustics*, 4th ed. John Wily & Sons, Inc., 2000.

MDPI

Article

Multielement Ring Array Based on Minute Size PMUTs for High Acoustic Pressure and Tunable Focus Depth

Eyglis Ledesma [ID], Iván Zamora [ID], Arantxa Uranga [ID] and Núria Barniol *[ID]

Departament d'Enginyeria Electrònica, Universitat Autònoma de Barcelona, 08193 Bellaterra, Spain; eyglis.ledesma@uab.es (E.L.); ivan.zamora@uab.es (I.Z.); arantxa.uranga@uab.es (A.U.)
* Correspondence: nuria.barniol@uab.es

Abstract: This paper presents a multielement annular ring ultrasound transducer formed by individual high-frequency PMUTs (17.5 MHz in air and 8.7 MHz in liquid) intended for high-precision axial focalization and high-performance ultrasound imaging. The prototype has five independent multielement rings fabricated by a monolithic process over CMOS, allowing for a very compact and robust design. Crosstalk between rings is under 56 dB, which guarantees an efficient beam focusing on a range between 1.4 mm and 67 μm. The presented PMUT-on-CMOS annular array with an overall diameter down to 669 μm achieves an output pressure in liquid of 4.84 kPa/V/mm^2 at 1.5 mm away from the array when the five channels are excited together, which is the largest reported for PMUTs. Pulse-echo experiments towards high-resolution imaging are demonstrated using the central ring as a receiver. With an equivalent diameter of 149 μm, this central ring provides high receiving sensitivity, 441.6 nV/Pa, higher than that of commercial hydrophones with equivalent size. A 1D ultrasound image using two channels is demonstrated, with maximum received signals of 7 mVpp when a nonintegrated amplifier is used, demonstrating the ultrasound imaging capabilities.

Keywords: PMUTs; annular array; ring array; ultrasound; AlN; ultrasound imaging; pulse-echo; PMUT-on-CMOS

1. Introduction

Ultrasound is widely used as an excellent noninvasive diagnostic tool for nondestructive testing and medical imaging. Nowadays, small ultrasound probes are being extensively pursued in areas such as in-body controllable catheter-based imaging for intravascular imaging [1–4], specific heat treatments based on high-intensity focused ultrasound (HIFU systems) [5,6], or brain stimulation for in vivo experiments [7,8]. In addition to these applications, power-free implantable prostheses for sensing biological parameters in animals or humans are also a rapidly evolving field of research towards digital medicine and in view of elderly population growth. Recently, powering and data transfer for these devices by ultrasound is being studied and presented as one of the alternatives in comparison with radiofrequency and inductive links [9–11].

For all these cases, tiny ultrasound transducers with very controllable and tunable focus depth are required. Among the different ultrasound probes, annular rings provide by layout this capability. Their dynamic focusing along the axial direction and their symmetry produce an acoustic pattern with a high spatial resolution (lateral and axial) and high levels of output pressure which have been efficiently used in most of the above-mentioned applications [1,3–6,8,9].

Annular rings for ultrasound systems have been fabricated with bulk piezoelectric materials in their thickness vibration mode. However, their complex fabrication process would limit their use in advanced ultrasound systems which require minute sizes, high reproducibility, cost-efficiency, and low power consumption [12,13]. Advances in the fabrication of micromachined ultrasonic transducers using MEMS-based technologies, either capacitive (CMUTs) or piezoelectrical (PMUTs) with the capability of direct integration

with CMOS, in a batch processing approach, decrease manufacturing cost and allow a reduction in size and increase in compactness of the overall ultrasound system [12,14,15]. Ring-shaped CMUT arrays have been widely described in the literature [3–5,12,14]. However, their eligibility can be affected by the high power consumption needed in the CMUT transducers. On the contrary, monolithic ultrasound systems based on PMUTs open the way to power-efficient single-chip ultrasound systems [15,16].

In PMUTs, the ultrasound wave is produced due to the flexural movement of the membrane, and its operational frequency will depend on both the different thicknesses of the material and the size of the transducer, allowing in this way different operation frequencies using different device layouts but with the same technological approach. Few examples of continuous annular rings under this flexural approach have been reported [6]. However, continuous annular array fabrication could be a challenge due to its dimensional constraints. In order to avoid this and increase the achievable output pressure at the acoustic axis, a finite number of small ultrasound transducers configured in an annular ring can be used (see for example [1,17]). The main advantage in this multielement ring configuration is given by the capability to decouple the acoustic wave frequency, due exclusively to the single element, from the overall ring diameter, keeping a longer-range tunable focus depth, as is shown in Section 2. Taking these demands into consideration, we have designed a multiple concentric annular ring ultrasonic transducer composed of multiple high-frequency piezoelectrical micromachined ultrasound transducers (PMUTs) capable of being monolithically integrated with CMOS technology [16]. The fabricated multielement ring ultrasound array provides high accurate tunable focus depth, high acoustic output pressure, and minute size which is operable in the 10 MHz frequency range in a liquid environment and can be a candidate for the above-mentioned applications. In addition, we have characterized the central ring of the array as an ultrasonic receiver, showing higher receiver sensitivity with smaller spatial averaging effects than commercial hydrophones with similar size.

This paper is organized into four sections: Section 2 explains the multielement ring array design and its benefit over the continuous ring array using analytical equations and FEM simulations (COMSOL Multiphysics); predictions of the acoustic performance with Field II software are also provided. Section 3 shows the experimental results, including the electrical and acoustic characterization and line-scan ultrasound imaging as a demonstration of the full transceiver ultrasound system. Finally, Section 4 concludes the paper.

2. Materials and Methods

2.1. Multielement Ring Array Design

As already explained, the main advantage of an annular ring is its capability to be axially focused; focus depth tunability, beam diameter at the focus point, and range of achievable pressure are its main parameters. The focus depth, F_d, is defined by Equation (1), where S is the transducer area (whatever its shape), λ is the wavelength, f is the frequency, and c is the sound velocity in the propagation medium [18]. It is evident that transducers with the same area will produce a greater focus depth with higher frequency.

$$F_d = \frac{S}{4\lambda} = \frac{S \times f}{4 \times c} \tag{1}$$

For the design of an efficient annular ring, the first question is how we can achieve the highest frequency using the same transducer area, which will give us the greatest focus depth. In our approach, we must consider flexural resonators as we are using a MEMS-based approach with AlN as the piezoelectrical material. We will analyze this focus depth capability considering a continuous annular ring array in comparison with a multielement annular ring array. Figure 1 top inset shows a conceptual schematic of a single element from a continuous annular ring array (green) and a single element (squared PMUT) that will form a multielement ring array, (blue). Here *2D*, *2d*, and *l* are the outer

diameter, inner diameter, and width of each ring in the annular array; a and w are the side and diagonal of each square PMUT in the multielement array.
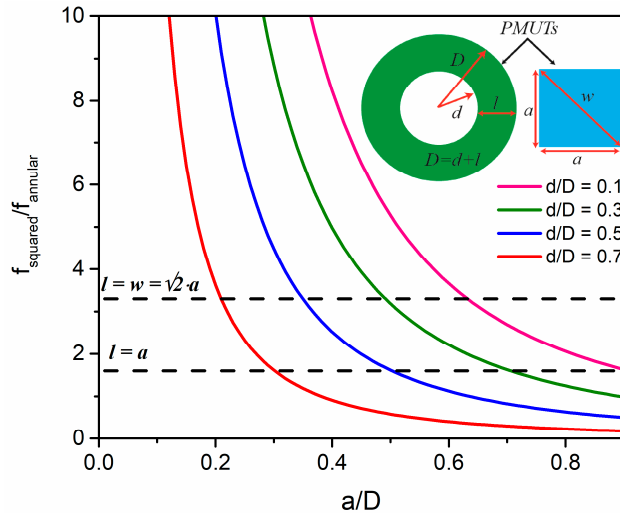

Figure 1. Theoretical frequency ratio, f_s/f_a, from two single elements of an annular array and a multielement multiring array with the same area according to Equation (4). Inset: Only one annular ring and one single square PMUT from the annular and multielement ring arrays are shown.

First, the resonance frequency for the first flexural mode for the annular ring array is giving by Equation (2), where $\lambda_{ij\_annular}$ is a dimensionless parameter associated with the vibration mode (i, j), D_r is the flexural rigidity, and μ is the mass per unit area [19]. Intuitively, higher resonance frequencies could be obtained with smaller devices, but the parameter $\lambda_{ij\_annular}$ is dependent on the ratio of d/D and boundary conditions, so in consequence, the same frequency can be obtained for rings with the same width (no matter how big the outer diameter is), even in the case of flexural resonant rings.

$$f_a = \frac{\lambda_{ij\_annular}^2}{2\pi D^2} \sqrt{\frac{D_r}{\mu}} \quad i = 1, 2, \ldots j = 1, 2, \ldots \tag{2}$$

Second, for a multielement ring array, the resonance frequency is fixed by the individual PMUTs, defined by Equation (3) for the first flexural mode considering square PMUTs [20].

$$f_s = \frac{35.99}{2\pi a^2} \sqrt{\frac{D_r}{\mu}} \tag{3}$$

Using Equations (2) and (3), the ratio f_s/f_a for the same layer stack is given by Equation (4) and computed in Figure 1 for different d/D ratios considering clamped boundaries where the parameter $\lambda_{ij\_annular}^2$ has been extracted from Table 11-2 in [19]. The multielement ring array achieves frequencies higher than the annular array when the PMUT side is much smaller than D. Dotted lines show the case when the ring width is equal to a (minimum side of the squared PMUT) or w, giving for all d/D ratios an improvement in multielement multiring frequency of 1.6× or 3.3×, respectively. This increase in the resonance frequency is translated into a higher focal length.

$$f_s/f_a = \frac{35.99}{(a/D)^2 \times \lambda_{ij\_annular}^2} \quad i = 1, 2, \ldots j = 1, 2, \ldots \tag{4}$$

Figure 2a shows an optical image of the proposed multielement ring array ultrasound transducer. The PMUTs are arranged in irregular polygons that are connected through the top electrode forming five concentric channels. The bottom electrode is common for all PMUT devices, and the gap between consecutive elements is 25 μm.
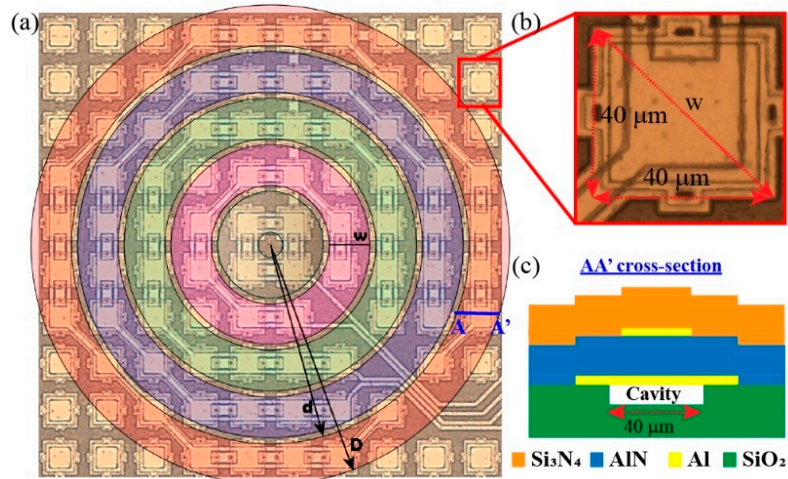

Figure 2. (**a**) Optical image of the multielement ring array transducer and schematic representation of the continuous rings over it; (**b**) zoom of the individual 40 μm AlN PMUT; (**c**) AA' cross-section of AlN-PMUT.

Every single element consists of a squared AlN-PMUT with a 40 μm side, fabricated using the MEMS-on-CMOS SilTerra technology [16,21]. The top electrode size was optimized to maximize the membrane velocity and consequently the output pressure. A 1.3 μm AlN piezoelectric material was deposited by physical vapor deposition (PVD) and sandwiched between two Al electrodes (0.35 μm thickness top electrode and 0.4 μm thickness bottom electrode). A 1.5 μm Si_3N_4 layer was deposited with a low-temperature plasma-enhanced chemical vapor deposition (PECVD) process; it acts as the elastic layer and seals the cavity. Figure 2c shows a cross-section profile (AA') of the square PMUT device, and Table 1 summarizes the material properties used in FEM COMSOL simulations and the principal geometric dimensions.

Table 1. Material properties and thickness used in FEM simulations.

PMUT Layer	Properties			Geometric	
	Mat.	Young's Modulus (GPa)	Density (kg/m³)	Side (μm)	Thick. (μm)
Substrate	SiO_2	70	2200	60	2
Bottom Elec.	Al	70	2700	46	0.4
Piezoelectric	AlN [1]	279	3230	60	1.3
Top Elec.	Al	70	2700	28.3	0.35
Passive	Si_3N_4	250	3100	60	1.5

[1] The piezoelectric coefficients e_{33} and e_{31} used in COMSOL are 1.55 C/m^2 and −0.6 C/m^2 respectively.

The first mode shape and its resonance frequency for a square 40 μm AlN PMUT were obtained in COMSOL Multiphysics; the value of 27.7 MHz was given, which is close to the value computed using Equation (3), 27.8 MHz. Dynamic simulations in a liquid environment (Fluorinert, FC-70, with a density ρ = 1940 kg/m³ and the sound velocity c = 685 m/s) give a maximum displacement at 13 MHz.

In order to compare the performance of this multielement ring array transducer with an equivalent continuous concentric ring, we considered the circles that surround the single-PMUT elements. The shape of each ring is close to an irregular polygon, and it is not possible to obtain rings that include all PMUTs of the polygon exactly. Figure 2a shows in different colors the geometric representation corresponding to each continuous ring, where D and d are the outer and the inner radii, respectively, and w is the width. The values of D and d were computed trying to include the highest number of PMUTs of each irregular polygon into the continuous ring. The width, w, corresponds to the PMUT diagonal (the furthest PMUT point inscribed in the continuous ring) and is 56.6 μm ($\sqrt{(40 \text{ μm})^2 + (40 \text{ μm})^2}$) (see Figure 2b). A gap of 8.4 μm between rings is obtained. Decreasing the ring width to $w = a$, higher resonance frequency for the continuous ring can be achieved at the expense of not including the largest number of PMUTs within it. Table 2 summarizes the computed dimensions taking into account all these considerations.

Table 2. Focus depth comparing multielement ring array with an equivalent continuous ring array using Equation (1) and the resonance frequencies obtained from the COMSOL simulations. The F_d is calculated with all actuated smaller rings. (c = 685 m/s).

Number of Rings	Dimensions		Focal Point → Fd (μm)	
	D (μm)	d (μm)	Continuous Ring; f = 2.3 MHz	Multielement Ring; f = 11.3 MHz
1	74.28	17.68	13.7	67.4
2	139.28	82.68	50.3	247.3
3	204.28	147.68	109.2	536.6
4	269.28	212.68	190.4	935.4
5	334.28	277.68	293.8	1444

As the parameter λij in Equation (2) and the added virtual mass are only known for defined d/D ratios [19,22], we performed some FEM simulations with COMSOL to find the resonance frequencies for the first continuous ring in air and liquid, obtaining 8.9 and 2.3 MHz respectively. The resonance frequency for the continuous ring is 3 times lower than that of the multielement ring (27.8/8.9), which is close to the $f_{squared}/f_{annular}$ ratio when the annular width corresponds to the square PMUT diagonal (see Figure 1 when $l = w$). Figure 3 shows the frequency response in liquid for the first ring corresponding to the continuous ring and the multielement ring array. The normalized pressure maps for both rings, considering a propagation medium of 200 μm radius, are shown in Figure 3b,c. The multielement array achieves a higher focus depth in comparison to a continuous ring (considering the same actuated rings) due to its higher operation frequency (see F_d in Table 2), concentrating the acoustic pressure in a narrower beam, but it is affected by side lobes. The focus depth (F_d) is presented in Table 2 for both the multielement ring array device and the continuous concentric ring device considering the same area in both cases. The advantage of focus depth control for the multielement ring array from 67 μm to 1.44 mm is clearly demonstrated.
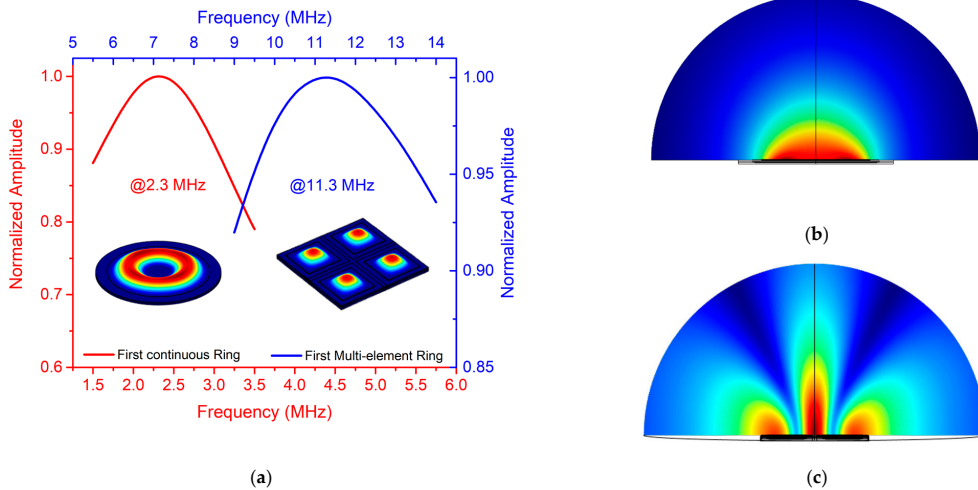
Figure 3. FEM COMSOL dynamic simulation in liquid for the first continuous ring and the first multielement ring: (**a**) frequency response where left-bottom (red curve) corresponds to continuous ring and right-top (blue curve) corresponds to multielement ring; (**b**) continuous ring pressure map at 2.3 MHz; (**c**) multielement ring pressure map at 11.3 MHz.

2.2. Acoustic Performance Simulation for the PMUT Array

Acoustic simulations using Field II [23,24] were performed to predict the acoustic performance of the multielement ring array working in liquid (FC-70, c = 685 m/s) at a center frequency of 11.3 MHz (according to the FEM COMSOL simulations shown in Figure 3).

Figure 4 shows the 2D normalized pressure map from 20 μm to 3 mm along the axial direction and from −500 μm to 500 μm laterally, keeping the array center at (0, 0) coordinates. Note that, as Table 2 shows, by playing with the number of active rings, the focal point can be changed without any extra delay. The beam focusing range from these Field II simulations is a bit higher, reaching 1.6 mm, due to the simulation considering the real element distribution inside the multielement ring array (gap spaces between elements), which is small and is not considered in Equation (1).
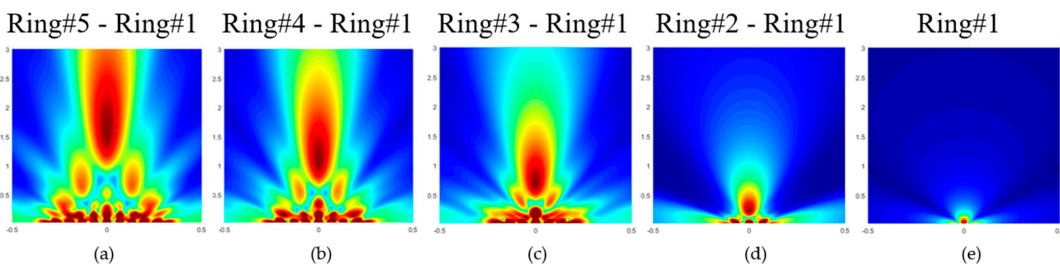
Figure 4. Field II simulated pressure map for the multielement array when transmitting with (**a**) all rings, (**b**) four rings (ring #1 to ring #4), (**c**) three rings (ring #1 to ring #3), (**d**) two rings (ring #1 to ring #2), and (**e**) one ring (ring #1). Axis: Scan in x-direction from −0.5 to 0.5 mm, z-direction from 0.02 to 3 mm.

On the other hand, controlling the applied signal phase, the focal point can also be modified (electronic focusing), achieving higher pressure levels than at the natural focus. In Figure 5a, the red axis shows the dependence of the transmission improvement on the acoustic focusing factor (Sac), defined as $Sac = Fac/N_0$ where Fac is the actual focus and

N_0 is the natural focus (1.6 mm). In the simulations, the delays were applied to all the elements that make up each ring. As expected, when the focus point is close to natural focus, there is no transmission sensitivity enhancement (value close to 1), so to ensure at least twice as much the transmission pressure, the acoustic focusing factor should be 0.8 (and consequently the focal point will be 1.3 mm). Furthermore, when it is focused, the acoustic energy is concentrated in narrow beams, decreasing the focus width, and consequently improving the capability to detect small targets. On the other hand, in Figure 5a, the blue axis shows the dependence of the beamwidth at -6 dB on the acoustic focusing factor. In this case, the beamwidth is wider when the acoustic focusing factor is close to 1, as expected.
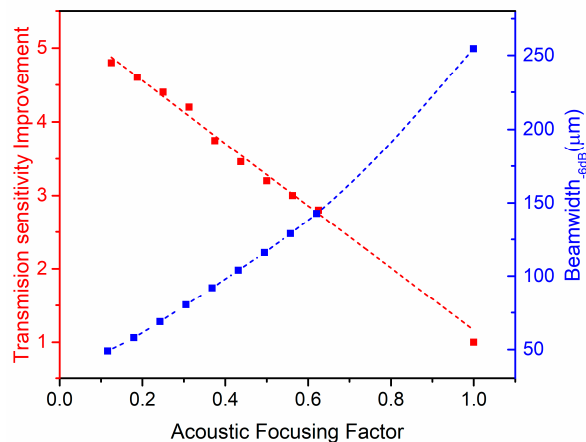
(a)
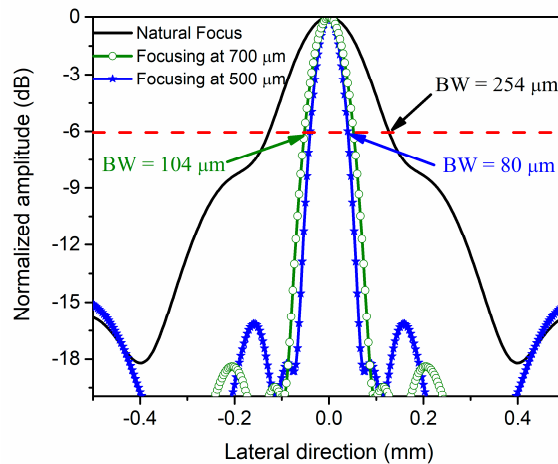
(b)

Figure 5. Field II simulations: (**a**) dependence of the transmission sensitivity improving factor (red curve) and the beamwidth (blue curve) on the acoustic focusing factor; (**b**) cross-section in lateral direction at two different focal points (500 and 700 μm, corresponding to acoustic focusing factors of 0.3 and 0.44, respectively).

Figure 5b shows the acoustic pressure field profile along the lateral direction at different focus points, including the natural focus (N_0). As can be seen, the multielement ring array is affected by the generation of unwanted lobes (side lobes). For focus depths greater than 500 µm, these side lobes are below -15 dB, which is proven to be the required dynamic range for imaging [25].

3. Experimental Results and Discussion

3.1. Electrical Characterization

The electrical characterization in the air was done using the multiring PMUTs bonded to a PCB and using a network analyzer (Agilent Technologies, Santa Clara, CA, USA). Figure 6a left inset shows a schematic of the experimental set-up. Each ring was powered with 10 dBm continuous wave to obtain the S-parameters. The frequency response, S_{11}, for each ring, gives a center value of 17.5 MHz, which corresponds to the resonance frequency of an individual PMUT (single clamped square PMUT, as reported in [26]).

(**a**)

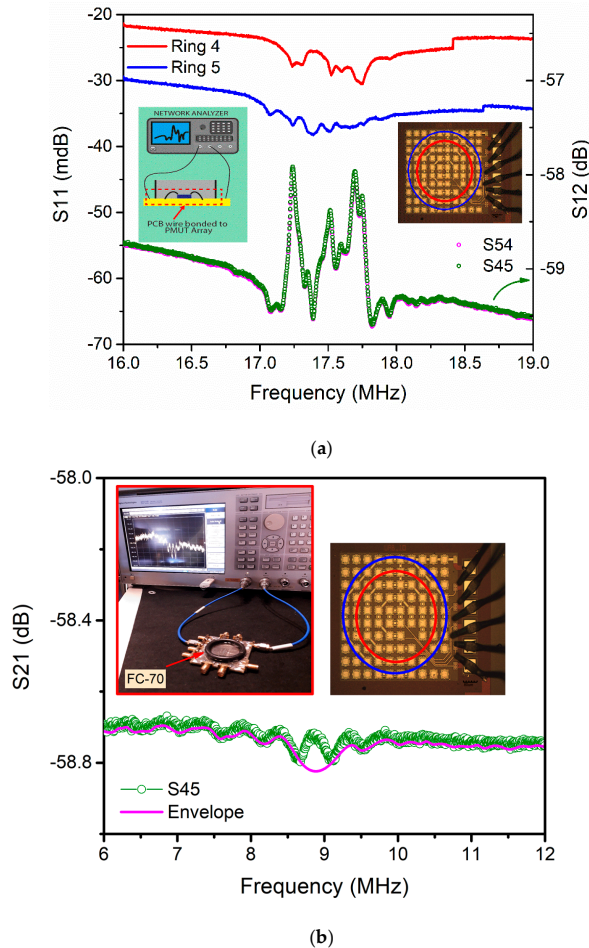(**b**)

Figure 6. Scattering parameter measurements (**a**) in air (S_{11}, red and blue curves with left axis; S_{12}, green and rose curves with right axis) using rings #4 and #5 and (**b**) in Fluorinert, S_{12} using rings #4 and #5.

In Figure 6a, the red curve shows the frequency response corresponding to ring #4, and the blue curve shows the ring #5 response. The multiple peaks are a consequence of the multiple individual PMUTs forming the ring.

In order to analyze the electrical crosstalk effect in the proposed device, the S_{21} magnitude between pairs of rings was obtained [27]. In Figure 6a, the dotted graph (green curve) corresponds to the measurements between ring #5 and ring #4. The crosstalk level was obtained considering the S_{21} at 19 MHz (out of the resonance peak), giving for this case −59.4 dB which represents 2.1 mVpp (for a 10 dBm input signal). Even if the crosstalk level during the resonance is considered, there would be no significant actuation voltage in the non-actuated rings, decreasing the risk of acoustic interferences. Table 3 summarizes the obtained crosstalk between rings. Note that the lowest level, −77 dB, is between ring #1 and ring #4 and not between the most widely spaced rings (ring #1 and ring #5). This can be attributed to the specific layout of the electrical pads (consecutive pads for rings #1 and #5). The low crosstalk levels (below −56.8 dB) between multielement rings will allow driving each ring independently, ensuring a well-controlled and efficient axial beam-focusing.

Table 3. Crosstalk between rings, according to S21 experimental magnitude at 19 MHz in air.

dB	1	2	3	4	5
1	×	−56.8	−76	−77	−70
2		×	−69.5	−74	−72.5
3			×	−62	−69.5
4				×	−59.4
5					×

The variation of resonance frequencies for each of the individual resonators due to mismatching during the fabrication can be a drawback. This problem can be alleviated when the system is under liquid operation due to the acoustic radiation mass loading effect from the liquid which widens the resonance frequency curve. For a square PMUT transducer under liquid operation in one side, this mass load damping can be quantified according to Equation (5) (where ρ_{liquid} is the liquid density, a is the transducer side, and μ is the mass per unit area) [28], which gives $\beta = 2.46$.

$$\beta = 0.342 \frac{\rho_{liquid} \times a}{\mu} \tag{5}$$

Then, the expected resonance frequency in liquid will be approximately half the air resonance frequency, i.e., 9.4 MHz ($f_{air}/\sqrt{(1 + \beta)}$). Figure 6b shows the electrical frequency response of the crosstalk between ring #5 and ring #4 in FC-70. The resonance peaks appear between 8 and 10 MHz, being in correspondence with the expected value (9.4 MHz). On the other hand, in liquid, the high acoustic radiation damping is translated into a low quality factor and consequently to higher fractional bandwidth, hence lowering the S_{21} magnitude at resonance and smoothing the single-element frequency peaks of the same ring.

3.2. Output Pressure Measurements

The multielement ring array was immersed in Fluorinert (c = 685 m/s, ρ = 1940 kg/m^3) and each ring was driven by a signal generator (Keysight, Santa Rosa, CA, USA) with four sine cycles with 24 Vpp. The acoustic pressure was measured with a commercial hydrophone from ONDA (Santa Clara, CA, USA) and displayed in an oscilloscope (Santa Rosa, CA, USA); Figure 7 shows the set-up. The experimental resonance frequency (tuned to maximize hydrophone signal) was 8.7 MHz in accordance with the electrical measurements.
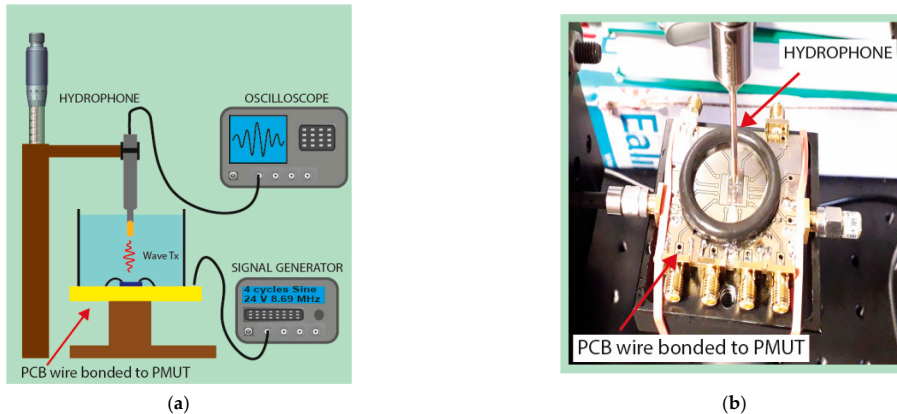
Figure 7. Set-up for the acoustic characterization as actuator in liquid environment (**a**) schematic set-up and (**b**) photo of the experimental set-up.

In order to avoid artifacts on the pressure field characterization due to spatial averaging effects (consequence of the influence of the hydrophone's diameter), there is a limitation on the minimum axial distance between the hydrophone and the ultrasound transducer. Equation (6) should be used [29] to estimate the maximum effective hydrophone radius (a_h), taking into account the transducer radius (a_1), the wavelength in the acoustic media ($\lambda = c/f$), and the distance between the hydrophone and the transducer (l). In our experimental set-up, a_h =100 µm (HNC-0200 radius), c = 685 m/s, and f = 8.69 MHz, giving the ratio $l/2a_1$ = 5.06, which means different minimum distances depending on the ring size; Table 4 summarizes these values for all cases (*Lmin* represents l in Equation (6)).

$$a_h = \frac{\lambda}{8a_1}\left(\sqrt{l^2 + a_1^2}\right) \tag{6}$$

Therefore, in the experiments, the hydrophone was placed at the distances detailed in Table 4 and raised every 50 µm to obtain the axial pressure at different heights without distortion. These distances are in the far-field, which allows defining the acoustic pressure by Equation (7) [18] (where R_0 is the Rayleigh distance, P_0 is the surface pressure, and z is the axial distance).

$$P(z) = \frac{P_0 R_0}{z} \tag{7}$$

Table 4. Individual ring characterization as actuator in FC-70 using HNC-0200 from ONDA (at 8.69 MHz). *Lmin* is computed from Equation (6); *NP* is experimentally measured.

Ring	*Lmin* (mm)	*NP* (kPa×mm)	Pressure (kPa) at 1.2 mm
1	0.531	6.33	5.28
2	1.19	10.04	8.37
3	1.84	14.92	12.43
4	2.2	15.41	12.84
5	3.16	14.2	11.79

The measured points were fitted according to Equation (7), obtaining from the slope the normalized pressure with the distance $NP = P_0 R_0$ (Pa×mm) for each ring (see the results in Table 4). From these measurements, the maximum attainable pressure at the natural focus (~1.2 mm according to Field II simulations at 8.69 MHz) can be computed,

evaluating the NP for each ring at 1.2 mm and adding them because, at this point, all acoustic waves are in phase, allowing constructive interference. Finally, the computed total pressure is 50.71 kPa$_{pp}$. This output pressure could be increased until 4.8 times, for example, focusing at 200 μm (see the improvement factor in Figure 5a).

The normalized acoustic pressure (ST) at 1.5 mm from a 1 mm^2 PMUT array area when it is driven with 1 V was used to compare the multielement ring array with other ultrasound transducers. Taking the previously computed pressure when all rings are excited, 50.71 kPa$_{pp}$, and normalizing with the distance (1.2 mm) and the applied voltage (24 Vpp), we obtain a surface pressure of 2.54 kPa$_{pp}$×mm×V^{-1}. According to this and considering the entire area of the multielement ring array ($\pi \times (D_5{}^2 - d_1{}^2) = 0.35$ mm^2), the normalized pressure at 1.5 mm is 4.84 kPa/V/mm^2. Table 5 compares the multielement ring array performance as an actuator with the state-of-the-art approaches, demonstrating a promising performance with a minute area. The normalized output pressure is 55% higher than that reported for arrays of annular AlN flexural rings (2.2 kPa/V/mm^2 using five-channel ring [6]) and even 92% higher than that for a system for intravascular imaging [2].

Table 5. Comparison of ring arrays with different technological approaches.

Parameters	[30]	[2]	[6]	This Work
	2011	2018	2019	
Transducer technology	CMUT	PZT matrix	AlN PMUT	AlN PMUT
Configuration	Multielement ring	Multielement ring	Continuous ring	Multielement ring
Medium	Vegetable oil	Water	Mineral oil	FC-70
Frequency (MHz)	1.2	14	6	8.69
Area (mm^2)	12.76 [1]	6.28 [1]	7.07 [1]	0.35
Pressure (kPa/V@mm)	13.2 @1.5 [2]	0.4 @6	2.8 @5.4	2.11 @1.2
NP (kPa×mm/V)	19.8	2.4	15.2	2.54
ST (kPa/V/mm^2)	1.11 [3]	0.38 [3]	2.18 [3]	4.84

[1] Computed considering the transducers' dimensions. [2] Taking the peak-to-peak pressure (2 × 66 kPa) and the applied voltage (10 V). [3] Computing as the ratio between NP evaluated at 1.5 mm and the area.

In order to complete a deeper characterization of the performance of the system as an actuator and compare the presented multielement array system with a continuous AlN flexural PMUT array [6], the pressure normalized with the area and energy density, ($\bar{p}$), defined in Equation (8) was computed (where V is the applied voltage (24 V), A_{ap} is the area (0.35 mm^2), $e_{31,f}$ is the piezoelectric coefficient ($e_{31,f} = e_{31} - \upsilon \times e_{33} = -1.065$ C/m^2), λ is the wavelength ($\lambda = c/f = 79.86$ μm), and p is the total pressure (50.71 kPa at 1.2 mm)).

$$\bar{p} = p \times \frac{\lambda}{V \times A_{ap} \times e_{31,f}} \tag{8}$$

Applying this expression at 1.2 mm (the natural focus) when the multielement five-ring array is used, a normalized pressure per area per energy density of 453 kPa×mm^{-2}/J×cm^{-3} is obtained, which is 2.5× better than that of the five-channel continuous ring array without delays presented in [6] (184 kPa×mm^{-2}/J×cm^{-3}). Compared with the result when the same system is focused at 1.9 mm (588 kPa×mm^{-2}/J×cm^{-3}, [6]), our multielement ring array still exhibits a competitive value and will allow higher pressure output at shorter focus depths if some phase-beam focusing is used.

3.3. Pulse-Echo Measurements

Thanks to its reduced area, the multielement ring array can be a candidate for catheter-based ultrasound imaging; consequently, it was also characterized as a pulse-echo acoustic system. In this case, the central ring was used as a receiver, and the rings #5, #4, and #3 were used as transmitters. The same signal generator was used to drive the transmission with four sine cycles at 8.69 MHz with 24 Vpp. The receiving ring was externally connected

to an integrated CMOS voltage amplifier with a gain of 25 dB [31]. The liquid thickness over the PMUT chip was tuned to obtain different times of flight (ToFs) and consequently different acoustic paths (*AP = ToF × c*) giving a round trip from 1 to 5 mm; Figure 8 shows the set-up.
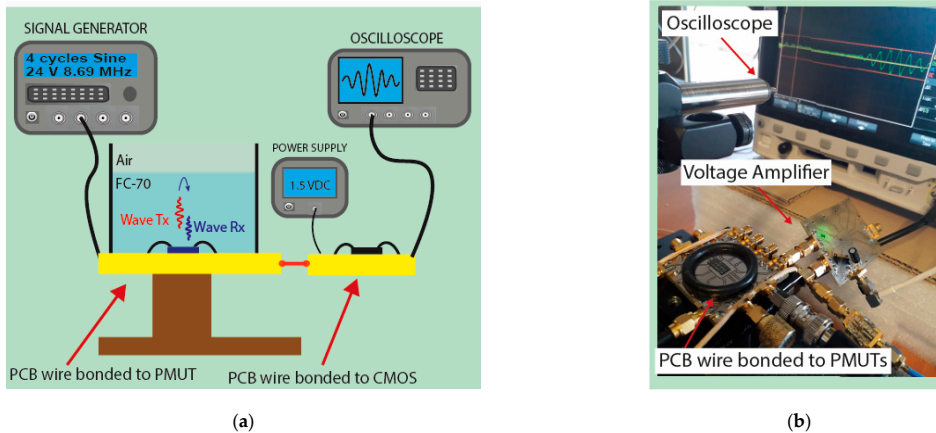

(a)   (b)

Figure 8. (**a**) Schematic set-up for pulse-echo measurements; (**b**) photo of the experimental set-up.

Figure 9 shows the measured echo voltage and its dependence on the acoustic path using ring #3 (blue points) (same measurements were also acquired for ring #4 and ring #5). Taking the fitting results, the receiving sensitivity (SR) can be computed as *Rx/Pt* (where *Pt* is defined by the normalized pressure, NP/z, in Table 4), giving an average value of 441.6 nV/Pa (($Rx_{central}/Pt_3 + Rx_{central}/Pt_4 + Rx_{central}/Pt_5$)/3). This receiving sensitivity is affected by the parasitic capacitances between the PMUT and voltage amplifier (PCB, connectors, cables, etc.) according to Equation (9) [32]:

$$SR = SR_{EOC} \times G \times \frac{C_{centralRing}}{C_{centralRing} + C_{inLNA} + C_{parasitic}} \tag{9}$$

where SR_{EOC} is the "end-of-cable open-circuit sensitivity"; *G* is the amplifier gain (25 dB); $C_{centralRing}$ is the receiving element capacitance (254.9 fF extracted from COMSOL); C_{inLNA} is the voltage amplifier equivalent capacitance (609 fF) [16]; and $C_{parasitic}$ is the parasitic capacitance associated with PCBs, connectors, cables, etc. (at 6.5 pF). Hence, the intrinsic sensitivity (SR_{EOC}) for the smaller inner ring is 717.8 nV/Pa. This value is very competitive in comparison with some commercial hydrophones with sizes comparable to our ring #1 (diameter of ~149 μm) but with smaller nominal SR_{EOC} pressure sensitivities: HNC-0200 from ONDA (200 μm diameter, SR_{EOC} = 28 nV/Pa [32]) or NH0200 from Precision Acoustics (200 μm, 55 nV/Pa with amplifier [33]).

The time-domain response shown as the red curve in Figure 10 corresponds to pulse-echo measurement when ring #4 is used to transmit and the central ring is used to receive. The time-of-flight of the received echo is 2.34 μs, which gives an FC-70 thickness of 800 μm ($FC70_{thickness} = ToF \times c/2$). Taking the ringdown, the fast Fourier transform was computed (see Figure 10, blue curve), giving a resonance frequency (f_0) of 8.8 MHz with fractional bandwidth at −6 dB close to 54%.
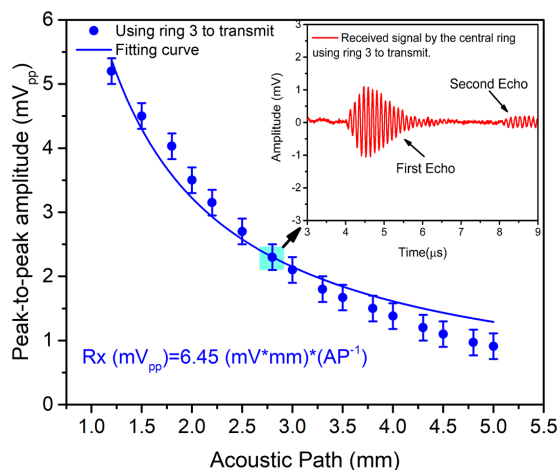
Figure 9. Pulse-echo experiment with ring #3 as transmitter and ring #1 as receiver. The received signal is plotted as a function of the acoustic path, *AP*, using FC-70-air interface as reflecting surface. Error bar = $\pm 200\ \mu$V. Inset: Time-domain signal at 2.8 mm round trip.
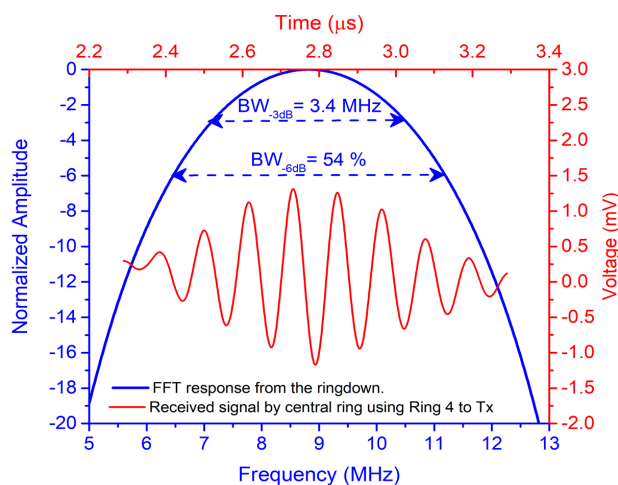

Figure 10. Acoustic pulse-echo measurement using ring #4 to transmit and central ring to receive (FC-70 thickness at 800 μm). Red curve (top-right red axis): time-domain response. Blue curve (left-bottom blue axis): FFT from the ringdown.

The acoustic beamwidth was determined through a pulse-echo experiment where ring #3 and ring #4 were used as transmitters and the central ring was used as the receiver. A 150 μm diameter conductive wire was used as a reflecting surface and was placed at 790 μm over the array's surface. The wire covered all PMUTs in one lateral direction, and in the other direction, it was mechanically displaced 500 μm to each side from the center of the array (see Figure 11 inset). Figure 11 provides experimental and simulation results (using Field II) for when only ring #3 or ring #3 + ring #4 were excited. According to the simulations, the beamwidth at −6 dB is around 160 μm when ring #3 + ring #4 are used (blue lines in Figure 11) and is 180 μm when only ring #3 is used (red lines in Figure 11).

Moreover, the maximum amplitude increases by about 6 dB when both rings are used. The experimental points demonstrate a very good agreement with the simulated ones.
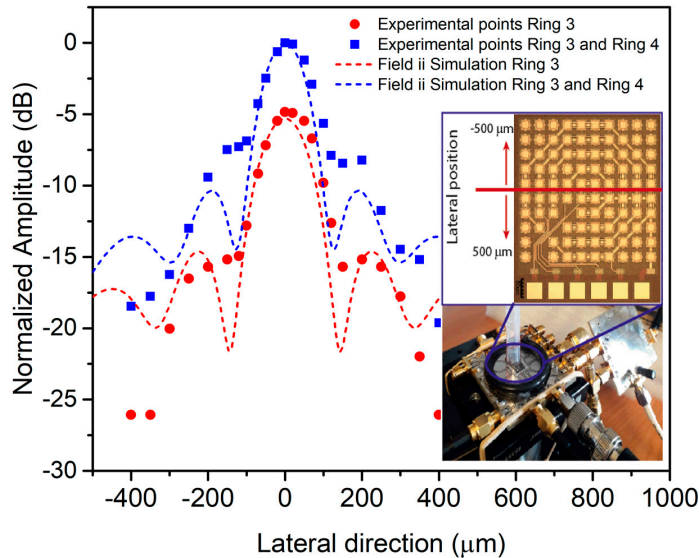

Figure 11. Simulated and experimental behavior along the lateral direction at 790 μm axial distance. Red curves correspond to ring #3 as transmitter and blue curves correspond to ring #3 + ring #4 (dots: experimental points; lines: Field II simulations). Inset: Experimental set-up.

3.4. Focusing Capabilities

The focusing capabilities were demonstrated through a pulse-echo experiment using ring #3 and ring #5 as transmitters and the central ring as a receiver (see set-up in Figure 8). The acoustic path was tuned in the same way, changing the FC-70 thickness and measuring the time-of-flight corresponding to ring #3 (nearest to receiver element).

Figure 12 (inset) shows the signal received by the central ring when ring #3 and ring #5 are used separately. As can be seen, the received acoustic waves from ring #3 and ring #5 are not in phase; in consequence, when both rings are driven together, the total acoustic pressure is less than the sum of both echoes. The behavior without any delays is shown in Figure 12 (green points), giving a maximum level of 6.59 mVpp close to 1.5 mm round trip (natural focus). Considering this value and the computed receiving sensitivity (441.6 nV/Pa), the pressure on the array's surface is 14.9 kPa_{pp}.

For electronic focusing or phased-array rings, 34 ns was applied to ring #3 during transmission to allow both acoustic waves to arrive in phase, achieving a maximum acoustic pressure at 0.6 mm (see Figure 12, orange points). Computing the focusing improvement factor as the ratio between maximum received echoes (8.4 mVpp/6.59 mVpp), a 1.3× improvement factor is obtained, which is translated into an acoustic pressure of 19.4 kPa_{pp} (1.3 × 14.9 kPa_{pp}).
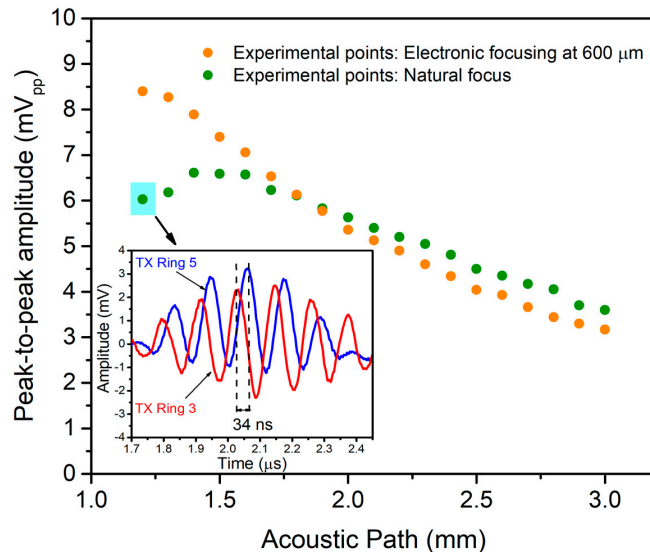
Figure 12. Voltage measured by the central ring when ring #3 and ring #5 are driven at the same time (green points) or electronically focused (orange points). Inset: Time-domain response of the echo signal from ring #3 and ring #5 to determine the needed time delay (34 ns).

3.5. 1D Line-Scan Imaging

The imaging capability was tested using a Cu grating phantom with three holes with different widths (600, 900, and 1040 μm) and gaps (1.2 and 1 mm) between them (see Figure 13 inset). The sample was immersed in FC-70 and placed at 790 μm on top of the multielement ring array. A micrometric system was used to displace it along the x-direction (perpendicular to the holes) with steps of 50 μm, while the y-direction was fixed at the sample's center. Two rings (#3 and #4) were driven with four cycles at 8.69 MHz with 24 Vpp, and the central ring (connected to the CMOS voltage amplifier as before) was used to detect the reflected echoes (see the set-up in Figure 8).

Figure 13 (red points) show the experimental peak-to-peak amplitudes received by the central ring, giving a maximum value of around 7.5 mV$_{PP}$ and clearly reproducing the AA' profile with the three holes.

On the other hand, a scatter phantom close to the grating was modeled in Field II with the purpose of obtaining the scanning pattern under the same assumptions. The normalized signal received by the central ring when rings #3 and #4 are excited is shown in Figure 13 (blue points), demonstrating a good agreement with the experimental one and validating the capability to perform acoustic imaging with the multielement ring PMUT presented.
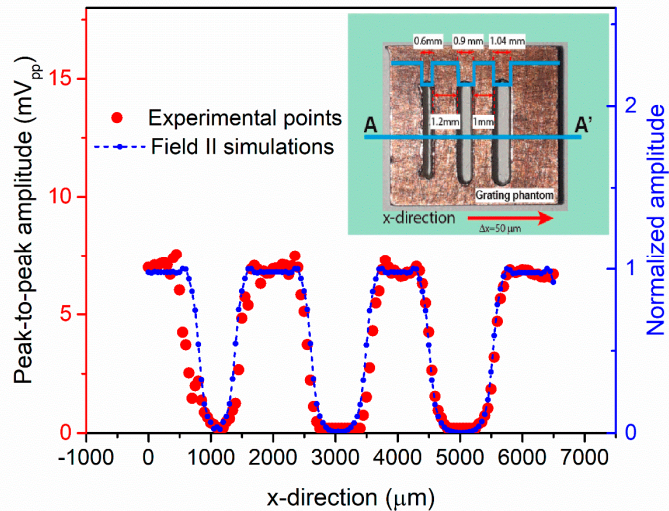
Figure 13. Pulse-echo ultrasonic 1D image of a grating phantom. Red curve: experimental points; blue curve: Field II simulations. Inset: Grating phantom with A-A' scanned profile.

4. Conclusions

This paper presents a multielement ring ultrasound transducer array based on AlN PMUTs fabricated with a MEMS-on-CMOS process. The presented multielement ring array eliminates the dependence of acoustic wave frequency on the diameters of the annular array and achieves accurate control of the focus depth (from 67 µm to 1.4 mm), which is 4.9 times greater than that of the equivalent continuous ring array. The low crosstalk between different rings (levels under −56.8 dB) allows it to be used in modern ultrasound applications where the maximum of the ultrasound beam must be controlled efficiently in the axial direction. The PMUT-based ring array, with a very reduced area, generates high pressure levels ($4.84\,kPa/V/mm^2$ at 1.5 mm) at 8.7 MHz in a liquid environment, being very competitive with other annular arrays using bulk piezoelectric, CMUT, or PMUT fabrication approaches. The pulse-echo experiments with a voltage amplifier (gain of 25 dB) externally connected to the central ring gave a receiving sensitivity of 441.6 nV/Pa, which could be increased around 700 nV/Pa when the PMUT is monolithically integrated on the CMOS circuitry. The 1D imaging test through mechanical scanning demonstrates the possibility to obtain high-performance ultrasound imaging systems. With this performance and considering its small size (below $1\,mm^2$), the presented multielement ring array fabricated with a PMUT-on-CMOS technology becomes an interesting ultrasound transducer for applications in which size, cost, reliability, and performance are a must, such as wearables and catheter-based systems. Greater focal depth and output pressure can be achieved at the same frequency by increasing the number of rings within the same technology.

Author Contributions: Conceptualization, E.L., A.U., and N.B.; device design, simulations, and acoustic experiments, E.L.; validation and analysis, E.L., I.Z., and N.B.; writing—original draft preparation, E.L.; writing—review and editing, I.Z., A.U., and N.B.; supervision, A.U. and N.B.; project administration, N.B. All authors have read and agreed to the published version of the manuscript.

Institutional Review Board Statement: Not applicable.

Informed Consent Statement: Not applicable.

Data Availability Statement: Not applicable.

References

1. Dangi, A.; Agrawal, S.; Tiwari, S.; Jadhav, S.; Cheng, C.; Datta, G.R.; Troiler-McKinstry, S.; Pratap, R.; Kothapalli, S.-R. Ring PMUT array based miniaturized photoacoustic endoscopy device. In Proceedings of the Photons Plus Ultrasound: Imaging and Sensing 2019, San Francisco, CA, USA, 3–6 February 2019; p. 1087811.
2. Janjic, J.; Tan, M.; Daeichin, V.; Noothout, E.; Chen, C.; Chen, Z.; Chang, Z.Y.; Beurskens, R.H.S.H.; Van Soest, G.; Van Der Steen, A.F.W.; et al. A 2-D Ultrasound Transducer With Front-End ASIC and Low Cable Count for 3-D Forward-Looking Intravascular Imaging: Performance and Characterization. *IEEE Trans. Ultrason. Ferroelectr. Freq. Control* **2018**, *65*, 1832–1844. [CrossRef]
3. Moini, A.; Nikoozadeh, A.; Choe, J.W.; Chang, C.; Stephens, D.N.; Sahn, D.J.; Khuri-Yakub, P.T. Fully integrated 2D CMUT ring arrays for endoscopic ultrasound. In Proceedings of the IEEE International Ultrasonics Symposium, IUS, Tours, France, 18–21 September 2016; pp. 9–12.
4. Zahorian, J.; Hochman, M.; Xu, T.; Satir, S.; Gurun, G.; Karaman, M.; Degertekin, F.L. Monolithic CMUT-on-CMOS integration for intravascular ultrasound applications. *IEEE Trans. Ultrason. Ferroelectr. Freq. Control* **2011**, *58*, 2659–2667. [CrossRef] [PubMed]
5. Bawiec, C.R.; N'Djin, W.A.; Bouchoux, G.; Sénégond, N.; Guillen, N.; Chapelon, J.Y. Preliminary Investigation of a 64-element Capacitive Micromachined Ultrasound Transducer (CMUT) Annular Array Designed for High Intensity Focused Ultrasound (HIFU). *IRBM* **2018**, *39*, 295–306. [CrossRef]
6. Eovino, B.E.; Liang, Y.; Lin, L. Concentric PMUT Arrays for Focused Ultrasound and High Intensity Applications. In Proceedings of the 2019 IEEE 32nd International Conference on Micro Electro Mechanical Systems (MEMS), Seoul, Korea, 27–31 January 2019; pp. 771–774.
7. Li, G.; Qiu, W.; Zhang, Z.; Jiang, Q.; Su, M.; Cai, R.; Li, Y.; Cai, F.; Deng, Z.; Xu, D.; et al. Noninvasive Ultrasonic Neuromodulation in Freely Moving Mice. *IEEE Trans. Biomed. Eng.* **2019**, *66*, 217–224. [CrossRef] [PubMed]
8. Kim, H.; Kim, S.; Sim, N.S.; Pasquinelli, C.; Thielscher, A.; Lee, J.H.; Lee, H.J. Miniature ultrasound ring array transducers for transcranial ultrasound neuromodulation of freely-moving small animals. *Brain Stimul.* **2019**, *12*, 251–255. [CrossRef] [PubMed]
9. Hosseini, S.; Laursen, K.; Rashidi, A.; Mondal, T.; Corbett, B.; Moradi, F. S-MRUT: Sectored-Multiring Ultrasonic Transducer for Selective Powering of Brain Implants. *IEEE Trans. Ultrason. Ferroelectr. Freq. Control* **2021**, *68*, 191–200. [CrossRef] [PubMed]
10. Weber, M.J.; Yoshihara, Y.; Sawaby, A.; Charthad, J.; Chang, T.C.; Arbabian, A. A Miniaturized Single-Transducer Implantable Pressure Sensor with Time-Multiplexed Ultrasonic Data and Power Links. *IEEE J. Solid-State Circuits* **2018**, *53*, 1089–1101. [CrossRef]
11. Shi, C.; Andino-Pavlovsky, V.; Lee, S.A.; Costa, T.; Elloian, J.; Konofagou, E.E.; Shepard, K.L. Application of a sub-0.1-mm^3 implantable mote for in vivo real-time wireless temperature sensing. *Sci. Adv.* **2021**, *7*, 1–10. [CrossRef]
12. Wang, J.; Zheng, Z.; Chan, J.; Yeow, J.T.W. Capacitive micromachined ultrasound transducers for intravascular ultrasound imaging. *Microsyst. Nanoeng.* **2020**, *6*, 73. [CrossRef]
13. Wang, D.; Filoux, E.; Levassort, F.; Lethiecq, M.; Rocks, S.A.; Dorey, R.A. Fabrication and characterization of annular-array, high-frequency, ultrasonic transducers based on PZT thick film. *Sensors Actuators A Phys.* **2014**, *216*, 207–213. [CrossRef]
14. Brenner, K.; Ergun, A.S.; Firouzi, K.; Rasmussen, M.F.; Stedman, Q.; Khuri-Yakub, B. Advances in capacitive micromachined ultrasonic transducers. *Micromachines* **2019**, *10*, 152. [CrossRef]
15. Jiang, X.; Lu, Y.; Tang, H.-Y.; Tsai, J.M.; Ng, E.J.; Daneman, M.J.; Boser, B.E.; Horsley, D.A. Monolithic ultrasound fingerprint sensor. *Microsyst. Nanoeng.* **2017**, *3*, 17059. [CrossRef]
16. Zamora, I.; Ledesma, E.; Uranga, A.; Barniol, N. Monolithic Single PMUT-on-CMOS Ultrasound System with +17 dB SNR for Imaging Applications. *IEEE Access* **2020**, *8*, 142785–142794. [CrossRef]
17. Lu, Y.; Heidari, A.; Horsley, D.A. A High Fill-Factor Annular Array of High Frequency Piezoelectric Micromachined Ultrasonic Transducers. *J. Microelectromechanical Syst.* **2015**, *24*, 904–913. [CrossRef]
18. Blackstock, D.T. *Fundamentals of Physical Acoustics*; John Wiley & Sons: New York, NY, USA, 2000; ISBN 0471319791.
19. Blevins, R.D. *Formulas for Natural Frequency and Mode Shape*; Van Nostrand Reinhold Co., Ed.; Litton Educational Publishing, Inc.: New York, NY, USA, 1979.
20. Horsley, D.; Lu, Y.; Rozen, O. Flexural Piezoelectric Resonators. In *Piezoelectric MEMS Resonators*; Bhugra, H., Piazza, G., Eds.; Springer International: Cham, Switzerland, 2017; pp. 153–173, ISBN 9783319286884.
21. Ledesma, E.; Zamora, I.; Uranga, A.; Barniol, N. Tent-plate AlN PMUT with a piston-like shape under liquid operation. *IEEE Sens. J.* **2020**, *20*, 11128–11137. [CrossRef]
22. Amabili, M.; Frosali, G.; Kwak, M.K. Free vibrations of annular plates coupled with fluids. *J. Sound Vib.* **1996**, *191*, 825–846. [CrossRef]
23. Jensen, J.A.; Svendsen, N.B. Calculation of pressure fields from arbitrarily shaped, apodized, and excited ultrasound transducers. *Ultrason. Ferroelectr. Freq. Control. IEEE Trans.* **1992**, *39*, 262–267. [CrossRef] [PubMed]
24. Jensen, J.A. Field: A program for simulating ultrasound systems. *Med. Biol. Eng. Comput.* **1996**, *34*, 351–352.
25. Przybyla, R.J.; Tang, H.; Member, S.; Guedes, A.; Shelton, S.E.; Horsley, D.A.; Boser, B.E. 3D Ultrasonic Rangefinder on a Chip. *IEEE J. Solid-State Circuits* **2015**, *50*, 320–334. [CrossRef]

26. Ledesma, E.; Zamora, I.; Tzanov, V.; Torres, F.; Uranga, A.; Barniol, N.; Marigó, E.; Soundara-Pandian, M. Liquid operable AlN PMUT with high output pressure capabilities. In Proceedings of the 2019 IEEE International Ultrasonics Symposium (IUS), Glasgow, UK, 6–9 October 2019; pp. 251–254.

27. He, L.M.; Xu, W.J.; Liu, W.J.; Wang, X.B.; Zhou, J.; Ren, J.Y. Performance and Crosstalk Evaluation of 2-D Array Piezoelectric Micromachined Ultrasonic Transducer with 3-D Finite Element Simulation. In Proceedings of the IEEE International Ultrasonics Symposium, IUS, Glasgow, UK, 6–9 October 2019; pp. 792–795.

28. Bernstein, J.J.; Finberg, S.L.; Houston, K.; Niles, L.C.; Daniel Chen, H.; Eric Cross, L.; Li, K.K.; Udayakumar, K. Micromachined high frequency ferroelectric sonar transducers. *IEEE Trans. Ultrason. Ferroelectr. Freq. Control* **1997**, *44*, 960–969. [CrossRef]

29. Smith, R.A. Are hydrophones of diameter 0.5 mm small enough to characterise diagnostic ultrasound equipment? *Phys. Med. Biol.* **1989**, *34*, 1593–1607. [CrossRef] [PubMed]

30. Cristman, P.; Oralkan, O.; Mandella, M.; Solgaard, O.; Contag, C.; Khuri-Yakub, B.T. Interdigitated annular CMUT arrays for ultrasound assisted delivery of fluorescent contrast agents. In Proceedings of the IEEE International Ultrasonics Symposium, IUS, Orlando, FL, USA, 18–21 October 2011; pp. 96–99.

31. Zamora, I.; Ledesma, E.; Uranga, A.; Barniol, N. Miniaturized 0.13-μm CMOS Front-End Analog for AlN PMUT Arrays. *Sensors* **2020**, *20*, 1205. [CrossRef] [PubMed]

32. Onda Corporation Hydrophone Handbook. Available online: http://ondacorp.com/Handbook/mobile/index.html#p=12 (accessed on 8 June 2021). [CrossRef]

33. Precision Acoustics Ltd. 0.2 mm Needle Hydrophone (NH0200). Available online: https://www.acoustics.co.uk/pal/wp-content/uploads/2016/05/nh0200-0.2mm-needle-hydrophone-tds.pdf (accessed on 8 June 2021).